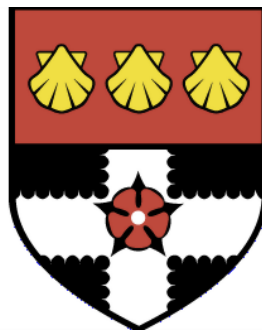# UNIVERSITY OF READING
Department of Meteorology

Characterising Mixing and Pollution Transport in the Urban Boundary Layer

Lewis Phillip Blunn

A thesis submitted for the degree of Doctor of Philosophy

January 2021

Declaration

I confirm that this is my own work and the use of all material from other sources has been properly and fully acknowledged.

Lewis P. Blunn

Abstract

Air quality models (AQMs) are a critical tool in the management of urban air pollution. They can be used for short-term air quality (AQ) forecasts, and in making planning and policy decisions aimed at abating poor AQ. Vertical turbulent mixing and horizontal advection of pollution are crucial processes controlling human exposure to pollution, since they are responsible for transporting pollution away from areas of high concentration.

A simple two-box model is used to investigate the relative importance of urban boundary layer (UBL) pollution transport processes on AQ throughout the day. The lower and upper boxes represent the pollution concentration in the urban canopy and mixed layer respectively. The investigation utilises UBL meteorology and AQ measurements made during an experimental field campaign in London. The results demonstrate that the vertical exchange timescale at canopy top is a key parameter influencing concentration in the canopy. However, canopy height and wind speed in the canopy are likely less important. These findings can be used to inform parametrisation of urban boundary layer pollution transport processes in AQMs.

To analyse the vertical mixing of pollution in the convective boundary layer, where the dominant turbulence ranges from mostly parametrised to mostly resolved in numerical weather prediction (NWP), the Met Office Unified Model (UM) is run at horizontal grid lengths ranging from 1.5 km to 55 m over London. A reduced analytical model is developed and used to determine vertical mixing timescales associated with surface released tracers in the UM. It is found that when vertical mixing is mostly resolved, distinctly different vertical mixing of tracers occurs on O(10 min) timescales. This results in a significant influence on surface level tracer concentrations at the city scale compared to when vertical mixing is mostly parametrised.

Turbulence in urban canopies is investigated using simulations of flow through a wide range of urban canopy geometries. The general characteristics of momentum mixing length profiles are established and a first-order mixing length closure is formulated that is appropriate for parametrisation of urban canopy turbulence in AQMs. Unlike in vegetation canopies the inflection in the time- and horizontally space-averaged velocity profile does not control turbulent mixing in urban canopies.

Overall, this thesis shows that good representation of pollution vertical mixing, both at the scale of the urban canopy and the entire UBL, is crucial for accurate urban AQ prediction.

Acknowledgements

My first acknowledgment goes to my supervisors Dr. Omduth Coceal, Prof. Bob Plant, Prof. Janet Barlow, Dr. Sylvia Bohnenstengel and Dr. Humphrey Lean. They were all very generous with their time, expertise and guidance. From them I have learnt many skills helping me to grow as an independent researcher. I would like to give Dr. Omduth Coceal special thanks for many long insightful discussions, encouraging me to pursue my ideas and for having belief in me.

Thanks to my monitoring committee, Prof. John Methven and Dr. Helen Dacre, for advice and reminding me to focus on the main themes of the thesis as the PhD progressed. Thanks to William McGinty for helping early on with the UM simulations. Thanks also to the National Centre for Atmospheric Science and the University of Reading for funding the PhD and several conference visits.

The Department of Meteorology has been a warm, friendly place in which to study, and I would like to thank the many friends I have made for making the PhD an enjoyable experience.

Finally, I must thank my parents, sister and Hannah for always being there for me.

Contents

Chapter 1

Introduction

1.1 Motivation

The link between poor air quality (AQ) and increased risk of morbidity and mortality is now well established (IARC, 2016). AQ tends to be worst in highly populated regions of the world where there are large pollution emissions (Marlier et al., 2016). Exposure to high levels of pollution is exacerbated by humans living increasingly in urban areas. Currently 50% of the world's population lives in cities and it is estimated that this will rise to 60% over the next 30 years (UN, 2018). The World Health Organisation (WHO) has set out threshold concentrations above which particulate matter (PM), O_3, NO_2 and SO_2 should not exceed (WHO, 2005). The UK government has since set out its own thresholds (DEFRA, 2018).

Air quality models (AQMs) predict pollution concentration and are a crucial tool in abating the exposure of humans to air pollution. AQMs are used to understand the processes leading to poor AQ, so that measures can be taken to meet AQ targets. For example, when designing urban areas, sensitivity of pollution concentrations to different pollution emissions and urban land use scenarios can be investigated, and issues can be tackled accordingly. AQMs are also used to project the influence of the changing environment on pollution concentration (Giorgi and Meleux, 2007). AQMs are necessary for producing an air quality index (e.g. DEFRA, 2020) which can be communicated to the public in a forecast. The forecast enables sensitive individuals to take precautionary measures.

AQMs are very complex. They include the representation of many processes such as pollution emissions, pollution transport, meteorology and chemical transformations. All processes are important and require good representation for AQMs to be accurate (Zhang et al., 2012b; Kukkonen et al., 2012). Pollution transport via time-mean advection and turbulent mixing is crucial since it is responsible for removing pollution from areas of high concentration. Buildings in the urban canopy have a profound impact on the transport processes but often little attention is paid to their representation in AQMs (Baklanov et al., 2014). The focus of this thesis is improving the understanding and modelling of pollution transport in urban areas from the scale of the street to the entire city.

Many investigations of the causes of poor AQ focus on an individual case study region, and use climatological data from AQMs and observations. They link poor AQ to

processes via statistical analysis (e.g. Elminir, 2005; Wise and Comrie, 2005; Pearce et al., 2011; Zhang et al., 2012a) or use simple deterministic models with climatological input data (e.g. Rigby et al., 2006; Rigby and Toumi, 2008). However, in both approaches detailed information on the system is lost, due to averaging over different synoptic and/or diurnal conditions. When the detailed dynamics of a certain process is studied, it is often done in isolation outside of the AQM. This is because the complexity of AQMs makes it prohibitively hard to disentangle the processes and study them individually.

In the context of climate modelling, Held (2005) proposed that a hierarchy of models should be considered when modelling complex systems. Often when aspects of a climate model are developed, they are patched onto the complex model and tested against observations. It is difficult to interpret why some attempts at representing a process perform better than others, because of the complexity of the model. By analysing the process in simpler climate models, a better understanding can be achieved, and progress becomes more efficient.

Taking inspiration from the hierarchical approach, the pollution transport processes in the urban boundary layer (UBL) will be studied in this thesis using Eulerian box models. They are simple to understand, processes can be directly attributed to individual terms in the governing equations, process budgets can easily be constructed and analytical solutions exist under certain conditions. There have been few studies using box models to investigate pollution transport processes in the UBL (e.g. Tennekes, 1977; Venkatram and Cimorelli, 2007; Jensen and Petersen, 1979; Topçu et al., 1993; Rigby et al., 2006). This is partly due to a lack of suitable observations of meteorology and AQ in the UBL for use in box model studies. However, simultaneous meteorological observations of London's boundary layer (BL) and pollution concentration at BT Tower from the ClearfLo (Clean Air for London) project (Bohnenstengel et al., 2015) are available to this work.

The urban canopy influences the horizontal advection and turbulent mixing characteristics near the surface (Britter and Hanna, 2003; Belcher, 2005). Previous studies of pollution dispersion in urban canopies tend to focus on either the vertical exchange between the canopy and the air above (e.g. Caton et al., 2003; Barlow et al., 2004; Salizzoni et al., 2009) or the distribution of pollution within the urban canopy (e.g. Branford et al., 2011; Coceal et al., 2014). Here, the urban canopy and the mixed layer (ML) of the BL will be represented by two separate boxes, coupled via vertical exchange. Thus, transport processes in the urban canopy and the ML, and the interaction between them, can be investigated simultaneously.

With the advance of computational power, the UK Met Office are considering running operational numerical weather prediction (NWP), online AQMs and regional climate models at O(100 m) horizontal grid length in the foreseeable future. At such grid lengths the dominant convective boundary layer (CBL) eddies become resolved explicitly. It is these eddies which are responsible for the majority of pollution vertical mix-

ing in the BL. The influence of vertical mixing representation in the Met Office Unified Model (UM) on pollution distribution in the UBL shall therefore be investigated, across horizontal grid lengths where the CBL eddies are mostly sub-grid and mostly resolved. Sub-grid CBL turbulence is parametrised in NWP, and when CBL turbulence is partially resolved (i.e. in the "grey zone") the parametrisation should be aware of the amount of turbulence that requires parametrisation. A reduced analytical model is developed to analyse the vertical mixing characteristics in the sub-grid and resolved vertical mixing representation regimes. To date there are only a few O(100 m) horizontal grid length NWP studies (e.g. Boutle et al., 2014; Ronda et al., 2017; Lean et al., 2019), and to the author's knowledge this is the first study that includes a passive tracer representing pollution.

A semi-implicit semi-Lagrangian (SISL) advection scheme is currently implemented in the UM (Davies et al., 2005; Wood et al., 2014), and is commonly used in other NWP models and chemical transport models (CTM) in AQMs (Baklanov et al., 2014). The scheme is non-conservative which has been found recently to be a particular issue in the grey zone of CBL turbulence (Lock et al., 2017). The tracer mass non-conservation issues shall be investigated in the UM at a range of horizontal grid lengths covering the sub-grid, grey zone and resolved regimes of CBL turbulence representation.

Exchange of momentum and scalar in the surface layer is typically performed using Monin-Obukhov similarity theory (MOST). However, in urban areas the interaction between the flow and the buildings means MOST breaks down below $2-5$ times the mean building height in the roughness sublayer (Rotach, 1993; Barlow and Coceal, 2009; Barlow, 2014). AQMs require improved turbulence representation in urban canopy models for more accurate pollution transport. AQMs typically use the output from NWP to drive time-mean advection of pollution, and either have their own turbulence parametrisations or use turbulence parameters such as diffusion coefficients from NWP.

An increasingly common approach in NWP has been to represent the energy exchange at building surfaces, the form drag exerted by the buildings and the turbulence in the urban canopy at multiple heights within the canopy (e.g. Martilli et al., 2002; Coceal and Belcher, 2004; Kondo et al., 2005; Hamdi and Masson, 2008). Parametrising the canopy processes in one-dimension (rather than as a single-layer) enables more detailed representation of the complex processes. These parametrisations are most suitable when each vertical profile in the NWP model represents an urban neighbourhood with similar canopy geometry characteristics. The move towards O(100 m) horizontal grid length is advantageous for the approach, since the morphological characteristics of individual neighbourhoods become resolved at this scale.

In multi-layer urban canopy models a constant turbulent length scale is often assumed within the canopy. However, the mixing-layer analogy invoked as justification in vegetation canopies (Raupach et al., 1996) is likely less valid in urban canopies, due to the smaller scale turbulent eddies generated at canopy top (Coceal et al., 2006; Barlow,

2014). The mixing-layer analogy shall therefore be tested in urban canopies. It will also be investigated whether a general profile for momentum mixing length exists in urban canopies.

1.2   Background

Sections 1.2.1 and 1.2.2 explain fundamental UBL concepts. Section 1.2.3 examines the pollution transport processes within, and in and out of the UBL. The current understanding of urban surface layer turbulence and its representation in NWP is reviewed in Sects. 1.2.4 and 1.2.5. Previous use of box models to understand the processes controlling UBL and urban canopy pollution concentration, and transport of tracers in contexts such as submerged aquatic canopies is explored in Sect. 1.2.6. The different types of AQMs are reviewed in Sect. 1.2.7 to give context on how the questions being addressed in this thesis will contribute towards their development.

1.2.1   The Urban Boundary Layer

The atmospheric BL (or planetary BL) is classically defined as the "part of the troposphere that is directly influenced by the presence of the Earth's surface, and responds to surface forcings with a timescale of about an hour or less" (Stull, 2012). Herein the atmospheric BL shall just be referred to as the BL. The BL is typically between 100 m and 3 km deep, and can be subdivided into two regions (Oke et al., 2017). An inner region (commonly called the surface layer) that is approximately the lower 10% of the BL, where flow is most influenced by friction with the Earth's surface, and an outer region where the thermal effects of the Earth's surface usually dominate.

As illustrated in Fig. 1.1, when rural BL air meets the rougher urban surface an internal BL (IBL) grows, within which air is influenced directly by the urban area. If the urban area is large enough, the IBL reaches the BL height (z_h) and occupies the entire BL. When the urban air meets the rural BL at the downstream edge of the urban area, another IBL develops. There is a so called urban plume isolated aloft of the growing rural BL. It retains the effects of the urban area for tens of kilometres downstream (Oke et al., 2017).

Figure 1.2a shows the typical structure of the UBL during the day. The daytime layers of the UBL can be defined as follows (Oke et al., 2017):

- Urban canopy layer (UCL) – this is the layer of air between the ground and the tops of buildings. Specifying an appropriate definition of this height is not simple because it is often the tallest buildings that have the largest influence on the flow (Xie et al., 2008), however for simplicity the mean building height (h) is often taken. The
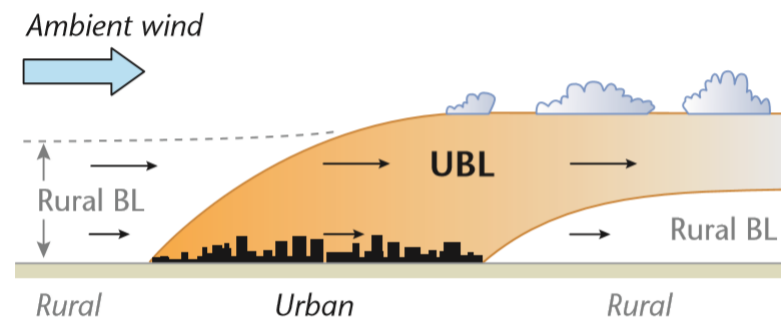
Figure 1.1: Schematic of the UBL at the regional scale. (Reproduced from Oke et al. (2017))

flow in the UCL experiences form drag due to the individual obstacles, and turbulence is generated in the wakes of obstacles, by wind shear and through buoyant effects. The surface energy balance (SEB) is modified due to human activities, and the UCL fabric and geometry. Latent heat flux tends to be lower than in rural areas because of the lower vegetation fraction. Sensible heat flux tends to be larger in urban areas, as dictated by SEB partitioning when latent heat flux is reduced. Also, anthropogenic heat sources act to effectively increase the sensible heat flux. The UCL fabric has large thermal inertia leading to appreciable storage heat flux. Radiation shadowing and reflections, and the different emissivity characteristics of the UCL fabric compared to rural surfaces, influence the incoming short-wave and outgoing long-wave radiation (although there is a small influence on net radiation flux) (Barlow, 2014).

- Roughness sublayer (RSL) – this is the layer of air between the ground and approximately $2-5$ times the mean building height (i.e. it includes the UCL). The top of the layer is the blending height. Between the top of the UCL and the blending height, flow is influenced by deviations in time-mean flow and turbulence caused by multiple obstacles.

- Inertial sublayer (ISL) – this is the layer of air influenced by the bulk effect of the underlying surface, where the logarithmic wind profile and MOST (Monin and Yaglom, 1975) apply. Turbulence is homogeneous and fluxes vary less than 5% with height within the whole ISL, so the layer is often referred to as the constant flux layer.

- Mixed layer (ML) – this layer typically occupies 90% of the BL, from the top of the ISL to the entrainment layer. Buoyant thermals heated by the surface transport atmospheric quantities to the capping inversion, before sinking after becoming negatively buoyant. Since the atmospheric quantities such as pollution, potential temperature, momentum and water vapour are vertically mixed efficiently, their horizontal average profiles tend to be almost uniform with height.

- Entrainment layer (or entrainment zone) – this is the layer of air between the ML

and the free atmosphere (FA). Within the region there is a capping inversion that is defined by a potential temperature inversion (going from cold to warm with height). Due to their inertia, when thermals reach the capping inversion, they can sometimes break through. Adjacent to these overshoot events are deep troughs (or pockets) of fluid, extending down from the FA (Sullivan et al., 1998). They become cut off from the FA above as the capping inversion re-forms, resulting in warmer (and generally less polluted) FA air becoming part of the BL.
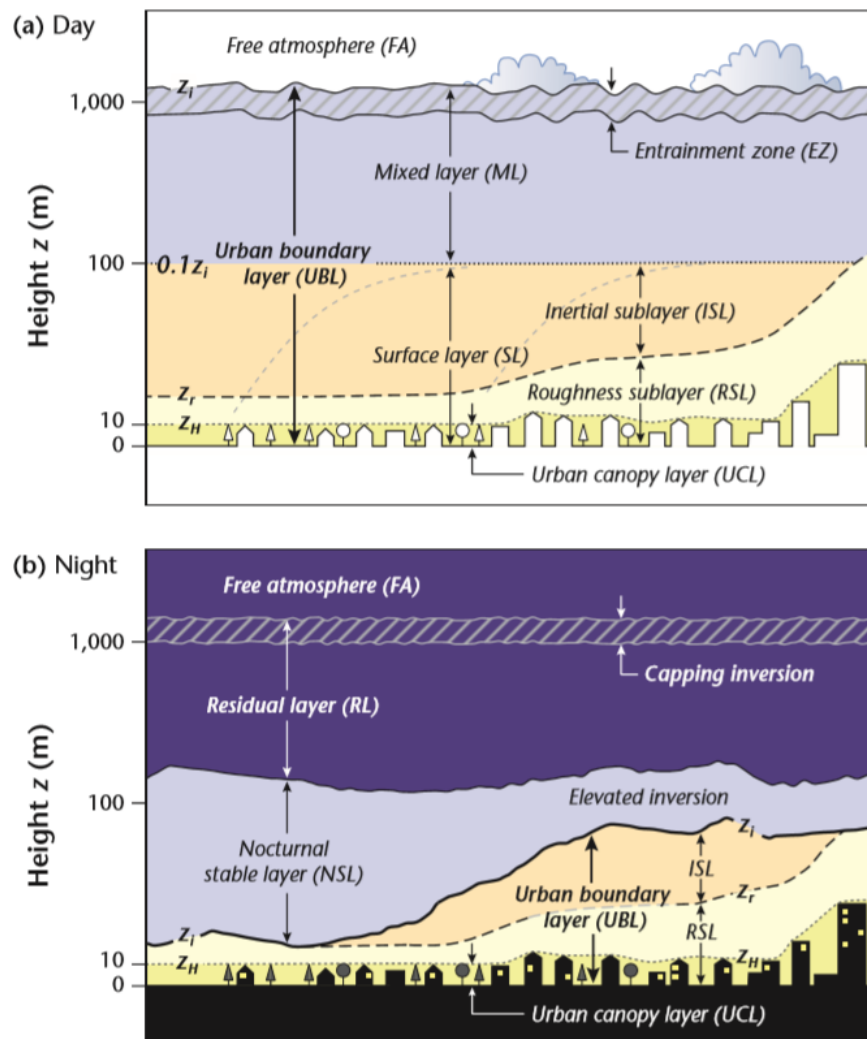
Figure 1.2: Schematic of the typical UBL structure during (a) daytime and (b) night-time. The vertical axes are logarithmic except near the surface. z_i, z_r and z_h represent the BL height, roughness sublayer height and the urban canopy height respectively, within this figure only. (Reproduced from Oke et al. (2017))

The urban surface layer is comprised of the ISL and RSL, which correspond to the upper and lower portions respectively. With increasing surface roughness, more of the surface layer tends to be occupied by the RSL. If the roughness elements are tall and/or the surface is very rough, an ISL may not exist. An ISL cannot exist when individ-

ual roughness elements become taller than approximately $0.1z_h$, as is often the case for high-rises in central business districts. The roughness and building height effects are illustrated in Fig. 1.2a as one moves from left to right.

As well as the blending height not being above $0.1z_h$, another criteria must be satisfied for an ISL to exist. The flow between the blending height and $0.1z_h$ must be in local equilibrium with the surface. Each time there is a change in general surface characteristics (e.g. between neighbourhoods), an IBL develops as illustrated by the dashed curved lines in Fig. 1.2a. The air within the IBL is directly influenced by the underlying surface. The depth of the layer that is in equilibrium with the surface roughness grows with fetch at a ratio of approximately 1:100 to 1:300 (Oke et al., 2017), so that it often takes several kilometres for the equilibrium layer to grow above the blending height. Since the neighbourhood scale is O(1 km) (see Sect. 1.2.2 for a full definition of the neighbourhood scale), the equilibrium layer associated with each neighbourhood does not always grow above the blending height before it reaches the next neighbourhood downstream. This prevents a region above the RSL developing where the flow is in equilibrium with the local surface roughness. Consequently, an ISL does not exist and the logarithmic wind profile and MOST are not valid. This is problematic for urban modelling since many of the commonly used parametrisations rely on MOST.

It is noted that the definition used for the blending height here is the one common to urban meteorology. There is another definition used more generally in meteorology, which often causes confusion between the urban and mesoscale NWP communities. When there is a change in surface roughness, a horizontal gradient in momentum occurs and is balanced by vertical stress divergence. This balance can be used to approximate a height above which flow is in equilibrium with the overall roughness of the surface, where the surface is approximated to be composed of patches with different roughness and a characteristic repeating length scale (Mason, 1988; Bou-Zeid et al., 2004). When calculated this way, studies of cities often find the blending height is in the ML (Barlow et al., 2008; Barlow, 2014). This is consistent with an ISL often not occurring in urban areas.

Figure 1.2b shows the typical structure of the nocturnal UBL. z_h collapses typically to $200 - 400$ m. Above z_h is a residual layer where there is little vertical mixing and atmospheric properties are largely preserved from the previous day. The layer is also capped by the previous day's temperature inversion. In rural areas the nocturnal BL tends to be stably stratified down to the ground. However, in more densely packed areas of cities, there is often weak convective mixing up to $50 - 300$ m above the ground. This is due to the release of heat stored from the previous day and anthropogenic heat emissions.

1.2.2   Urban Horizontal Scales

Urban areas are heterogeneous across a wide range of scales. They act as an obstacle to the flow at the scale of the city down to the scale of individual buildings. The influence on the time-mean flow and turbulence in turn affects the characteristics of the BL. A common way of classifying the different urban scales is as follows (Britter and Hanna, 2003):

- Regional scale / mesoscale (up to 100 or 200 km) – this is the area affected by the urban area. The urban influence can be viewed as a perturbation to the synoptic meteorology caused by changes in the surface-energy budget, thermal effects such as urban heat island (UHI) circulations, and deceleration and deflection of the flow associated with the enhanced urban roughness compared to the rural surroundings.

- City scale (up to 10 or 20 km) – this is the average diameter of the urban area. At this scale the flow around individual buildings or groups of buildings has usually averaged out into a bulk effect.

- Neighbourhood scale (up to 1 or 2 km) – this scale assumes an area can be defined where the characteristics of the buildings are similar. The bulk influence of the urban surface on the flow within each neighbourhood might then still be treated statistically.

- Street scale (less than ~100 to 200 m) – this is the scale of individual streets, intersections and buildings. The flow is highly heterogeneous and three-dimensional, with turbulence generated by individual obstacles and channelling of the flow along streets.

One of the main difficulties when modelling urban areas is poor "scale separation". There are often multiple scales that are important at a given point in space within the UBL. For example, a point in the roughness sublayer could simultaneously be influenced by city scale UHI circulations, the wake of a tall building 1 km upstream, and time-mean horizontal velocity deflections and turbulence generated by smaller underlying buildings. The challenge for urban meteorologists is to better understand the processes at each scale and the interactions between them, develop models whose parametrisations can treat them accurately and consistently, and inform design and planning of future cities.

1.2.3   Pollution Transport in the Urban Boundary Layer

The main pollution transport processes in the UBL are illustrated in Fig. 1.3. The removal of pollution from the atmosphere due to dry and wet deposition is discussed in

Sect. 2.5. The main transport processes that control transport of pollution in and out of the UBL are entrainment and horizontal advection (Seinfeld and Pandis, 2016). Entrainment of air into the UBL can either occur through vertical mixing across the entrainment layer (as explained in Sect. 1.2.1) or due to BL growth. When the BL grows it envelops air from above the BL with (generally) lower pollution concentration, reducing pollution concentration in the BL (Lee et al., 2019). When air is stagnant over large urban areas (e.g. under high pressure systems with slack winds), entrained air can be highly polluted, since the nocturnal residual layer can contain pollution from the previous day (Blumenthal et al., 1978).
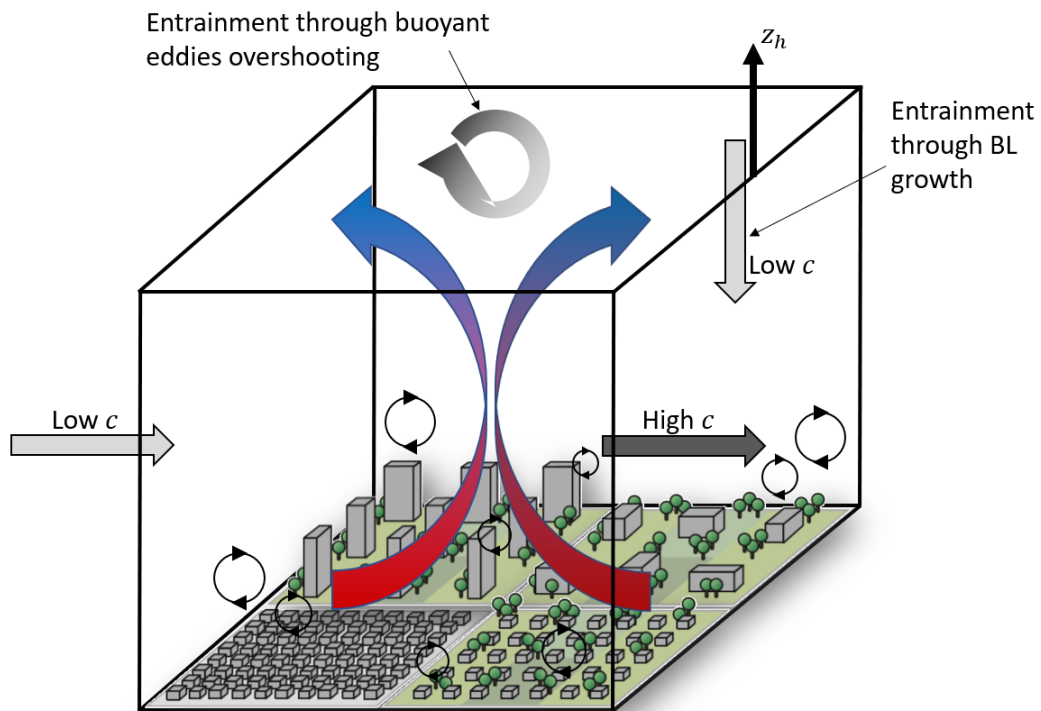
Figure 1.3: Schematic of the main UBL transport processes. Horizontal arrows represent horizontal advection of pollution in and out of the UBL. The large, curved arrows represent z_h scale buoyant eddies. Small (black, circular) eddies represent turbulence generated predominantly by mechanical production due to wind shear near the surface. The eddies are generally larger with increasing height above the UCL. Urban surface characteristics are chosen to represent those that might typically be associated with different neighbourhoods in a city, and are adapted from local climate zone (LCZ) schematics presented in Oke et al. (2017). Other than the LCZs this is an original schematic.

When the BL collapses in the evening, pollution is left behind in the nocturnal residual layer. This process of detrainment is not usually discussed in the AQ literature, since it often has very little immediate influence on the BL pollution concentration. Assuming the BL is well-mixed in the day, when it collapses the pollution left behind is of the same concentration as the pollution in the BL, so it is neither a source or a sink of BL pollution concentration.

Horizontal advection brings in background air, replacing the air within the urban

area. Since background air is usually from the rural BL, it tends to be of lower pollution concentration than air within the UBL (Seinfeld and Pandis, 2016). Sometimes this is not the case for example when highly polluted high pressure systems over the continent are advected over London. The wind speed at which the UBL is flushed is predominantly determined by the synoptic scale weather.

The roughness of the urban surface can perturb the synoptic flow on the regional and city scales. The increased drag that the urban surface exerts causes the flow near the surface to decelerate over the city. This leads to reduced horizontal advection of air in and out of the city which is bad for AQ. However, the deceleration of air causes convergence over the urban area, and can result in z_h increasing by hundreds of metres, diluting pollution (Oke et al., 2017). Also, coastal outflow can lead to efficient horizontal advection of pollution out of urban areas situated near the coast (Angevine et al., 2006; Dacre et al., 2007; Peake et al., 2014) as discussed in Sect. 1.2.6.4.

There are some processes not illustrated in Fig. 1.3 that under certain meteorological conditions can result in transport of pollution in and out of urban areas. Under clear sky conditions with light winds, cities often develop their own air circulations. The UHI (where the temperature of the urban surface is larger than the rural surface) is associated with larger urban than rural surface sensible heat fluxes. These lead to low-level horizontal convergence of air into the city and large vertical updrafts over the city (Oke, 1995). This gives rise to increased z_h, thus diluting pollution, whilst at the same time resulting in advection of cleaner air into the UBL. Also, the UHI can both enhance sea-breezes resulting in increased horizontal advection of pollution out of urban areas and cause sea-breeze circulations leading to stagnant air and poor AQ (Lo et al., 2007). Shallow, deep and frontal convection can lead to transport of pollution from the BL to the FA (Dickerson et al., 1987; Gimson, 1997; Esler et al., 2003).

The vertical distribution of pollution within the UBL is largely determined by vertical turbulent mixing. The mixing of pollution in the RSL is more strongly controlled by turbulence associated with mechanical than buoyant production, although buoyant production can become dominant when there is very light wind and large incoming solar radiation (Oke et al., 2017). In the ISL, the turbulence behaviour can be described by MOST (as discussed in Sect. 1.2.4.3). The eddies in the surface layer are smaller than those in the ML (as illustrated in Fig. 1.3).

In the ML the appropriate stability parameter is $-z_h/L_{MO}$, where

$$L_{MO} = \frac{-u_*^3 \bar{\theta} \rho c_p}{\kappa g Q_H},$$
(1.1)

is the Obukhov length, u_* is the friction velocity, $\bar{\theta}$ is the time-averaged potential temperature, ρ is the air density, c_p is the specific heat capacity of air at constant pressure, κ is the von Kármán coefficient, g is the acceleration due to gravity and Q_H is the surface

sensible heat flux. $|L_{MO}|$ can be interpreted as the height at which buoyant production of turbulence is equal to mechanical production of turbulence, and above $|L_{MO}|$ buoyant production dominates. For stable conditions L_{MO} is positive, for neutral stratification $L_{MO} \to \infty$, for unstable conditions L_{MO} is negative, and for free convective conditions $L_{MO} \to 0$.

$-z_h/L_{MO}$ has been demonstrated to define the changes in structure of CBL turbulence between weak and strong convective conditions (Salesky et al., 2017). Under weakly convective conditions ($-z_h/L_{MO} \approx 1$) the updrafts tend to organize into horizontal convective rolls, quasi-2D structures that align with the geostrophic flow. With increasing $-z_h/L_{MO}$ the turbulence quickly transitions towards open cell type structures, similar to those found in Rayleigh-Bénard convection. At $-z_h/L_{MO} \approx 20$ the structures are predominantly open cellular and further increasing $-z_h/L_{MO}$ results in ever less pronounced changes in streamwise versus spanwise structure of the turbulence (Grossman, 1982; Weckwerth et al., 1999; Salesky et al., 2017).

Figure 1.4 shows a schematic of the spectral density of turbulent kinetic energy (TKE) against wavenumber k (and turbulence length scale) in the ML. It can be seen that the peak has been chosen to coincide with 1 km, which is the approximate scale of the buoyant ML thermals. They are driven by surface heating, are the most energetic eddies in the BL and are very efficient at mixing pollution. When turbulence of this scale becomes partially resolved in NWP, it is known as the grey zone of atmospheric BL turbulence (Wyngaard, 2004). The z_h scale thermals break up into smaller eddies and cascade through a continuous spectrum to ever smaller scales in what is known as the inertial subrange. The spectral density of TKE is proportional to $k^{-5/3}$ in this region. When the turbulence reaches the Kolmogorov scale (a few millimetres) the TKE is dissipated as heat.

LES resolve most of the dominant turbulent eddies responsible for the majority of pollution vertical mixing in the CBL. LES have been demonstrated to accurately represent CBL turbulence and tracer dispersion compared to experiments (Willis and Deardorff, 1976, 1981; Weil et al., 2002), and have therefore been used extensively to investigate the influence of CBL conditions on tracer dispersion in the CBL (Lamb, 1984; Nieuwstadt and De Valk, 1987; Liu and Leung, 2001; Dosio et al., 2003). Tracers are passive particles that are often released in simulations and experiments to understand pollution transport without the added complexity of particles undergoing chemical reactions.

Deardorff (1972a) conducted LES of puff released particles in the BL under different atmospheric stability conditions. Figure 1.5 shows the centre of mass (CoM) trajectories with $-z_h/L_{MO} = 0.0$, 4.5, and 45. For approximately $-z_h/L_{MO} \geq 4.5$, Deardorff (1972a) found that the relevant velocity scaling parameter in the ML becomes the convective velocity scale

$$w_* = \left(\frac{g z_h Q_h}{\bar{\theta} \rho c_p} \right)^{1/3} , \tag{1.2}$$
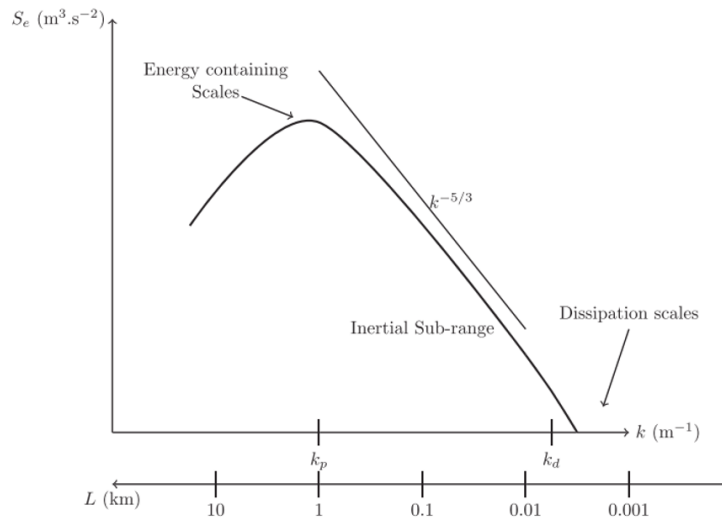
Figure 1.4: Schematic of the spectral density of TKE against wavenumber (and $L = 2\pi/k$) in the ML of the BL. L represents the turbulence length scale in this figure only. The scale is log-log. k_p and k_d are the wavenumber of the turbulence production and dissipation scales. (Reproduced from Honnert et al. (2020))

and the height scale for ML turbulence is z_h. It can be seen that the CoM trajectories for $-z_h/L_{MO} = 4.5$ and 45 demonstrate reasonable collapse in Fig. 1.5, when time is scaled by w_*/z_h. The CoM trajectories overshoot CoM/$z_h = 0.5$ after approximately $1.6z_h/w_*$, which is characteristically 15 min, and can be taken as an approximate time for the particles to become well-mixed. The overshoot occurs because particles released near the surface have a tendency to horizontally converge into z_h scale eddies, which transport the particles to near the top of the BL, before becoming well-mixed. Under neutral conditions eddies are mechanically generated, tend to be smaller than the scale of the BL and therefore do not lead to the particles exhibiting an overshoot behaviour. The particles did not become well-mixed within the BL during the simulation period. It was estimated that the time to become well-mixed under neutral conditions would have been one to two orders of magnitude longer than the time it took under convective conditions.

The "diffusive" and "non-local" parametrisations of vertical mixing in NWP do not represent this overshooting behaviour of particles released near the surface (as discussed in Sects. 3.6.1.2 and 3.6.2). When the dominant buoyant eddies are resolved in NWP at O(100 m) horizontal grid length it is likely that the overshooting behaviour will be observed, although it has not yet been demonstrated in the literature. The lofting of particles at times ~ 15 min after release results in a concentration decrease near the surface. It is possible that surface pollution concentrations in cities will be influenced on O(5 km) (i.e. bulk BL velocity multiplied by ~ 15 min) horizontal scales. This has not been demonstrated in LES or experiments since the downstream extent which they can represent is limited. However, it is now possible to conduct NWP at O(100 m) horizon-

---
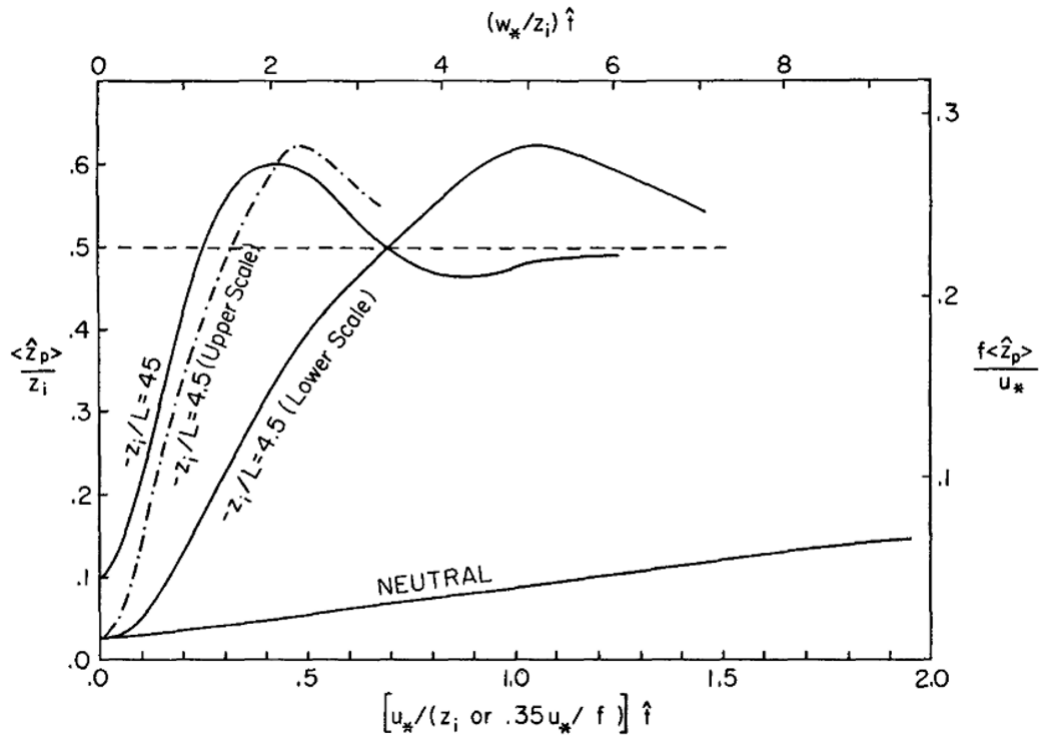
Figure 1.5: Centre fo Mass (CoM) trajectories of puff released particles in the LES of Deardorff (1972a). L, $\langle \hat{z}_p \rangle$ and z_i represent the Obukhov length, height of the CoM and BL height respectively in this figure only. $\hat{t}$ is the non-dimensionalised time. The upper axis corresponds to time scaled by w_*/z_h, and applies to $-z_i/L = 45$ and (dash-dotted line) $-z_i/L = 4.5$. The lower axis corresponds to time scaled by z_i/u_* or $0.35/f$ which apply to $-z_i/L = 4.5$ and (solid line) $-z_i/L = 4.5$, respectively. The left and right axes correspond to $-z_i/L > 0$ and neutral conditions, respectively. The puff release height was $0.025z_h$ for all simulations except $-z_i/L = 45$, which had a puff release height of $0.1z_h$. (Reproduced from Deardorff (1972a))

tal grid length in domains larger than individual cities (Leroyer et al., 2014; Ronda et al., 2017; Lean et al., 2019).

1.2.4 Urban Surface Layer Turbulence and Drag

The urban roughness causes distinct differences in the flow and pollution dispersion in the urban surface layer compared to flow over a flat surface. In this section, the current understanding of the influence of the urban canopy on pollution transport in the urban surface layer shall be explored. Also, current approaches to representing vertical mixing in urban canopies shall be reviewed.

1.2.4.1 Vegetation Canopies: A Source of Inspiration for Urban canopies

It is often assumed that canopies of different scales (e.g. sediment-bed, aquatic, plant, tree and urban canopies) share flow characteristics owing to their inherently similar dy-

namics (Finnigan, 2000; Ghisalberti, 2009). Raupach et al. (1996) argued that turbulence in vegetation canopies is largely controlled by eddies generated at canopy top analogous to those found in plane mixing-layers. It has been demonstrated to apply well across a range of canopy flows (Ghisalberti, 2009).

According to the mixing-layer analogy the dominant turbulent length scale in vegetation canopies is the shear length scale at canopy top. The form drag (i.e. drag caused by a pressure difference over the canopy element faces) causes the flow to decelerate in the canopy within an adjustment zone corresponding to (ii) in Fig. 1.6. The velocity is then significantly lower beneath than above the canopy top. The contribution of the canopy as a whole (rather than any specific canopy element) leads to an inflection in the time- and horizontally space-averaged (double-averaged) velocity profile, which causes an inviscid instability and large coherent eddies develop as illustrated in (iii) of Fig. 1.6. Poggi et al. (2004) investigated turbulence in a vegetation canopy (represented by tall cylindrical rods) using a recirculating flume. They found that von Kármán vortex streets generated by the rods dominated in the lower canopy, and argued that mixing-layer eddies only play a large role above the canopy displacement height, d.
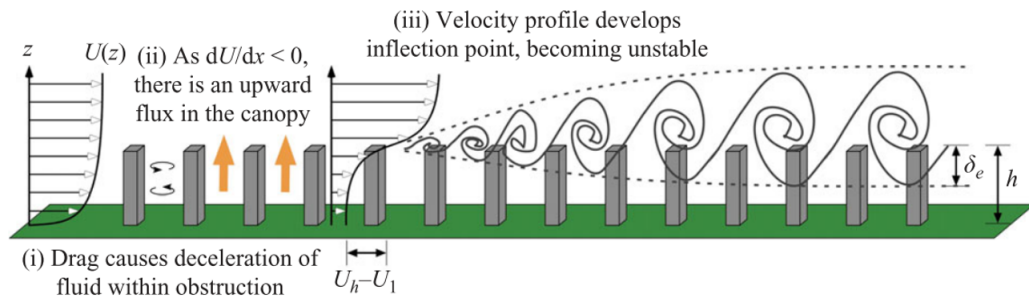
Figure 1.6: Schematic of mixing-layer eddies developing at the top of a submerged aquatic canopy. (Reproduced from Ghisalberti (2009))

The flow within vegetation canopies at any one point is strongly three-dimensional. The geometry of the vegetation canopy however, is quasi-homogeneous in the horizontal on the scale of several canopy elements. A double-averaging procedure is therefore commonly applied to the equations of motion. This is discussed in detail in Sect. 4.4. A simplified version of the momentum equation is often then solved, and is given by (Harman and Finnigan, 2007)

$$-\frac{\partial \tau_m(z)}{\partial z} = F_d(z), \tag{1.3}$$

where τ_m is the turbulent momentum flux and F_d is the form drag. Both are distributed with height from the ground, z, within the canopy. A first-order mixing length turbulence closure is often used (e.g. Inoue, 1963; Katul et al., 2004; Poggi et al., 2004; Harman and Finnigan, 2007), so that $\tau_m = \rho l_m(z)^2 |\partial \langle \bar{u} \rangle / \partial z| \partial \langle \bar{u} \rangle / \partial z$, where l_m is the momentum mixing length, u is the velocity in the direction of time-mean flow, superscript overbar represents time-averaging and $\langle \rangle$ represents spatial-averaging. Typically the form drag

is parametrised as $F_d = \rho\langle\bar{u}\rangle^2/L_c$, where $L_c = (S(z)C_d(z))^{-1}$ is the canopy drag length scale, and $S(z)$ is the sectional obstacle area density (obstacle area facing the wind divided by canopy air volume) and C_d is the sectional drag coefficient.

The mixing-layer analogy is commonly used as justification for choosing a constant l_m in vegetation canopies, since it implies there is one dominant turbulent length scale within the canopy. For deep, dense vegetation canopies where most of the momentum is absorbed by the canopy rather than the ground, and if $S(z)$ and $C_d(z)$ are constant, Finnigan et al. (2015) postulated that there is only one relevant length scale in the canopy. For drag it is L_c and since there is only one relevant length scale in the canopy it is proportional to l_m. Taking l_m and L_c as constant, and assuming $\tau_m \to 0$ as $z \to -\infty$, then the solution to Eq. 1.3 is the classical exponential velocity profile (Inoue, 1963), given by

$$\langle\bar{u}(z)\rangle = \langle\bar{u}(h)\rangle e^{\beta(z/h-1)}, \tag{1.4}$$

where β is a positive constant and h is the mean canopy height. Harman and Finnigan (2007) developed a model for vegetation canopies that coupled an exponential profile in the canopy to MOST in the ISL. Modified MOST stability functions were used in the roughness sublayer (in the region above canopy top), which included the shear length scale as a scaling parameter in addition to the standard MOST ones. A good match between model predictions and observations for velocity and scalar variables were found for deep, dense vegetation canopies, under a wide range of stability conditions (Harman and Finnigan, 2007, 2008).

The double-averaging procedure, turbulence closures and form drag parametrisations developed for vegetation canopies, have provided frameworks and inspiration for understanding and parametrising urban canopies (Inoue, 1963; Wilson and Shaw, 1977; Raupach and Shaw, 1982; Katul et al., 2004).

1.2.4.2 Turbulence and Drag Characteristics in Urban Canopies

Towards developing a conceptual picture of turbulence in the urban surface layer, analogous to those formed for vegetation canopies (e.g. Raupach et al., 1996; Poggi et al., 2004), Coceal et al. (2007b) conducted DNS of flow over an aligned array of cubes. It was found that turbulent organised structures with low momentum streaks (consistent with Kanda (2006)) and hairpin vortices occur in the ISL, as illustrated in Fig. 1.7. The low momentum streaks tend to be associated with upward transport of low-momentum air (ejections). The legs of the hairpins tend to be associated with downward turbulent transport of high-momentum air (sweeps). The ejections dominate the contribution to τ_m compared to sweeps (as documented in a related paper (Coceal et al., 2007a)), and the spanwise width of the low momentum regions increases linearly with height consistent with the attached-eddy hypothesis (Townsend, 1980). These characteristics are

shared with those found in the ISL of smooth and rough wall flows. This is different to vegetation canopies where head-up and head-down hairpin vortex pairs form in the ISL (Finnigan et al., 2009).
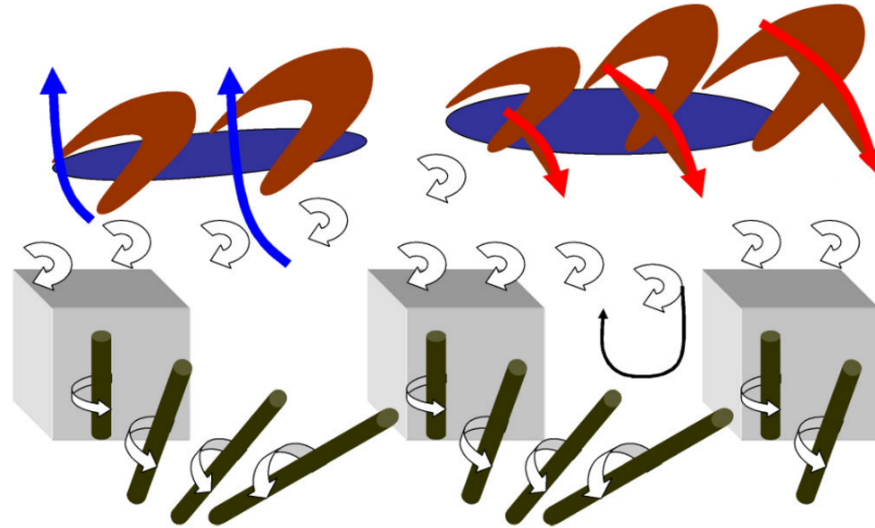
Figure 1.7: Conceptual schematic of the unsteady flow dynamics within the urban surface layer. The red inverted U-shaped structures are hairpin vortexes and the blue regions between their legs are low momentum streaks. The blue and red arrows represent ejections and sweeps, respectively. White arrows represent canopy top eddies which sometimes interact with the flow above (left of figure) and sometimes interact with the flow below, for example driving turbulent recirculations in the canopy (right of figure). Green rods represent the eddies shed off the windward vertical edges of the cubes. (Reproduced from Coceal et al. (2007b))

Coceal et al. (2007a) found the velocity inflection at canopy top to be local to the cubes. This suggests the shear generated eddies at urban canopy top are much smaller than the mixing-layer eddies in vegetation canopies, and they therefore do not dominate deep down into the canopy. Near canopy top sweeps dominate the contribution to τ_m compared to ejections. This is consistent with the small shear layer eddies having mixing-layer eddy characteristics, and is supported qualitatively by instantaneous snapshots of the flow (Coceal et al., 2006; Letzel et al., 2008). The shear layer eddies interact with the flow in the ISL and sometimes impinge upon downstream cubes, driving cavity recirculations as illustrated in Fig. 1.7.

Within the canopy Coceal et al. (2007b) concluded that there is no dominant turbulent length scale. This is in contrast with vegetation canopies where it has been argued either that mixing-layer eddies dominate in the canopy (Raupach et al., 1996), or that near the top and bottom of the canopy, mixing-layer eddies and wake generated eddies dominate respectively (Poggi et al., 2004). In urban canopies there are eddies generated by different mechanisms often interacting with each other, at a range of heights within the canopy. For example there are eddies shed from the vertical edges of the cubes (see Fig. 1.7), mixing-layer type eddies transported downwards, sweeps and ejections from

the ISL, shear generated eddies associated with the no-slip condition at the ground and sometimes flow separation causing flapping motions at canopy top. This makes defining a height dependent turbulent length scale within the canopy challenging. It is not yet well understood how important each of these turbulence types are in determining momentum and scalar transport in different urban canopy geometries.

Figure 1.8 shows various statistics from DNS of different $\lambda_p = 0.25$ cube array geometries. λ_p is the plan area density, and is equal to A_p/A_t where A_p and A_t are the total plan area of buildings and total plan area respectively. From Figs. 1.8a-c it can be seen that the velocity variance peaks at canopy top, which is due to the intense shear there. The variances decrease below h, but remain reasonably constant in the canopy apart from very close to the surface, consistent with Britter and Hanna (2003).

Unlike in vegetation canopies where the canopy elements occupy a negligible volume, urban canopy elements are larger causing significant deflection of the time-mean flow. This results in contributions to vertical momentum transport through time-mean velocity correlations or "dispersive stress" (see Fig. 1.8e). It has recently been demonstrated using LES of a realistic urban canopy geometry, that dispersive stress in flows oblique to the building faces can contribute as much as turbulent (or Reynolds) stress to the total turbulent stress (Giometto et al., 2016). Whether this result applies more generally to oblique flows of different canopy geometries is not known.

From Fig. 1.8i it can be seen that the magnitude of C_d varies greatly between geometries and is not constant with height (particularly near the surface and for the staggered array). C_d has been found to vary with height and have large dependence on urban canopy geometry by many other studies (e.g. Macdonald, 2000; Cheng and Castro, 2002; Coceal et al., 2006; Santiago et al., 2008; Leonardi and Castro, 2010). This makes parametrising C_d difficult in urban canopies. Also, l_m is far from constant as seen in Fig. 1.8j, consistent with there not being one dominant turbulent length scale in urban canopies. The exponential velocity profile is therefore a poorer estimate for urban canopies than vegetation canopies (Castro, 2017).

Coceal and Belcher (2004) used L_c to estimate the downstream extent of canopy required for the flow to reach a new equilibrium, in response to a change in canopy roughness. It was found to be O(100 m) for typical packing densities. This suggests that compared to above the canopy, the flow reaches an equilibrium with the local roughness much more rapidly.

1.2.4.3 MOST in the Urban ISL

Historically, the effect of the urban surface on the atmosphere above has been of primary interest in NWP, and much less the details of the meteorology within the roughness sublayer. It is therefore common practice in NWP to use MOST to represent the aerodynamic
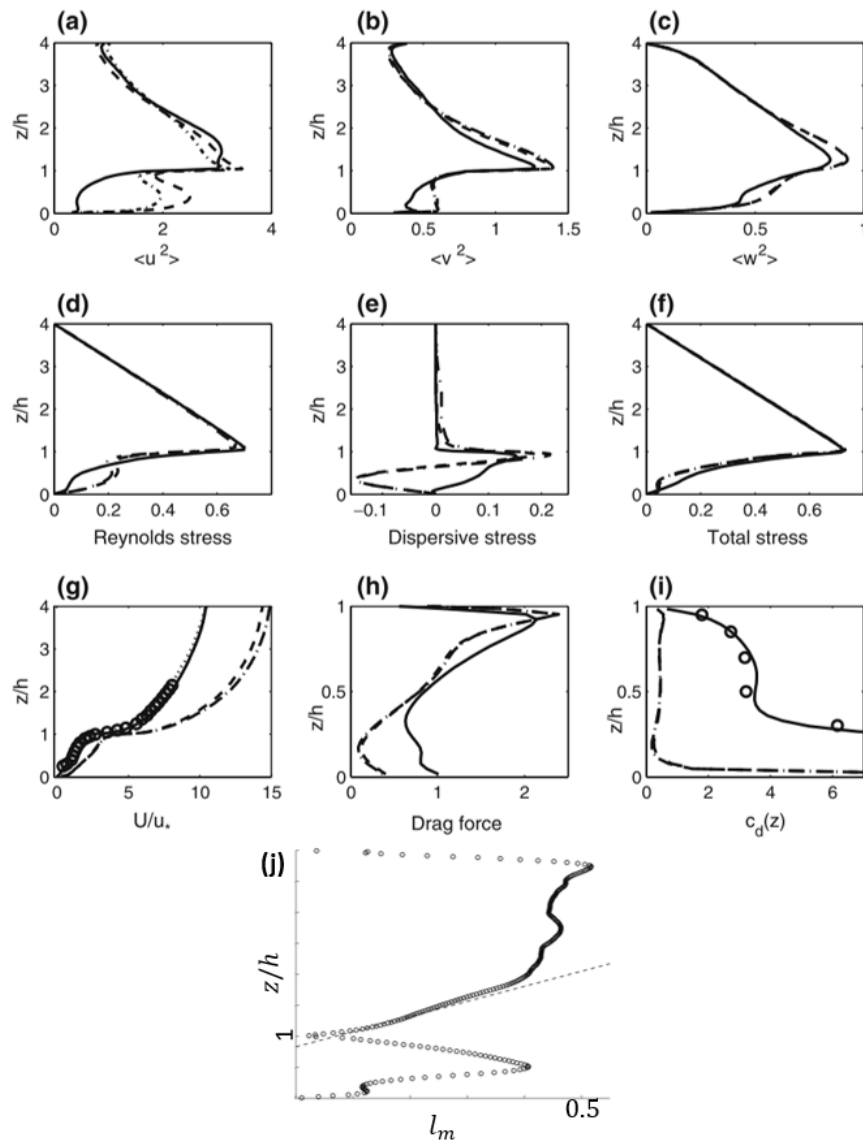
Figure 1.8: Various statistics from DNS of different $\lambda_p = 0.25$ cube array geometries. Solid, dashed and dot-dashed lines correspond to staggered, aligned and square arrays respectively. (a), (b) and (c) are the streamwise, spanwise and vertical velocity variances respectively. (d), (e) and (f) are τ_m, dispersive stress and the sum of the two respectively. (g) Double-averaged streamwise velocity. (h) and (i) are F_d and the sectional drag coefficient respectively. For many of the statistics the aligned and cube arrays are indistinguishable. (j) Momentum mixing length for the staggered array with a linear regression fitted in the ISL. (Modified from Coceal et al. (2006))

drag of the urban surface and turbulent exchange from it. MOST has been shown to be valid in the ISL (when one exists) above urban canopies (Roth, 2000; Coceal et al., 2007b). This is convenient because the ISL directly experiences the bulk effect of the surface with which it is in equilibrium. Parametrisation using MOST does not require direct representation of street scale processes.

Based on dimensional arguments Monin and Obukhov (1954) hypothesised that in the ISL the gradients of time-mean quantities and turbulence characteristics scale with

only: 1) u_*, 2) the friction temperature $T_{\mathrm{SL},*} = Q_H/(u_* \rho c_p)$, 3) the effective height from the ground $z - d$ (where d has been included in the definition of the effective height from the ground, because the roughness elements occupy a non-negligible fraction of the surface layer, unlike in the original work of Monin and Obukhov (1954)), and 4) the buoyancy ratio $g/\bar{\theta}$. From these, the dimensionless ISL stability scaling parameter $\zeta = (z - d)/L_{MO}$ can be formed, where L_{MO} is defined by Eq. 1.1.

Monin and Obukhov (1954) found that the vertical gradient of the time-average velocity obeys

$$\frac{\partial \bar{u}}{\partial z} = \frac{u_*}{\kappa(z - d)} \Phi_m(\zeta), \tag{1.5}$$

where $\bar{u}$ is the time-average velocity and $\Phi_m(\zeta)$ is a gradient stability function for momentum. Common functional forms for $\Phi_m(\zeta)$ exist under different stability conditions (e.g. Dyer and Hicks, 1970). Equation 1.6 can be integrated to obtain

$$\bar{u} = \frac{u_*}{\kappa} \left(\ln\left(\frac{z - d}{z_0}\right) - \Psi_m(\zeta) + \Psi_m\left(\frac{z_0}{L_{MO}}\right) \right), \tag{1.6}$$

where z_0 is the aerodynamic roughness length, and $\Psi_m(\zeta)$ is an integral involving ζ and Φ_m. In the limit of neutral conditions $\Psi_m(\zeta) \to 0$ and the logarithmic law is obtained. Under unstable conditions (i.e. $Q_H > 0$) $\Psi_m(\zeta) < 0$, and velocity in the ISL is increased compared to neutral conditions due to enhanced vertical mixing of momentum down towards the surface. The converse is true for stable conditions. Similar relations to Eq. 1.6 exist for scalar variables such as heat and tracers.

Before MOST can be used to parametrise the aerodynamic drag and turbulent exchange from the surface, z_0 and d must be defined, for which semi-empirical relationships are often used (Grimmond and Oke, 1999). d represents the height which the flow effectively experiences as being the ground. It shifts upwards from the true ground because most of the momentum is absorbed by the tops of the buildings. z_0 is a measure of the aerodynamic drag the surface exerts on the flow. Figure 1.9a gives an example of the wind speed in the urban surface layer under neutral conditions, with a log-law fitted. It can be seen that the log-law is a poor fit in the UCL, but with increasing height in the RSL the fit improves, and the fit is good in the ISL. The height at which the log-law wind goes to zero is $d + z_0$.

Figure 1.9b shows a schematic of the z_0 and d variation with λ_p. The shaded regions represent the range of values typically found in the literature for different UCL geometries in cities. Three different conceptual regimes are usually used to describe z_0 and d behaviour in the context of idealised two-dimensional street canyons. The "isolated roughness" regime occurs when $h/W \leq 0.35$, where W is the mean downstream building separation. In this regime there is a (time-mean) recirculating vortex behind each building. The buildings are far enough apart that the flow interaction between buildings
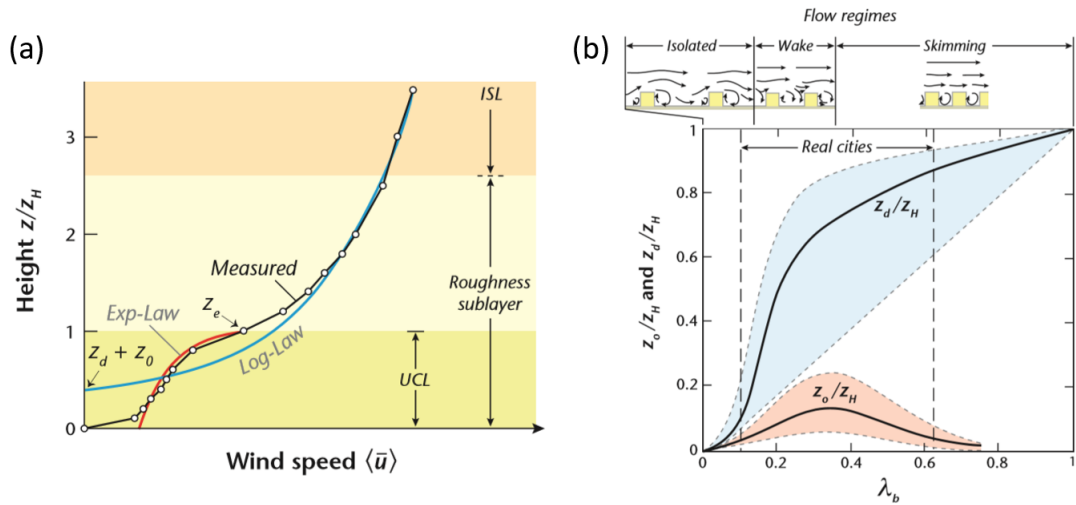
Figure 1.9: (a) Example of a wind speed profile in the urban surface layer. Also plotted are a log-law and exponential profile that have been fitted to the wind speed. (Reproduced from Oke et al. (2017), who modified from Macdonald (2000)). (b) Schematic of the z_0 and d variation with plan area density. Shaded regions represent the range of values typically found in the literature. (Reproduced from Oke et al. (2017), who modified from Grimmond and Oke (1999)). In this figure only, z_H is the mean building height, z_d is the displacement height and λ_b is the plan area density.

is small. z_0 and d increase with λ_p.

The "wake interference" regime occurs when $0.35 < h/W < 0.65$. The distance between buildings in the downstream direction is small enough so that the vortex behind each building, is reinforced by flow down the windward face of the downstream building. z_0 peaks at $\lambda_p \approx 0.35$ because of two competing effects. At first, as λ_p increases there is more obstruction (to a high momentum flow), and consequently more form drag. For further increases in λ_p the flow has much lower momentum, since more obstruction results in less flow penetrating down into the canopy (i.e. d/h is larger), and there is less form drag. The "skimming flow" regime occurs when $h/W \geq 0.65$, and flow skips over the tops of the buildings. z_0 decreases and d continues increasing. In the limit of $\lambda_p \to 1$, $d \to h$, and a new ground surface can be defined at h.

1.2.4.4   Dispersion in Urban Canopies

Based on scaling laws for vertical velocity variance and the bulk velocity in urban canopies, Britter and Hanna (2003) argued that the ground-level concentration in building arrays should scale with $\lambda_f^{-1/2}$, $\lambda_f^{-1/6}$ and $\lambda_f^{1/2}$ in the isolated roughness, wake interference and skimming flow regimes respectively. Such a scaling relationship has yet to be demonstrated by experimental or computational fluid dynamics (CFD) studies. The frontal area density is given by $\lambda_f = A_f/A_t$ where A_f is the total frontal area of buildings facing the wind. The scaling relationship of Britter and Hanna (2003) sug-

gests that ground-level concentration should decrease in the canopy with increasing density of buildings (assuming λ_p is roughly proportional to λ_f), in the isolated roughness and wake interference regimes. This is because when λ_f is small, increasing λ_f results in larger turbulence intensity due to turbulence generated by the buildings. Pollution therefore disperses more rapidly in the vertical compared to over a smooth surface. In the skimming flow regime the relationship implies increasing the density of buildings results in increased ground-level concentration. For large λ_f, increasing λ_f results in reduced penetration of flow into the canopy. Consequently, there is less mean kinetic energy that can be converted to TKE and less efficient dispersion in the canopy.

As well as building arrays, street canyons are a very important urban canopy geometry for AQ applications. They are commonly associated with busy roads and areas of large human activity. They have been more extensively studied than cube geometries (Vardoulakis et al., 2003) and are better understood owing to their simpler quasi-2D geometry. Figure 1.10a shows the typical cross-canyon vortex flow pattern that develops for street canyons with $h/W \approx 1$ and approach flow perpendicular to the long axis of the canyon. The vortex exists in a time-mean sense (apart from when winds are very light) but it is also turbulent due to interactions with the roof level shear layer. The mixing timescale associated with the vortex in the canyon is $T_\perp \approx (h + W)/u_\perp$, where $u_\perp = u_h \sin(\theta_s)$, u_h is the wind speed at canyon top and θ_s is the angle of the wind to the street (Belcher, 2005). Since the vortex is efficient at mixing pollution, it is often assumed that the concentration is uniform within the street canyon (Caton et al., 2003; Soulhac et al., 2011). However, horizontal and vertical pollution concentration gradients do exist within street canyons, and observations have found concentrations to be up to two times greater at the leeward wall (Xie et al., 2003).

For idealised street canyon geometries where $h/W \geq 2$, stacked counter-rotating vortices occur, as illustrated in Fig. 1.10b. This results in poor AQ since pollution can become trapped in the lower vortices (Zhong et al., 2015). However, from measurements of flow in a real street canyon with $h/W = 2.1$, Eliasson et al. (2006) found that a single vortex exists rather than counter-rotating vortices in a time-mean sense, and a second lower vortex was only observed intermittently for short periods.

When the approach flow is not perpendicular to the street, a helical pattern forms as shown in Fig. 1.10c. The flow is a superposition of channelling along the street and across street mixing. Figure 1.10d illustrates "channelling", where in the limit of $\theta_s \rightarrow 0°$ recirculation stops and flow is all directed along the street. In reality flow is turbulent so it is not always aligned with the street.

The vertical exchange velocity at street canyon top depends both on the external turbulence (i.e. upstream roughness and stability conditions) and the local canyon geometry through the influence of the canopy top shear layer (Salizzoni et al., 2011; Perret et al., 2017). The canopy top shear layer has complex dependence on canyon geometry and interactions with the external flow. Typically operational models assume the vertical
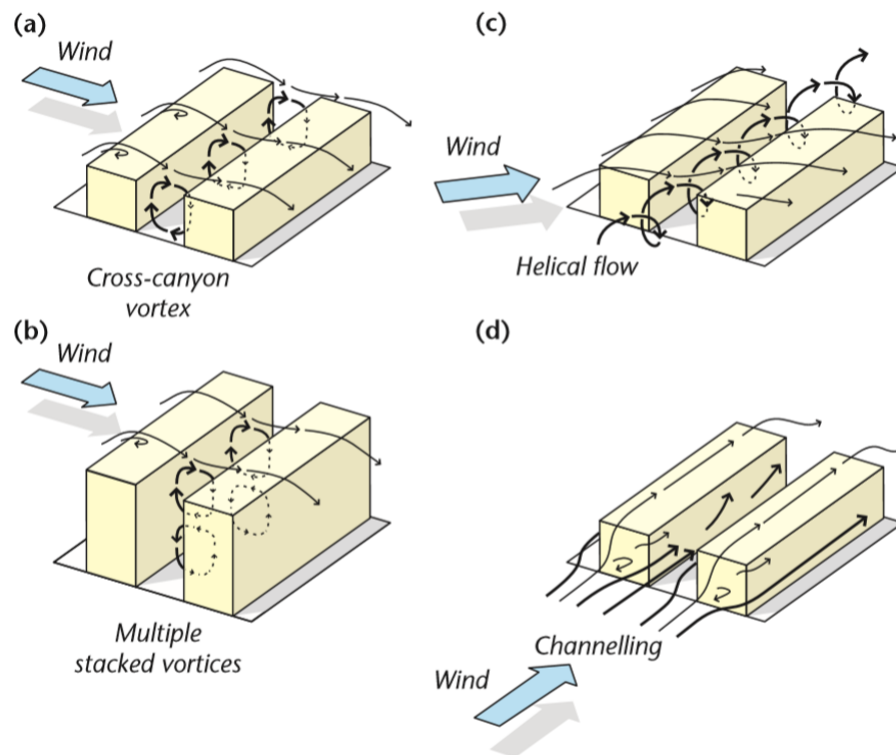
Figure 1.10: Typical flow patterns for street canyons with (a) $h/W \approx 1$ and $\theta_s = 90°$, (b) $h/W \approx 2$ and $\theta_s = 90°$, (c) $h/W \approx 1$ and $\theta_s = 45°$ and (d) $h/W \approx 1$ and $\theta_s = 0°$. (Reproduced from Oke et al. (2017))

exchange velocity only depends on the external turbulence, and results often compare well with observations (Berkowicz, 2000; Soulhac et al., 2012).

1.2.5 Parametrisation of Urban Surface Layer Turbulence and Drag in NWP

Most regional scale NWP represent the urban canopy as a single layer coupled with the first atmospheric model level. Another approach that is becoming increasingly common is to apply a double-averaging procedure to the flow in the UCL, so that it is represented in one dimension, with multiple atmospheric model levels in the vertical. An example of each type of urban canopy modelling approach will now be given. A more detailed overview of urban canopy models used in NWP is included in Sect. 4.2.

The surface scheme used in the UM is the Joint UK Land Environment Simulator known as JULES (Best et al., 2011). It is responsible for calculating the SEB and providing the surface forcing to the atmospheric model. Within each grid box the surface is split into different land types (or tiles), the surface energy exchange is calculated for each of them, and then averaged considering the proportion of each land type within the grid box (Essery et al., 2003). The Met Office-Reading Urban Surface Exchange Scheme (MORUSES) module was included in the surface scheme for urban areas (Porson et al.,

2010; Bohnenstengel et al., 2011), so that there are urban tiles representing canyons and roofs.

MORUSES is a single-layer model, since there is only direct interaction between the buildings and the first atmospheric model level. The blending height is taken to be the first atmospheric model level, above which it is assumed that the Reynolds-averaged flow is horizontally homogeneous within each grid box. The exchange of momentum is parametrised using MOST, with z_0 and d determined according to the morphometric method of Macdonald et al. (1998). When calculating the exchange of sensible heat, latent heat and radiation, the urban canopy is taken to be a 2D street canyon, and averages are taken over street orientations. Sensible and latent heat fluxes are calculated using an exchange coefficient. Resistances to exchange over the internal boundary layers along the roof and canyon facets are calculated, and combined using a resistance network model based on Harman et al. (2004) to obtain the exchange coefficient. The resistance network depends on the canyon geometry through the ratio h/W.

The most widely used multi-layer urban canopy model in NWP is that presented by Martilli et al. (2002). It has several atmospheric model levels within the canopy. At the height of each atmospheric model level the surface scheme calculates a separate SEB, and the surface scheme is coupled to the atmospheric model at each level. MOST is only assumed for the scalar exchange between the building facets and the air. The atmospheric model solves the double-averaged equations within the canopy air space. The equations have extra terms compared to the Reynolds-averaged equations, which arise from the double-averaging procedure, and have direct interpretation as canopy processes. For example, the momentum equation has a term accounting for the form drag exerted by the canopy obstacles. Martilli et al. (2002) parametrise form drag based on the approach used in vegetation canopies (as described in Sect. 1.2.4.1) with a constant C_d. As discussed in Sect. 1.2.4.2, it is known that C_d is not constant in urban canopies. Dispersive stresses are neglected in the model.

The turbulent fluxes are parametrised using K-theory. The diffusion coefficient is determined using the $k-l$ turbulence closure of Bougeault and Lacarrere (1989), which involves solving an extra prognostic equation for TKE. The turbulent mixing lengths used for TKE production and dissipation are the harmonic mean of two length scales. One length scale is the street canyon height (which is weighted based on the proportion of canyon heights in a grid box), and the other length scale depends on the height from the ground and building roofs. This does not result in the turbulent mixing length going to zero at the surface as it should (see Fig. 1.8j).

1.2.6 Box Models

As explained in Sects. 1.2.3 and 1.2.4 the pollution transport processes in the UBL and its urban canopy are very complex. Box models are common tools used to investigate pol-

lution and tracer transport from the regional to the street scale. They are simple allowing an intuitive understanding of the transport processes to be developed. In this section, the literature on the use of box models to investigate UBL and urban canopy pollution transport will be reviewed, as well as literature from other research areas such as submerged aquatic canopies and regional scale pollution transport to provide additional context.

1.2.6.1   UBL Box Models

The Eulerian one-box model represents the volume-averaged pollution concentration, within the three-dimensional volume the box encloses. It assumes that pollution becomes uniformly distributed instantaneously upon entering the box. Lettau (1970) investigated urban AQ using a one-box model, and a schematic of the model is given in Fig. 1.11a. The length and width of the box were taken to be the horizontal dimensions of the city. The box model was formulated so that at some height fluxes out of the box due to vertical mixing could be specified. It was suggested that when there is a capping inversion, the height of the box should be the depth of the BL, and that "flushing by eddy fluxes" (labelled at the top of the box in Fig. 1.11a) is approximately zero. Whilst entrainment of clean air via turbulent mixing across the capping inversion might generally be small over urban horizontal advection timescales, it is known that entrainment due to BL growth can be important (Kaser et al., 2017; Lee et al., 2019). However, it was not represented by Lettau (1970). Also, the air advected into the box was assumed to be totally unpolluted, but it is known that pollution in background advected air can have a large influence on urban AQ (Elminir, 2005; Bo et al., 2020).

Lettau (1970) identified the "flushing frequency" equal to the bulk wind speed in the box divided by the streamwise dimension of the box as a key parameter determining pollution concentration. As illustrated in Fig. 1.11b, when the bulk wind speed is small, the flushing frequency (and flushing rate) is small, and the pollution concentration is large. When the streamwise dimension of the box is large, the flushing frequency is small, and the pollution concentration is large. Therefore, AQ is often poorest in large cities under slack wind conditions. Also, the pollution concentration takes longer to respond to changing emissions and atmospheric conditions in large cities, since it takes longer for previous emissions to be flushed from the city.

Since the work of Lettau (1970), there have been few studies taking a box model approach to understanding the influence of transport processes on UBL pollution. Those that do also tend to neglect advection of background pollution and entrainment (e.g. Jensen and Petersen, 1979; Topçu et al., 1993; de Leeuw et al., 2002; Rigby et al., 2006). Studies also tend to use climatological daily averaged input data (e.g. Topçu et al., 1993; Rigby et al., 2006). Pollution concentration often varies widely throughout the day, due to diurnal changes in atmospheric conditions and emissions, and changes in synoptic
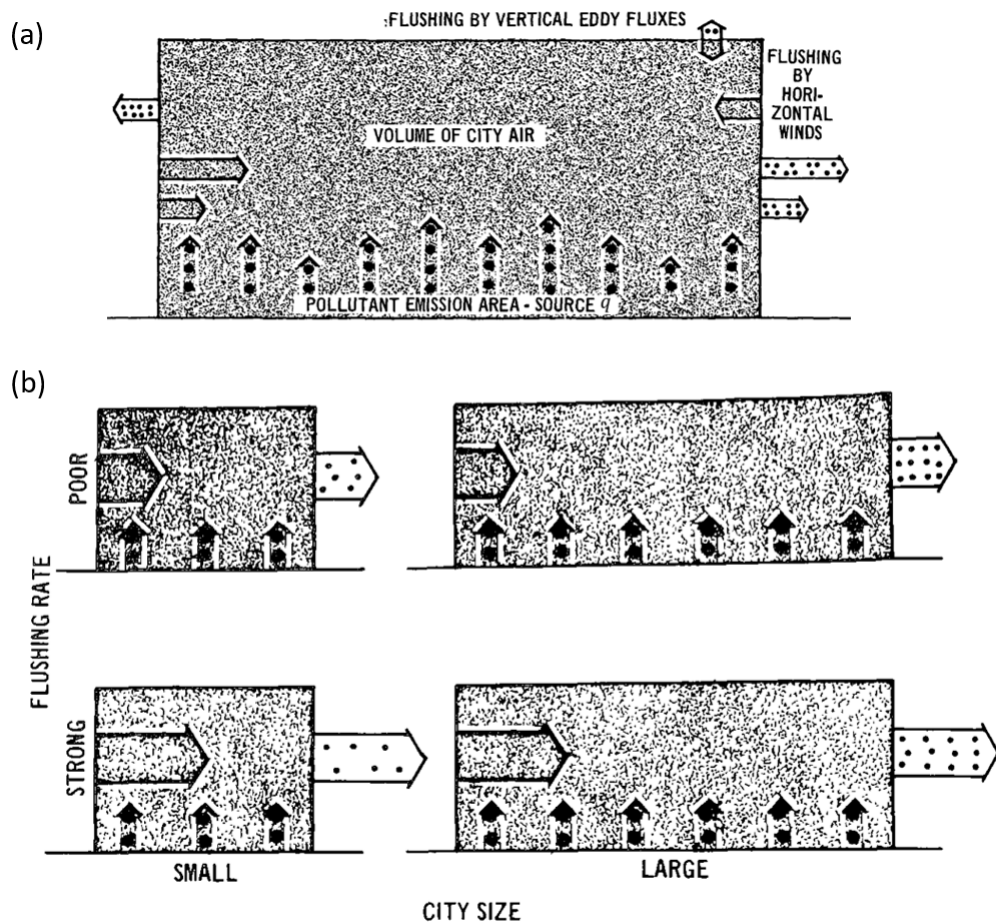
Figure 1.11: (a) Eulerian one-box model schematic. (b) Illustration of the effects of flushing rate and streamwise city dimension on pollution concentration. In (a) and (b) upward dotted arrows represent pollution emissions, shaded horizontal arrows represent clean air advected into the box and dotted horizontal arrows represent advection of polluted air out of the box. The density of the dots represents the pollution concentration of the air. (Adapted from Lettau (1970))

conditions. By using daily averaged data, the details of the processes are lost. It is therefore worth revisiting the box model, with variations in atmospheric conditions during the day included, and with previously unrepresented processes. The box model study presented in this thesis has the benefit of continuous wind speed measurements above the surface layer, continuous lidar measurements of BL depth and background pollution concentration measurements. These were not simultaneously available in earlier studies.

1.2.6.2 Canopy Box Models

Salizzoni et al. (2009) used a two-box model to investigate the exchange processes and their associated timescales in a street canyon. In a wind tunnel experiment, tracer was continuously released from a line source at ground-level in the centre of the canyon. Once a steady state was obtained the release was cut off, and the change in concentration

within the centre and outer regions of the canyon was measured. As illustrated in Fig. 1.12a, they represented the centre of the canyon as a circular box and the remaining volume of the canyon with another box. This decision was made based on the observation that the tracer residence time is longer in the centre compared to the outer region of the canyon. They used two transfer velocities to represent the tracer exchange between the centre box and the surrounding box, and the exchange across the shear layer between the surrounding box and the external air. The box model predicted decay in tracer concentration matched well with the experimental data as shown in Fig. 1.12b. The exchange velocities were obtained by optimising the fit between the model and measurements. By varying the intensity of the turbulence in the external flow, they demonstrated that it has a direct influence on the transfer velocity for canyon top exchange.
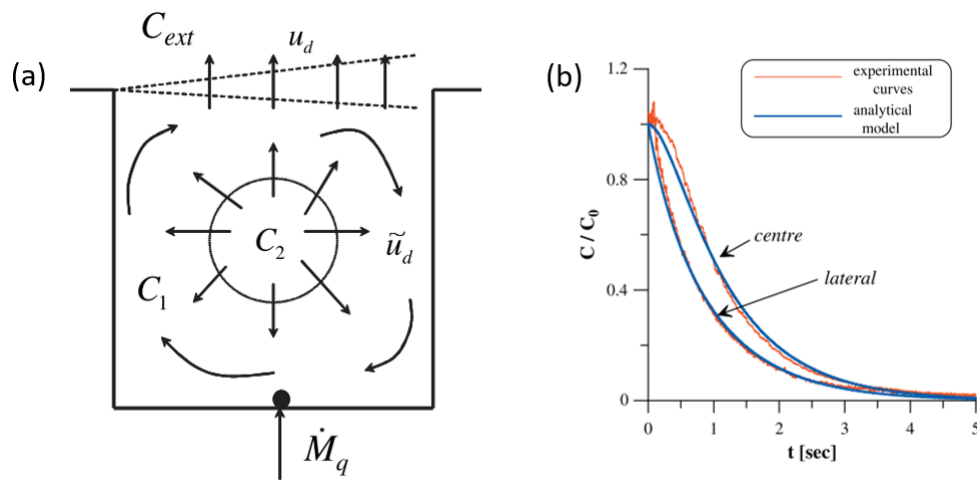
Figure 1.12: (a) Schematic of the two-box model presented by Salizzoni et al. (2009). Tracer is released at the ground, and is exchanged with two different velocities between the centre and lateral box, and the lateral box and external air. There are three concentrations corresponding to tracer in the centre and lateral boxes, and the tracer external to the canyon. "Centre" and "lateral" describe the centre of the canyon and outer region of the canyon boxes respectively. (b) Comparison between experimental and two-box model results. (Both (a) and (b) are adapted from Salizzoni et al. (2009).)

In the context of submerged aquatic canopies, Nepf et al. (2007) constructed a two-box model that considered the canopy to consist of two layers. As illustrated in Fig. 1.13, the boxes consist of an upper layer (or "exchange zone") where turbulent transport is dominated by canopy top shear layer turbulence (mixing-layer eddies), and a lower layer where turbulence is due to stem generated wake turbulence. They defined two vertical exchange timescales corresponding to tracer transport between the lower and upper layer, and the upper layer and the external flow. The two-box model had an equation for each box, with concentration time-derivative and vertical exchange terms, but no sources or advection sinks. The concentrations in the two boxes were initially set equal. The concentrations predicted by the two boxes decayed with time. An overall vertical exchange timescale for the canopy was defined by considering the decay of the

mean tracer concentration in the two boxes.

They defined a horizontal advection timescale that was based on a bulk advection velocity in the canopy and the length of the canopy. They then analysed the vertical exchange and horizontal advection timescales for varying values of parameters such as canopy height, length and density. It was concluded that the vertical exchange timescale and velocity in the canopy, define the minimum canopy length for which vertical exchange dominates horizontal advection. Shorter canopies are dominated by horizontal advection. A weakness in the investigation is that the processes of vertical exchange and horizontal advection were studied separately. Since both influence and depend on the concentration within the canopy, their variation with canopy geometry may have interesting behaviours unrepresented in the two-box model of Nepf et al. (2007).
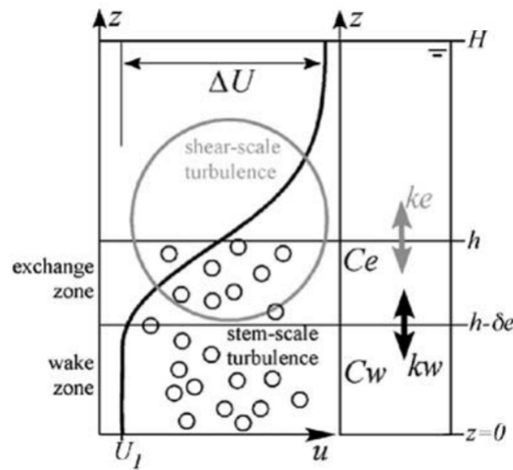
Figure 1.13: Schematic from Nepf et al. (2007) showing the partition of the canopy into a "wake zone" and "exchange zone".

Although box models have been used to understand tracer and pollution exchange in a range of canopy types, to the author's knowledge there have been no studies representing the urban canopy and ML as two separate boxes to understand the most important parameters controlling pollution concentration in the BL. Street network models (discussed in more detail in Sect. 1.2.7.3) represent each street and intersection in the urban canopy as a separate box, and exchange between the boxes is parametrised. The parametrisations of vertical exchange at canopy top could be used as inspiration for the parametrisation of vertical exchange between a single box model representing the entire canopy and the ML box above.

1.2.6.3 Box Models With Chemistry

Box models are often used to study chemistry in the CBL (e.g. Jin and Demerjian, 1993; Middleton, 1998; Aumont et al., 2003; Hamer and Shallcross, 2007; Pugh et al., 2010a). They are very computationally cheap allowing resources to be spent on complex chem-

istry schemes rather than BL transport processes. Pugh et al. (2010b) highlighted one weakness of box models. Their investigation concerned the prediction of O_3 and NO_x concentrations in the nocturnal BL over a rainforest. It was found that treating pollution as well-mixed resulted in poor concentration prediction above the canopy. Only when the stable stratification of the atmosphere was accounted for and vertical concentration gradients were allowed to develop using a one-dimensional BL model, could reasonable predictions be made.

As well as the CBL, box models can be used to investigate complex chemistry schemes in street canyons (e.g. Liu and Leung, 2008; Murena, 2012; Zhong et al., 2015). Since mixing timescales within the canyon are typically shorter than reaction timescales (except for those involving very fast reacting species e.g. OH, HO_2), the well-mixed assumption of box models is usually reasonable. The detailed dependence of pollution concentration in street canyons on chemical reactions, pollution mixing and the vertical exchange at canyon top is typically investigated using Reynolds-Averaged Navier-Stokes (RANS) models and LES (Li et al., 2006; Zhong et al., 2016). From such investigations box model parameters can be derived. Box models are then used to understand which are the most important processes controlling the pollution concentrations of individual chemical species (Zhong et al., 2015).

1.2.6.4   Regional Scale Box Models

Human population and pollution tends to be large along coastal regions. Coastal outflow is important for ventilation of those areas (Dacre et al., 2007). A stable internal boundary layer often occurs over the ocean so that outflow from the continent becomes decoupled from the ocean surface. The layer above the internal marine boundary layer is termed the "coastal outflow layer" and often has elevated wind speeds due to the decoupling from the surface. Peake et al. (2014) ran a regional NWP model over the eastern side of North America, with ground-level release of exponentially decaying tracer, for 27 days during the summer of 2004. Six boxes were used to represent different portions of the atmosphere over land and sea. The average mass of tracer in the boxes and the fluxes between the boxes was determined. They found horizontal ventilation of the continental BL via coastal outflow to have similar magnitude to vertical ventilation during the case study. The behaviour of the coastal outflow was understood in terms of box model parameters, such as the ratio of the advection rate and decay rate, and the relative heights of the continental and marine BLs.

1.2.7   Air Quality Models

An overview of continental (i.e. O(1000 km)) to street scale AQMs is given in this section. There are two main types of AQMs – offline and online (Baklanov et al., 2014). A

schematic of the two types of AQM is given in Fig. 1.14.
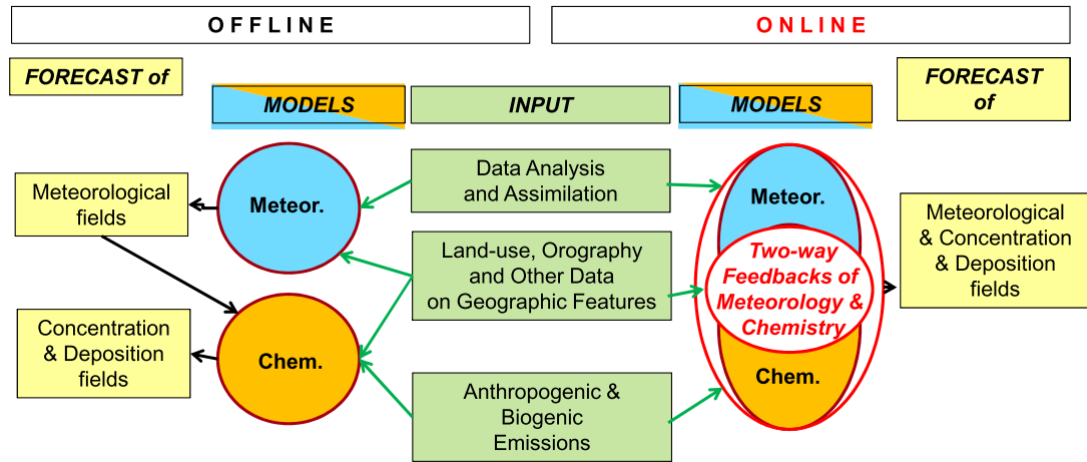
Figure 1.14: Schematic from Baklanov et al. (2014) showing the coupling approaches used in AQMs.

Offline models use meteorological fields from NWP to drive a CTM. There is no two-way exchange of information between the NWP and the CTM. The CTM uses the meteorological fields to transport pollutants, in processes such as dry and wet deposition, and in chemical reactions. Chemical reactions are dependent on meteorological variables such as specific humidity, temperature and solar radiation.

Online models allow the chemistry to access information on meteorological processes that occur on timescales shorter than NWP output (Zhang, 2008). Online models can be split into so called online "access" models and online "integrated" models. In online access models the NWP and CTM are separate, but meteorological and chemical data are simultaneously available (although often not at the same time step). The grids and numerical schemes of the NWP and CTM can be different. Information is regularly exchanged (sometimes both ways) via an interface between the NWP and CTM. In online integrated models the CTM and NWP are not separate. The transport of meteorological variables and chemical species is done consistently on the same grid, with the same advection scheme and turbulence parametrisations. The chemical reactions also take place on the same grid. Feedbacks (e.g. between chemical composition and radiative exchange) occur at every timestep.

1.2.7.1 Eulerian AQMs

Transport of chemicals in Eulerian AQMs is calculated on a fixed grid. Eulerian AQMs used for operational AQ forecasts are typically run at regional, continental and sometimes global scales. Kukkonen et al. (2012) reviewed 18 European operational regional and continental scale AQMs. Of those 15 were Eulerian, two had the option of being run in Eulerian or Lagrangian mode, and only one model was Lagrangian. Only three of the

AQMs had online coupling, all of which were Eulerian. It is likely that future Eulerian AQMs will increasingly have online coupling due to the advantages of being able to incorporate feedbacks, the CTM having access to better temporal resolution meteorological data, and the treatment of meteorology and chemistry being more consistent (Kukkonen et al., 2012; Baklanov et al., 2014). Despite this, most current operational AQMs are offline. Reasons include lowered computational cost due to NWP being already provided, the suitability for ensemble simulations, meteorology and chemistry being independent making interpretation of model output easier when working on CTM developments, and the ability to run the CTM (and its emissions) at higher spatial resolution than NWP (Schlünzen and Sokhi, 2008).

The Eulerian AQMs reviewed by Kukkonen et al. (2012) tended to have O(20 km) horizontal grid length when run at regional and continental scales. There were some examples of offline Eulerian models, that when nested within coarser models, had O(2 km) horizontal grid length. The limit on horizontal grid length is often largely set by the computational expense of the chemistry scheme (Stockwell et al., 1990).

The UK Met Office have an online integrated model called the AQUM (Air Quality in the Unified Model) (Savage et al., 2013). The domain covers most of Western Europe, meaning that it can capture regional scale O_3 and PM events affecting the UK. The AQUM runs with 12 km horizontal grid length and 38 vertical levels up to a top model height of 39 km. Over land in the UK, the NAEI (National Atmospheric Emissions Inventory) provides emissions at 1 km resolution, and in Europe outside the UK, EMEP (European Monitoring and Evaluation Program) provides emissions at 50 km resolution. The UK Department for Food and Rural Environmental Affairs (DEFRA) use the AQUM to derive an AQ index that is reported to the public (DEFRA, 2020).

Schaap et al. (2015) investigated the effect of systematically increasing the horizontal resolution in five offline Eulerian AQMs over Europe. Meteorology was provided at 12 km horizontal grid length using reanalysis data, and emissions data was available at 7 km spatial resolution. The CTMs were run at 56 km, 28 km, 14 km and 7 km horizontal grid length. While increasing the resolution did not improve the predicted rural concentrations, it did improve the predicted concentrations near cities. Largest improvements were seen between 56 km and 14 km horizontal grid length. By 14 km horizontal grid length, the pollution concentration signal on the scale of large cities was reasonably predicted. To predict sub-city scale concentrations, more detailed emissions data, surface representation and meteorology would be required.

1.2.7.2   Lagrangian AQMs

Lagrangian (or "Lagrangian Trajectory") AQMs are offline and use meteorology from NWP. The CTM solves an ordinary differential equation for the trajectories of the individual pollution particles. The CTM does not have to solve the advection term, avoiding

numerical diffusion and allowing large time steps to be used which reduces the computational cost. The particle trajectories are interpolated onto an Eulerian grid to obtain pollution concentrations.

Since the meteorology is typically provided to offline models at a frequency of hours, Lagrangian AQMs do not resolve the turbulence or all of the mesoscale eddies. The unresolved motions are usually parametrised using random walk techniques. These can range in complexity from a simple well-mixed BL approach (e.g. Sofiev et al., 2006) to solving the Langevin equation (e.g. Thomson, 1987). In a dispersion modelling context (i.e. when chemistry is not included) these models are often termed Lagrangian Stochastic Models (LSMs).

A commonly used Lagrangian AQM is the UK Met Office NAME (Numerical Atmospheric-dispersion Modelling Environment) model (Jones et al., 2007). Its development was prompted in response to the Chernobyl nuclear disaster, so that long range transport and deposition of radioactive material could be modelled. It has since been used in other emergency response situations such as the 2011 Eyjafjallajökull volcanic eruption (Dacre et al., 2011) and the 2001 foot and mouth outbreak (Gloster et al., 2003). It also has the capability of calculating back trajectories necessary in source apportionment investigations. For AQ modelling the STOCHEM chemistry module is used (Collins et al., 1997). AQ studies have been conducted from city to continental scales.

NAME has two separate random walk schemes for near and far field dispersion (Webster and Thomson, 2018). For continental scale AQ modelling usually only the far field scheme is used. When the near field dispersion is of interest (e.g. at the city scale), the near field dispersion scheme is typically used for the first $30-60$ min of a particle's trajectory, before switching over to the far field dispersion scheme. The far field dispersion scheme is diffusive (or to put more formally it represents dispersion as a Wiener process). The trajectory calculation has a component due to advection by the mean flow, and two separate Gaussian random walk components representing turbulence and mesoscale eddies. The magnitude of the random walks is determined by a diffusivity parameter. The near field trajectory is obtained by solving the Langevin equation, which includes memory of the particle's previous velocity. The Langevin equation is discussed in more detail in Sect. 3.6.2.

In complex topography (e.g. the UCL) and at short ranges from emission, Lagrangian models that track individual particles require large computational resources. For small scale structure in the concentration field to be captured on the output grid, a very large number of particles is required. A solution is the so called particle-puff model. It has been adopted recently in NAME, and is used in other AQMs such as the widely used open access model CALPUFF (Ghannam and El-Fadel, 2013). A puff is released, and the CoM of the puff is advected using the Lagrangian trajectory method. Around the CoM is a (typically Gaussian) distribution of pollution which spreads with time (Leelőssy et al., 2014). In the case of NAME, to prevent each puff growing so large that it ends up being

within two flow regimes, the puff keeps splitting, until it is well-mixed within the BL (Jones et al., 2007).

1.2.7.3 Street Scale AQMs

AQMs that provide real-time street scale pollution forecasts are offline. They require knowledge of the street scale flow, which NWP currently cannot provide. Flow therefore has to be parametrised in the CTM. When the details of the processes controlling AQ are of interest, computational fluid dynamics (CFD) simulations with online chemistry coupling are often carried out for limited areas (e.g. street canyons or small portions of a city) (Zhong et al., 2015, 2016). They can be used to improve understanding and parametrisation of the processes, driving development of real-time AQMs.

Gaussian plume models are the most widely used and one of the earliest dispersion models developed for point and line sources. They are an analytical solution to the advection-diffusion equation (Stockie, 2011), and require empirically defined diffusion parameters in the lateral and vertical. Some of the key assumptions of the model are: 1) during the time it takes a parcel to travel the downstream length of a plume, emissions from each source are at a constant rate, there is steady-state flow and constant meteorological conditions, 2) Gaussian distribution of mean concentration with lateral and vertical distance downstream of the source, and 3) no wind shear in the vertical (Arya, 1999). Advanced versions have been developed that account for complex topography and atmospheric stratification. These advanced Gaussian plume models are commonly used as AQMs, where chemistry and processes such as wet deposition are incorporated. They tend to be computationally inexpensive. Examples include ADMS-urban (McHugh et al., 1997; CERC, 2017) and AERMOD (Cimorelli et al., 2005).

ADMS-urban is the most commonly used street scale AQM and has been evaluated by many studies (e.g. Sabatino et al., 2008). It uses continuous or finite-duration emissions from inventories, includes chemistry, accounts for BL structure using L_{MO} and z_h, and has skewed-Gaussian vertical concentration profiles under convective meteorological conditions. To model street canyon and individual building dispersion effects it uses OSPM (Operational Street Pollution Model) (Berkowicz, 2000) and the ADMS-BUILD module (Robins and McHugh, 2001) respectively. Since Gaussian models are computationally inexpensive, ADMS-urban can be used to give detailed street scale pollution concentration predictions at the city scale. Having high-resolution concentration predictions is particularly useful when there are large concentration gradients typical of busy roads in cities.

ADMS-urban has been coupled to the CMAQ (Byun, 1999) regional scale (offline Eulerian) AQM. Pollution concentrations were predicted on a 20 m $\times$ 20 m grid over the entirety of Greater London (Beevers et al., 2012). Meteorology was provided by the WRF NWP model (Skamarock et al., 2019) to both CMAQ and ADMS-urban. The coupling

involved summing the pollution concentrations predicted by CMAQ and ADMS-urban. This to their own admission led to double counting. An improved method of coupling ADMS-urban to a regional scale AQM was presented by Hood et al. (2018). The street scale pollution was isolated by running two ADMS-urban runs for 1 hr, one with gridded and one with explicit emissions, and subtracting the two. The result was added to the regional scale AQM. However, the coupling is such that the regional and street scale AQMs still have no knowledge of one another.

There are fast street scale Largrangian dispersion models that can be used for emergency response purposes (Hertwig et al., 2018). For example, the QUIC-PLUME model (Williams et al., 2004). Its canopy velocity field is based on empirical-diagnostic representations, and its Lagrangian trajectory is obtained by solving the Langevin equation, with extra terms accounting for inhomogeneities in the urban canopy turbulence. However, unlike at the city and regional scales, to the author's knowledge there are no street scale Lagrangian models that have representation of chemical reactions, enabling use as AQMs.

Another street scale AQM that is becoming more common, is the street-network model. Street canyons and intersections are treated as boxes, in which the pollution is uniformly distributed, and concentration fluxes are passed between boxes. Although the buildings are not represented explicitly, the model is aware of the street layout. The only operational street-network models are SIRANE (Soulhac et al., 2011) and the unsteady version SIRANERISK (Soulhac et al., 2016). Bulk velocity in each box, vertical turbulent exchange at the canopy top and vertical exchange at intersections is parametrised. The parametrisations require knowledge of the external flow, which is provided by a parametrisation of the BL above.

A multi-scale AQM called SinG (Lugon et al., 2020) has recently been developed. It has two-way dynamic coupling between a street-network model and the first atmospheric model level of a regional scale AQM. The model was run with one-way and two-way coupling. The two-way coupling meant that the street-network model could influence the concentrations above the canopy, which led to up to 67% pollution concentration differences within the canopy compared to the one-way coupling.

Another type of street scale AQM are land-use regression models (Briggs et al., 1997; Hoek et al., 2008; Karroum et al., 2020). They are statistical models that do not require information of BL and UCL processes. Information such as road traffic, land cover and altitude are used to form a geographic information system (GIS) for an area. These are provided as independent variables to a multiple linear regression, which minimises the error between the regression equation and pollution concentration measurements made at multiple sites, typically over a period of weeks. Once a regression equation has been formed, it is used to create a spatially continuous map of pollution concentration within the area. Land-use regression models are limited by the coverage and density of pollution concentration measurements, and predictions can only be made based on past

trends.

1.2.7.4 The Next Generation of Regional to Street Scale AQMs

The UK Met Office are considering developing regional scale AQMs, with O(100 m) horizontal grid length, for use over urban agglomerations in the foreseeable future (personal communication Dr Humphrey Lean). At this scale the pollution emissions and surface characteristics of individual neighbourhoods become resolved. To accurately predict surface level pollution concentrations in individual neighbourhoods, good representation of the influence of the urban canopy on pollution transport, both within and above the urban canopy will be necessary. This requires improved NWP parametrisations of turbulence and drag in the surface layer, regardless of whether the AQM is online or offline. NWP provides the velocity to the CTM in offline and online access models. NWP is used for advection and vertical turbulent mixing of pollution in online integrated models. The CTMs in offline and online access models have their own turbulence parametrisations, which require improved representation of UCL processes.

There is a choice over whether regional to street scale AQMs are Eulerian or Lagrangian. In the context of regional scale AQMs, DEFRA conducted a review (Williams et al., 2011) that considered the advantages and disadvantages of Eulerian and Lagrangian AQMs. They concluded that Eulerian models are more appropriate for regional scale AQ modelling, since Lagrangian models are harder to nest, and have difficulties representing pollutants not directly released and specifying background pollutant concentrations. When vertical mixing of pollution in the UBL is of interest, Lagrangian AQMs (such as NAME) have the advantage of incorporating memory of the particles in the vertical mixing, which is important at O(10 min) timescales from release in convective conditions. It has been demonstrated that O(100 m) horizontal grid length NWP resolves the majority of CBL turbulence (Boutle et al., 2014; Lean et al., 2019), and it follows that online Eulerian AQMs should too. This means that the O(10 min) vertical mixing processes, which are largely controlled by z_h scale overturning eddies, are likely well represented in online Eulerian AQMs. The short timescale vertical mixing advantage of Lagrangian models over online Eulerian models, might therefore be less important at O(100 m) horizontal grid length.

At O(100 m) horizontal grid length, the flow in the urban canopy cannot be resolved. This means that street scale pollution predictions will still be made using AQMs like ADMS-urban and SIRANE, which parametrise the flow and dispersion. They tend to have their own parametrisations of turbulence and velocity in the entire UBL. The regional scale and street scale AQMs could be coupled at the top of the surface layer, so that the transport above the surface layer is performed by the regional scale AQM. This might be particularly beneficial when regional scale AQMs are run at O(100 m) horizontal grid length and the majority of turbulence is resolved in the ML. This is because

they should pass improved pollution concentrations and velocities as boundary conditions (BC) to the street scale AQM, compared to parametrisations of the BL in street scale AQMs.

1.2.8   Summary

The previous sections highlighted several gaps in the existing literature. Previous box model studies investigating transport processes controlling urban air pollution tend to use daily averaged input data, do not simultaneously represent background pollution and entrainment, and do not have both BL depth measurements and meteorological measurements in the ML. The ClearfLo meteorological and pollution observations of the London BL provide an opportunity to investigate the importance of different transport processes (including advection of background pollution and entrainment) throughout the day with a box model constrained by high quality input data. Also, to the author's knowledge there have been no studies representing the urban canopy and ML of the BL as two separate boxes, to investigate the most important transport processes affecting urban canopy pollution concentration.

To the author's knowledge there have also been no previous studies comparing the vertical mixing of tracer in NWP when vertical mixing is parametrised versus when the dominant CBL eddies are almost fully resolved. Differences in the vertical mixing could have large implications for the concentration distribution of pollution at the city scale.

The turbulent mixing length within urban canopies is known to be zero at the surface, exhibit a maximum near the middle of the canopy and a minimum at the canopy top (Coceal et al., 2006; Castro, 2017). How much this characteristic shape varies between urban canopy geometries and flow regimes with different packing density, different building array configurations, and different incident wind directions requires further investigation. It has not been established how significant mixing-layer type eddies generated at urban canopy top are for turbulent mixing in urban canopies. Also, the influence of the building fraction on turbulent and time-mean momentum transport is often neglected in models, but it has recently been demonstrated to be more important than previously thought (Giometto et al., 2016; Schmid et al., 2019).

The overarching questions this thesis addresses are: 1) how is pollution vertically mixed in the UBL at vertical scales ranging from the urban canopy depth to z_h? 2) How should vertical mixing of pollution be represented in NWP and AQMs?

Investigations of vertical mixing within the urban canopy will be limited to neutral conditions, since neutral flows are very complex in even the simplest urban geometries and are not well-understood at a fundamental level. Also, mechanical production of turbulence tends to dominate buoyant production of turbulence in urban canopies across neutral to moderately convective BL conditions (Britter and Hanna, 2003).

Investigations at the vertical scale of the UBL shall focus on the CBL, since box models assume a well-mixed BL and because representation of CBL turbulence in NWP requires renewed attention, with grid lengths becoming small enough to resolve the dominant buoyant eddies.

1.3   Thesis Structure and Aims

Chapter One has introduced the topic of research and reviewed the current understanding in the literature.

Chapter Two uses one- and two-box models to analyse the pollution transport processes in the UCL and ML of the UBL. Aims:

- Determine the relative importance of different transport processes controlling pollution concentration in the UCL and ML of the UBL throughout the day.

- Calculate timescales associated with the transport processes.

Chapter Three investigates vertical mixing of passive tracer in the UM at horizontal grid lengths ranging from 1.5 km to 55 m. Aims:

- Ascertain the limitations of current NWP advection and vertical mixing schemes in the CBL grey zone.

- Quantify the influence of representing turbulence at $O(100 \text{ m})$ versus $O(1 \text{ km})$ horizontal grid length on the distribution of tracer in the UBL.

- Develop a reduced analytical model to understand the vertical mixing characteristics and determine tracer vertical mixing timescales when the UM is run with $O(100 \text{ m})$ and $O(1 \text{ km})$ horizontal grid lengths.

Chapter Four utilises LES and DNS data to examine turbulent mixing across different urban canopy geometries and to motivate development of a first-order mixing length turbulence closure. The chapter is in the form of a paper which will be submitted to the journal Boundary Layer Meteorology. Aims:

- Establish whether the mixing-layer analogy explains turbulent mixing behaviour in urban canopies.

- Formulate a first-order momentum mixing length turbulence closure suitable for multi-layer urban canopy models.

- Identify the general characteristics of momentum mixing length profiles across urban canopy geometries.

- Analyse the effect of the building fraction on momentum transport in urban canopies.

Chapter Five synthesises the main research findings and considers their implications for urban canopy, NWP and AQ modelling.

Chapter 2

One- and Two-box Modelling of an Inert Pollutant in London's Boundary Layer

2.1 Introduction

In this chapter, Eulerian box models are used to investigate the relative importance of different transport processes in determining city scale pollution concentration. Eulerian box models provide a simple framework in which to understand the complex processes and their interactions throughout the day (as previously discussed in Sects. 1.1 and 1.2.6). The terms in the box model equations represent individual transport processes, and the solutions to the equations can be used to calculate their budgets.

The analysis is conducted using data from the ClearfLo project, during which measurements of pollution and meteorological conditions were made in London's BL (Bohnenstengel et al., 2015). The meteorological measurements are processed to derive input parameters to the box models. NO_x concentration measurements made at the top of the BT Tower are compared against NO_x concentrations predicted by the box models. NO_x to a reasonable approximation can be treated as a chemically inert tracer during the case study (see Sect. 2.4.1). As there are simultaneous measurements of NO_x and meteorological conditions, when box model predictions are compared to the NO_x measurements, analysis can be made of which processes not represented by the box models might be important.

The case study period was chosen to be between $12^{th} - 17^{th}$ August 2012, during an intensive observation period (IOP). In Sects. 2.4 and 2.5, timescales associated with the different meteorological processes are calculated during the case study, and the validity of the box model assumptions are assessed.

The one-box model represents the average concentration in the UBL at a given time. Since pollution concentration is typically greater near the surface than in the air above, particularly in urban canopies where air is often poorly ventilated, the addition of a second box enables a more accurate representation of the vertical pollution distribution.

Therefore, a two-box model is formulated in Sect. 2.8, where the bottom box represents the urban canopy layer, and the top box represents the ML of the BL. This two-box model is used to investigate the difference in NO_x concentration between air in Greater London's urban canopy and air in the ML of the BL above. Sensitivity studies are performed using the one- and two-box models, to understand which transport processes affecting AQ are most important across a range of typical convective meteorological conditions. Parameters associated with the urban canopy are also varied, to determine their impact on AQ in the urban canopy and the ML above.

2.2 One-box Model Formulation

The Eulerian box model presented here predicts the time evolution of volume-averaged concentration within the three-dimensional volume the box encloses. The top of the box is taken to be the mixing height, z_{MH}, and the length and width are the approximate dimensions of the urban area. The model assumes that all parameters and variables can be represented by a spatial average, and that mixing of emissions from the surface occurs instantaneously.

Chemical reactions, dry deposition and wet deposition (physico-chemical processes) are not represented in the box model. Chemical reactions would add significant complexity to the box model dynamics. Dry deposition tends to be small over typical transport timescales in urban areas (see Sect. 2.5.1). It is difficult to accurately represent wet deposition in the box model due to limited measurements of precipitation during the case study. Wet deposition is treated as a limitation of the box model and its influence is assessed in Sect. 2.5.2.

The mass conservation equation governing the concentration of a passive pollutant is given by (Seinfeld and Pandis, 2016)

$$\dot{c} = \frac{q}{z_{MH}} + \frac{c_b - c}{\tau} + \frac{c_a - c}{z_{MH}} \dot{z}_{MH} \theta_H(\dot{z}_{MH}), \qquad (2.1)$$

where dot above symbols represents time rate of change, θ_H is the Heaviside step function defined to be 1 when its argument is positive and zero otherwise, c is the pollutant concentration, q is the pollutant mass emission rate per unit area, c_b is the background pollutant concentration (concentration upstream of the box), c_a is the pollutant concentration aloft of the box, and $\tau = L/U$ is the horizontal advection timescale, where L is the length and width of the box, and U is the wind speed. The first term on the right-hand side will be referred to as the source term. The second term on the right-hand side will be referred to as the advection term, and represents horizontal advection of c_b into and c out of the box. The third term on the right-hand side will be referred to as the entrainment term. During BL growth the BL entrains air of concentration c_a, which, depending

on whether it is lower or higher concentration than c, determines whether it decreases or increases c respectively.

In this chapter the one-box model represents the Greater London BL. L is taken to be 50 km, assuming that Greater London can be defined as an area of large pollution emissions enclosed by the M25 motorway. In Sects. 2.3.3 and 2.3.2 box model parameters are estimated using measurements of meteorology, pollution and traffic. The parameters are chosen to be representative of the Greater London BL during the case study.

2.3   Observational Data

The ClearfLo project ran for three years from January 2010, where long term measurements of meteorology and air pollution were made within London's BL. Measurements were made at street level and at elevated sites in urban and rural locations (see Fig. 1 in Bohnenstengel et al. (2015)). The aim was to better understand pollution in the BL and improve predictive capability for air quality. There were two intensive observation periods (IOPs) – one winter (6th Jan – 11th Feb 2012) and one summer (21st Jul – 23rd Aug 2012).

The 12th–17th Aug are the focus throughout this chapter due to data availability and suitability of meteorological conditions. The winter IOP did not have long periods of highly unstable atmospheric conditions required for the box model instantaneous mixing assumption to be reasonably satisfied. Due to technical issues with the instruments, 12th–17th Aug was the only period where there were simultaneous eddy covariance measurements of meteorology and NO_x measurements at BT Tower (BT), and Doppler Lidar z_{MH} measurements at Sion Manning School in North Kensington (NK).

Measurements of pollutant concentrations (including NO_x) and meteorological conditions were made at a height of 190 m near the top of the BT Tower. Under convective conditions, 190 m above the surface is generally in the ML of the BL, so NO_x concentrations should be reasonably representative of values throughout the depth of the BL. NO_x measurements at 190 m above the ground are less influenced by local emissions, and are therefore likely to be more representative of the NO_x concentration throughout the Greater London BL than surface level measurements. The only site with measurements suitable for representing rural background concentration of NO_x entering London was at Harwell, approximately 80 km west of Central London. A map of the measurement sites is given in Fig. 2.1.

2.3.1   Synoptic Conditions

In this section the synoptic conditions during the case study are described on a daily basis using surface analysis charts, dispersion model particle trajectories and precipitation

Figure 2.1: The two red dots indicate the locations of BT Tower and Sion Manning school in North Kensington. On the right of the top right caption is Greater London and the red rectangle indicates the area covered by the figure. On the left of the top right caption is the UK and the black dot represents Harwell to the west of Greater London. Source: Google Earth.

measurements in London. Figure 2.2 shows surface analysis charts during each day of the case study at 12:00 UTC. Figure 2.3 (adapted from Bohnenstengel et al. (2015)), shows the percentage time air arriving in London spent over different regions during the previous 24 hr. Calculations were performed using back trajectories from the UK Met Office's NAME (Numerical Atmospheric-dispersion Modelling Environment) atmospheric dispersion model (Jones et al., 2007). Figure 2.4 shows the locations of six sites measuring rainfall in London. Five of which contribute to the UK Met Office MIDAS (Met Office Integrated Data Archive System) database and will be termed MIDAS sites herein. Rainfall at the MIDAS sites was measured with tilting syphon gauges and data was provided on request by the Centre for Environmental Data Analysis. The other site is BT Tower which had a Vaisalla WXT520 weather station. It has a sensor that detects rain by the pressure it exerts on impact. Figure 2.5 shows total hourly rainfall at each of the sites during the case study period.

2.3.1.1   12$^{\text{th}}$ Aug

From Fig. 2.2a it can be seen that on the 12$^{\text{th}}$ there was high pressure over Scandinavia and the North Sea, and low pressure over Benelux, France and the Atlantic. London was near the edge of the two systems. From Fig. 2.3 it can be seen that much of the air
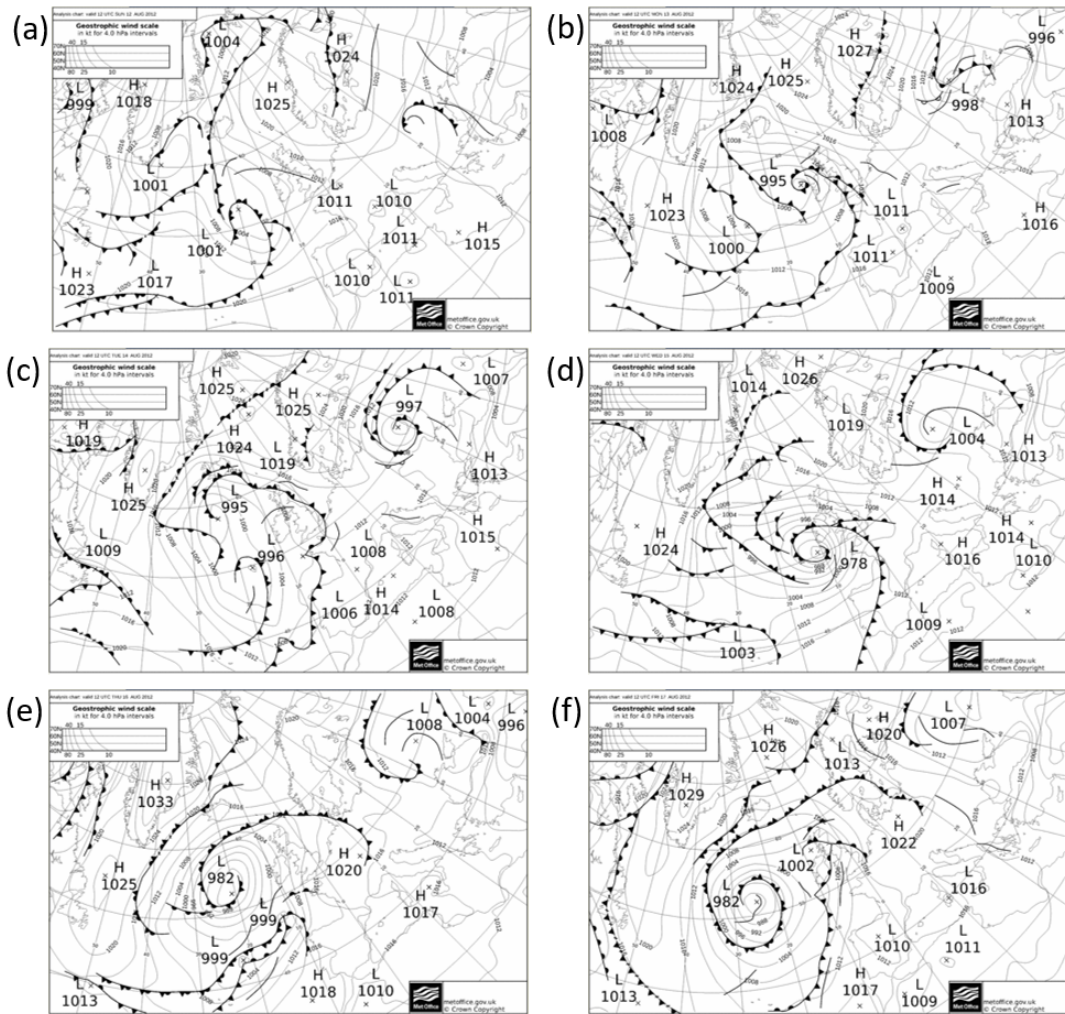
Figure 2.2: Surface analysis charts at 12:00 UTC on (a) 12th, (b) 13th, (c) 14th, (d) 15th, (e) 16th and (f) 17th Aug 2012. Courtesy of the Met Office (UK Met Office, 2012).

was travelling from Benelux and the North Sea before approximately 12:00 UTC. After which there was a significant contribution from France. A trough passed over London at approximately 12:00 UTC, as seen in Fig. 2.2a. Troughs are typically associated with low pressure near the surface and low level convergence. There was no precipitation over London during the day.

2.3.1.2   13th Aug

From Fig. 2.2b it can be seen that on the 13th low pressure over the Atlantic moved closer to London. A warm front moved through London between 12:00-18:00 UTC. From Fig. 2.3 it can be seen that until approximately 12:00 UTC air originated mostly from South East England and the Channel, but after 12:00 UTC originated mostly from France. This is likely due to a change in air mass over London when the front passed through. There was light rain at five of the sites across London in the afternoon and evening as seen in

Chapter 2. One- and Two-box Modelling of an Inert Pollutant in London's Boundary Layer
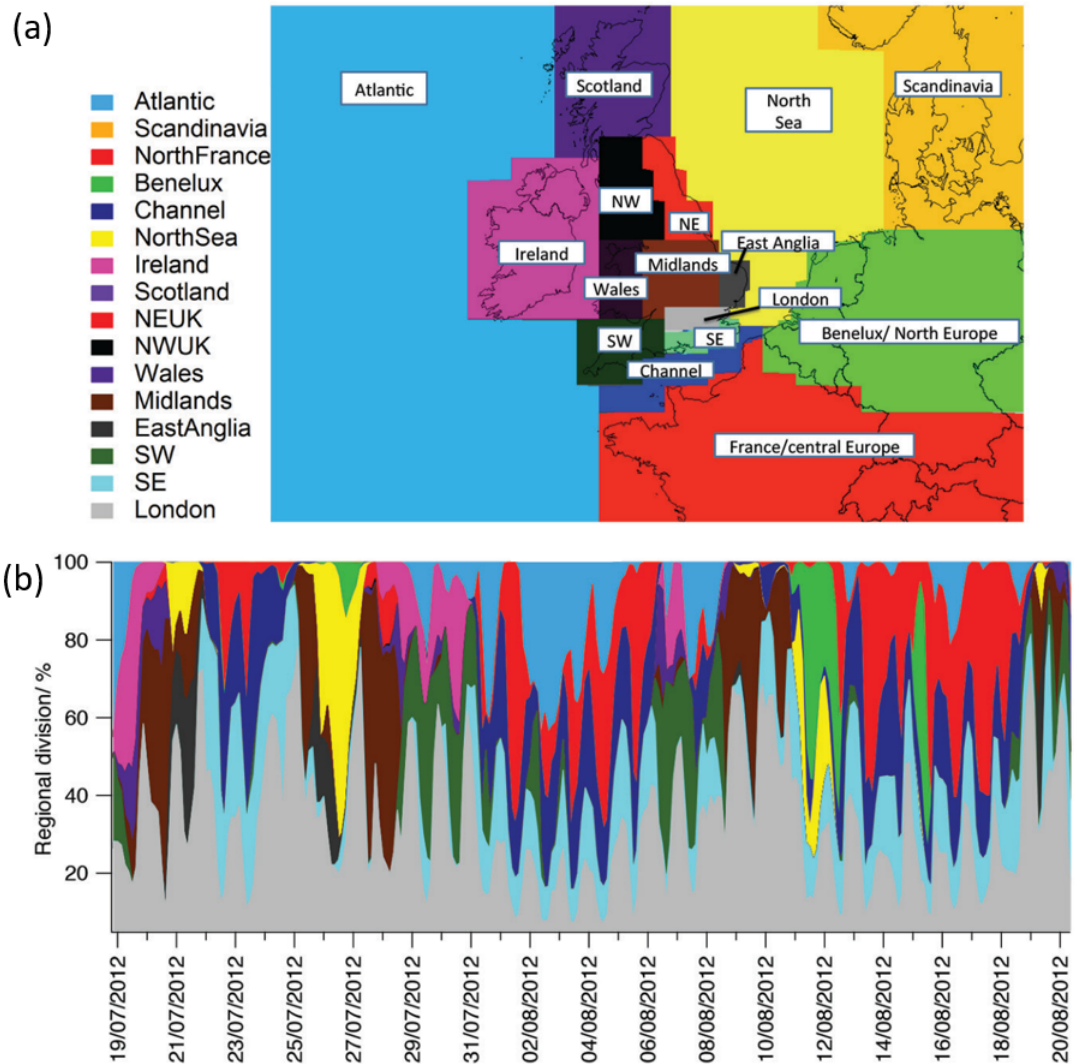
Figure 2.3: (a) Regions that air travelled through on their way to London and (b) percentage time that air spent over each region during the 24 hr NAME back trajectories. Adapted from Bohnenstengel et al. (2015).

Fig. 2.5.

2.3.1.3 14th Aug

A cold front passed over London between 00:00-12:00 UTC on the 14th, and at the start of this period there was rain as seen in Fig. 2.5. The rest of the day had no precipitation. As seen in Fig. 2.3, air originated mostly from the Channel, France and South East England, in changing proportions throughout the day.
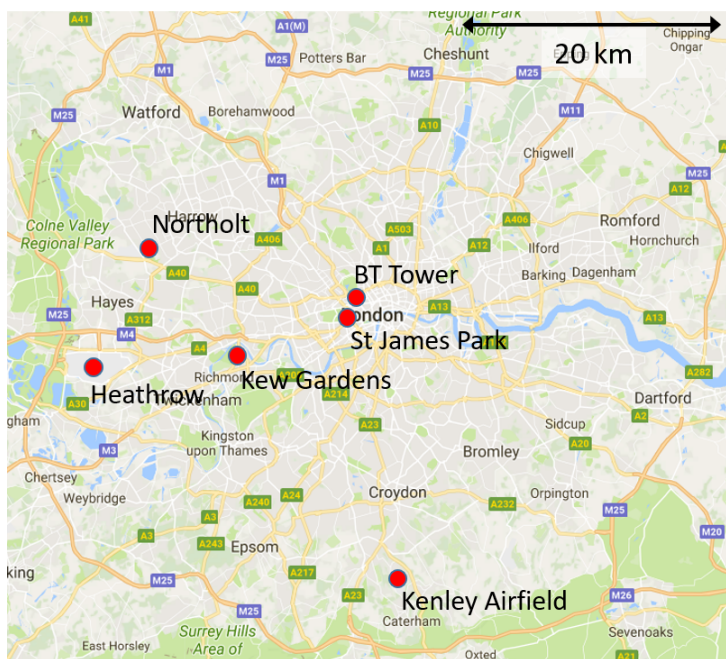
Figure 2.4: Location of the UK Met Office MIDAS sites and BT Tower where rainfall measurements were made. Source: Google Maps.
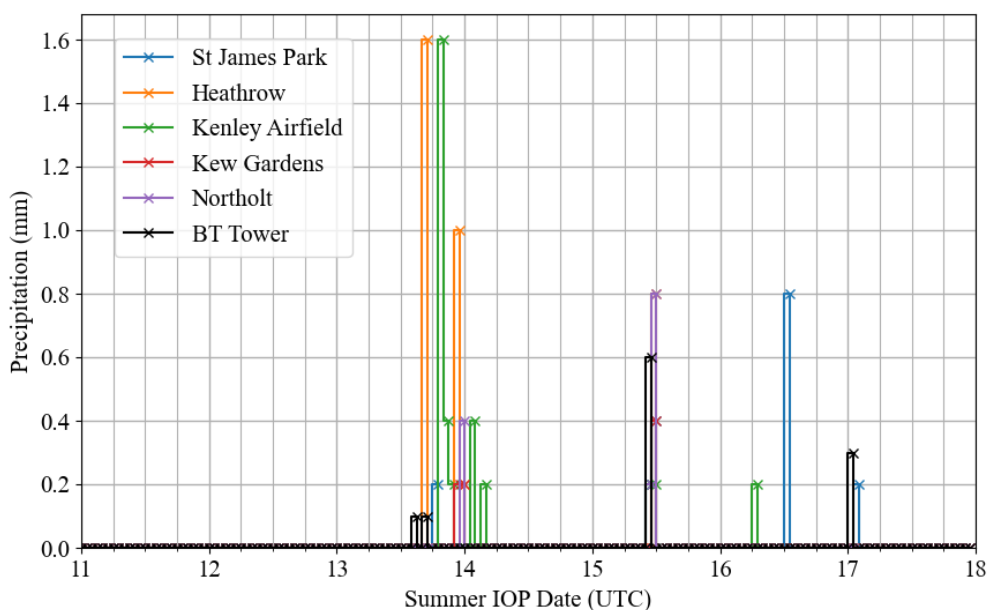
Figure 2.5: Hourly rainfall at each of the MIDAS sites and BT Tower during the case study period.

2.3.1.4   15$^{\text{th}}$ Aug

As seen in Fig. 2.2d, the low pressure system over the Atlantic moved in over England on the 15$^{\text{th}}$, bringing a warm front quickly followed by a cold front at approximately

12:00 UTC. This coincided with a small amount of rain at 4 of the 6 sites as seen in Fig. 2.5. From Fig. 2.3 it can be seen that before 12:00 UTC air originated mostly from Benelux but afterwards air originated mostly from France.

2.3.1.5   16th Aug

It can be seen in Fig. 2.2e that on the 16th there was high pressure over Benelux and France, and the low pressure moved back out to the Atlantic. There was no frontal activity, but a small amount of rain likely associated with convective showers was seen at two separate sites at 06:00 UTC and 12:00 UTC, as seen in Fig. 2.5. From Fig. 2.3 it can be seen that until approximately 12:00 UTC, air originated mainly from Benelux and South East England, but afterwards had large contribution from France.

2.3.1.6   17th Aug

From Fig. 2.2f it can be seen that on the 17th, London was on the edge of high pressure over Benelux and low pressure over the Atlantic. A warm front passed through London between 00:00 UTC and 06:00 UTC, after which there was no more frontal activity. There was a small amount of rain at two sites at approximately 01:00 UTC. Most of the air originated from France as seen in Fig. 2.3.

2.3.1.7   Suitable Case Study Dates

Based on the synoptic conditions, it is likely that the box model will perform best between 06:00–24:00 UTC on the 17th. During this period there were no fronts, troughs or rain. Depending on the influence of localised rainfall on BT Tower NO_x measurements on the 16th, the box model might compare well to observations that day. On all days, the regions from which background air was advected changed throughout the day. The weather during the case study is changeable, due to London generally being on the edge of low pressure over the Atlantic and high pressure over Europe.

2.3.2   Measurement Sites and Equipment

2.3.2.1   BT Tower

BT Tower (lat. 51° 31′ 17.31″ N, lon. 0° 8′ 20.12″ W) is situated in Central London and the Greater London Built-up Area surrounds it by approximately 25 km in all directions. BT Tower is the tallest building for several kilometres and is approximately 9 times the local mean building height (Barlow et al., 2009). Within a few kilometres of the tower urban land usage is generally parks, roads, commercial and domestic buildings (no industrial

areas) (Wood et al., 2010). As seen in Fig. 2.1, there are several parks within 5 km, for example less than 1 km north west is Regent's park and 2 km south west is Hyde park. In terms of local climate zones (LCZs), within 2 km of BT Tower the urban surface is best described as a combination of compact midrise (LCZ 2) and scattered trees (LCZ B), but between 2–10 km from BT Tower is best described as a combination of compact lowrise (LCZ 3) and LCZ B.

BT Tower has a 12.2 m tall scaffolding at the top of the main tower resulting in a combined height of 190 m as described in Lane et al. (2013). Turbulent fluxes were processed using methods described in Wood et al. (2010). Attached to the top of the mast were a gas inlet, a Gill Instruments R3-50 ultrasonic anemometer and a Kipp and Zonen CNR4 radiometer. The anemometer sampled at 20 Hz and was raised 0.75 m from surrounding objects so that it had good exposure to wind in all directions. BT Tower and scaffolding distort airflow at the anemometer, and correction factors were developed by Barlow et al. (2011b). The correction factors were approximately 2% of mean wind speed. This is small compared to the uncertainties associated with the box model study hence corrections were not applied. Gas was pumped down a tube from the inlet to a room within BT Tower where a Ecophysics 780TR measured NO_x using the chemiluminescence technique (Lee et al., 2009). During a period including this case study, Lee et al. (2015) estimated that the error on NO and NO_2 concentration measurements was 10% and 15% respectively.

2.3.2.2 NK

During the winter and summer IOPs, Sion Manning school (lat. 51° 31' 15", lon. -0° 12' 49") in NK hosted many measurements. NK is a highly trafficked suburban area approximately 5 km west of BT Tower (see Fig. 2.1). Surface level NO_x measurements were made with an Air Quality Design Fast NO_x Monitor, which like the Ecophysics 780TR at BT Tower, measured NO_x using the chemiluminescence technique. z_{MH} measurements were made with a Halo Photonics Streamline Doppler lidar. The lidar emitted 1.6 μm wavelength light in vertical stare mode, and measured changes in frequency of scattered light due to vertical movements of aerosol. From changes in light frequency due to the Doppler effect, a vertical profile of vertical velocity was derived. The sample rate was 0.278 Hz, the gate length was 18 m and the lowest gate height was 63 m.

z_{MH} was defined by considering when vertical velocity variance drops below a threshold value (Barlow et al., 2015). The vertical velocity variance was calculated over 30 min averaging periods, as a compromise between capturing all of the turbulence scales and diurnal variation. The mean threshold value of 0.1 m^2s^{-2} was varied using 21 values between ±30%, and z_{MH} calculated for each of the values. z_{MH} was taken to be the average z_{MH} calculated for each of the 21 variance thresholds. Using the difference between the minimum and maximum z_{MH}, Barlow et al. (2015) estimated that the

average uncertainty in z_{MH} was 6%.

2.3.2.3 Harwell

Surface level measurements of NO_x at the Harwell Automatic Urban and Rural Network (AURN) site (lat. 51° 34′ 16″, lon. -1° 19′ 31″) were available during the case study period. They are taken to be representative of NO_x concentrations entering London, as has previously been assumed in the literature (e.g. Masiol and Harrison, 2015). Harwell is approximately 80 km west of Central London and its location is indicated in Figure 2.1. The surrounding area is rural and is dominated by agricultural fields. The nearest road is a minor road approximately 140 m away. When wind is from the east some of the air at Harwell will have passed through London. This means it will contain NO_x emitted in the city and is therefore not as representative of air entering London. Harwell was the only rural site near London with NO_x data available during the case study so it is used for background concentration in all wind directions.

2.3.3 Measurements and Estimation of Box Model Parameters

In this section measurements of meteorology, NO_x concentration and traffic data are presented. They are used to derive parameter values for the one-box model and are used in later sections to interpret the case study results. Data input to the box model should be representative of spatially averaged conditions in the box. As shown in Sect. 2.3.3.1, during the case study the average time it takes air to travel through the box is approximately 2 hr. So that parameters are representative of flow within the entire box, measurements used to derive parameters throughout this section have a 2 hr symmetric moving mean average (i.e. 1 hr either side) applied to them. NO_x measurements made at BT Tower also have a 2 hr moving average applied, for consistency in comparison with box model predicted NO_x.

2.3.3.1 Wind Velocity, Sensible Heat Flux, Mixing Layer Height and Incoming Solar Radiation

The ultrasonic anemometer at BT Tower measured the u, v and w components of the wind. Using the eddy covariance technique (Wood et al., 2010), sensible heat flux (Q_H) was calculated and was 30 min averaged before being output. The z_{MH} measured at NK was also processed to give 30 min averages. z_{MH} and Q_H are shown in Fig. 2.6. Only z_{MH} has a 2 hr moving average applied, since Q_H is not used as an input parameter to the box model. z_{MH} fell below 190 m during the night on the 13th, 14th and just before midnight on the 16th. During these times BT Tower is measuring above the BL, so values are not representative of the BL. This means that meteorological measurements made at

BT Tower, which are used as inputs to the box model, break the box model assumptions during these periods.
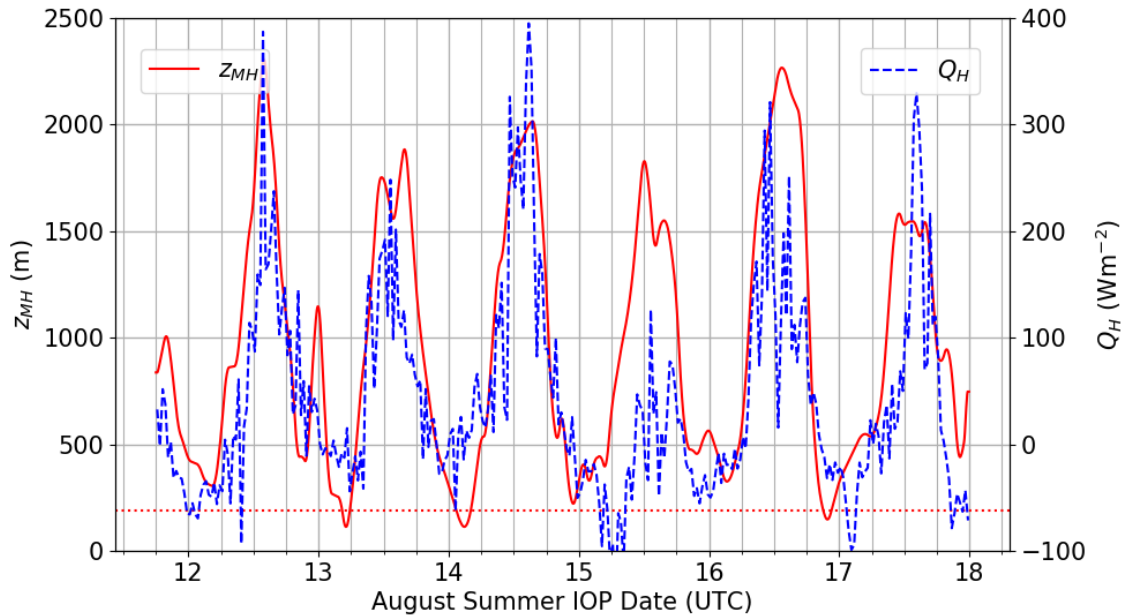
Figure 2.6: z_{MH} measured by a Doppler lidar in NK (solid red) and Q_H measured by an ultrasonic anemometer on top of the BT Tower (dashed blue) during the case study. The horizontal dotted red line represents $z = 190$ m.

With the exception of the 15th, Q_H was generally positive between 07:00 UTC and 19:00 UTC, and had a maximum greater than 200 Wm^{-2}, both of which are indicative of highly convective conditions. Sunrise and sunset were 04:45 UTC and 19:24 UTC respectively. On the 15th Q_H is low, but z_{MH} still reaches large heights. This is likely because of large wind speed that day. There are periods of negative Q_H, particularly during the night. This indicates that during those times the BL was stably stratified and the assumption of a well-mixed BL is not valid. When the atmosphere is stably stratified, pollution takes longer to disperse from the surface, so that concentration tends to be much greater there. Daylight hours are approximately between 04:45 UTC and 19:24 UTC during the case study. The reason that Q_H does not become positive until approximately 09:00 UTC on the 12th and 13th is less clear. It is possible that there was large shear near z_{MH} due to low-level jets on those mornings, entraining warm air down into the BL and causing negative Q_H at BT Tower (Halios and Barlow, 2018). z_{MH} demonstrates a diurnal cycle that is typical of convective conditions during daytime and stable conditions during night-time. z_{MH} is lowest in the night, grows in the morning, reaches a maximum greater than 1.5 km generally in the early afternoon and collapses in the evening.

Figure 2.7 shows the wind speed and direction measured using the ultrasonic anemometer at BT Tower. Wind speed is 2 hr moving averaged but wind direction is

not since it is not used in the box model. Under strong convective conditions, most of the BL is occupied by the ML, and wind profiles are typically approximately constant with height (Garratt, 1994). It is assumed that the top of the BT Tower is in the ML of the BL, so that measured wind speed is representative of the average wind speed in the box. The wind speed at BT Tower is used in the horizontal advection timescale (τ). The average wind speed during the case study was $7.2\,\mathrm{ms^{-1}}$, which for a 50 km box implies $\tau = 1.93$ hr. τ can be interpreted as a flushing timescale, since it determines the time it takes pollution to be advected out of the box.
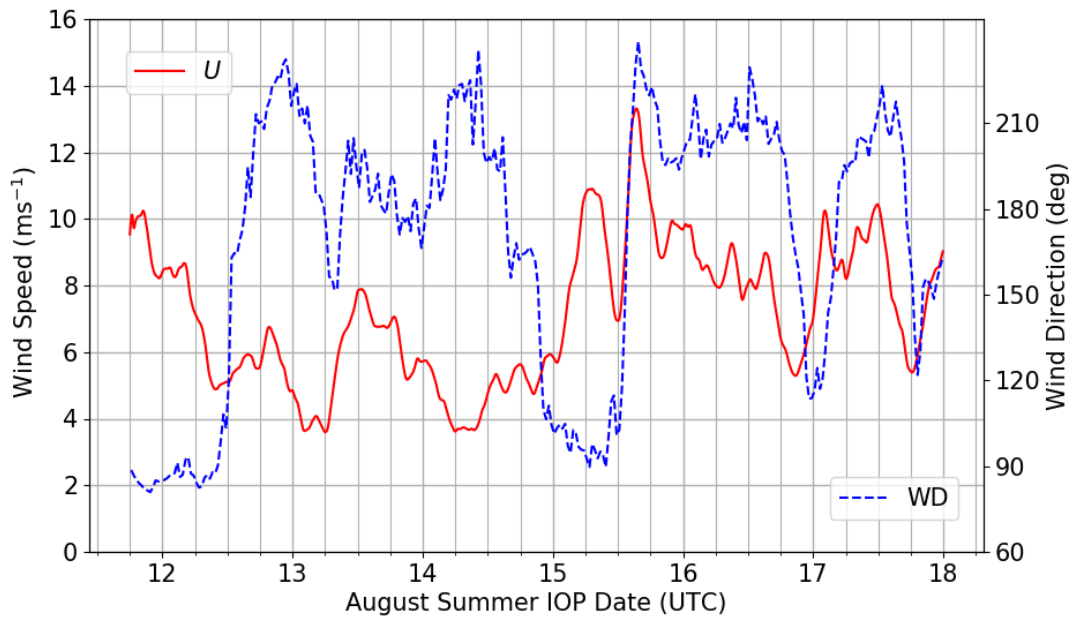
Figure 2.7: Wind speed (solid red) and direction (dashed blue) measured by the ultrasonic anemometer on top of the BT Tower during the case study.

Wind direction was generally between south and south-west, apart from the 12th and 15th mornings, and a short period around midnight between the 16th and 17th, when wind was from the east. This is consistent with the back trajectories shown in Fig. 2.3. On the 12th and 15th mornings, air was predominantly advected directly from Benelux which is east of London. On the 17th a warm front passed just after 00:00 UTC. These easterly wind periods tend to coincide with stronger negative Q_H in Fig. 2.6. This could be due to warm air advection associated with frontal activity or strong wind shear in the night-time residual layer causing mixing down of warm air.

Incoming solar radiation (S_{in}) was measured by the net radiometer at BT Tower and is shown in Figure 2.8. There are large periods of high S_{in} particularly on the 12th, 14th, 16th and 17th. This suggests these days had little cloud cover and conditions were conducive to a well-mixed BL. The 15th has particularly low S_{in}, which is consistent with the day having low Q_H. The 15th was associated with frontal activity and had large loud cover.
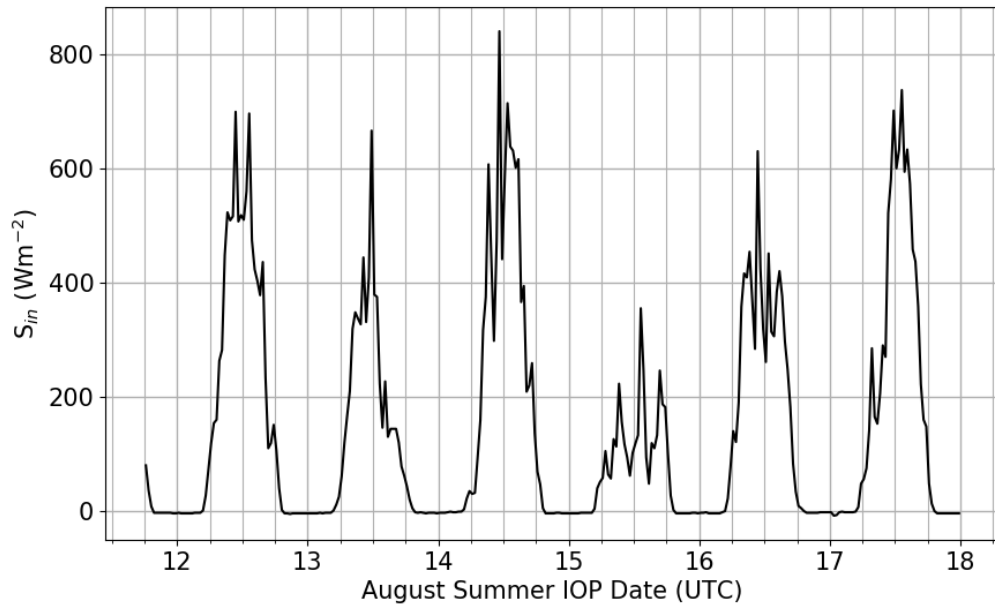
Figure 2.8: Incoming solar radiation measured at BT Tower during the case study.

2.3.3.2 NO$_x$

NO$_x$ concentrations from BT Tower and Harwell during the case study are shown in Fig. 2.9a. NO$_x$ concentration at BT Tower is discussed in detail in Sect. 2.6. The concentration was generally larger at BT Tower than Harwell as expected, since the Harwell site is rural background (RB). The concentration was largest at both sites before 12:00 UTC on the 12th and on the 15th. This is when air arriving in London had a significant proportion of its trajectory over the Benelux region. At other times concentration at Harwell was not so well correlated with concentration at BT Tower. This suggests concentration at BT Tower was generally more dominated by local emissions during those times.

Also plotted in Fig. 2.9a is the NO$_x$ concentration used aloft of the box (c_a). It was taken to be the average of c_b at 13:00 UTC on the 13th, 14th, 16th and 17th. The background concentration was used because air aloft of the BL over London is likely to be similar to upwind rural air. There is little mixing over the capping inversion between the ML and the troposphere, and because the time air spends aloft of the BL over London is short ($\approx$ 2 hr), London emissions are not likely to significantly affect the concentration aloft. 13:00 UTC was chosen since it is when z_{MH} and Q_H are highest, so the BL is likely to be most well-mixed down to the surface. This makes NO$_x$ measurements at the surface more representative of concentrations in the rural air higher up in the atmosphere. The choice of dates is based on wind direction being predominantly from the south and west on those days. When wind is easterly, air at Harwell has passed through London, so is not representative of air entering London. The approach taken is similar to that of Jin
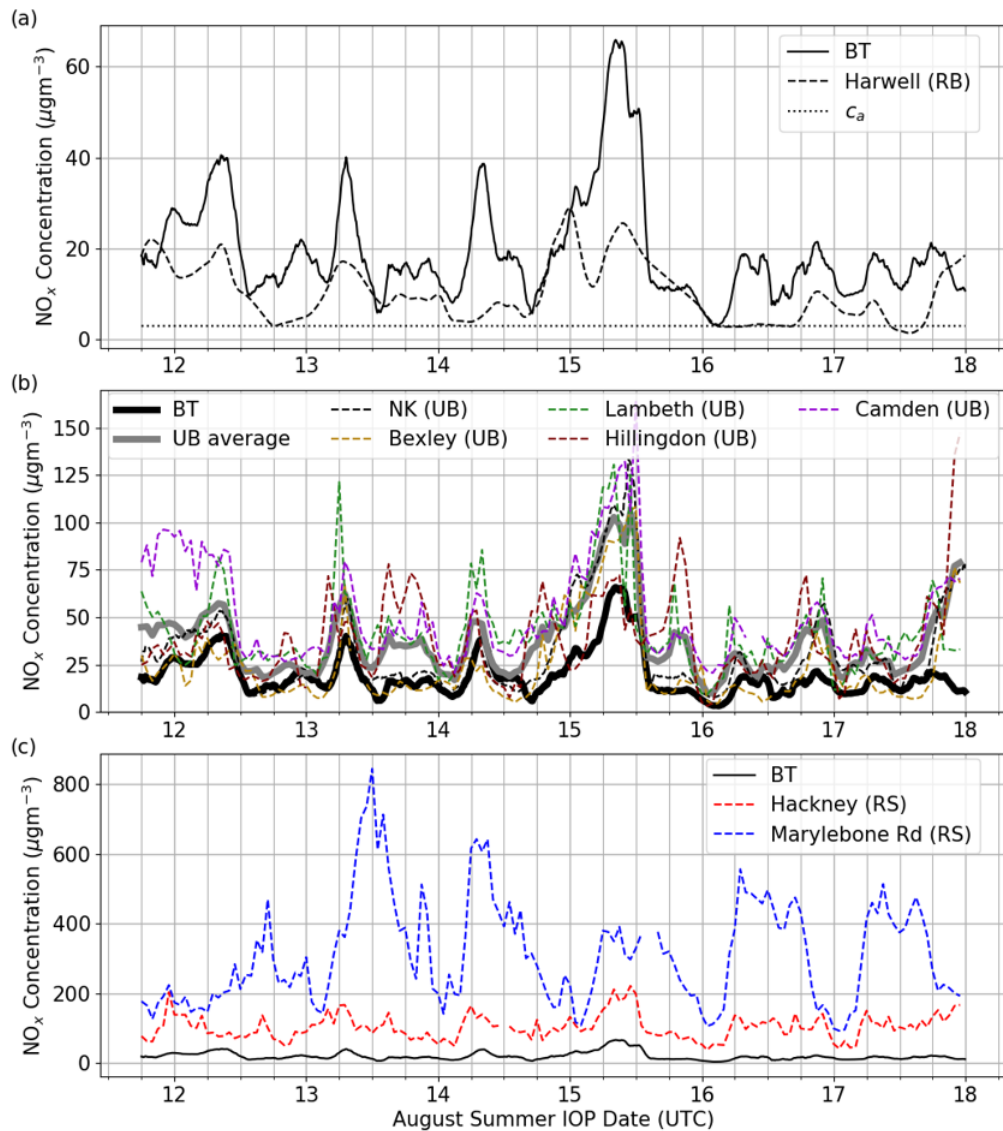
Figure 2.9: NO_x concentration measurements used during the case study. (a) NO_x concentration measured at BT Tower and Harwell. Both have a 2 hr moving average applied. Also plotted is the concentration aloft of the box (c_a) that is entrained during BL growth. (b) NO_x concentration measured at BT Tower and different UB sites, and the average of the UB sites. (c) NO_x concentration measured at BT Tower and RS sites.

and Demerjian (1993), who used rural background measurements of O_3 upwind of St Louis, for estimates of concentration aloft of the UBL.

Figure 2.9b shows hourly averaged NO_x measurements made at several AURN urban background (UB) sites throughout Greater London. Also plotted is their average. UB sites are located such that they are representative of urban locations away from major sources. Their locations are given in Fig. 2.10. Measurement heights ranged between $2 - 4$ m above the ground across the different UB sites. They are therefore closer to the sources of emissions, which explains why they have higher concentration than measurements made at BT Tower. BT Tower and average UB concentration are reasonably well

---
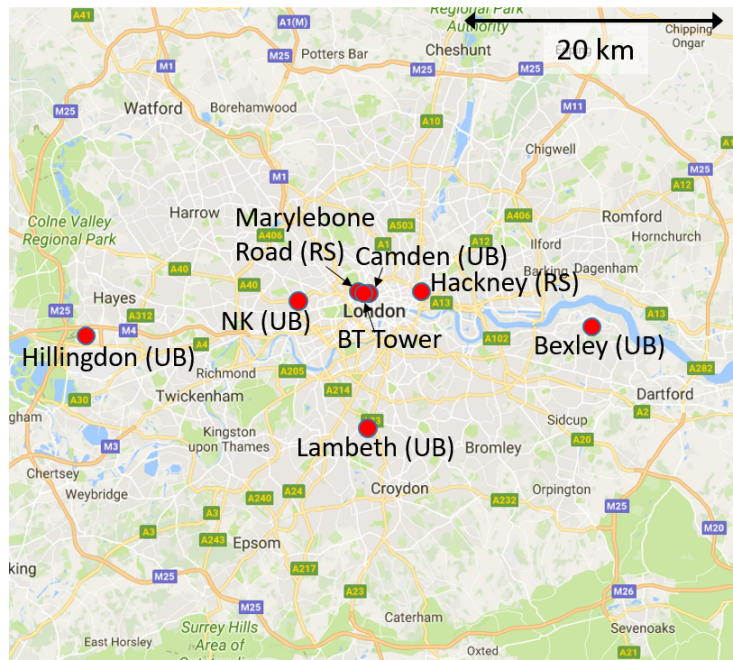
Figure 2.10: Locations of the NO_x measurement sites within Greater London. Labels have the same meaning as in Fig. 2.9. Source: Google Maps.

correlated. There is large variability in concentration across the UB sites.

Figure 2.9c shows NO_x measurements made at two AURN roadside (RS) sites. Their locations are given in Fig. 2.10. The concentrations are much larger than those at BT Tower and the UB sites, particularly at Marylebone Road. They also have much poorer correlation with BT Tower and UB concentrations, which is likely because they are dominated by very local vehicle NO_x emissions. This shows that there is very large heterogeneity in street level NO_x concentration near BT Tower.

2.3.3.3 Estimation of NO_x Emissions

The NO_x emission rate used in the box model was derived primarily from Automatic Traffic Counters data measured during the case study period. The data was provided on request by Transport for London. The data contained the number of vehicles passing in both directions at 242 sites across Greater London. The average across sites was taken to obtain a representative time series of car count for Greater London.

Lee et al. (2015) used 20 car count sites within the flux footprint of BT Tower to generate car count diurnal time series. Trends in NO_x fluxes at BT Tower were shown to match reasonably well with traffic volume during the day. This suggests at those times that traffic emissions are the main source of NO_x in Central London. This supports using car count data to generate a diurnally varying q.

The NO_x flux footprints of Lee et al. (2015) were calculated using measurements of

NO_x flux at BT Tower and the Kormann and Meixner footprint model (Kormann and Meixner, 2001). In their analysis 33 days were used from March-April 2013 and 6 days from June-August 2012 (the data also available to this study). It was estimated that 90% of NO_x flux originated between 150 m and 20 km of BT Tower, with median distance of 4.7 km. This suggests the assumption that BT Tower measurements are representative of NO_x concentration throughout the Greater London BL is limited. One possible approach to alleviate this problem might be to use a smaller box that still includes the BT Tower. That way emissions contributing to the concentration in the box and at BT Tower might be more alike. However, depending on the stability conditions, the flux footprint varies significantly, so the box size should too. Such a box model would be significantly more complex, contradicting the reason for choosing the box model as an investigative tool. Also, there are no other elevated measurements of pollution concentration in London during the case study, so there would be no appropriate choice of background concentration.

The London Atmospheric Emissions Inventory (LAEI) estimates that in 2013, 48,000 tonnes of NO_x was emitted into Greater London (Greater London Authority, 2016). Across the entire area of the box this corresponds to $q = 1.09 \ \mu gm^{-2}s^{-1}$. It is assumed that emissions were similar in 2012 to 2013, and that q varied diurnally and between days in the week, but not seasonally. The diurnal variation in q was accounted for by multiplying the LAEI average q by the car count time series (scaled so that its mean equalled one). After initial box model runs it was found that NO_x concentrations measured at BT Tower were on average higher than those predicted by the box model. A likely reason is that NO_x at BT Tower tends to have a large contribution from local sources. BT Tower is situated in Central London, where emissions are generally higher than in Greater London as a whole. So that the box model predictions could be compared relative to measurements at BT Tower, it was decided to increase q to $1.57 \ \mu gm^{-2}s^{-1}$. This choice of q gave the same time average prognostic (box model) and observed (BT Tower) concentrations during the analysis period. By scaling q, it is possible that some systematic errors due to other input parameters, unrepresented processes and poorly represented processes in the box model have been removed.

The final q used in the box model is shown in Fig. 2.11. q does not have a 2 hr moving average applied. This is because the car count time series was generated from many sites across Greater London, so short time scale variations at individual sites are averaged out. On the 13th–17th mornings and evenings, rush hour peaks can be seen. The 12th has lower emissions, particularly in the morning, as might be expected since it is a Sunday. The shape of the emissions profile during the week in Fig. 2.11 is similar to the car count time series generated by Lee et al. (2015) with 20 sites local to BT Tower.
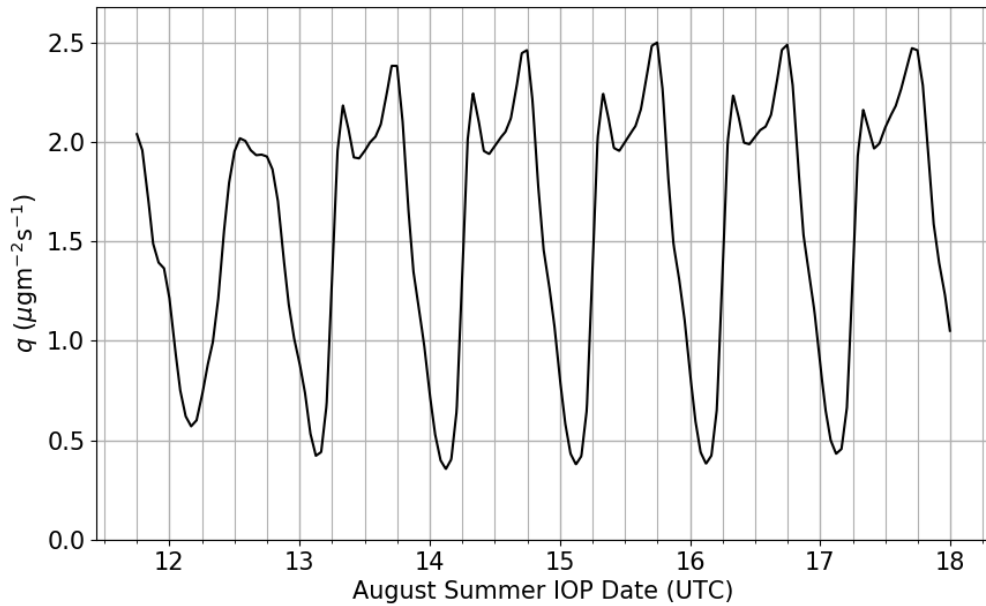
Figure 2.11: Emissions profile used for the box model during the case study.

2.4 Box Model Timescales

In this section, timescales associated with vertical mixing and entrainment are estimated for the Greater London BL during the case study. Also, based on the horizontal advection and vertical mixing timescales, the assumption that NO_x can be treated as an inert tracer is examined.

2.4.1 NO_x Lifetime and Vertical Mixing Timescales

During the daytime NO_2 can be oxidised by OH to produce HNO_3, and NO and NO_2 can react with peroxy radicals (RO_2). Following Slowik et al. (2011), it is assumed that the oxidisation reaction is the dominant reaction, so that the sum of NO_x and its products is $NO_y = NO_x + HNO_3$. The ratio of NO_x to NO_y can be used to estimate the photochemical age of an air mass, since the ratio decreases with time as more NO_x becomes oxidised. The time rate of change of NO_x concentration within an air mass can be written as

$$\frac{d NO_x}{dt} = k_{NO_x + OH}[NO_x][OH],$$ (2.2)

where $k_{NO_x + OH}$ is the rate constant which is estimated to be 7.9×10^{-12} cm^{3}s^{-1} at 1 atm and 300 K (Brown et al., 1999). Immediately after emission $[NO_x]_{t=0} = [NO_y]$, so that

Eq. 2.2 becomes

$$\frac{[\text{NO}_x]_t}{[\text{NO}_y]} = \exp\left(-k_{\text{NO}_x+\text{OH}}[\text{OH}]\Delta t\right), \qquad (2.3)$$

where Δt is the time since emission.

As part of the RONOCO (ROle of Nighttime chemistry in controlling the Oxidising Capacity of the atmOsphere) campaign, on 3rd September 2010 a daytime flight made three anticlockwise circuits around London's M25 at about 660 m altitude. The flight aimed to investigate NO_x chemistry and its role in the production and loss of O_3, and alkyl and multifunctional nitrate within London's urban plume (Aruffo et al., 2014). The UK at the time was located under a high pressure system. London had clear skies and experienced gentle north easterly winds of approximately 2.5 ms^{-1}. The mean OH concentration measured during the M25 circuits was 1.77×10^6 molecules cm^{-3}. This is used as an estimate of OH concentration in London under well-mixed conditions when the box model is expected to perform well. AURN sites could not be used to obtain an estimate since they do not measure OH. From $k_{\text{NO}_x+\text{OH}}(= 7.9 \times 10^{-12}$ cm^{3}s$^{-1})$ and $[\text{OH}](= 1.77 \times 10^6$ molecules cm$^{-3})$, a timescale $\tau_{\text{NO}_x} = 1/(k_{\text{NO}_x+\text{OH}}[\text{OH}])$ can be defined, and is equal to approximately 20 hr.

Most of the NO_x measured at BT Tower originates from within 5 km according to Lee et al. (2015). The trajectory of NO_x from emission to the top of the BT Tower is partly in the surface layer, where wind speed is slower than the average value of 7.2 ms^{-1} in the ML. If the average wind speed is taken to be approximately 3 ms^{-1} along a 5 km NO_x trajectory, the time it takes NO_x to reach the top of the BT Tower is approximately 30 min. Barlow et al. (2011a) calculated the time it took tracer emitted at ground level, 1300 m upstream of BT Tower, to first reach the top of the BT Tower. Mean wind speed of 12.3 ms^{-1} was measured at BT Tower and conditions were near neutral. A value of 9 min was obtained, which suggests a vertical mixing timescale of O(10 min) between ground level emission and the top of the BT Tower. This might be an underestimate of the vertical mixing timescale for the ClearfLo dates studied here, since wind speed was lower than 12.3 ms^{-1}, meaning there was less mechanical vertical mixing. The convective conditions observed during the ClearfLo days likely offset this to some extent, since convective updrafts originating near the surface are efficient at vertical mixing. For emissions within 5 km of BT Tower during the case study, it is likely that it is the horizontal advection timescale (O(30 min)) that places the upper limit on how long it takes tracer to reach BT Tower, rather than the vertical mixing timescale (O(10 min)).

Using a value of $\Delta t = 30$ min in Eq. 2.3 gives a ratio of 0.975. If the average horizontal advection timescale of the box model during the case study is used so that $\Delta t = 2$ hr, the ratio is 0.90. τ (the horizontal advection timescale of the box model) ranged between 1.0–3.5 hr during the case study, giving an lower limit on the ratio of 0.84. This suggests that NO_x reactions have a very small effect on NO_x concentration between the time of emission and measurement, and generally a small influence during the time it takes to

travel across London. To a good approximation NO_x can be treated as a chemically inert tracer on O(2 hr) timescales.

2.4.2 Entrainment Timescale

The third term on the right-hand side of Eq. 2.1 is the box model entrainment term, which represents air above the BL being enveloped within the BL as it grows. A timescale for the entrainment term and z_{MH} growth, can be defined as

$$\frac{1}{\tau_a} = \frac{1}{z_{MH}} \frac{dz_{MH}}{dt}. \tag{2.4}$$

Figure 2.12 shows τ_a calculated between 04:45 UTC (sunrise) and 14:00 UTC each day. Between 05:30 UTC and 11:00 UTC, τ_a demonstrates most consistent values, and those times will be used to define an average τ_a. Equation 2.4 has solution

$$\ln\left(\frac{z_{MH}}{z_{MH}(t_0)}\right) = \frac{t - t_0}{\tau_a}, \tag{2.5}$$

where $t_0 = 5.5$ hr. Figure 2.13 shows $\ln(z_{MH}/z_{MH}(t_0))$ against t each day. Also plotted is $\ln(z_{MH}/z_{MH}(t_0))$ averaged over all days with a linear regression fitted. The reciprocal of the gradient is $\tau_a \approx 4$ hr. The advection timescale of the box model is approximately 2 hr. Therefore the timescale of entrainment is approximately twice that of advection during the case study.
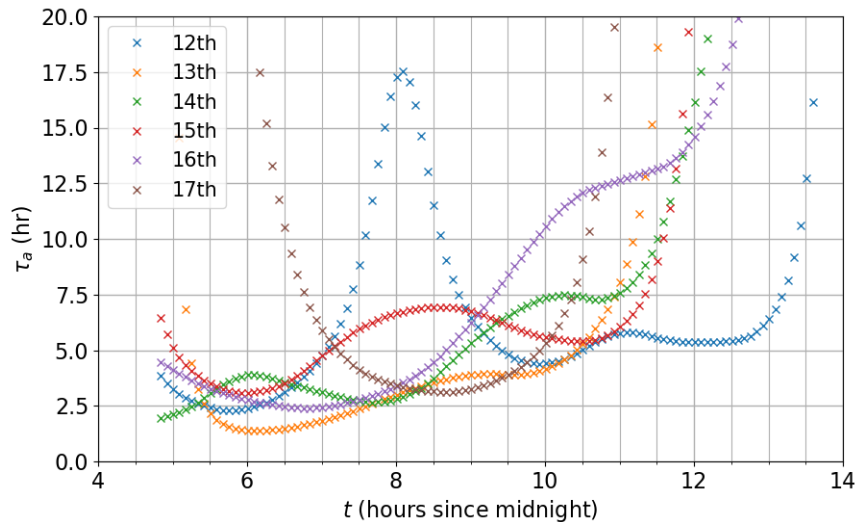
Figure 2.12: Entrainment timescale for each case study day between 04:45 UTC (sunrise) and 14:00 UTC.
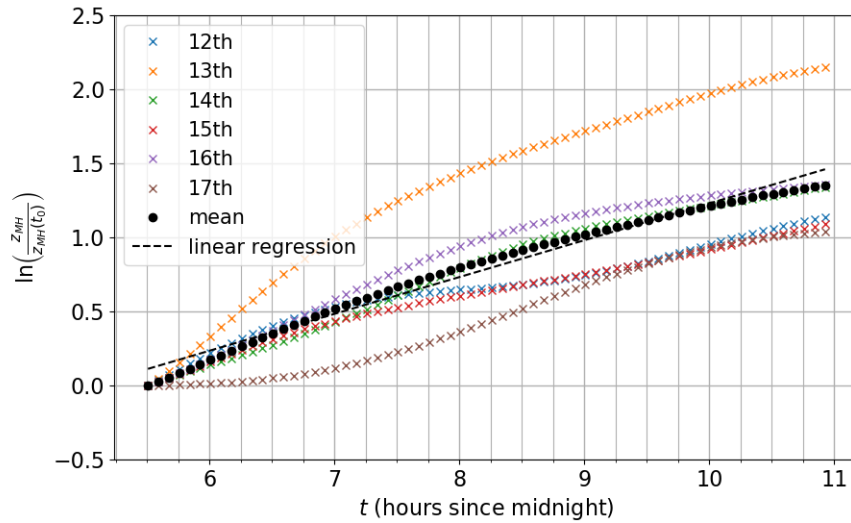
Figure 2.13: Plot showing $\ln(z_{MH}/z_{MH}(t_0))$ against t each day, and their average with a linear regression fitted.

2.5 Dry and Wet Deposition

In this section, the influence of dry and wet deposition on NO_x concentration in Greater London during the case study period is assessed.

2.5.1 Dry Deposition

Mass flux of a chemical substance due to dry deposition is typically parameterised as

$$F_{dry} = -v_d c, \tag{2.6}$$

where v_d is the dry deposition velocity. v_d is commonly calculated using an approach analagous to Ohm's Law, so that (Wesely, 1989; Wesely and Hicks, 2000)

$$v_d = (R_a + R_b + R_c)^{-1}, \tag{2.7}$$

where R_a represents the aerodynamic resistance above the surface, R_b is the quasi-laminar resistance in the air which is in contact with the surface and R_c is the bulk surface resistance. All models require parameters such as the Obukhov length and wind speed to describe the stability conditions, and constants such as land use fractions to describe the surface characteristics.

Since NO has low oxidizing ability and is not very soluble, dry deposition of NO is usually treated as negligible (Wesely and Hicks, 2000; **?**). NO_2 is often assumed to behave like O_3 since it has large oxidizing ability and is not very soluble. However, emissions of

NO from soils and rapid conversion to NO_2 often complicates this assumption (Wesely, 1989). Typical O_3 v_d values are between 0.1-1 cms^{-1}, for a range of dry rural land types with moderate wind speeds (Wesely and Hicks, 2000).

The rate of change of concentration due to dry deposition can be approximated by F_{dry}/z_{MH}, if it is assumed that the BL is well-mixed (Seinfeld and Pandis, 2016). Equation 2.6 can then be written as

$$\frac{dc}{dt} = -\frac{v_d}{z_{MH}}c,$$ (2.8)

and has solution

$$\frac{c}{c(0)} = \exp\left(-\frac{v_d}{z_{MH}}t\right).$$ (2.9)

If 0.1-1 cms^{-1} is taken as the range of v_d values and z_{MH} is assumed to be ~ 1 km, then the exponential decay timescale $\tau_{dry} = z_{MH}/v_d$ is approximately $1 - 10$ days. This is an order of magnitude longer than the flushing time of NO_x due to horizontal advection, so can be neglected in the box model. It is likely that that dry deposition of NO_2 becomes more important during stable conditions, when z_{MH} is low. Under stable conditions the box model assumptions are already not met, so for simplicity it was decided to not include dry deposition within the box model. Tests with and without dry deposition for different v_d in the box model did not improve box model predictions compared to BT Tower measurements.

Most studies of dry deposition (of all chemicals) are concerned with deposition on vegetation, but the uptake of chemicals by building surfaces is known to be different (Wesely, 1989). There are few measurements of v_d for both NO and NO_2 in localised urban environments due to difficulty in obtaining reliable measurements (Cherin et al., 2015). Improved estimates of v_d are required for pollutants in urban environments.

2.5.2 Wet Deposition

The ADMS (Atmospheric Dispersion Modelling System) dispersion model is produced by Cambridge Environmental Research Consultants (CERC, 2017) and is used by the UK Environment Agency for short range dispersion modelling. Wet deposition in the model assumes that pollution lies below the precipitation source, that once pollution is within the precipitation it cannot escape and that precipitation cannot become saturated with pollutant. Mass flux of wet deposition in the model is given by

$$F_{wet} = \int_{z=0}^{z_{MH}} \Lambda c \, dz,$$ (2.10)

where Λ is the washout coefficient equal to EP^G. P is the rate of rainfall (mmhr^{-1}), and E (mm^{-1}) and G are constants. E and G are typically taken to be the same for all pollutants apart from CO_2 and SO_2 due to pH related solubility (The Environment Agency,

2008). Analysis presented here for NO_x during the case study therefore applies to most other pollutants. Values of Λ from studies by the National Radiological Protection Board (NRPB) are between 3×10^{-5} s^{-1} and 3×10^{-4} s^{-1} (National Radiological Protection Board, 1984). The default ADMS model values of E and G are 10^{-4} and 0.64 respectively. This means $\Lambda = 10^{-4}$ s^{-1} when $P = 1$ mmhr^{-1}, so Λ is in the middle of the NRPB's range of values.

If Λ and c are constant with height in the BL then

$$F_{wet} = EP^G c z_{MH}. \tag{2.11}$$

Assuming c is constant with height, the rate of change of concentration due to wet deposition is equal to $-F_{wet}/z_{MH}$. Combined with Eq. 2.11, one obtains

$$\frac{dc}{dt} = -EP^G c, \tag{2.12}$$

which has solution

$$\frac{c}{c(0)} = \exp\left(-EP^G t\right). \tag{2.13}$$

If the default values of E and G are used, and the highest rainfall rate of 1.6 mm hr^{-1} during the case study is used, then an exponential decay due to wet deposition takes approximately 2 hr. This is the same as the horizontal advection timescale during the case study. When rain occurred it was quite sporadic both spatially and temporally (see Fig. 2.4). This suggests that for largest rainfall during the case study, 2 hr is a lower limit on the wet deposition timescale for the entire air mass within the box.

On the 16th at 12:00 UTC, NO_x concentration decreases suddenly by approximately 50% (see Fig. 2.9a). At this time 0.8 mm of rainfall was measured at St James MIDAS site, which is only 2 km from BT Tower (see Fig. 2.4). Also at this time, there was a decrease in S_{in} at BT Tower (see Fig. 2.8), indicating large cloud cover. This suggests the decrease in concentration was due to wet deposition, especially as there was no large change in wind speed, wind direction or z_{MH} at that time. Using Eq. 2.13 with $P = 0.8$ mmhr^{-1} for one hour gives $c/c_0 = 0.73$, a 27% decrease in concentration due to wet deposition. Since the rainfall measurement was made at a fixed location, it is difficult to estimate how much precipitation fell through the column of air, in the air mass that was measured at BT Tower. Accounting for such effects in the box model is very difficult. Wet deposition is not represented in the box model. Box model results during periods of precipitation are instead treated with caution.

2.6 One-box Model NO$_x$ Case Study

In this section the one-box model equation (Eq. 2.1) is solved during the case study period with time-dependent input parameters described earlier in this chapter. The equation is solved using the Second Order Runge-Kutta finite difference method (Durran, 2010) with 5 min time step to ensure numerical stability and accuracy. The solution is compared to the BT Tower NO$_x$ concentration measurements. The budgets of the individual box model terms are calculated.

2.6.1 Comparison of Predicted and Measured Concentrations

Figure 2.14a shows the box model NO$_x$ input parameters (c_b and c_a), box model predicted NO$_x$ concentration and measured NO$_x$ at BT Tower. Figure 2.14b shows the percentage difference between predicted and measured NO$_x$. Figures 2.14c-e show the input parameters, as well as Q_H and wind direction to aid analysis. The hatched areas of the plots correspond to periods when: the box model assumptions are not met (i.e. when $Q_H < 0$ and there is precipitation at any of the MIDAS sites or BT Tower); c_b measurements are unreliable inputs to the box model (i.e. when wind direction is easterly); and when NO$_x$ measurements at BT Tower are not representative of concentrations throughout the Greater London BL (i.e. when $z_{MH} < 190$ m, $Q_H < 0$ and there is precipitation at any of the MIDAS sites or BT Tower). Periods of negative Q_H are indicative of stable conditions at BT Tower, when the BL is typically poorly mixed and the assumption that the box model is well-mixed is poor. For $z_{MH} < 190$ m the measurements at the top of the BT tower are above the BL. When wind direction is easterly (taken to be between 45° and 135°), NO$_x$ background measurements are less reliable since Harwell is downwind of London. Precipitation is not represented in the box model, and its influence on the air both in Greater London and arriving at BT Tower is uncertain due to sparse measurements. It was shown in Sect. 2.5.2 that isolated showers can have a significant influence on NO$_x$ measured at BT Tower. The unhatched regions of the plot are where the box model is expected to perform best and measurements at BT Tower are most representative of the entire Greater London BL.

Visually there is some correlation between the measured and box model predicted concentration. The box model concentration is within 50% of the measured concentration 63% of the time. When only the unhatched periods are considered, the box model is within 50% of the measured concentration 77% of the time. It was expected that the box model would perform best during the unhatched periods on the 16th and 17th (for reasons explained in Sect. 2.3.1.7). On the 17th, the shape of the box model predicted concentration follows the concentration measured at BT Tower reasonably well. However, discrepancies of approximately 50% were still observed. On the 16th, the BT Tower concentration decreased sharply at 12:00 UTC, unlike the box model concentration. This
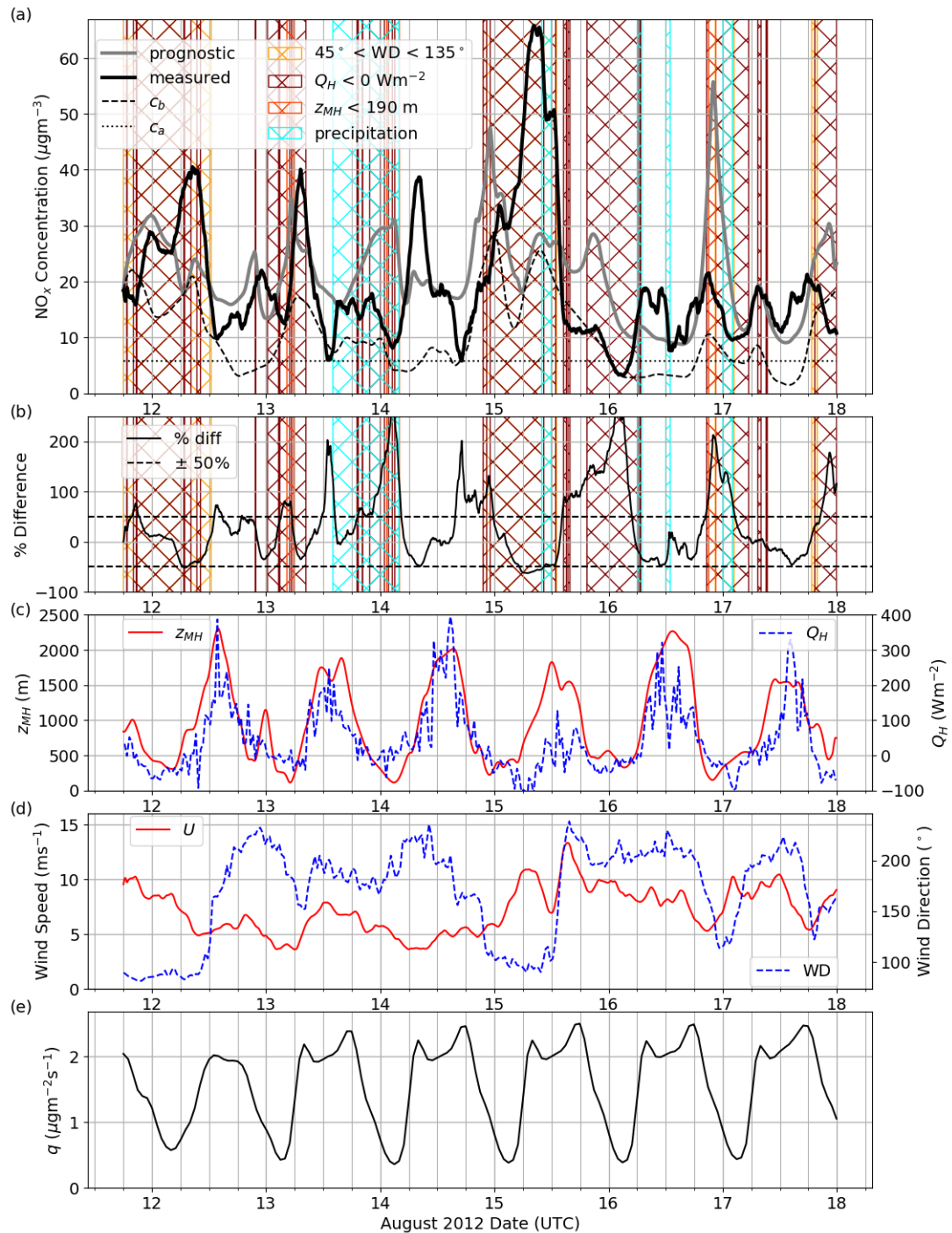
Figure 2.14: Plot showing the box model predicted (prognostic) and BT Tower observed NO_x concentration, and meteorological conditions during the case study period. a) Box model NO_x input parameters, box model predicted NO_x concentration and measured NO_x concentration at BT Tower. b) Percentage difference between predicted and measured NO_x. The hatched areas in (a) and (b) correspond to periods of negative Q_H, $z_{MH} < 190$ m, wind direction between $45°$ and $135°$ and periods where precipitation was observed at any MIDAS site in London or BT Tower. c) z_{MH} input to the model and Q_H. d) Wind speed input to the model and wind direction. e) The NO_x emissions profile input to the model.

was likely due to a convective shower as discussed in Sect. 2.5.2.

The $15^{th} - 17^{th}$ typically had wind speeds of approximately 9 ms^{-1}, compared to approximately 6 ms^{-1} on the other days. On the 16th and 17th, the predicted and measured concentration was generally smaller than on the other days. This suggests that ventilation by horizontal advection of pollution has a large influence on concentration. Wind speed tended to vary more with the synoptic conditions than the diurnal cycle during the case study. It therefore has a lower frequency influence on NO$_x$ concentration than other variables such as q and z_{MH}. The predicted and particularly the measured concentration was large on the 15th. This is because easterly winds arriving in London that day had spent a significant amount of time over Benelux, as shown by the NAME trajectories presented in Sect. 2.3.1. Benelux is a densely populated part of Europe with large pollution emissions. It is likely that when the easterly winds initially arrived in London on the 15th, that the concentration of background air was larger than air in London. Horizontal advection can be a net source of pollution if background air is more polluted than air in London.

On the 12th, 16th and 17th when there was least frontal activity, there tended to be two BT Tower concentration peaks, each occurring some time within 07:00–10:00 UTC and 18:00–23:00 UTC. These correspond to periods during the morning and evening when there is large q and low z_{MH}. The box model does generally predict peaks around these times but with the wrong magnitude. In the morning and evening the concentration tends to be under and over predicted respectively by the box model.

In the evening between 18:00–23:00 UTC the air at BT Tower tends to be stable or very weakly convective. This means that little NO$_x$ is likely to mix up to 190 m, so that concentration measured there is lower than in the BL below. This is consistent with the surface level UB concentrations in Fig. 2.9 often being much larger than those as BT Tower during the evening. The BT Tower NO$_x$ measurements are not a suitable estimate of the NO$_x$ concentration in the BL during the evening. Neither is the box model, since it assumes the BL is well-mixed.

From Fig. 2.14c it can be seen that by 07:00 UTC, z_{MH} has often grown to between $0.5 - 1$ km, but Q_H at BT Tower is often still negative. This suggests that the BL is not unstable up to z_{MH}. z_{MH} used in the box model is too large during the start of BL growth, so that concentration is under predicted. Kotthaus et al. (2018) showed that z_{MH} generally grows 20–105 min before aerosol layer height in the morning. It was suggested in their work that this is due to a lag associated with the time it takes aerosol to mix up to z_{MH}. However, in Sect. 2.4.2 it was estimated that the timescale associated with z_{MH} growth is approximately 4 hr. The timescale of convective BL mixing is O(10 min) in fully developed convective BLs (Garratt, 1994). During z_{MH} growth this vertical mixing timescale is more uncertain, since convective mixing during z_{MH} growth is less well understood in the literature. However, since there is approximately an order of magnitude difference, it is likely that the timescale of vertical mixing is short enough, so

that pollution should be mixed up to z_{MH} quicker than z_{MH} grows.

Another possible explanation is that convective eddies are trapped near the surface due to stable air in the residual layer above. The convective eddies can agitate the stable layer, causing waves that contribute to the vertical velocity variance but not to the turbulent transport of pollution. This could have caused large enough vertical velocity variance in the stable air, that the lidar diagnosed z_{MH} to be much higher than the height of the unstable layer where NO_x is efficiently mixed. Non-turbulent regions of large vertical velocity variance in the residual layer during the morning transition have been identified by Doppler lidar, and techniques have been developed to remove them when diagnosing z_{MH} (Bonin et al., 2017, 2018).

It can be seen that periods where rainfall occurred are generally associated with significant decreases in measured concentration at BT Tower. The main outlier to that trend is at 06:00 UTC on the 16th. However, at that time only 0.2 mm of rainfall was measured at Kenley Airfield, which is approximately 25 km south of BT Tower.

During the unhatched periods on the 17th when the box model performed best, it still had up to 50% discrepancies with BT Tower measurements, generally underestimating concentration. One possible reason for this is that a large proportion of NO_x measured at BT Tower is from sources within 5 km (Lee et al., 2015), rather than from the whole of Greater London as assumed by the box model. The area of London's surface where emissions contribute most significantly to NO_x at BT Tower is sensitive to atmospheric stability. Under convective conditions when the box model performs best, the area becomes closer to BT Tower (Lee et al., 2015). Pollution emissions are largest in Central London so this may have caused large NO_x at BT Tower during those times. It was demonstrated in Sect. 2.3.3.2 that there are very large roadside concentrations within 5 km of BT Tower, for example at Marylebone Road. Changes in wind direction of $O(10°)$ could result in contributions to NO_x at BT Tower, from emissions that were previously being advected wide of BT Tower. The measurements at BT Tower are only approximately representative of NO_x within Greater London.

It was assumed that q can solely be attributed to car emissions. However, the LAEI estimates that just over half of NO_x emissions are caused by road transport, and that there are significant contributions from industry and domestic heating (Greater London Authority, 2020). Their contribution was not included in q since information on their diurnal variation was not available. Also, domestic heating emissions of NO_x (which account for approximately 7% of emissions during the year (Greater London Authority, 2020)) are likely to mostly occur during the winter and not during the case study.

London was on the edge of high and low pressure systems during the case study. High pressure air over continental Europe tends to be more polluted than other air masses that transport air into London. Harwell is 80 km west of Central London, so it could be that concentration at Harwell was quite different to much of the air advected

into London. Also, there were no measurements of c_a so that it had to be estimated from c_b. The wind speed used to advect the air in the box model was taken from point measurements made at BT Tower. It is possible that there was large heterogeneity in wind speed within Greater London's BL, and that particularly under periods of weak convective conditions, the wind speed had large vertical variation throughout the depth of the BL.

During the REPARTEE field campaign in autumn 2007 (Barlow et al., 2011a), a Doppler lidar was used to measure z_{MH} and aerosol layer height. Aerosol layer height tended to be lower than z_{MH} during the afternoon. This has since been verified for more case study dates by Kotthaus et al. (2018). z_{MH} used in the box model is therefore likely an overestimate of the height to which pollution mixes up to under convective conditions. Also, z_{MH} is only measured at NK in Central London. z_{MH} in the centre of cities tends to be larger than the rest of the city due to the urban heat island effect.

2.6.2   Transport Process Budgets

Figure 2.15 shows the budget of each term in Eq. 2.1 contributing to the box model dc/dt. During the entire case study period, on average the source, advection and entrainment terms contributed 2.02×10^{-3} $\mu \mathrm{gm}^{-3}\mathrm{s}^{-1}$, -1.47×10^{-3} $\mu \mathrm{gm}^{-3}\mathrm{s}^{-1}$ and -0.54×10^{-3} $\mu \mathrm{gm}^{-3}\mathrm{s}^{-1}$ respectively. The two most important terms are therefore generally the source and advection terms. During the unhatched periods, on average the source, advection and entrainment terms contributed 1.78×10^{-3} $\mu \mathrm{gm}^{-3}\mathrm{s}^{-1}$, -1.31×10^{-3} $\mu \mathrm{gm}^{-3}\mathrm{s}^{-1}$ and -0.32×10^{-3} $\mu \mathrm{gm}^{-3}\mathrm{s}^{-1}$ respectively. Therefore, the source and advection terms tend to dominate under convective conditions too.

The source term tends to peak whenever z_{MH} is lowest, generally in the late evening or night. The advection term tends to peak as well at those times, but with smaller magnitude. The advection term peaks coincide with low z_{MH} since the advection term is proportional to concentration. Shortly after the source term peak the entrainment term tends to peak. This is because z_{MH} starts to grow after minimum z_{MH}, at the same time as there being very high concentration. The entrainment term is proportional to the rate of change of z_{MH} and concentration. Although the entrainment term is zero during most of the day, and therefore small on average, during initial BL growth in the morning it often has similar magnitude peak to the source term. Entrainment therefore has its largest role in reducing urban air pollution during initial BL growth. The entrainment term is largest on days with very small z_{MH} minimum, since low concentration air becomes entrained into a small volume.
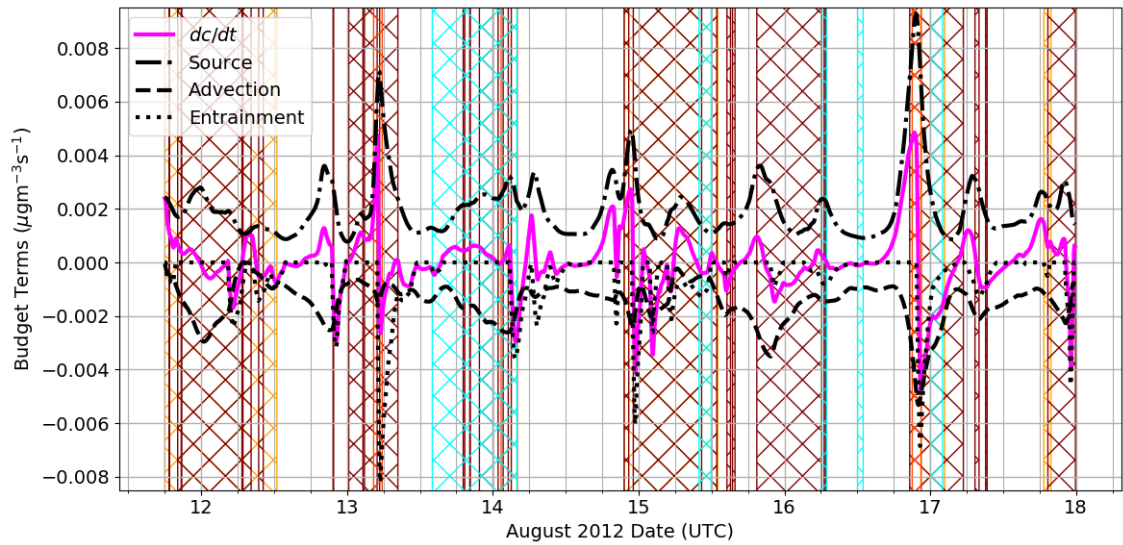
Figure 2.15: The box model budget terms during the case study. Source, advection and entrainment correspond to the first, second and third terms on the right-hand side of Eq. 2.1 resepctively. dc/dt is the rate of change of box model predicted concentration and is equal to the sum of the three terms. The hatched areas have the same meaning as in Fig. 2.14.

2.7 One-box Model Sensitivity Study

This section examines the dependence of c on c_b, c_a, z_{MH}, q and τ in more detail. Since the box model is only a reasonable representation of the UBL when it is unstable, it is decided to focus on this stability regime.

2.7.1 Composite Profiles

On all days apart from the 15th Q_H first became positive at approximately 07:00 UTC. Q_H typically became negative in the evening at approximately 19:00 UTC. Since Q_H is generally positive between 07:00–19:00 UTC, it is the period when the box model well-mixed assumption should be reasonably satisfied, and is therefore used in the coming sensitive studies.

Figure 2.16a shows z_{MH} for all case study days except the 15th and their composite. z_{MH} profiles were fairly similar across the case study dates used in the composite, and maximum z_{MH} values of 1.8 km are not uncommon under highly convective conditions. The composite z_{MH} profile is therefore likely to be fairly representative of z_{MH} for London under highly convective conditions in summer-time, when days are long.

It can be seen from Fig. 2.16b that q varies very little between weekdays (13th − 17th). Weekdays are chosen as they have larger emissions and therefore generally poorer AQ than weekends. Since traffic volume in the UK does not vary much throughout the year (Department for Transport, 2020), the q composite in Fig. 2.16b is reasonably representative of weekdays more generally.

Composites of τ and c_b using all case study days are shown in Figs. 2.16c and 2.16d respectively. τ is approximately constant throughout the day, which is likely because it is determined more by synoptic conditions, and therefore variations each day tend to cancel after averaging. c_b tends to be larger in the mornings than in the late afternoon in Fig. 2.16d. However, inspecting Fig. 2.9a it can be seen that at Harwell, peaks in concentration at approximately 08:00 UTC are not a general trend. The two largest morning peaks were on the 12th and 15th when winds were easterly and therefore from Benelux. c_b is likely determined most strongly by synoptic conditions.

c_a measurements were not made during ClearfLo so cannot be examined. However, c_a is also likely to be determined most strongly by synoptic conditions, since it is composed of air advected in far from local urban emissions. When air is very stagnant over a city it is also possible that c_a has similar value to the previous day's ML concentration. This is not the case during this case study since high pressure never remained over London for successive days and τ is much smaller than the duration of the night.

2.7.2 Closed-form and Analytical Solutions to the One-box Model Equation

Before investigating the sensitivity of c to the box model parameters numerically, it is worth looking at closed-form and analytical solutions to Eq. 2.1. The general solution is investigated when c_b, c_a, z_{MH} and q are allowed to vary with time, but τ is held constant in time. Little progress can be made unless τ is treated as a constant. Using an integrating factor, it can be shown that when $\dot{z}_{MH} > 0$, the solution is

$$
\begin{aligned}
c = {} & \frac{c(0)z_{MH}(0)}{z_{MH}}e^{-t/\tau} + \frac{e^{-t/\tau}}{z_{MH}}\int_0^t q e^{t/\tau}dt + \left(c_a - \frac{c_a(0)z_{MH}(0)}{z_{MH}}e^{-t/\tau}\right) \\
& + \frac{e^{-t/\tau}}{\tau z_{MH}}\int_0^t (c_b - c_a - \dot{c}_a\tau)z_{MH}e^{t/\tau}dt,
\end{aligned}
\tag{2.14}
$$

where t is the time since $\dot{z}_{MH}$ last turned positive. For $\dot{z}_{MH} \leq 0$, the solution is

$$
c = c(0)e^{-t/\tau} + e^{-t/\tau}\int_0^t \left(\frac{q}{z_{MH}} + \frac{c_b}{\tau}\right)e^{t/\tau}dt,
\tag{2.15}
$$

where t is the time since $\dot{z}_{MH}$ was last equal to 0. For the case when c_b and c_a are also taken to be constant then Eq. 2.14 reduces to

$$
\begin{aligned}
c = {} & \frac{c(0)z_{MH}(0)}{z_{MH}}e^{-t/\tau} + \frac{e^{-t/\tau}}{z_{MH}}\int_0^t \left(\frac{(c_b - c_a)z_{MH}}{\tau} + q\right)e^{t/\tau}dt \\
& + c_a \left(1 - \frac{z_{MH}(0)}{z_{MH}}e^{-t/\tau}\right),
\end{aligned}
\tag{2.16}
$$
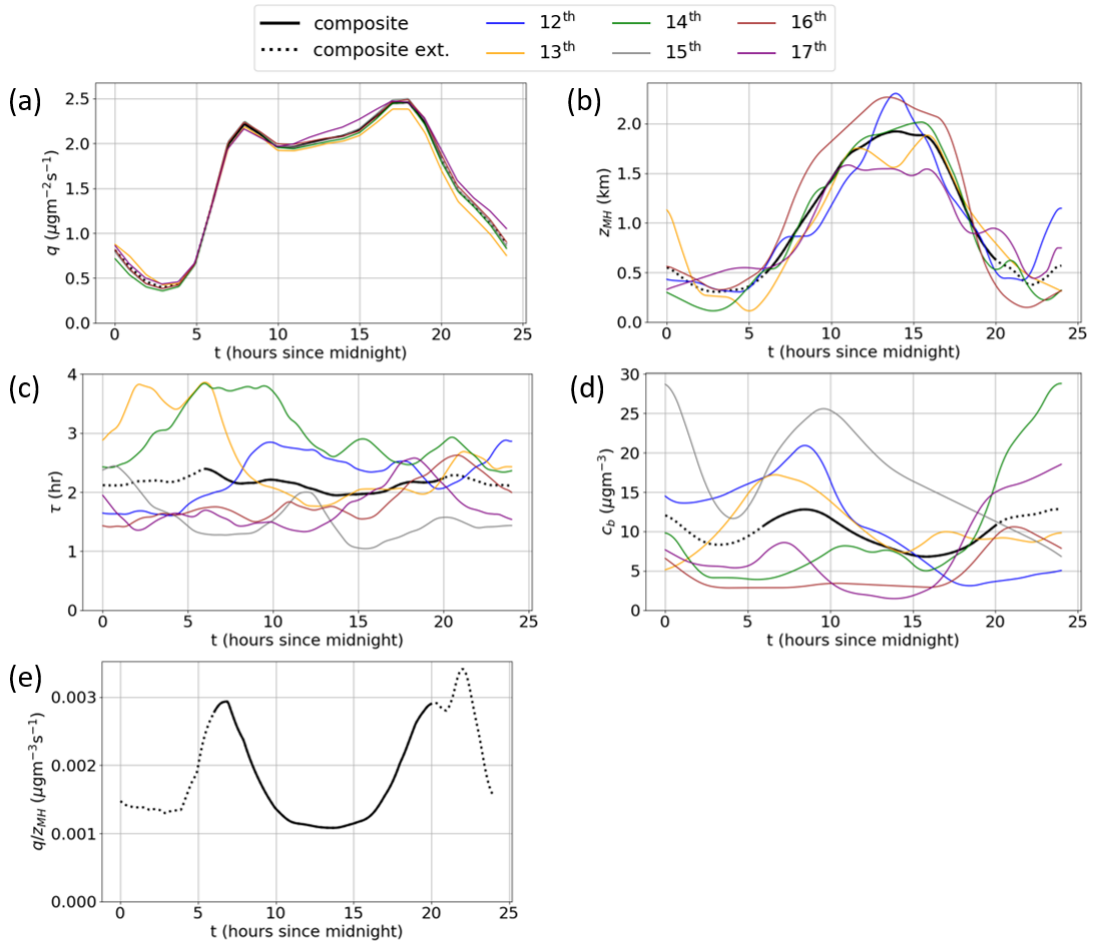
Figure 2.16: Composite profiles throughout the entire day ("composite ext.") and between 07:00–19:00 UTC ("composite"), and the individual day profiles used in the composites profiles for (a) z_{MH}, (b) q, (c) τ and (d) c_b. All days from the case study except the 15th are used in (a), 13th − 17th (weekdays) are used in (b) and all days are used in (c) and (d). (e) Shows the ratio of the q and z_{MH} composites.

and Eq. 2.15 reduces to

$$c = c(0)e^{-t/\tau} + c_b(1 - e^{-t/\tau}) + e^{-t/\tau} \int_0^t \frac{e^{t/\tau}q}{z_{MH}}dt. \tag{2.17}$$

These are all closed-form solutions that include a residual integral, which can always be evaluated numerically for a general z_{MH} and q. When z_{MH} and q are also constant, the integral can be evaluated analytically, and Eqs. 2.16 and 2.17 reduce to

$$c = \left(c(0) - \frac{q\tau}{z_{MH}} - c_b\right)e^{-t/\tau} + \frac{q\tau}{z_{MH}} + c_b. \tag{2.18}$$

Chapter 2. One- and Two-box Modelling of an Inert Pollutant in London's Boundary Layer

In the steady state limit (i.e. when $t \gg \tau$ and parameters are constant) then the following analytical solution is obtained

$$c = \frac{q\tau}{z_{MH}} + c_b. \tag{2.19}$$

In Sect. 2.7.6 it is investigated how good an approximation the steady state solution is to the full solution using the composite profiles. The steady state solution is often used in UBL ventilation and chemistry box model studies (e.g. Middleton, 1998; Rigby et al., 2006).

As can be seen from inspection of Eqs. 2.14 and 2.15, scaling q, c_b or c_a by a constant α would result in c being linearly proportional to α. If one scales z_{MH} by α then c is inversely proportional to α. However, scaling τ by α results in c having a more complex dependence on α, as it occurs in the exponential terms. It is difficult to understand the c dependence on τ by just inspecting the equations, since the residual integral terms involve the product of $e^{t/\tau}$ and time dependent functions whose form varies during the day.

2.7.3   Sensitivity to Parameters During the Composite Case Study

The sensitivity of the time average concentration, $\bar{c}$, predicted by the box model during the composite day, to multiplying each parameter individually by a constant α is investigated. This will be referred to as the "default case study" herein. The relationship between $\bar{c}/\bar{c}_{\alpha=1}$ and α can be expressed exactly as $\bar{c}/\bar{c}_{\alpha=1} = m\alpha + b$ for c_b, c_a and q, where m is a dimensionless constant, b is equal to $1 - m$ and $\bar{c}_{\alpha=1}$ is $\bar{c}$ calculated with $\alpha = 1$. It is investigated whether the relationship approximately holds for τ. The relationship between $\bar{c}/\bar{c}_{\alpha=1}$ and α for z_{MH} can be expressed exactly as $\bar{c}/\bar{c}_{\alpha=1} = m/\alpha + b$. The value of m in the linear and inverse relationships is determined.

The composite z_{MH} and q profiles, and the time average values of $c_b (= 9.33 \, \mu\mathrm{gm}^{-3})$, $\tau (= 2.09 \, \mathrm{hr})$ and $c_a (= 5.78 \, \mu\mathrm{gm}^{-3})$ between 07:00–19:00 UTC throughout the case study are used. Equation 2.1 was solved using the Second Order Runge-Kutta finite difference method with 5 min time step. The initial value of c was taken to be the steady state analytical solution (Eq. 2.19) value.

Figure 2.17 shows $\bar{c}/\bar{c}_{\alpha=1}$ plotted for various α. Only one parameter is multiplied by α at a time. As expected the relationship between $\bar{c}/\bar{c}_{\alpha=1}$ and α is exactly linear for q, c_b and c_a, and exactly inversely proportional for z_{MH}. The relationship between $\bar{c}/\bar{c}_{\alpha=1}$ and α for τ is almost exactly linear, and its linear regression in Fig. 2.17 is virtually indistinguishable. This must mean that exponential terms arising from the residual integrals in Eqs. 2.16 and 2.17 at least partially cancel with terms involving exponentials and that any remaining exponential terms are small. Also, a term must arise that is linearly proportional to τ. This is associated with the $qe^{t/\tau}$ residual integral term in Eqs. 2.16 and 2.17.
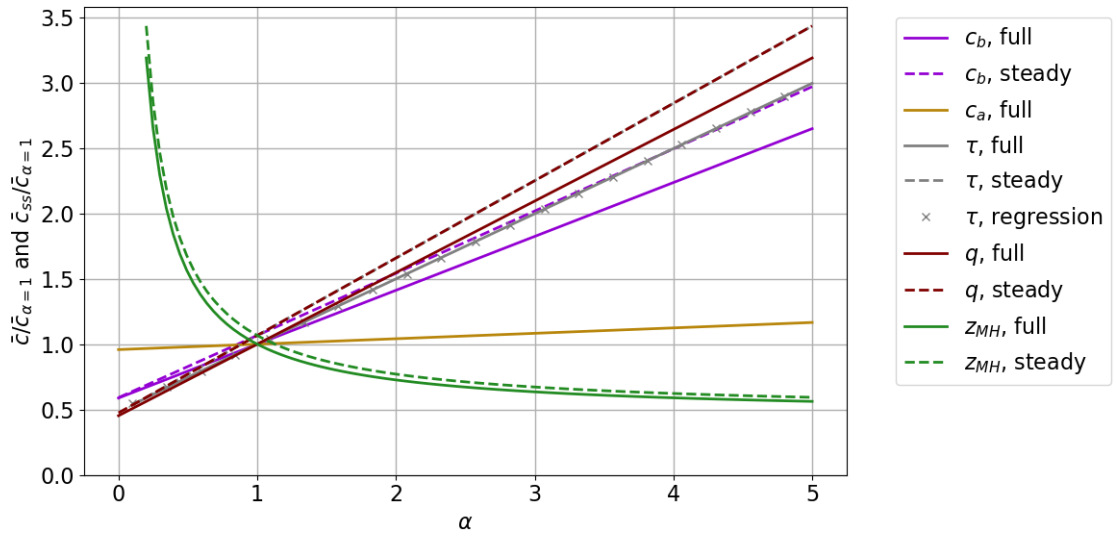
Figure 2.17: The relationships between $\bar{c}/\bar{c}_{\alpha=1}$ and α for the full numerical solution and between $\bar{c}_{ss}/\bar{c}_{\alpha=1}$ and α for the steady state solution. Each parameter is multiplied by the constant α individually. The gray cross markers are a linear regression to the τ full numerical solution. The τ steady state solution is exactly underneath the q steady state solution.

The values of m are in Table 2.1. When c_b, c_a, τ and q are multiplied by a factor α, then $\bar{c}$ changes by the amounts $0.41\bar{c}_{\alpha=1}(\alpha-1)$, $0.04\bar{c}_{\alpha=1}(\alpha-1)$, $0.50\bar{c}_{\alpha=1}(\alpha-1)$ and $0.55\bar{c}_{\alpha=1}(\alpha-1)$ respectively. The concentrations are therefore very sensitive to c_b, τ and q, and are much less sensitive to c_a during the case study. Note that τ is equal to L/U, so that when τ doubles, it is equivalent to the wind speed halving or the size of the urban area doubling.

Entrainment only influences concentration during BL growth. When $\bar{c}/\bar{c}_{\alpha=1}$ was calculated by averaging the solutions between 07:00–11:00 UTC, $m = 0.055$ which is larger than $m = 0.041$ calculated between 07:00–19:00 UTC. However, during BL growth c_a still has much less influence on $\bar{c}$ than the other parameters. During initial BL growth it is likely that entrainment (and therefore c_a) have a larger influence on $\bar{c}$. When air with different pollution concentration compared to that within the BL is entrained into a small BL, it has a large effect on the BL concentration, since the entrainment term is inversely proportional to z_{MH}. As discussed in Sect. 2.6.1, there is uncertainty in the timing of rapid increase in the height over which pollution is efficiently mixed. If z_{MH} is used as the height to which pollution is efficiently mixed, then from Fig. 2.12 it can be seen that there were periods before 07:00 UTC when τ_a was smaller than 2.5 hr on the 12th, 13th, 14th and 16th. This is significantly smaller than $\tau_a = 4$ hr estimated for BL growth in Sect. 2.4.2, indicating that entrainment has its largest influence on concentration before 07:00 UTC on those days.

The value of m for z_{MH} is 0.55, which is the same as the m value for q. This is not a coincidence as can be seen from the form of the second and third terms on the right-

Sensitivity Study	Solution Type	c_b	c_a	τ	q	z_{MH}
		m				
Default Case Study	Full	0.412	0.041	0.499	0.547	0.547
Default Case Study	Steady State	0.475	0.000	0.591	0.591	0.591
$3c_b = 27.99\ \mu gm^{-3}$	Full	0.677	0.022	0.238	0.300	0.300
$3c_b = 27.99\ \mu gm^{-3}$	Steady State	0.782	0.000	0.324	0.324	0.324
$3\tau = 6.27\ hr$	Full	0.168	0.044	0.751	0.788	0.788
$3\tau = 6.27\ hr$	Steady State	0.238	0.000	0.889	0.889	0.889
$3c_a = 17.34\ \mu gm^{-3}$	Full	0.380	0.115	0.499	0.505	0.505
$3c_a = 17.34\ \mu gm^{-3}$	Steady State	0.434	0.000	0.546	0.546	0.546
$0.5\times$ composite z_{MH}	Full	0.266	0.027	0.654	0.707	0.707
$0.5\times$ composite z_{MH}	Steady State	0.287	0.000	0.765	0.765	0.765

Table 2.1:: The m values for each parameter from the different sensitivity studies. The sensitivity studies were conducted with the full numerical solution and the steady state solution. "Default case study" corresponds to the sensitivity study in Sect. 2.7.3 where parameters were derived solely from the case study parameters. "$3c_b = 27.99\ \mu gm^{-3}$", "$3\tau = 6.27\ hr$", "$3c_a = 17.34\ \mu gm^{-3}$", and "$0.5\times$ composite z_{MH}" correspond to the sensitivity studies in Sect. 2.7.4, where c_b, τ, c_a and the composite z_{MH} were modified respectively. Note that in the $3c_a = 17.34\ \mu gm^{-3}$ sensitivity study, the steady state m values only change from the default case study ones because $\bar{c}_{\alpha=1}$ varies (not $\bar{c}_{ss}$) when c_a is modified.

hand side of Eqs. 2.16 and 2.17, respectively. When z_{MH} is multiplied by a factor α then $\bar{c}$ changes by $0.55\bar{c}_{\alpha=1}(1/\alpha - 1)$. The concentration is very sensitive to small values of z_{MH}, since m is large and $\bar{c}$ is inversely proportional to α.

2.7.4   Sensitivity to Different Meteorological Conditions

It is investigated whether the relationship between $\bar{c}/\bar{c}_{\alpha=1}$ and α is similar for a wider range of meteorological conditions than observed during the case study. Again, the full numerical solution to Eq. 2.1 is used. When meteorological conditions are changed, $\bar{c}_{\alpha=1}$ is affected and different relationships between $\bar{c}/\bar{c}_{\alpha=1}$ and α exist.

The sensitivity study is repeated four times with the following parameters modified one at a time: $\tau = 6.27\ hr$, $c_b = 27.99\ \mu gm^{-3}$ and $c_a = 17.34\ \mu gm^{-3}$ ($3\times$ their default case study values), and with composite z_{MH} multiplied by 0.5. The default case study values of c_b, c_a, τ, and composite q and z_{MH} are used for the parameters that are not being modified. $\tau = 6.27\ hr$, $c_b = 27.99\ \mu gm^{-3}$ and $c_a = 17.34\ \mu gm^{-3}$ are chosen to represent values that might be seen under high pressure systems. Typically in such conditions wind speed is lower, air is stagnant within the system and the residual layer air entrained during BL growth has the same concentration as the previous day's ML. z_{MH} is chosen to represent values that might be observed under low pressure systems where conditions are more weakly unstable or under high pressure conditions where there is very large subsidence. The values of m from the four investigations are given in Table 2.1.

When $c_b = 27.99 \ \mu\text{gm}^{-3}$ is used, the influence of c_b on $\bar{c}/\bar{c}_{\alpha=1}$ becomes more important than the influence of other parameters. The background pollution advected in becomes the most dominant source of pollution. When $\tau = 6.27$ hr is used, air spends longer over London, increasing the importance of local emissions. This means that for high pressure systems, the concentration of background advected air and local emissions are both likely to be important. The combination of high background concentration and decreased wind speed is what leads to large urban pollution concentrations under such conditions. If the high pressure system is persistent over South East England, it is likely that local emissions in London would start contributing significantly to c_b.

When $c_a = 17.34 \ \mu\text{gm}^{-3}$ is used rather than $c_a = 5.78 \ \mu\text{gm}^{-3}$, m increases from 0.041 to 0.115. m is still considerably smaller for c_a than the other parameters. When only 07:00–11:00 UTC was used in calculating $\bar{c}/\bar{c}_{\alpha=1}$, m increased from 0.115 to 0.148 (not shown in Table 2.1), and was still a factor of two smaller than the m values of the other parameters. Therefore, for a reasonable range of c_a (i.e. from $c_a \ll c$ to $c_a \approx c$), it is the parameter that $\bar{c}$ is least sensitive to.

When the composite z_{MH} was multiplied by 0.5, $m \approx 0.7$ for τ, q and z_{MH}. The volume of the BL is halved so that local emissions become more important. When z_{MH} halves, the difference in concentration between c and c_b becomes larger. τ therefore also becomes more important because advection removes more pollution.

2.7.5 Sensitivity to Changing Wind Speed

In the previous sensitivity studies it was assumed that τ is constant. Here the influence of time varying τ on concentration is investigated. Plotted in Fig. 2.18a is τ from the 15th calculated using wind speed measured at BT Tower, and the average τ during the 15th. The 15th was chosen as it had large increases and decreases in wind speed, which varied by approximately a factor of two during the day. Plotted in Fig. 2.18b are the full (Eq. 2.1) and steady state (Eq. 2.19) solutions for variable and constant τ. The same composite z_{MH} and q, and constant c_b and c_a are used from the default case study. When comparing variable and constant τ, the full solutions are always within 7.5% of one another. This suggests that typical variations in wind speed with time are much less important than the average value of the wind speed in determining pollution concentrations.

When variable τ starts to decrease after 12:00 UTC in Fig. 2.18a, the steady state analytical solution (Eq. 2.19) using the wind speed on the 15th has a turning point in Fig. 2.18b. The full solution using variable τ has a turning point approximately an hour later. It takes time of $O(\tau)$ for the pollution currently in the box to be flushed and replaced by pollution with concentration characteristic of the new wind speed. This lag is not represented in the steady state solution which adjusts instantaneously to changes in meteorological conditions and emissions.
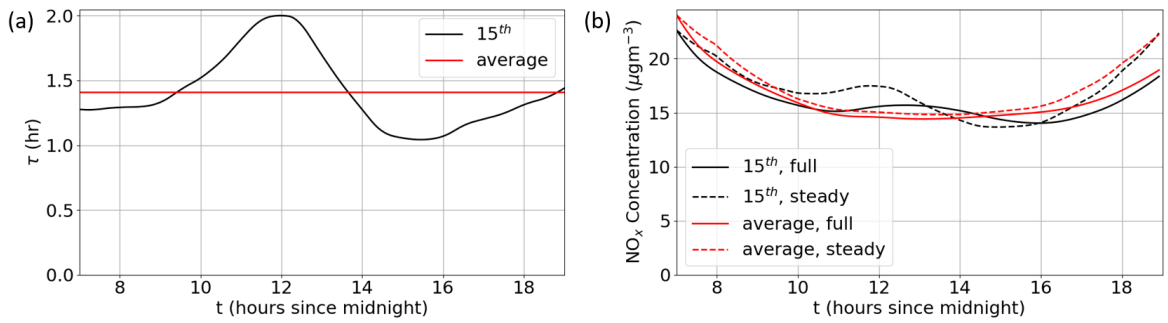
Figure 2.18: (a) τ calculated using wind speed measured at BT Tower on the 15th and its average. (b) The full numerical solution and the steady state solution, using both τ on the 15th and its average.

2.7.6   Robustness of the Steady State Solution

Plotted in Fig. 2.17 are the relationships between $\bar{c}_{ss}/\bar{c}_{\alpha=1}$ and α for the different parameters, and is a repeat of the default case study with the steady state analytical solution rather than the full numerical solution. $\bar{c}_{ss}$ is the time average concentration using the steady state solution. c_a does not have a steady state curve as entrainment is not accounted for in the steady state solution. It can be seen that the curves have reasonably similar gradient and intercept to the full solution curves. The m values of the relationships are given in Table 2.1.

The steady state m values are approximately 10% larger than the full solution values, apart from τ, whose m value is approximately 20% larger. This is also the case when one compares the steady state and full solution m values in Table 2.1 for the different meteorological conditions sensitivity studies (presented in Sect. 2.7.4). The full solution is generally less sensitive to changes in α than the steady state solution.

Plotted in solid black in Fig. 2.19 is the full numerical solution to Eq. 2.1, calculated with the 07:00–19:00 UTC composite z_{MH} and q profiles, and average values of c_b, τ and c_a from the default case study. It can be seen that the concentration tends to be largest in the morning and evening, and smallest in the middle of the day. This is because the source term (q/z_{MH}) is largest in the morning and evening (see Fig. 2.16e). Also plotted in dashed black is the steady state solution (Eq. 2.19). The steady state average concentration is 10% larger than the full solution average concentration, making it generally a good approximation. The error is largest in the evening when the steady state solution overestimates the concentration by up to 27%.

Inspecting Eqs. 2.16 and 2.17 it can be seen that the integral term involving q is multiplied by $1/z_{MH}$ outside and inside the integral, respectively. This highlights a distinct difference in the influence of z_{MH} in the morning and evening when the BL is growing and decaying, respectively.

In the evening z_{MH} decrease has no immediate effect on concentration, as the BL
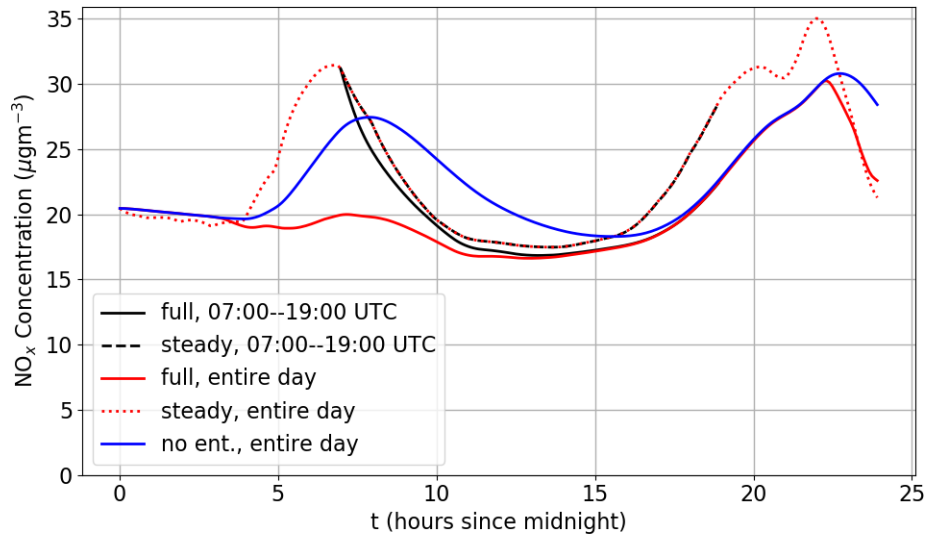
Figure 2.19: The full numerical solution to Eq. 2.1, the steady state solution (Eq. 2.19) and the numerical solution to Eq. 2.1 with the entrainment term neglected. The solutions use composite z_{MH} and q profiles, and the time average values of $c_b (= 9.33 \ \mu\mathrm{gm}^{-3})$, $\tau (= 2.09 \ \mathrm{hr})$ and $c_a (= 5.78 \ \mu\mathrm{gm}^{-3})$. The full numerical solution and steady state solution are plotted once between 07:00–19:00 UTC and again for the entire composite day. All solutions had their initial value specified by the steady state solution.

is like a permeable lid leaving the previous day's pollution behind, and concentration within the BL remains the same. The decrease in z_{MH} only influences concentration later as new pollution is emitted into a smaller volume. There is a O(τ) lag between changes in q/z_{MH} and concentration, which mathematically is due to q/z_{MH} in Eq. 2.17 being multiplied by an exponential before integration. This explains why the steady state solution overestimates most in the evening, since it does not account for the time it takes the concentration in the box to respond to the decrease in z_{MH}. The influence of the lag can be expected to be largest for light winds and large cities so that τ is large.

In the morning when z_{MH} increases the BL concentration is immediately diluted. There is only a lag in response to changing q rather than q/z_{MH}, because z_{MH} is not exponentially weighted during BL growth (seen Eq. 2.16). From Figs. 2.16a and b it can be seen that q does not vary much after 07:00 UTC in the morning, but that z_{MH} is still increasing rapidly. Therefore, when q/z_{MH} starts decreasing at 07:00 UTC (see Fig. 2.16e) it is due to increasing z_{MH}. Since the steady state solution does not require z_{MH} weighting during BL growth and q does not vary much after 07:00 UTC, the steady state solution is a better approximation in the morning (after 07:00 UTC) than in the evening.

Plotted in solid and dotted red in Fig. 2.19 are the full numerical solution and steady state solution, respectively, for the entire day. They are shown so that the box model behaviour during large influence from entrainment and rapid q increase before 07:00 UTC can be analysed. The composite z_{MH} and q profiles used are shown in Figs. 2.16a and b, respectively, and c_b, τ and c_a are taken to be the average values from the default

case study. Between 07:00–19:00 UTC the entire day steady state solution is exactly the same as the 07:00–19:00 UTC steady state solution as expected. The entire day and 07:00–19:00 UTC full solutions tend towards one another as the day progresses, since the full solution's memory of its initial concentration diminishes with time.

The entire day steady state solution average concentration is 18% larger than the entire day full solution average concentration, making it a reasonable approximation. The error is largest in the early morning at approximately 07:00 UTC when the entire day steady state solution overestimates the concentration by up to 61%. The entire day steady state solution overestimation of 18% is 8% larger than the 07:00–19:00 UTC steady state solution. This is because the assumptions of the steady state solution are least valid at times prior to 07:00 UTC.

The numerical solution to Eq. 2.1 with the entrainment term neglected is plotted in solid blue in Fig. 2.19 for the entire day. During the morning the peak concentration solution without representation of entrainment is up to 38% larger than when entrainment is represented. Entrainment tends to reduce concentration most early in the morning when z_{MH} is low. The steady state solution does not represent entrainment. This partly explains why the entire day steady state solution overestimates concentration by such a large amount at approximately 07:00 UTC.

From Fig. 2.16e it can be seen that q/z_{MH} increases rapidly between 04:00–06:00 UTC. This is due to the rapid increase in emissions during the period as seen in Fig. 2.16a. The entire day steady state solution increases instantly in response to the source term increasing, but the entire day full solution does not since Eq. 2.16 involves the integral of an exponentially weighted q. The lag effect acts to smooth peaks in concentration due to rapid changes in q. This is partly why the entire day full solution without entrainment has smaller and delayed concentration peak compared to the entire day steady state solution. It is therefore a combination of the concentration having a time lag in response to rapidly increasing q and entrainment not being represented, that results in the entire day steady state solution overestimating compared to the entire day full solution in the early morning.

Rigby and Toumi (2008) also found that daily average concentration is overestimated for the steady state solution compared to the full solution (see their Fig. 7). They performed a box model analysis driven by NWP reanalysis data output at 6 hr frequency over a period of several years. They found that the steady state model solution overestimates least when τ is small and concentrations are small. They attributed this to the lag effect having least influence during these times since low concentrations tend to coincide with small τ. Contrary to the views of Rigby and Toumi (2008), it is also likely that not representing entrainment has a large contribution towards the steady state solution overestimating pollution concentration.

In summary, the steady state solution gives a reasonable estimate of the concentra-

tion within the well-mixed UBL. It is useful for understanding the leading order effects on the average pollution concentration. For typical CBL conditions like those used in this composite case study, the steady state solution can be expected to overestimate daily average pollution concentration by $\sim 10 - 20\%$. When there are rapid changes in the box model parameters greatest errors occur since the steady state solution does not account for the time lag effect. The problem is accentuated when τ is large. Rapid changes in box model parameters are generally associated with q and z_{MH} as they have large variation in the morning and evening. Other parameters tend to vary most when there is large frontal activity, when the assumptions of the box model are typically already not valid. In the early morning during BL growth large overestimation in steady state concentration arises because of the time lag effect and entrainment not being represented. Errors were smallest during the afternoon when the UBL is most efficiently mixed and parameters vary least.

2.8   Inclusion of an Urban Canopy Box

In the previous sections it was assumed that the average concentration is representative of the concentration throughout the depth of the BL. This is a good approximation throughout the majority of the unstable BL, since the ML occupies the majority of the BL, where concentration tends to be reasonably homogeneous. However, near the surface concentration gradients are typically larger, due to the close vicinity of pollution sources and less efficient turbulent mixing than in the ML. This is exacerbated by dense urban canopies, which tend to reduce vertical mixing of pollution away from sources compared to if the surface were smooth (as discussed in Sect. 1.2.4.4). This impacts the AQ experienced by humans in cities, as the majority of daily life occurs in the urban canopy.

In this section, a second box will be coupled to the one-box model. A box extending from the ground to the mean building height represents the concentration in the urban canopy. It is coupled to a box directly above that represents the concentration in the ML. The ClearfLo measurements will be used again to derive parameters. The ML box uses parameters derived previously for the one-box model. Parameters such as vertical exchange velocity between the two boxes and urban canopy box horizontal advection velocity require parametrisation (see Sects. 2.8.1.1 and 2.8.1.2 respectively).

The following are investigated:

- The extent to which the urban canopy has elevated pollution concentration compared to the ML.

- Whether horizontal advection in the urban canopy or vertical exchange at canopy top is the dominant canopy ventilation process.

- Timescales associated with horizontal advection and vertical exchange.

- Which parameters are most important in controlling pollution concentration in the urban canopy.

2.8.1 Two-box Model Formulation

The derivation of the coupled two-box model equations is outlined in Appendix A. The urban canopy box equation is given by

$$\dot{c}_1 = \frac{q_{fix}}{h_1} + \frac{c_b - c_1}{\tau_1} - \frac{c_1 - c_2}{\tau_{ex,1}}, \tag{2.20}$$

and the ML box equation is given by

$$\dot{c}_2 = \frac{c_b - c_2}{\tau_2} + \frac{c_1 - c_2}{\tau_{ex,2}} + \frac{c_a - c_2}{h_2} \dot{h}_2 \theta_H(\dot{h}_2). \tag{2.21}$$

c_1 and c_2 are the concentrations in the urban canopy and ML boxes respectively. The NO_x mass emission rate per unit area of ground is defined as $q_{fix} = q/(1 - \lambda_p)$, so that the NO_x mass emission rate (equal to $q_{fix}L^2(1 - \lambda_p)$) is independent of λ_p. Due to buildings occupying air space in the canopy box, q is now defined more strictly as the NO_x mass emission rate divided by the total horizontal area of the canopy box (L^2). h_1 and $h_2 (= z_{MH} - h_1)$ are the heights of the urban canopy and ML boxes respectively. $\tau_1 = L/U_1$ and $\tau_2 = L/U_2$ are the advection timescales in the urban canopy and ML boxes respectively, and have horizontal advection speeds U_1 and U_2 respectively. $\tau_{ex,1}$ and $\tau_{ex,2}$ are vertical exchange timescales from the urban canopy box to the ML box and from the ML box to the canopy box respectively.

The first, second and third terms on the right-hand side of Eq. 2.20 are the canopy box source, advection and vertical exchange terms respectively. The first, second and third terms on the right-hand side of Eq. 2.21 are the ML box advection, vertical exchange and entrainment terms respectively.

c_b is assumed the same in the canopy and ML boxes. There are far lower NO_x emissions in rural areas so NO_x concentration entering London in the surface layer should not be much different from the ML. It is assumed that air is well-mixed in the urban canopy and ML boxes. There are therefore no vertical gradients in concentration with height, apart from at canopy top, where there is a step change. By assuming that the ML box extends down to the canopy top, vertical concentration gradients in the roughness sublayer (above canopy top) and inertial sublayer have been neglected.

The urban canopy wind speed and vertical ventilation is dependent on the surface characteristics of individual neighbourhoods throughout London. It will be assumed that by averaging the surface properties throughout London (i.e. within the 50 km $\times$

50 km urban canopy box), that reasonable estimates of the depth-averaged velocity and vertical exchange timescales across the entire London urban canopy can be made. It is also assumed in Eqs. 2.20 and 2.21 that there is no net vertical advection of air into or out of the canopy due to city scale flow (e.g. due to UHI circulations as discussed in Sect. 1.2.3) or due to convergence when horizontal wind speed changes significantly between neighbourhoods. These processes could be included within the two-box model formulation. Extra mass continuity equations would be required to compensate for net vertical transport of air between the two boxes through horizontal flow convergence and divergence. Vertical advection due to city scale flow would result in different horizontal advection velocities into and out of the boxes. The added complexity is not incorporated here.

2.8.1.1 Parametrisation of Vertical Exchange

Vertical exchange between the canopy and ML is parametrised following SIRANE (Soulhac et al., 2011), a widely used operational urban atmospheric dispersion model. The model assumes that vertical exchange is proportional to a vertical exchange velocity that does not directly depend on the geometry of the canopy, but only on the external flow conditions in the BL above (i.e. BL scaling parameters). The vertical exchange velocity is given by

$$v_e = \frac{\sigma_w(u_*, w_*, h_1, z_{MH})}{\sqrt{2\pi}}.$$ (2.22)

For $Q_H > 0$, vertical velocity variance at canopy top is defined as (Hunt et al., 1988)

$$\sigma_w = \sqrt{\sigma_{w,c}^2 + \sigma_{w,n}^2},$$ (2.23)

where

$$\sigma_{w,c} = \sqrt{0.4} w_* 2.1 (h_1/z_{MH})^{1/3} (1 - 0.8 h_1/z_{MH}),$$ (2.24)

is the convective vertical velocity variance at canopy top, and

$$\sigma_{w,n} = 1.3 u_* (1 - 0.8 h_1/z_{MH}),$$ (2.25)

is the neutral vertical velocity variance at canopy top. For $Q_H \leq 0$, vertical velocity variance at canopy top is defined as (Hunt et al., 1988)

$$\sigma_w = \sigma_{w,s} = 1.3 u_* (1 - 0.5 h_1/z_{MH})^{3/4},$$ (2.26)

where $\sigma_{w,s}$ is the vertical velocity variance under stable conditions.

Timescales for vertical exchange between the two boxes can be defined (as shown in

Appendix A). They are given by

$$\tau_{ex,1} = \frac{h_1}{v_e}, \tag{2.27}$$

for the urban canopy box, and by

$$\tau_{ex,2} = \frac{h_2}{v_e(1 - \lambda_p)}, \tag{2.28}$$

for the ML box. $1 - \lambda_p$ only appears in $\tau_{ex,2}$ due to buildings occupying the canopy and not the ML (see Appendix A).

2.8.1.2   Parametrisation of Depth Averaged Urban Canopy Velocity

The depth averaged velocity is calculated according to Bentham and Britter (2003). In a control volume of air within the urban canopy, they assume that the total force imparted by the urban surface on the flow (i.e. surface stress multiplied by the floor area, A_{floor}), is equal to the bluff body drag imparted by the buildings. Therefore

$$\rho u_*^2 A_{\text{floor}} = 0.5\rho U_1^2 \sum_{\text{buildings}} (C_d A_{\text{frontal}}), \tag{2.29}$$

where ρ is the air density, C_d is the sectional drag coefficient of each building and A_{frontal} is the area normal to the prevailing flow direction for each building. This can be rearranged to give

$$U_1 = u_* \left(\frac{2}{C_d \lambda_f}\right)^{1/2}, \tag{2.30}$$

where λ_f is the frontal area density equal to $((\sum A_{\text{frontal}})/A_{\text{floor}})$. C_d and λ_f are assumed constant within the canopy, so that U_1 is a constant representing the depth averaged velocity within the canopy.

2.8.2   Urban Canopy Wind Speed and Vertical Exchange Velocity

To derive τ_1, $\tau_{ex,1}$ and $\tau_{ex,2}$ it is necessary to obtain estimates of the average morphological properties of Greater London, namely h_1, λ_p and λ_f. A valuable tool in making such estimates has been the Virtual London dataset, licensed to the Centre for Advanced Spatial Analysis (CASA) at University College, London (Evans, 2009). It is a three-dimensional digital model of the buildings in London.

Using the Virtual London dataset, Wood et al. (2010) estimated that within 1–10 km of BT Tower the mean building height in London is 8.8 ± 3.0 m, and beyond that in suburban Greater London the mean building height is 5.6 ± 1.8 m. Since the box represents the entirety of Greater London, h_1 will be approximated as 6 m. Padhra (2010) calculated

λ_p and λ_f in 1 km^2 tiles using the Virtual London dataset. He calculated their average values with mean distance from Central London which was taken to be at the location of maximum λ_p. Maximum λ_p and λ_f were 0.58 and 0.44 respectively, their values reduced quickly to approximately 0.17 and 0.12 respectively by 10 km from Central London, and at 25 km from Central London their values were 0.08 and 0.05 respectively. Buildings are therefore sparse in large areas of suburban Greater London and representing the entire layer of air above the surface of Greater London with one urban canopy box is a large simplification. Values of $\lambda_p = 0.17$ and $\lambda_f = 0.12$ will be taken to be representative of the average urban morphology in Greater London.

For λ_p and λ_f approximately equal to 0.15, typical values of C_d from RANS and LES studies are ~ 2 (Santiago and Martilli, 2010; Nazarian et al., 2020). Plotted in Fig. 2.20 is $\tau_1 = L/U_1$ calculated according to Eq. 2.30 with $C_d = 2$, and the ratio τ_2/τ_1. The mean value of τ_1 is approximately 10 hr and it typically varies between 5–20 hr. The ratio τ_2/τ_1 is approximately 0.2 indicating that the advection timescale is 5 times longer within the canopy than the ML and that the wind speed in the canopy is approximately 5 times smaller than in the ML.
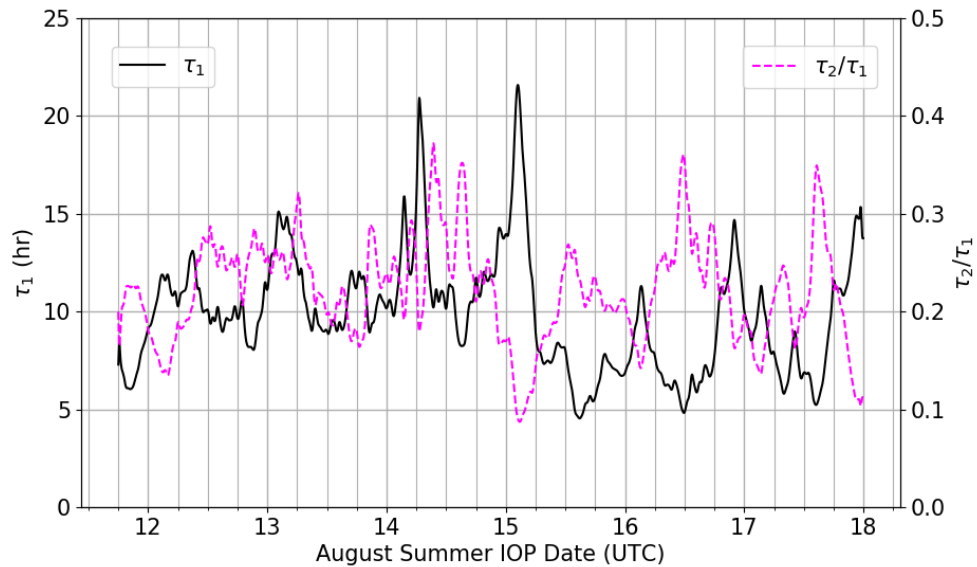
Figure 2.20: The horizontal advection timescales within the canopy and ML during the case study.

v_e was calculated using u_* measured at BT Tower in Eqs. 2.22-2.26. Figure 2.21a shows v_e and u_*, which visually have large correlation. v_e and u_* are approximately 50% larger on the 15th − 17th than the 12th − 14th. This is because the wind speed was larger on the 15th − 17th (see Fig. 2.7). By inspecting $\sigma_{w,c}$ and $\sigma_{w,n}$ (not shown) it was seen that under unstable conditions $\sigma_{w,n} \approx 2\sigma_{w,c}$ on the 12th − 14th and that $\sigma_{w,n} \approx 3\sigma_{w,c}$ on the 15th − 17th. Therefore during convective conditions σ_w was mostly determined by

Chapter 2. One- and Two-box Modelling of an Inert Pollutant in London's Boundary Layer

$\sigma_{w,n}$. $\sigma_{w,n}$ is a function of u_* but not w_*, which explains the large correlation between v_e and u_*, and suggests u_* is the dominant parameter in determining v_e. In the CBL, buoyancy driven turbulence dominates in the ML but mechanically generated turbulence still dominates at canopy top.

Figure 2.21b shows $\tau_{ex,1}$ and the ratio $\tau_{ex,1}/\tau_{ex,2}$. The average value of $\tau_{ex,1}$ was 40 s and was approximately 34 s during convective conditions. $\tau_{ex,1}$ was generally a third smaller on the $15^{\text{th}} - 17^{\text{th}}$ than the $12^{\text{th}} - 14^{\text{th}}$, which is expected since $\tau_{ex,1} \propto 1/\sigma_w$. The ratio $\tau_{ex,1}/\tau_{ex,2}$ equals $h_1(1 - \lambda_p)/h_2$, and was approximately 0.005 during convective conditions. The ratio was larger under stable conditions when h_2 is smaller, and the maximum value of the ratio was 0.047. Therefore, $\tau_{ex,2}$ on average during convective conditions was approximately 2 hr, but could be as low as 20 min when h_2 was small.
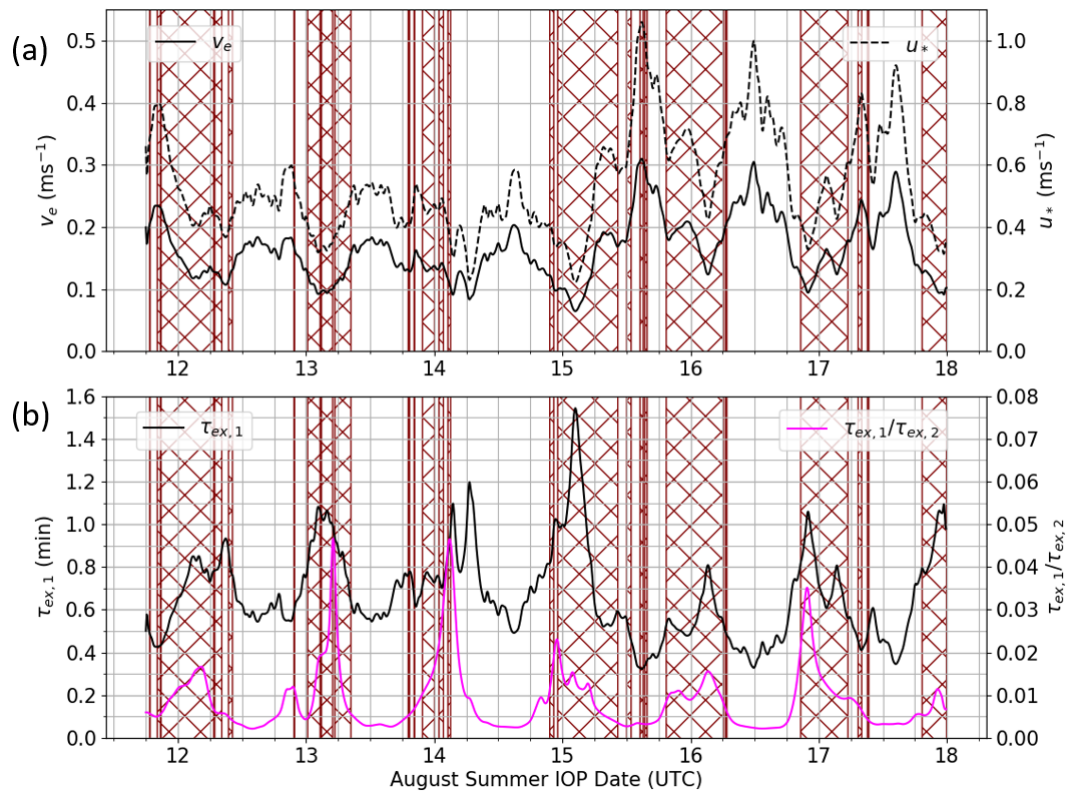
Figure 2.21: (a) Vertical exchange velocity and friction velocity during the case study. (b) Vertical exchange timescale for the canopy box, and the ratio of the canopy box and ML box vertical exchange timescales. The hatched regions indicate times when $Q_H < 0$.

2.8.3 Two-box Model NO_x Case Study

The coupled two-box model equations are solved for the case study period. The input parameters used are those described earlier in this section, and c_b and c_a are the same as those derived for the one-box model case study in Sect. 2.6. $q_{fix} = q/(1 - \lambda_p) = 1.57/(1 - 0.17) = 1.89 \ \mu\text{gm}^{-2}\text{s}^{-1}$ so that the rate at which NO_x mass was emitted into

London's BL was the same as the one-box model case study. The equations are solved using the Second Order Runge-Kutta finite difference method with 5 min time step.

Figure 2.22a shows c_1 and c_2 predicted by the two-box model, NO_x concentration predicted by the one-box model (taken from Fig. 2.14), NO_x concentration measured at BT Tower and the average NO_x concentration measured across the UB measurement sites. c_1 follows the UB concentration trend apart from when there is large frontal activity (e.g. the 15th). c_1 is visually better correlated with the UB concentrations than c_2 is with the BT Tower concentrations. This is consistent with the percentage difference in Fig. 2.14b being smaller between c_1 and UB concentration than c_2 and BT Tower concentration. The absolute value of the percentage difference between c_1 and UB concentration was 27.6% on average using all times during the case study. Therefore, by including an urban canopy box reasonable estimates of the urban canopy concentration can be made. The percentage difference between c_2 and BT Tower concentration was 57.7%, more than twice that between c_1 and UB concentration.

c_1 tends to be large under stable conditions consistent with the observed UB concentrations. c_2 also tends to be large under stable conditions but is generally larger than measurements made at BT Tower. Under stable conditions the difference in concentration between the ground and 6 m above the ground (the mean canopy height), is likely smaller than between the canopy top and the top of the BL. This makes the average canopy box concentration more representative of the UB concentration measurements, when compared to how representative the average ML box concentration is of the BT Tower concentration measurements. Also, since concentration gradients are likely smaller in the canopy box than the ML box under stable conditions, it means the well-mixed assumption is more valid in the canopy box than the ML box during stable conditions.

When only unhatched regions of Fig. 2.22 were used in the calculations, the average absolute value of the percentage differences between c_1 and UB concentration, and c_2 and BT Tower concentration, were 22.0% and 40.4% respectively. The percentage differences therefore reduce when periods of stable atmospheric stability are removed from the calculations. This is expected since the assumption that NO_x is well-mixed in the canopy and ML boxes is most valid under convective conditions. The reason that the percentage difference is larger for the ML box, is likely in large part due to BT Tower NO_x concentration measurements not being representative of the BL throughout Greater London. The UB measurements were available across several locations, making their average more representative of the whole of Greater London.

The difference between c_1 and UB concentration was smallest on the 16th and 17th. This was expected since there was no frontal activity apart from the warm front around 00:00 UTC on the 17th. The front passed quickly so did not have large influence before approximately 18:00 UTC on the 16th and after 06:00 UTC on the 17th. The isolated convective shower measured at St James Park MIDAS station at 12:00 UTC on the 16th, which
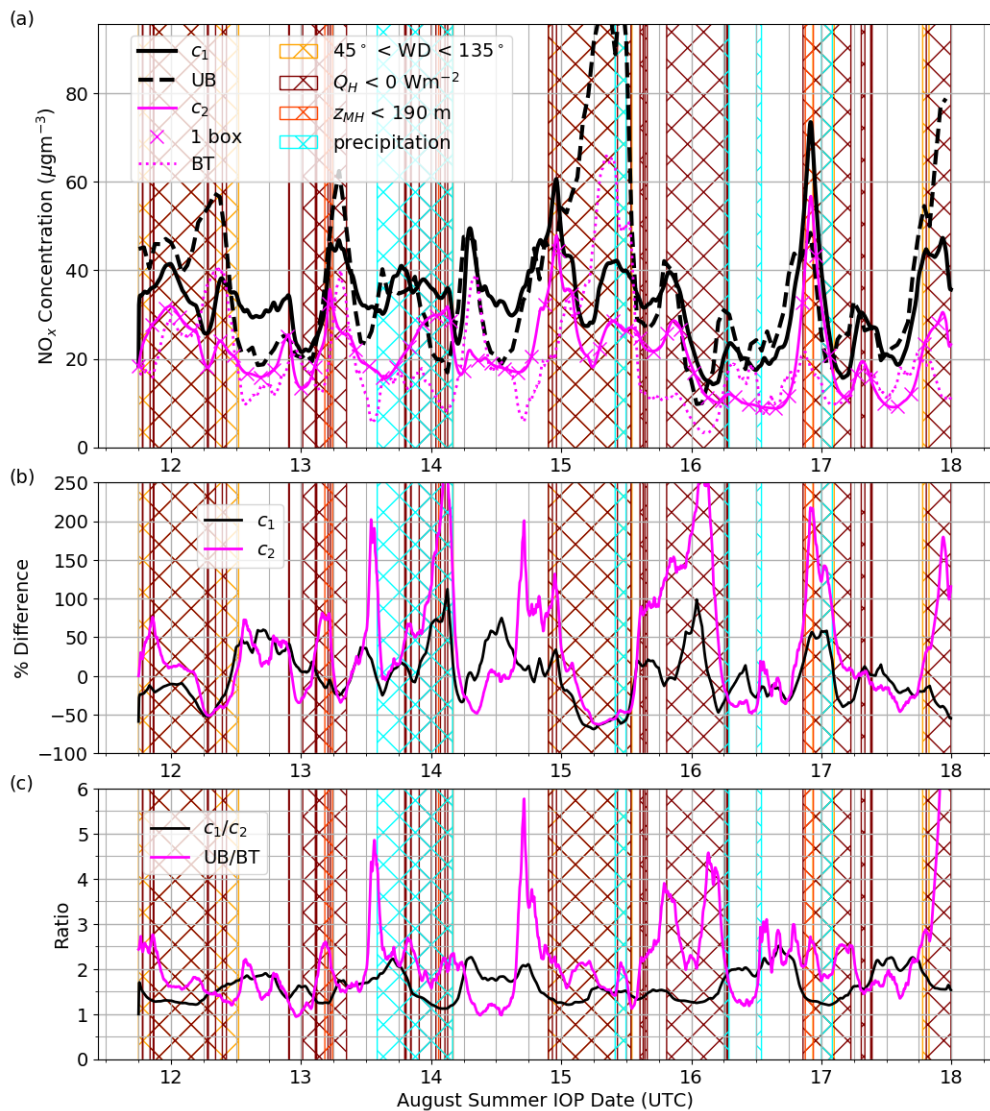
Figure 2.22: (a) Two-box model predicted c_1 and c_2, NO_x concentration predicted by the one-box model, NO_x concentration measured at BT Tower and the average NO_x concentration measured across the UB measurement sites during the case study. (b) The percentage difference between c_1 and UB concentration, and c_2 and BT Tower concentration. (c) The ratio of c_1 and c_2, and UB concentration and BT Tower concentration.

likely caused a decrease in BT Tower NO_x concentration at that time, had no observable influence on the average UB concentration. Thus c_1 closely followed UB concentration on 16th and 17th, whereas c_2 only matched well with BT Tower NO_x measurements on the 17th.

As seen in Fig. 2.22a, c_2 and the one-box model concentration are almost exactly the same. Including the canopy box has little influence on the ML concentrations. The reason for this is explained in Sect. 2.8.3.1.

Figure 2.22c shows the ratios c_1/c_2 and UB NO_x concentration divided by BT Tower NO_x concentration. When only unhatched regions of Fig. 2.22 were used, the average

values of the ratios were 1.84 and 1.98 for the two-box model and measurements respectively. This suggests that Greater London NO_x concentrations near the surface were on average almost twice that in the ML. Therefore, vertical mixing of pollution from the urban canopy into the air above is an important process controlling surface level AQ in urban areas. The similarity in the average ratios suggests that the parametrisation of vertical mixing between the canopy and ML boxes was reasonable.

c_1/c_2 tends to be larger under convective conditions than stable conditions. This is perhaps surprising given that stable conditions generally lead to less efficient dispersion in the BL. Differences between c_1 and c_2 are largely determined by the magnitude of pollution emissions into the canopy box and the time it takes pollution to be vertically mixed out of the canopy box. This is discussed further in Sects. 2.8.3.1 and 2.8.3.3. $\tau_{ex,1}$ was approximately 30% smaller under convective conditions than stable conditions, and small $\tau_{ex,1}$ tends to decrease c_1/c_2 towards unity. However, q was several times larger in the day (when the BL is typically convective) compared to the night (when the BL is typically stable). This tends to increase c_1/c_2 during the day compared to the night and outweighs the influence of $\tau_{ex,1}$.

The ratio of UB to BT Tower concentration was not larger under convective conditions than stable conditions. Marucci and Carpentieri (2020) recently conducted a wind-tunnel study of dispersion of tracer from a ground source in an array of cuboids. They found that unstable stratification can result in a factor of 3 decrease in tracer concentration compared to neutral conditions within the canopy. It is therefore possible that parametrisations of v_e need to be updated so that vertical exchange at canopy top is more efficient under convective conditions. This would result in smaller $\tau_{ex,1}$ and lower ratios of c_1/c_2 during convective conditions. Also, under stable conditions it is likely very little pollution gets mixed up to the top of the BT Tower, even when $z_{MH} > 190$ m. This would make NO_x concentration at BT Tower an underestimate of the average concentration in the BL during those times, thus increasing the ratio of UB to BT Tower concentration.

2.8.3.1 Two-box Model Budgets

Figure 2.23a shows the budget of the canopy box terms on the right-hand side of Eq. 2.20. The advection term is negligible, and is approximately three orders of magnitude smaller than the source and vertical exchange terms. The source and vertical exchange terms are in a quasi-equilibrium. When the source term changes in time, the influence on c_1 is large due to the small volume of the canopy box. The exchange term is directly proportional to $c_2 - c_1$, so it responds to the change in the source term through c_1, until a new quasi-equilibrium is reached. The source and vertical exchange terms reach their quasi-equilibrium with a timescale of $O(\tau_{ex,1})$. Inspecting Eq. 2.21 it can be seen that the ML box exchange term is directly proportional to $c_1 - c_2$. c_2 responds to changes in c_1

with a timescale of $O(\tau_{ex,2})$. Changes in c_2 then feedback to the canopy box through the canopy box exchange term with a timescale of $O(\tau_{ex,1})$.
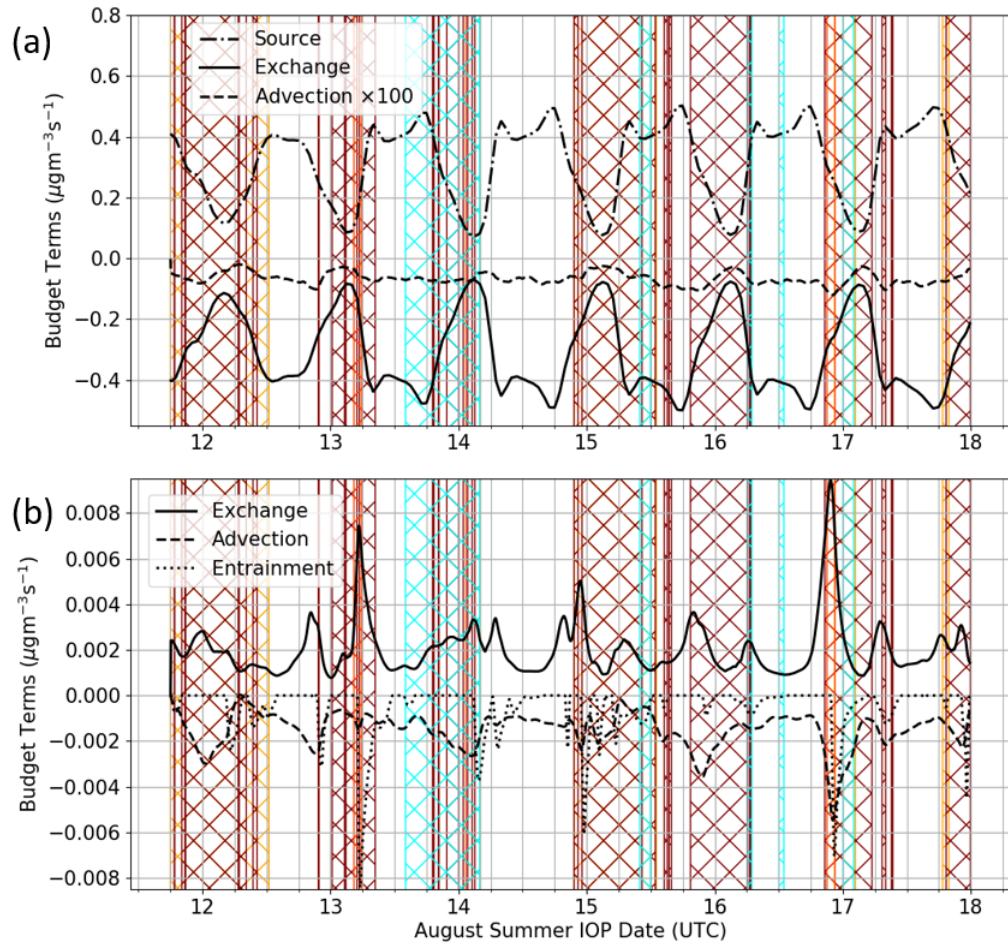
Figure 2.23: The budget terms for (a) the canopy box (Eq. 2.20a) and (b) the ML box (Eq. 2.20b) during the case study. The canopy box advection term has been multiplied by 100. The hatched areas have the same meaning as in Fig. 2.22.

Figure 2.23b shows the budget of the ML box terms on the right-hand side of Eq. 2.21. The vertical exchange, advection and entrainment terms are almost exactly equal to the source, advection and entrainment terms respectively from the one-box model budget in Fig. 2.15. The ML box behaves the same as the one-box model to a very good approximation. It is as if the source term is at the bottom of the ML box. This is because there are negligible advective losses from the canopy box and there are no other sink terms in the canopy box, so that the vast majority of pollution is transported into the ML box, with timescale $O(\tau_{ex,1})$. The ML box and one-box model terms are approximately the same since $h_2 \approx z_{MH}$ and $U_2 = U$. The dominant sink term of NO_x in the BL is horizontal advection in the ML.

As seen in Fig. 2.23, the canopy box source and vertical exchange budget terms are two orders of magnitude larger than the ML box budget terms. This is because the time and height scales are much smaller for the canopy box than the ML box (with the

exception of the canopy box advection budget term).

2.8.3.2 Canopy Box Steady State Solution

When the parameters and c_2 are treated mathematically as constant, the analytical solution to the canopy box equation (Eq. 2.20) is given by

$$
\begin{aligned}
c_1 &= \left(c(0) - \frac{\tau_1 \tau_{ex,1}}{\tau_1 + \tau_{ex,1}} \left(\frac{q_{fix}}{h_1} + \frac{c_b}{\tau_1} + \frac{c_2}{\tau_{ex,1}} \right) \right) e^{-t\left(\frac{1}{\tau_1} + \frac{1}{\tau_{ex,1}} \right)} \\
&\quad + \frac{\tau_1 \tau_{ex,1}}{\tau_1 + \tau_{ex,1}} \left(\frac{q}{h_1} + \frac{c_b}{\tau_1} + \frac{c_2}{\tau_{ex,1}} \right).
\end{aligned} \tag{2.31}
$$

In the steady state limit where $t \gg \tau_1 \tau_{ex,1} / (\tau_1 + \tau_{ex,1})$, Eq. 2.31 reduces to

$$
c_1 = \frac{\tau_1 \tau_{ex,1}}{\tau_1 + \tau_{ex,1}} \left(\frac{q_{fix}}{h_1} + \frac{c_b}{\tau_1} + \frac{c_2}{\tau_{ex,1}} \right). \tag{2.32}
$$

It was demonstrated in Sect. 2.8.2 that $\tau_1 \gg \tau_{ex,1}$ and in Sect. 2.8.3.1 that q/h_1 and $c_2/\tau_{ex,1}$ are much larger than c_b/τ_1. Noting also that $\tau_{ex,1} = h_1/v_e$, Eq. 2.32 can therefore be approximated as

$$
c_1 = \frac{q_{fix}}{v_e} + c_2, \tag{2.33}
$$

and will be referred to as the steady state solution herein.

The numerical solution to the two-box model equations (taken exactly from Fig. 2.22), was compared to the two-box model solution where c_1 was approximated by Eq. 2.33 and coupled to the full ML box equation which was solved numerically for c_2. Visually c_1 and c_2 from the numerical solution were indistinguishable without close inspection when compared to their corresponding values from the hybrid numerical (ML box) and analytical (canopy box) solution. The error is negligible for c_1 and therefore does not introduce errors into c_2. The reason the steady state canopy box solution (Eq. 2.33) is such a good approximation to c_1 is that the source and vertical exchange terms are in a quasi-equilibrium with an O(1 min) response time. All of the parameters in the two-box model and c_2 vary on the timescale of hours so can be approximated as constant in the canopy.

The steady state canopy box solution to a good approximation can be used to interpret the influence of the canopy parameters on canopy concentration. The parameters determining canopy concentration are q_{fix} and v_e, and the variable controlling canopy concentration is c_2.

2.8.3.3   Two-box Model Sensitivity to Urban Canopy Parameters

The values of the exchange timescales are based on a simple parametrisation of v_e that only depends on conditions external to the canopy. It is known that the geometry of the urban area has a large influence on the vertical exchange of scalar from the canopy, both due to the characteristics of the shear layers shed from the buildings and the three-dimensional recirculations that occur when urban canopies are more complex than quasi-2D canyons (Salizzoni et al., 2011). The exchange timescales are therefore associated with large uncertainty.

Figure 2.24a shows the sensitivity of c_1 and c_2 to varying both $\tau_{ex,1}$ and $\tau_{ex,2}$ (i.e. v_e) by 0.5 and 2.0, whilst keeping all other parameters the same as those used during the rest of the two-box model case study. The term "default" will be used to describe the two-box model solution when none of the parameter values are varied. The two-box model equations (Eqs. 2.20 and 2.21) were solved numerically. c_2 changes negligibly from its default curve. This is because the situation where the ML box is to a good approximation equivalent to the one-box model has not changed. Advection is still negligible in the canopy, all NO_x is passed into the ML box rapidly (on a timescale of O(1 min)), $h_2 \approx z_{MH}$ and $U_2 = U$.

c_1 is only influenced directly by $\tau_{ex,1}$ in the steady state canopy box solution ($c_1 \propto \tau_{ex,1}$). There is no indirect influence from $\tau_{ex,2}$ through c_2, since c_2 is influenced negligibly by $\tau_{ex,2}$. When $\tau_{ex,1}$ increases, the exchange term in Eq. 2.20 becomes smaller, the advection term remains negligible, and the source term does not change since it depends only on q and h_1. To reach a new equilibrium $\dot{c}_1$ must become positive so that c_1 increases. In turn, the exchange term increases (since it contains c_1), until the exchange term balances the source term. The average c_1 values using the default parameter values, and exchange timescales multiplied by 0.5 and 2.0, were 30.5 μgm^{-3}, 23.8 μgm^{-3} and 43.7 μgm^{-3}, respectively. Only conditions suitable for use of the box model (i.e. the unhatched regions in the previous figures) were used in the averages.

As well as the vertical exchange timescales, there was uncertainty in the value of U_1. $C_d = 2$ used in Eq. 2.30 is an approximate value. Also, in some areas of London where buildings are much sparser, there is likely large drag through skin friction, not just form drag. Sensitivity to U_1 is not plotted in Fig. 2.24 since for reasonable U_1 values, c_1 and c_2 are negligibly affected. This is because U_1 only appears in the canopy box advection term which is negligible (and therefore does not appear in the steady state canopy box solution). λ_f only appears in the U_1 parametrisation and therefore has negligible influence on c_1 and c_2. How important it is to incorporate the influence of the canopy geometry and local flow on vertical exchange (i.e. v_e) is an open research question (Salizzoni et al., 2011). However, based on the success of SIRANE (Soulhac et al., 2012) and the reasonable match between c_1 and UB concentration in Sect. 2.8.3, it is a reasonable approximation to represent v_e using only the external flow conditions. This supports the
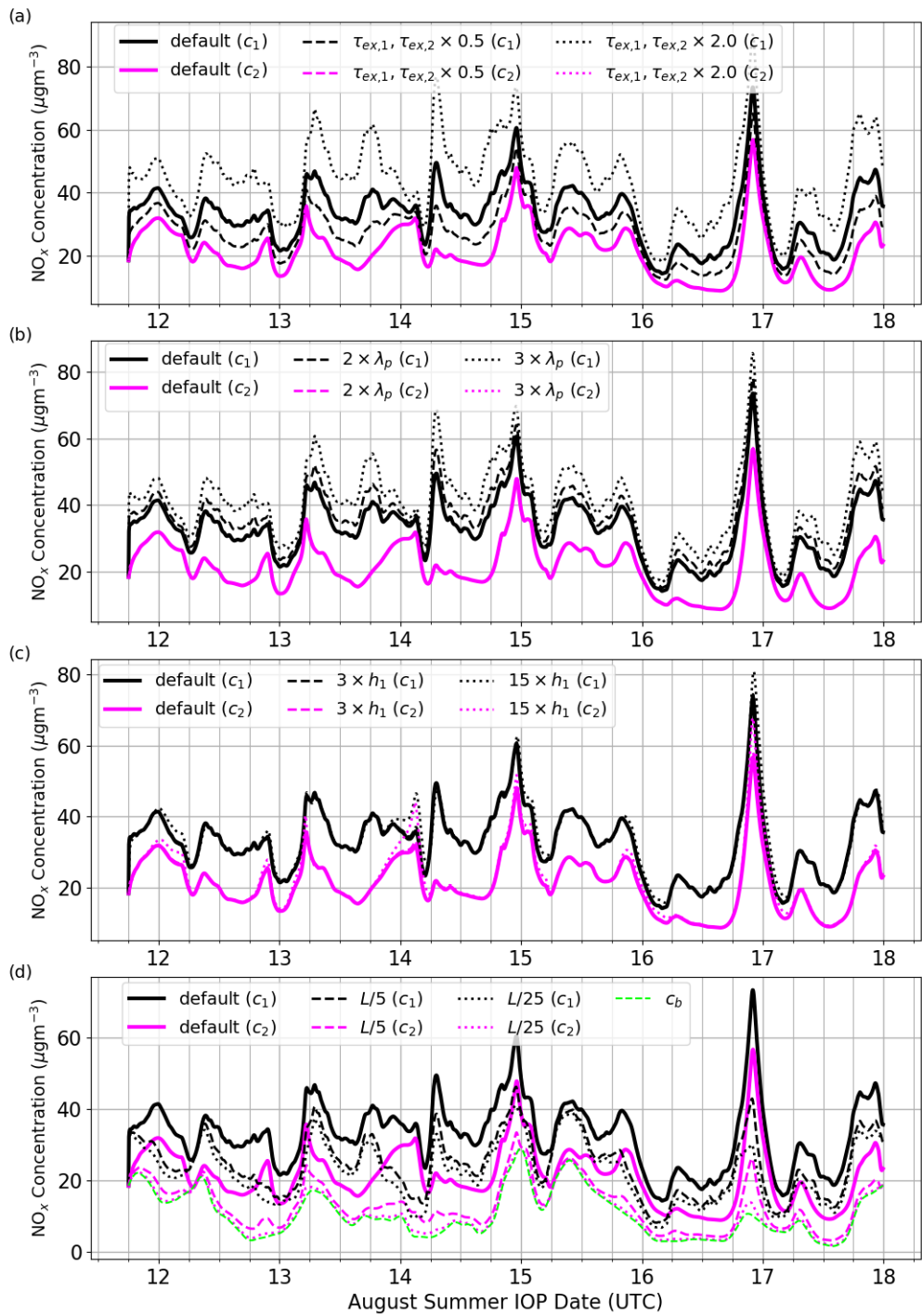
Figure 2.24: Sensitivity of the two-box model concentrations to different urban canopy parameters during the case study. Default indicates that the parameter values were those used throughout the rest of the case study. c_1 and c_2 curves represent the concentrations in the canopy and ML boxes respectively. Sensitivity to (a) varying the vertical exchange timescales $\tau_{ex,1}$ and $\tau_{ex,2}$ simultaneously by the same amounts, (b) increasing λ_p, (c) increasing the height of the urban canopy and (d) decreasing the horizontal extent of the urban canopy. The green curve in (d) is c_b measured at Harwell.

argument that U_1 is of lesser importance in controlling c_1.

Figure 2.24b shows the sensitivity of c_1 and c_2 to λ_p, with λ_p equal to two and three times its default value of 0.17. λ_p influences the concentration in the boxes through its presence in $\tau_{ex,2}$ and q_{fix}. Since $\tau_{ex,2}$ becomes longer with increasing λ_p, the ML box vertical exchange term becomes smaller, and one might expect a lag to be introduced in c_2 relative to c_1. However, as can be seen in Fig. 2.24b, c_2 varies negligibly with λ_p, so the influence of λ_p through $\tau_{ex,2}$ is very small. This is likely because when $\tau_{ex,2}$ becomes longer with increasing λ_p, c_1 increases so that the magnitude of the ML box vertical exchange term is unchanged. c_1 is inversely proportional to $1 - \lambda_p$ through its presence in q_{fix} within the steady state canopy box model solution. c_1 increased on average (during conditions suitable to use of the box model) by 11% and 30% when λ_p was multiplied by 2 and 3, respectively.

Figure 2.24c shows the sensitivity of c_1 and c_2 to varying h_1, but with $z_{MH} (= h_1 + h_2)$ kept the same. When h_1 was multiplied by 3 and 15, the average values of c_1 and c_2 changed very little. The influence on c_1 was small because horizontal advection of NO_x from the canopy was negligible. This means changes in c_1 in the canopy box equation can only be due to the source and exchange terms, both of which are inversely proportional to h_1. Consequently, they change by the same amount when h_1 is varied, and their sum and $\dot{c}_1$ do not change. This is why h_1 does not appear in the steady state canopy box solution. Varying h_1 also generally had little effect on c_2. This result implies the depth averaged concentration in the canopy at a given time does not change much with canopy height. In tall canopies it is possible that large vertical concentration gradients exist within the canopy, so that the surface level concentration increases with increasing canopy height.

The only times varying h_1 had non-negligible influence on c_1 and c_2 was for $h_1 \times 15$ when z_{MH} was very small. During these times the canopy occupied a large fraction of the BL. The effective source at the bottom of the ML box then emits into a ML box with reduced volume. Also, the BL is occupied by more urban canopy, reducing the horizontal advection of NO_x from the ML. c_2 increases, which feeds back on the canopy box through the exchange term, increasing c_1.

Figure 2.24d shows the sensitivity of c_1 and c_2 to decreasing L by a factor of 5 and 25. This represents decreasing the horizontal extent of the urban canopy to 10 km and 2 km respectively, which are typical of medium sized cities and towns respectively. Time average c_2 reduces from its default value of 17.2 μgm^{-3}, to 9.5 μgm^{-3} and 7.5 μgm^{-3} for $L/5$ and $L/25$ respectively. The advection timescales are smaller by 1/5 and 1/25 respectively. It can be seen that $c_2 \approx c_b$ for $L/25$ and $L/5$, since advection removes local pollution and replaces it with background air very efficiently. Advective losses from the canopy have a negligible influence on c_1 even for $L/25$, and therefore L does not appear in the steady state canopy box solution. However, c_1 is influenced by variation in L through c_2 in the exchange term. For $L/5$, $c_2 \approx c_b$ so that the exchange term becomes

approximately $(c_1 - c_b)/\tau_{ex,1}$. The time average value of c_1 is reduced from its default value of 30.5 μgm^{-3} to 22.7 μgm^{-3}. When $L/25$ is used $c_1 = 20.4$ μgm^{-3}, which is not much different from the $L/5$ value. This is because $c_2 \approx c_b$ for both. As L is decreased, c_1 becomes controlled by q_{fix}, $\tau_{ex,1}$ and c_b, unlike for large L where c_1 depends on c_2 rather than c_b.

2.9 Summary

Using one- and two-box models, the influence of pollution transport processes on NO$_x$ concentration was analysed in the UBL. The one-box model was used to predict the average NO$_x$ concentration in the Greater London BL, and the two-box model was used to predict the average concentrations in the Greater London urban canopy and MLs. The investigation focused on unstable atmospheric conditions, when the box model assumptions are reasonably met. Meteorological and pollution measurements made during a period ($12^{\text{th}} - 17^{\text{th}}$ August 2012) of the ClearfLo field campaign were used, both as inputs to the box models and to compare with box model predicted NO$_x$ concentrations.

Using the one-box model it was shown that the daytime average UBL concentration was approximately equally sensitive to c_b, τ, q and z_{MH}, and much less sensitive to c_a, when typical parameter values during the case study were used. For modelling daytime average AQ in the UBL it is more important to have good representation of c_b, τ, q and z_{MH} than c_a.

The magnitude of the concentration peaks was largely controlled by how small z_{MH} was and when small values of z_{MH} occurred relative to the morning q increase. Late onset in z_{MH} growth tended to result in small z_{MH} coinciding with large q, and therefore higher concentration peaks. This suggests that for predicting peaks in concentration it is important to have accurate representation of the development of turbulence in the early morning and z_{MH} diagnosis methods in AQMs. Unlike z_{MH} and q which have diurnal variation, τ and c_b varied more with synoptic conditions and generally had a lower frequency influence on concentration.

The entrainment term was much less important in determining the daily average concentration in the UBL than the source and advection terms. However, it did play a significant role in reducing morning concentration peaks, particularly when the minimum z_{MH} was low. The average advection timescale during the case study was $\tau = 50$ km / 7 ms$^{-1} \approx 2$ hr. The z_{MH} growth timescale was $\tau_a \approx 4$ hr, approximately twice that of τ. This explains why although entrainment had a significant contribution to reducing concentration in the morning, advection was generally a more efficient sink of pollution from London's BL. τ is very dependent on wind speed in the BL so its value is particular to this case study. However, the value of τ_a is likely reasonably representative for London under summer-time convective conditions.

Chapter 2. One- and Two-box Modelling of an Inert Pollutant in London's Boundary Layer

The NO_x concentration predicted by the one-box model and measured at BT Tower were in closest agreement on the 17th as expected. This day was least influenced by frontal activity and rainfall. The NO_x concentration predicted by the one-box model and measured at BT Tower were generally in better agreement when the BL conditions were unstable than stable. This is because vertical mixing is more efficient under unstable conditions so that the assumption of a well-mixed BL is more reasonable. Vertical mixing is a crucial process controlling pollution concentration throughout the UBL. It determines vertical concentration gradients, the height in the atmosphere to which pollutants are transported up to and therefore also the amount by which they are diluted. Considering that wind speed varies with height, the vertical distribution of pollution also specifies the wind speed at which pollution is advected. This in turn affects the horizontal distribution of pollution throughout the city and its removal from the city. The role of vertical mixing in determining the vertical distribution of pollution in the UBL, and how the vertical distribution of pollution evolves with downstream distance over the city is investigated in Chapter 3.

The concentration and budget terms for the ML box (of the two-box model) compared to the one-box model were almost identical. It was estimated that the depth averaged velocity in the canopy was approximately 5 times smaller than the depth averaged value in the entire BL, and therefore the horizontal advection timescale in the canopy was approximately 10 hr. A vertical exchange timescale between the canopy and the ML was estimated to be approximately 40 sec on average during the case study. This is three orders of magnitude shorter than the canopy horizontal advection timescale, suggesting the vast majority of pollution is transported vertically from the canopy into the ML, before being horizontally advected out of the BL. For the ML box it as if the source were at the top of the canopy. Given also that the canopy occupies a negligible volume of the BL, it explains why the ML box behaves like the one-box model.

A steady state analytical solution was found for the urban canopy box concentration. The canopy box is in a quasi-equilibrium where the vertical exchange term adjusts to the source term with $O(\tau_{ex,1} = 1 \text{ min})$ timescale. c_1 adjusts to changes in parameters and c_2 much quicker than the time over which they vary. The steady state solution is therefore an excellent approximation to the full urban canopy box equation. The steady state solution is proportional to only q, $1/(1 - \lambda_p)$, $1/v_e$ and c_2. This implies that canopy height is not an important parameter controlling urban canopy pollution concentration. Although the extent to which large canopy heights lead to concentration gradients within the canopy is little understood in the literature.

The urban canopy wind speed is also not present in the urban canopy box steady state solution. This is because horizontal advection of pollution out of the canopy was negligible. This implies that the wind speed in the urban canopy is not an important parameter controlling urban canopy pollution concentration. It is known that the local canopy geometry and velocity in the urban canopy influence v_e (Salizzoni et al., 2011).

However, given that the SIRANE parametrisation of v_e has been demonstrated to work well in the literature (Soulhac et al., 2012) and in investigations presented here, it is a reasonable approximation to represent v_e using only the external flow conditions.

The urban canopy box predicted concentrations were generally closer to the average of the urban background NO_x measurements, than the ML box predicted concentrations were to the BT Tower measurements. This is likely because the average urban background concentration was obtained from several sites across Greater London, whereas only one measurement site at BT Tower was available in the ML. Also, the well-mixed assumption is likely better for the canopy box than ML box under all stability conditions since turbulence is more mechanically dominated in the canopy. The average ratio between the canopy box and ML box concentration was 1.84, which is close to 1.98, the average ratio of the urban background to BT Tower NO_x measurements. This demonstrates that the SIRANE vertical exchange parametrisation performed well, concentrations in the urban canopy are greatly elevated compared to the concentrations in most of the BL and that vertical mixing of pollution from the urban canopy into the air above is an important process controlling surface level AQ.

The multi-layer urban canopy models used in NWP predict the pollution concentration at several model levels within and above the canopy, rather than using one bulk value to describe the concentration in the canopy. The vertical mixing representation is typically based on local gradients of velocity and concentration. Towards developing improved vertical mixing parametrisations in multi-layer urban canopy models, in Chapter 4 turbulence and time-mean flow structures within the urban canopy and near canopy top will be investigated.

Chapter 3

Numerical Weather Prediction in the Urban Boundary Layer Convective Grey Zone

3.1 Introduction

As computing power increases there is a trend towards using smaller horizontal grid lengths (Δ_{xy}) in NWP and climate applications. With decreasing Δ_{xy} less of the flow has to be parametrised since it is explicitly resolved on the grid. Turbulence in the atmosphere occurs across a range of spatial scales, for example deep convective thermals and CBL scale eddies are O(1 km), eddies in growing and decaying CBLs are O(300 m), convective updrafts forming in the superadiabatic layer are O(100 m) and mechanically generated eddies in neutral BLs are $\approx 25 - 800$ m (Honnert, 2019). Consequently there is no choice of Δ_{xy} between O(25 m) and O(1 km) that avoids some of the main energy producing turbulence being partially resolved (i.e. neither fully resolved or sub-grid), across different atmospheric BL conditions. This is commonly referred to as the grey zone problem of atmospheric turbulence (Wyngaard, 2004).

At O(10 m) grid lengths modelling is in the LES regime, where the vast majority of energy producing eddies within the BL are resolved explicitly on the grid. The role of the sub-grid turbulence scheme is then to carry energy from the smallest resolved scale to the dissipation scales, across the inertial subrange. The Smagorinsky-Lilly scheme (Smagorinsky, 1963; Lilly, 1967) is the most common of such schemes. At the other extreme, when $\Delta_{xy} > 1$ km as is traditionally the case in mesoscale NWP, turbulent eddies are entirely filtered out and are represented using turbulence parametrisations. Typically, these comprise of a local part based on K-theory, where the turbulent flux is related to the local gradient of the modelled quantity through a diffusion coefficient, and a non-local part representing the turbulent transport from the ground to the top of the BL by convective thermals (Deardorff, 1972a; Busch et al., 1976; Lock et al., 2000).

When Δ_{xy} is decreased below O(1 km), more of the flow is resolved but its prediction in NWP does not necessarily improve. There is no clear scale separation between the

CBL scale thermals and the filter length l_f (the effective resolution of the model once numerical diffusion is considered). The turbulence of scale l_f is partially resolved. It can have unphysical structure, turbulent transport can be double counted by the turbulence parametrisation and the assumption in turbulence parametrisations that there are several energy producing structures per grid box breaks down. A recent review of turbulence schemes being developed and used by NWP in the atmospheric grey zone is given by Honnert et al. (2020).

The UM addresses the double counting problem and to some extent the unphysical structure problem by using a so called "blended" BL scheme (Boutle et al., 2014). The amount of sub-grid mixing is a function of Δ_{xy}/z_h. It specifies the proportion of sub-grid mixing that is handled by the 3D Smagorinsky-Lilly subfilter turbulence scheme (3D Smag) versus the 1D BL scheme (Lock et al., 2000). The function is an adaptation of the one determined by Honnert et al. (2011), who in a LES coarse-graining experiment established the resolved and sub-grid partitioning of TKE with varying Δ_{xy}/z_h. The blended scheme therefore only parametrises the turbulence that is expected to be sub-grid based on TKE partitioning with Δ_{xy}/z_h. This avoids the double counting of turbulence by the 1D BL scheme, and reduces the amount of poorly resolved turbulence at the scale of l_f.

There are many reasons to move to smaller Δ_{xy} than O(1 km) typically used in current regional NWP models. The UK Met Office's operational forecast model (the UKV) runs at 1.5 km grid length over the UK (Lean et al., 2008). Météo-France uses the AROME-France model at 1.3 km grid length (Seity et al., 2011) as well as an ensemble forecast model at 2.5 km grid length (Raynaud and Bouttier, 2017). For $\Delta_{xy} > 1$ km, to a good approximation all CBL turbulence is sub-grid, but deep convective structures become partly resolved. To prevent over counting, deep convection parametrisation schemes are often turned off, but this can result in poorer prediction of smaller showers (Clark et al., 2016). Also, the small initial convective plumes are not resolved, delaying the initiation of convection (Lean et al., 2008; Kealy et al., 2019; Honnert et al., 2020). Moving to smaller grid lengths would help solve this. Deep convection parametrisation schemes should be scale selective, for example in a way analogous to the UM "blending scheme" for the CBL grey zone.

Many operational weather and AQ centres are conducting research towards developing city scale models that use smaller Δ_{xy} than O(1 km). Such models have the potential to improve prediction of hazards such as the UHI, flooding and poor AQ events at weather and climate timescales (Lean et al., 2019). The UK Met Office have a $\Delta_{xy} = 300\,\text{m}$ research model running routinely over London (Boutle et al., 2016) and is primarily used for fog forecasts at Heathrow airport. High resolution of the orography enables better representation of the kilometre scale variations in atmospheric stability near the ground. Simón-Moral et al. (2020) ran uSINGV, a tropical configuration of the UM that includes the MORUSES urban surface scheme (Porson et al., 2010), over Singapore. $\Delta_{xy} = 300\,\text{m}$

was chosen so that neighbourhood scale variations in the urban canopy characteristics are resolved. The influence of changing urban morphology within individual neighbourhoods on screen-level temperature was demonstrated to be well represented by the model. Leroyer et al. (2014) modelled a sea-breeze event in Vancouver, and showed that the sea-breeze convergence line was more accurately represented at 250 m than 1 km grid length, based on comparison with observations.

It is possible that large improvements in the predictive capability of NWP and city scale AQ transport in AQMs will be made when $\Delta_{xy} \approx 100$ m. It is only then that the majority of CBL ML turbulence is resolved (Honnert et al., 2011), so that realistic turbulent structures such as horizontal rolls and open cells are produced. It is well known that neutrally buoyant tracers released near the ground exhibit a "lift off" behaviour, where after a brief period of being advected horizontally near the surface, the tracers are elevated rapidly in updrafts to high in the BL (Deardorff, 1972b; Willis and Deardorff, 1976; Gopalakrishnan and Avissar, 2000). Whilst tracer concentration is large in the upper BL the ground level concentration beneath the updraft is small. The timescale of this process is on the order of the Deardorff convective timescale $\tau_* = O(10\text{min})$, which for typical horizontal advection velocities results in city scale variation in ground level concentration. To the authors' knowledge the magnitude of these variations has not been investigated for city scale pollution emissions.

This chapter focuses on the CBL turbulence representation in the UM at Δ_{xy} ranging from 1.5 km to 55 m, and how its representation influences the vertical mixing and horizontal heterogeneity of tracer. Two homogeneously distributed ground sources of tracer are included. One is puff release and the other is continuous release. The former is used to study the time evolution of tracer in the vertical and the latter is used to represent pollution emissions over London. In Sect. 3.3 the UM BL turbulence blending scheme is analysed, to see whether it correctly partitions the resolved and parametrised tracer fluxes.

CBL scale eddies contain narrow updrafts with large velocity and temperature compared to the surrounding air. Numerical schemes tend to have problems whenever there are sharp gradients. In the CBL grey zone updrafts are partially resolved, and the SISL advection scheme used in the UM can suffer from momentum and scalar non-conservation issues (as discussed in Appendix. B). Tracer non-conservation issues are explored at different diurnal stages of CBL development across the 1.5 km to 55 m model simulations in Sects. 3.4.1–3.4.3.

Turbulence statistics from the O(100 m) grid length simulations are analysed in Sect. 3.5, and it is examined whether turbulence behaves the same in NWP when it is largely resolved, compared to more idealised LES and laboratory studies. The horizontal heterogeneity of tracer concentration at the top of the surface layer is also analysed, giving an indication of the effect CBL structures might have on ground level pollution concentration heterogeneity. Apart from a few exceptions (Boutle et al., 2014; Ronda et al.,

2017; Lean et al., 2019, e.g.), NWP studies at O(100 m) grid length are sparse, and to the authors' knowledge it is the first time passive scalar has been included in such a study.

In Sect. 3.6, the characteristics of tracer vertical mixing are compared in simulations at 1.5 km, 100 m and 55 m grid length. Since NWP at $\Delta_{xy} = 1.5$ km does not resolve the lofting of tracer in thermals from near the surface, it is possible the $t < O(\tau_*)$ vertical mixing behaviour of tracer released near the ground is poorly represented. The influence of vertical mixing representation on ground level concentration over London is estimated. A reduced analytical model for vertical mixing is formulated and used to understand the vertical mixing behaviour across simulations. The differences are quantified by vertical mixing timescales that appear as effective parameters in the reduced model.

3.2 UM Simulations

In this section details of the UM simulations, tracer sources and case study date are presented.

3.2.1 Simulation Configurations

The simulations are carried out using version 10.5 of the UM. Simulations were performed on the UK Met Office and NERC (Natural Environment Research Council) joint supercomputer system (MONSooN). The model suite is one-way nested and each nests' domain is highlighted in Fig. 3.1. Model configurations are given in Table 3.1. The UKV model is the outermost nest and has variable Δ_{xy}, but is approximately 1.5 km over most of the UK including South-East England. Archived operational UKV model output are used to provide hourly lateral BCs (LBCs) and to initialise the UKV model. The UKV nest is used to provide LBCs to a $\Delta_{xy} = 500$ m model, the output from which is provided as the LBCs to a $\Delta_{xy} = 300$ m model, which in turn passes LBCs to drive both the $\Delta_{xy} = 100$ m and $\Delta_{xy} = 55$ m models. LBCs were passed between the 500–55 m models every 15 min. The nests are centred on London. The simulation time period common to all models was 06:00–22:00 UTC.

The 500 m and 300 m model domain sizes were chosen to be large enough that flow fully adjusts to the new model grid (or "spins up") before reaching the boundary of the next nest in. Lean et al. (2019) used an almost identical UM nesting suite and tested a 100 m model domain of 30 km $\times$ 30 km. They showed that spin up effects persisted $10 - 15$ km downstream of the inflow boundary and into London. By extending the domain to 80 km $\times$ 80 km, Lean et al. (2019) found the flow to have satisfactorily spun up before it reached the London area (approximately 50 km $\times$ 50 km). The case study was clear-sky CBL like the one presented here, so the same 80 km $\times$ 80 km domain is used for the 100 m and 55 m models. It is shown to be sufficient in Sect. 3.3.1. The domain top in
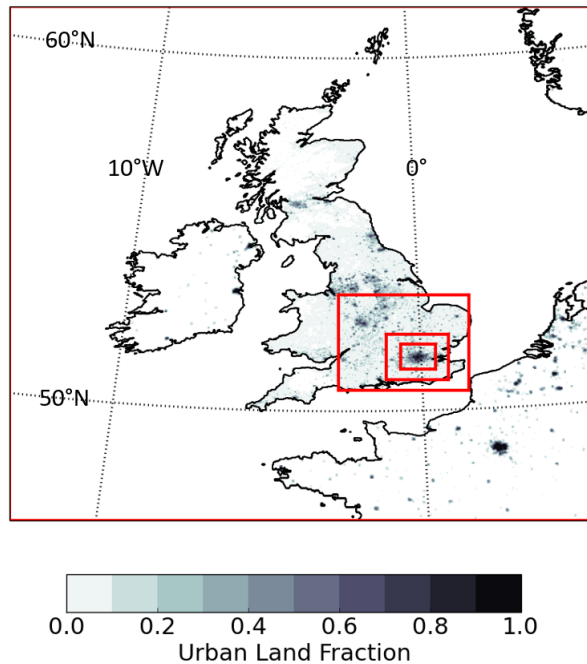
Figure 3.1: Nesting suite schematic with urban fraction plotted. Each nest is highlighted in red. The outermost nest is the UKV model, and in decreasing domain size order the other nests are the 500 m, 300 m, 100 m and 55 m models. The 100 m and 55 m models have the same domain size.

all models is 40 km and vertical grid spacing is quadratic so that there is better vertical resolution within the BL than above. A similar UM set up has been used by Hanley et al. (2015).

The scale-aware blended BL scheme was used for vertical turbulent mixing. The horizontal mixing is calculated using an unblended Smagorinsky-Lilly scheme. For CBLs the BL scheme determines z_h by performing an adiabatic moist parcel ascent. z_h is diagnosed as the height where the parcel becomes negatively buoyant. The surface scheme used in the UM is JULES, which includes a module known as MORUSES which treats the urban aspects of the surface (as discussed previously in Sect. 1.2.5).

The current UM dynamical core is known as "ENDGame". It solves fully compressible, non-hydrostatic, deep-atmosphere dynamics using semi-implicit semi-Lagrangian (SISL) numerical integration (Davies et al., 2005; Wood et al., 2014). See Appendix B for

Model (horizontal grid length)	Domain size (grid points)	Time step	Vertical levels
UKV (≈ 1.5 km)	744×928	60 s	70
500 m	600×600	10 s	140
300 m	430×430	10 s	140
100 m	800×800	3 s	140
55 m	1440×1440	2 s	140

Table 3.1:: Model configurations used.

an overview of SISL advection and associated mass conservation schemes. A tracer conservation scheme is not used in the simulations since the Priestly Algorithm (PA) and the Optimised Conservative Filter (OCF) have only been implemented for the purpose of using tracers in global models. Currently the UM does not have a method (such as the Zero Lateral Flux (ZLF) method) for including tracer fluxes at limited area model (LAM) boundaries in tracer conservation schemes. A recent correspondence with Dr Adrian Lock suggests that using PA or OCF in conjunction with ZLF might in principle be possible with little extra work. However, this was too late in the PhD to be investigated. One model simulation was carried out with OCF (and without treatment of tracer fluxes at lateral boundaries) and results from that are only presented in Sect. 3.4.3.

3.2.2   Tracer Sources

A large amount of UM development work was carried out as part of this study – most notably updating the urban surface scheme to MORUSES and including tracer ground area sources. Technical information on including the tracer ground area sources is given in Appendix C. Two tracers were included in the simulations, one with continuous release and the other with puff release. The release areas are illustrated in Fig. 3.2. The same tracer source areas and emission rates were used in all of the nested models to facilitate their comparison.

The continuous release is from a homogeneous ground source with horizontal dimensions 50 km $\times$ 50 km. It is centred on the maximum urban fraction, determined as the maximum of two fourth order polynomials fitted to the longitudinal and latitudinal average urban fraction within the 100/55 m domain. The location is shown as a red dot in Fig. 3.2. Because the area of the source corresponds roughly to the size of Greater London and it is continuous in nature, it provides a simplified framework in which to study city scale variation in tracer concentration over London. Also, since the tracer is released from an area large enough to contain many CBL scale eddies, horizontally averaged profiles of tracer can be calculated that are statistically representative.

A puff release is also made from a homogeneous ground source, with its horizontal extent covering the entire 100/55 m domain. This release was made to analyse vertical mixing timescales. This is the largest source area that could be used across all models. The large source area makes it possible to choose an analysis region where clean (zero tracer) air advected in from the domain boundaries does not reach the analysis region within the hour. Each hour the tracer was released from the surface into the domain and at the end of the hour the tracer was completely flushed from the domain before the next release. By releasing the tracer every hour the vertical mixing could be analysed several times throughout the day, whilst leaving enough time between releases to allow the tracer to become well-mixed.
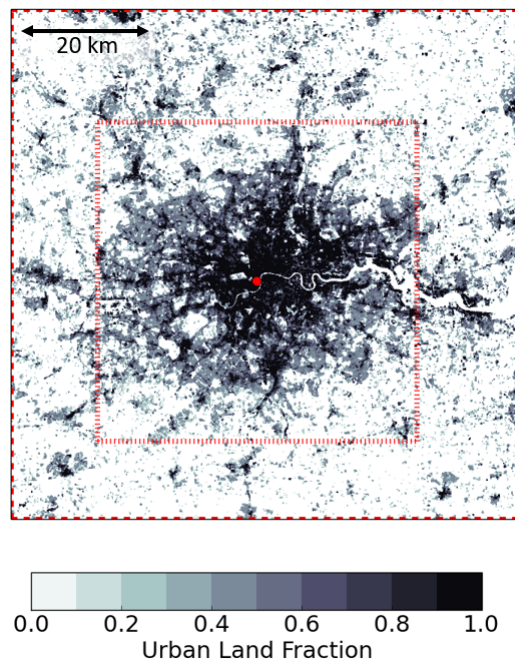
Figure 3.2: Schematic illustrating the two tracer ground sources used in the investigation. The dashed and dotted lines represent the puff and continuous release source areas respectively. Urban fraction is also plotted and the red dot ($-0.129°$W, $51.500°$N) is the centre of the continuous release source area.

3.2.3 Case Study

The chosen case study date is 4th May 2016. According to the London Urban Meteorological Observatory (LUMO; Kotthaus and Grimmond (2014)) it was a clear-sky day, based on the definition that at least 3 of the 4 ceilometers had no overhead cloud at any height more than 99% of the time. This is consistent with the near infra-red band of the NOAA-19 High-Resolution Infra Red sounder in Fig. 3.3a, which shows little signal over the vast majority of England at 14:00 UTC. Sunrise and sunset were 05:24 UTC and 20:30 UTC respectively. A clear-sky day was chosen since clear-sky conditions are conducive to strong CBL mixing, and are the most simple conditions in which to study CBL mixing since there is no influence from cloud generated turbulence or latent heating.

As seen from the surface chart in Fig. 3.3b, South-East England was under a high pressure system centred on continental Europe. The Reading University Atmospheric Observatory (RUAO; `https://research.reading.ac.uk/meteorology/atmospheric-observatory/atmospheric-observatory-data/`) is approximately 60 km west of Central London. The hourly-average 10 m wind direction was predominantly from the south between 08:00 UTC and 22:00 UTC, varying between $165°$ and $203°$ with mean of $186°$. This is consistent with geostrophic flow direction according to the isobars in Fig. 3.3b. Flow during the night (01:00–07:00 UTC) was more changeable, varying between $104°$ and $235°$.

Data was available from a network of three scintillometers separated by $1 - 3$ km in Central London (Crawford et al., 2017). They measure Q_H integrated over the path between the infra-red beam sources and receivers, which is largely above the blending height of the buildings. Between 11:00 UTC and 15:00 UTC hourly averaged Q_H was $300 - 400$ Wm^{-2} for the different scintillometer paths. At RUAO the average 10 m wind speed was 2.8 ms^{-1} during the same period. Given the moderate wind speeds and large Q_H, the case date is suitable for the study of a highly CBL.

3.3   BL Scheme Scale Awareness

The blended BL scheme used within the UM to parametrise sub-grid vertical tracer fluxes is detailed in Sect. 3.3.2. Comparison is made between predicted and expected behaviour based on knowledge of the blended scheme and BL theory. This serves two purposes – first to provide an estimate of the partitioning between sub-grid and resolved fluxes, and second to analyse the performance of the blended scheme and vertical mixing in the UM. The former is important when interpreting results in later sections. Vertical profiles of concentration of passive tracer c, potential temperature θ and velocity at 08:00 UTC, 13:00 UTC and 21:00 UTC are shown to give an overview of the meteorological conditions predicted by the models throughout the day.

3.3.1   Analysis Region

First, the choice of analysis region used throughout this chapter is explained. It is desirable that within the analysis region there is little variation in the flow on the scale of the analysis region and that it contains more than 10 CBL scale eddies, so that horizontally averaged properties are statistically representative of the local flow.

Horizontal cross-sections of wind speed at 13:00 UTC and $z = 300$ m from the UKV and 55 m models are shown in Fig. 3.4. The choice of analysis region is illustrated by a solid black line and has dimensions 40 km $\times$ 15 km. The UKV model wind speed field is much smoother than the 55 m model. The 55 m model wind speed has O(1 km) horizontal variations due to resolved motions influenced by z_h scale vertical mixing. The wind field however is statistically similar on the scale of the analysis region, since it is large enough to contain many z_h scale eddies. The average wind speed within the UKV and 55 m model cross-sections is approximately 8 ms^{-1} and on the scale of the analysis region changes in wind speed are only approximately 1 ms^{-1}.

Figure 3.5 shows z_h zonally averaged across the longitudinal extent of the analysis region (40 km), plotted against downstream distance from the south 100/55 m domain boundary. The UKV model z_h tends to increase with downstream distance whilst the BL adjusts to the urban surface. There is generally much less variation after approximately
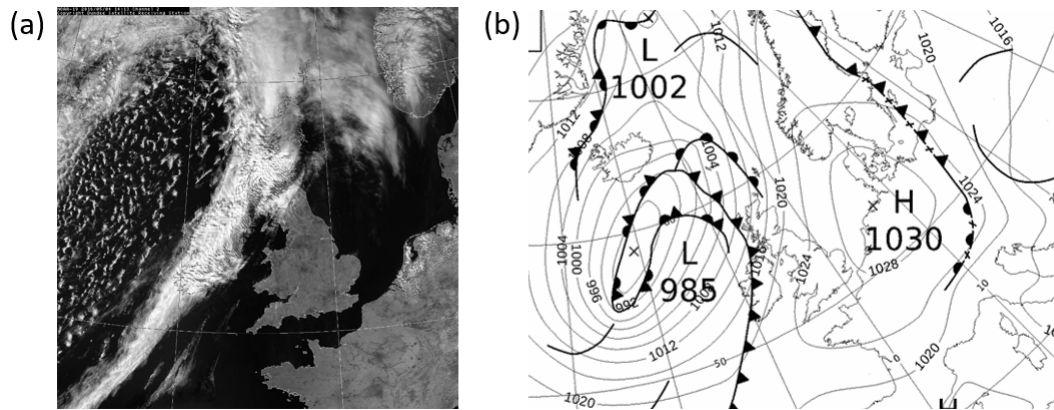
Figure 3.3: Synoptic conditions on 4th May 2016. (a) Near infra-red 0.725–1.100 μm, NOAA-19 High-Resolution Infra Red sounder, at 14:00 UTC (courtesy of Dundee satellite receiving station http://www.sat.dundee.ac.uk/abin/browse/avhrr/2016/5/4). (b) Surface chart at 12:00 UTC (courtesy of www.wetter3.de).

40 km downstream. Surface roughness and Q_H (not shown) tend to be elevated within the urban area leading to large z_h. The surface roughness leads to more mechanical vertical mixing, and Q_H warms up and deepens the BL as the air flows over the urban area.

The 55 m model z_h is lower at its inflow boundary than the UKV model at the same location. This is because of issues with 300 m model dynamics, the flow from which is passed as a BC to the 55 m model, and is discussed further in Sect. 3.4.1. z_h increases with downstream distance and like the UKV model tends to flatten by approximately 40 km downstream. This suggests that the city scale flow in the UKV and 55 m models has adjusted to the urban surface, and has little influence from the LBCs when it reaches the analysis region. The analysis region (indicated by black vertical lines in Fig. 3.5) is chosen 30 km downstream of the southern edge of the continuous source and extends 15 km downstream. The analysis region is not extended further downstream since it would then include less urbanised area north of London, where the flow characteristics near the surface are different.

3.3.2 The Blended Boundary Layer Scheme

The total vertical turbulent flux for a passive scalar variable χ in NWP is given by

$$\overline{w'\chi'}_{tot} = \overline{w'\chi'}_{sbg} + \overline{w'\chi'}_{res},$$ (3.1)

where $\overline{w'\chi'}_{sbg}$ and $\overline{w'\chi'}_{res}$ are the sub-grid and resolved fluxes respectively. Superscript prime represents departures from the time mean. The UM blended BL scheme uses a weighting function W_{1D}, to control the amount of sub-grid flux mixing. W_{1D} is a function of the dimensionless parameter Δ_{xy}/z_h. The form of W_{1D} is designed to give the

(a)

20 km

(b)

20 km

0   2   4   6   8   10   12
Wind Speed (ms^{-1})
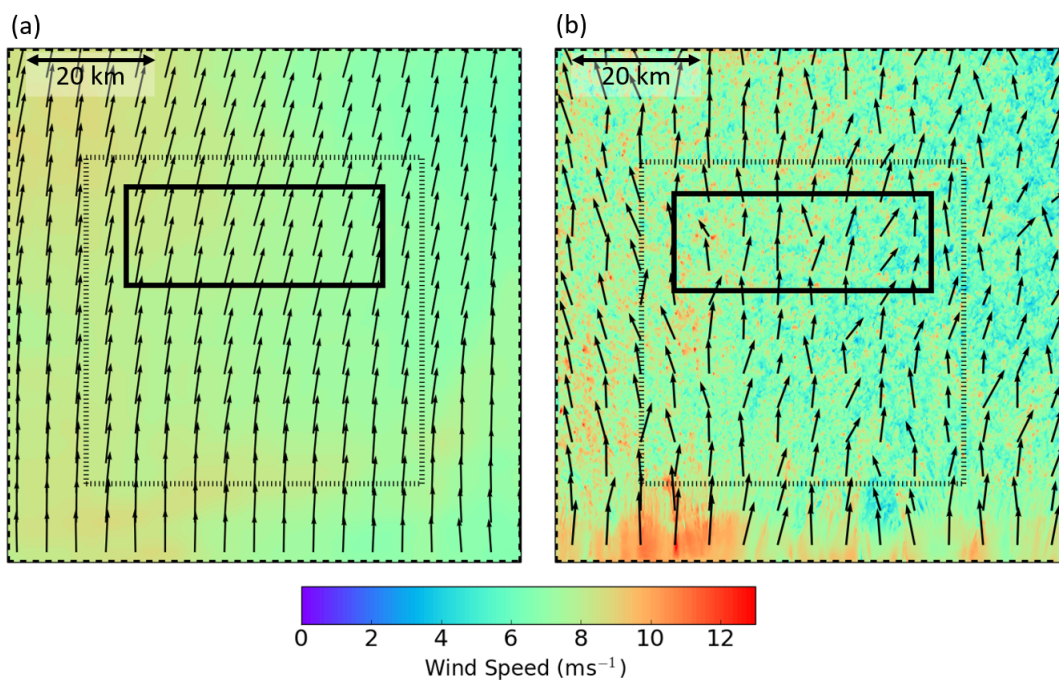
Figure 3.4: Horizontal cross-sections of wind speed at 13:00 UTC and $z = 300$ m from (a) the UKV model and (b) the 55 m model. Arrows are flow vectors at individual grid points. The dashed, dotted and solid lines represent the extent of the puff release source, continuous release source and analysis region respectively.
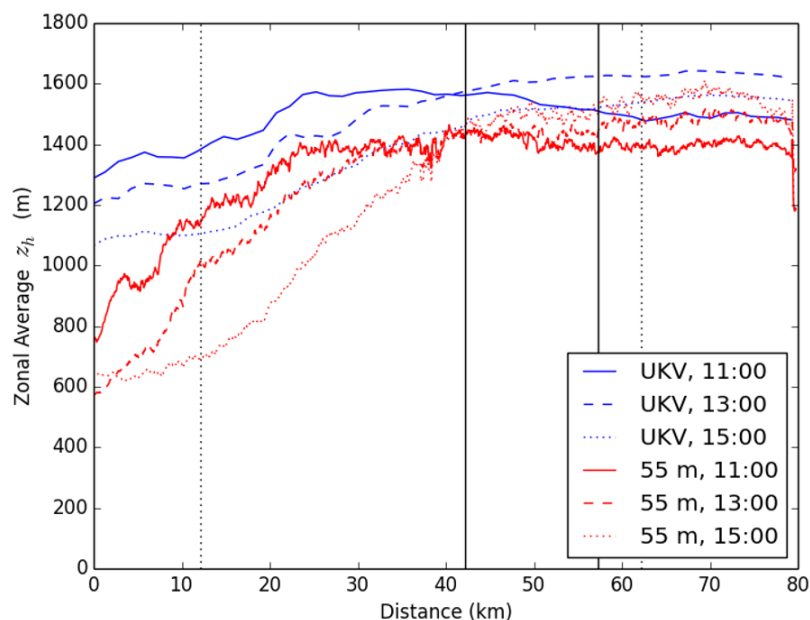
Figure 3.5: z_h zonally averaged between the longitudinal extent of the analysis region, plotted against distance downstream from the south 100/55 m domain boundary. Results are shown from the UKV and 55 m models at 11:00, 13:00 and 15:00 UTC. Dotted and solid vertical lines represent the continuous source and analysis region extent respectively.

proportion of TKE that is resolved versus sub-grid in LES at various horizontal grid lengths (Honnert et al., 2011; Boutle et al., 2014). Under clear-sky conditions it is given by (Boutle et al., 2014; Lock et al., 2016)

$$W_{1D} = 1 - \tanh\left(0.15\frac{z_h}{\Delta_{xy}}\right) \max\left[0, \min\left[1, \frac{4}{15}\left(4 - \frac{\Delta_{xy}}{z_h}\right)\right]\right]. \tag{3.2}$$

When Δ_{xy}/z_h is large, W_{1D} is large and more of the turbulence is treated as sub-grid.

The sub-grid scalar flux must be parametrised, and in the UM under cloud free conditions is given by (Lock et al., 2016)

$$\overline{w'\chi'}_{sbg} = -\max\left[W_{1D}K_\chi^{NL}, K_\chi(Ri)\right]\frac{\partial\chi}{\partial z} + W_{1D}K_\chi^{NL}\gamma_\chi, \tag{3.3}$$

where K_χ^{NL} is a non-local diffusivity, $K_\chi(Ri)$ is a local diffusivity, Ri is the local Richardson number and γ_χ is a height independent parameter determined by the surface and entrainment fluxes. The γ_χ term is an extra non-local term (i.e. it does not depend on local gradients) and is included to make χ profiles more well-mixed. However, it is only included when $\chi = \theta$. Specific humidity profiles tend to be less mixed due to drying at the ML top, so for them the extra non-local term is not included. Tracers do not have their own tailored treatment in the UM and consequently there is no extra non-local term. The γ_χ term need not be considered in analysis of tracers presented herein.

The first term on the right-hand side of Eq. 3.3 is based on K-theory, and depends on the weighted diffusivity and the local χ gradient. If within the ML of the BL vertical mixing is poorly resolved, the maximum function in Eq. 3.3 equals $W_{1D}K_\chi^{NL}$. In this case sub-grid vertical mixing of tracer is proportional to W_{1D}. $K_\chi(Ri)$ is used close to the surface under near neutral conditions or when vertical mixing is well resolved in the ML. $K_\chi(Ri)$ is a function of stability, local shear and a length scale l_{blend}. l_{blend} is a function of a 1D BL scheme mixing length and a 3D Smag mixing length. W_{1D} is used to weight l_{blend} towards the 3D Smag mixing length when turbulence in the ML is well resolved (i.e. for small Δ_{xy}/z_h).

Plotted in Fig. 3.6a is the analysis-area-averaged z_h for each of the models throughout the day. The reason the 500 m and 300 m models have lower z_h in the afternoon is discussed in Sect. 3.4.1. Figure 3.6b shows W_{1D} calculated using z_h in Eq. 3.2. In the early morning and late evening when z_h is small W_{1D} is large. During these times most of the turbulence should be treated by the model as parametrised. W_{1D} is much smaller in the afternoon when the BL has grown. Based on W_{1D}, approximately 15%, 35%, 55%, 95% and 100% of the vertical mixing within the ML should be treated as resolved in the UKV, 500 m, 300 m, 100 m and 55 m models respectively, between 11:00–15:00 UTC.
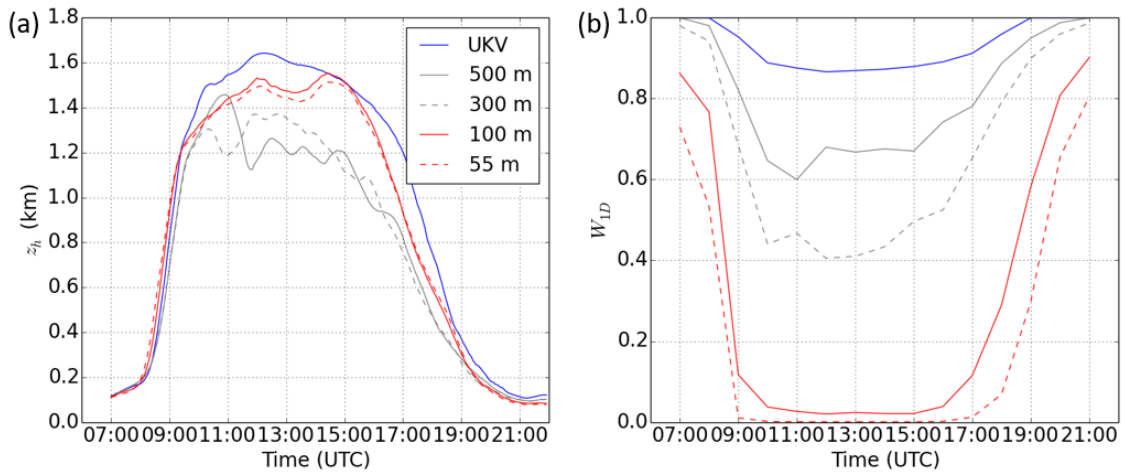
Figure 3.6: (a) and (b) correspond to the analysis region averaged z_h and W_{1D} respectively for each of the models throughout the day.

3.3.3 Sub-grid and Resolved Turbulent Tracer Flux Partitioning Throughout the Day

3.3.3.1 Expected Total Vertical Flux Behaviour

Before inspecting the total vertical tracer flux profiles, let us examine their expected behaviour. The continuity equation for our tracer is given by

$$\frac{\partial c}{\partial t} + \nabla.(c\boldsymbol{u}) = \delta_d(z)Q, \tag{3.4}$$

where $\delta_d(z)$ is the Dirac delta function (units m^{-1}) which is zero for $z \neq 0$, equal to ∞ at $z = 0$ and has integral $\int_0^\mu \delta_d(z)dz = 1$ for $\mu > 0$. Q is the continuous surface source release rate equal to 5×10^{-5} $kgm^{-2}s^{-1}$ in the UM simulations. $\boldsymbol{u} = (u, v, w)$ is the wind field, where u, v and w are the wind speed in the x, y and z axes, where x is aligned from west to east. One can decompose the instantaneous variables into their time mean and fluctuating components, for example $c = \bar{c} + c'$ where $\bar{c}$ is the time mean tracer concentration. The time mean is generally assumed longer than the timescale of BL eddies ($\sim$ 10 min) but shorter than changes in the larger scale flow ($<$ 1 hr). After decomposing the variables, the time average of Eq. 3.4 is the Reynolds averaged continuity equation

$$\frac{\partial \bar{c}}{\partial t} + \frac{\partial \bar{u}\bar{c} + \overline{u'c'}}{\partial x} + \frac{\partial \bar{v}\bar{c} + \overline{v'c'}}{\partial y} + \frac{\partial \bar{w}\bar{c} + \overline{w'c'}}{\partial z} = \delta_d(z)Q. \tag{3.5}$$

It has been assumed that the time mean of fluctuating components is zero. If one also assumes that the horizontal turbulent flux gradient terms are negligible compared to the vertical flux derivatives, that flow is predominantly meridional and $\bar{w} = 0$ so that the

---

Chapter 3. Numerical Weather Prediction in the Urban Boundary Layer Convective Grey Zone

zonal and vertical advection terms can be neglected, then

$$\frac{\partial \bar{c}}{\partial t} = -\frac{\partial \bar{v}\bar{c}}{\partial y} - \frac{\partial \overline{w'c'}}{\partial z} + \delta_d(z)Q. \tag{3.6}$$

Following Wyngaard and Brost (1984), it will be argued that when one takes the vertical partial derivative of Eq. 3.6, all resulting terms are approximately zero. Equation 3.6 is the same as their Eq. 2, except they also neglect the advection due to the mean flow term. Unlike most experiments where $\bar{c}$ can be assumed horizontally homogeneous, in the UM simulations average $\bar{c}$ in the BL increases approximately linearly with downstream distance from the start of the continuous release source area, since the amount of tracer released into the air increases linearly with downstream distance. The rest of this section therefore follows the arguments of Wyngaard and Brost (1984), but with the additional advection term.

Let us take the partial z derivative of Eq. 3.6 so that

$$\frac{\partial}{\partial t}\frac{\partial \bar{c}}{\partial z} = -\frac{\partial}{\partial y}\frac{\partial \bar{v}\bar{c}}{\partial z} - \frac{\partial^2 \overline{w'c'}}{\partial z^2} + \frac{\partial \delta_d(z)Q}{\partial z}. \tag{3.7}$$

By inspecting the left-hand side term, it can be seen that it is zero so long as the vertical gradient of $\bar{c}$ is also zero, even when $\bar{c}$ is changing with time. This is the case for boundary layers where scalar distribution has reached a steady state, which is common in well-mixed BLs during the middle of the day, where the vertical scalar gradient remains approximately zero with height.

The third term on the right-hand side of Eq. 3.6 is zero above the surface. The first term on the right-hand side of Eq. 3.6 is also zero if the vertical gradient of $\bar{v}\bar{c}$ does not change with downstream distance. Between 11:00–15:00 UTC, z_h predicted by the models is approximately 1.4 km and according to the Scintillometers over London $Q_H \approx 300 - 400$ Wm^{-2} (consistent with typical modelled surface Q_H over Central London), which corresponds to $w_* \approx 2$ ms^{-1}. One eddy turnover time (or Deardorff convective timescale $\tau_* = z_h/w_*$) therefore corresponds to ≈ 11 min. If N_{et} eddy turnovers are required for the tracer to become well-mixed then this time corresponds to approximately $11N_{et}$ min. Below z_h wind speed in the different models is typically 7 ms^{-1}. The distance tracer travels before becoming well-mixed is therefore approximately $11N_{et} \times 60 \times 7 = 4.5N_{et}$ km. The middle of the analysis region is 37.5 km downstream of the southern edge of the continuous source. The proportion of tracer that is well-mixed at the middle of the analysis region is therefore $\approx (37.5 - 4.5N_{et})/37.5 = 1 - 0.12N_{et}$. If $N_{et} \approx 2$ then approximately 76% of tracer should be well-mixed within the analysis region. Therefore vertical gradients of $\bar{c}\bar{v}$ should be reasonably constant with downstream distance within the analysis region between 11:00–15:00 UTC, so that the first term on the right-hand side of Eq. 3.6 is approximately zero.

Chapter 3. Numerical Weather Prediction in the Urban Boundary Layer Convective Grey Zone

The second term on the right-hand side of Eq. 3.6 must also equal zero if all others are. Integration of this term gives

$$\overline{w'c'} = \overline{w'c'}_0(1 - z/z_h) + \overline{w'c'}_{z_h}(z/z_h), \tag{3.8}$$

where $\overline{w'c'}_0$ is the surface flux equal to Q and $\overline{w'c'}_{z_h}$ is the flux at z_h. For a BL with strong capping inversion $\overline{w'c'}_{z_h} \approx 0$. Between 11:00–15:00 UTC when the BL is highly convective and the flow is reasonably steady (i.e. z_h and wind speed do not vary much in time), $\overline{w'c'}$ should be a linearly decreasing function, from Q at the surface to approximately zero at z_h.

3.3.3.2   Simulated Vertical Tracer Flux and Meteorology at 13:00 UTC

Figures 3.7b and c show horizontally averaged profiles of θ and wind speed respectively within the analysis region at 13:00 UTC. The θ profiles are approximately constant with height (< 0.5 K variation) in the ML, as is expected in strongly convective conditions. The wind speed is between 6–8 ms^{-1} within the BL for all models except the 500 m model which has larger maximum and smaller minimum. The UKV model u is less than 2 ms^{-1} demonstrating that the majority of the modelled flow is meridional, as suggested by observations in Sect. 3.2.3.

The 100 m and 55 m model continuous release tracer concentration profiles in Fig. 3.7a are almost constant with height for $0.1 < z/z_h < 0.8$. This is consistent with a large proportion (estimated previously to be 76%) of the tracer being well-mixed within the analysis region. It is therefore surprising that the UKV model profile decreases significantly with height in the ML. This is likely due to insufficient vertical mixing within the UKV model, so that $N_{et} > 2$ for the flow to become well-mixed within the analysis region. A possible solution is to include a non-local term for tracers in Eq. 3.3. A new non-local turbulence parametrisation that applies a separate non-gradient based term to both tracers and moisture is being developed in the UM (personal communication Dr. Adrian Lock). However, due to arguments presented in Sect. 3.6.1.2 this is likely inappropriate for city scale AQ modelling.

The 500 m and 300 m models have large concentration peaks at $z/z_h \approx 1.2$ which is unexpected. The tracer concentrations are generally much larger in the BL for the 500 m and 300 m models compared to the UKV model. This is also the case to a lesser extent for the 100 m and 55 m models. Differences in the horizontal advection between the models cannot explain these large c differences. The 3D flow fields and tracer non-conservation issues are discussed further in Sect. 3.4.

Figures 3.7d-f show profiles of the sub-grid, resolved and total tracer vertical turbulent fluxes respectively. The resolved flux is calculated assuming Taylor's hypothesis (or the "frozen turbulence hypothesis") (Garratt, 1994), whereby departures (denoted by

---

Chapter 3. Numerical Weather Prediction in the Urban Boundary Layer Convective Grey Zone
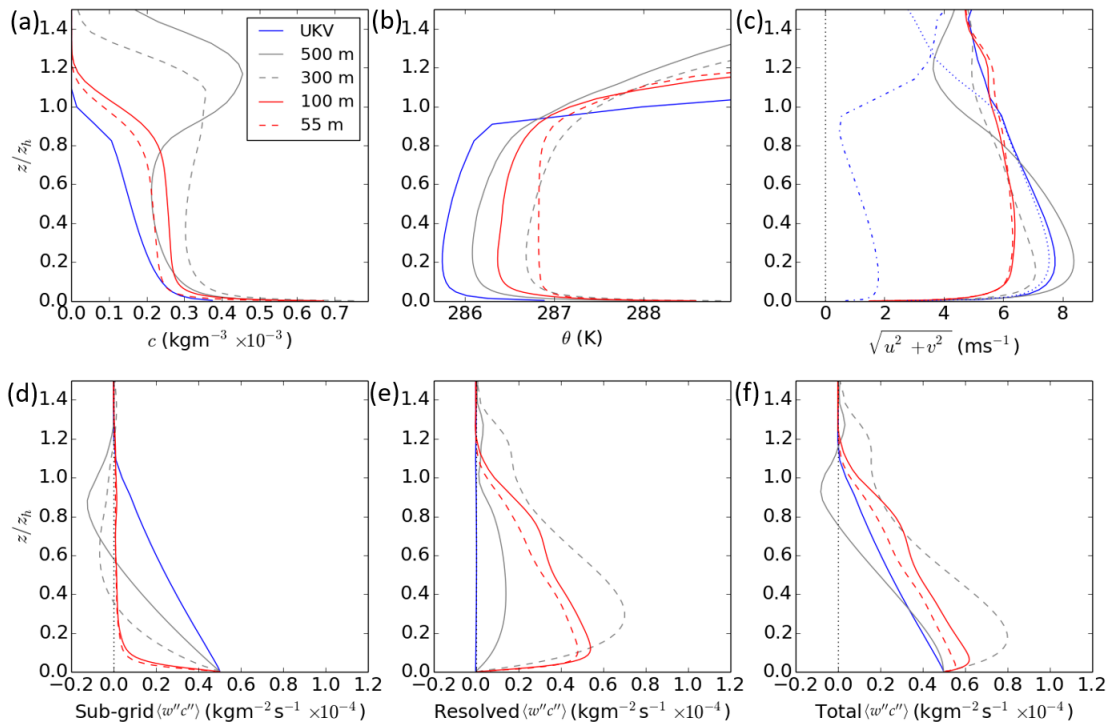
Figure 3.7: Horizontally averaged profiles within the analysis region at 13:00 UTC. (a) Concentration of the continuous release tracer, (b) θ and (c) wind speed. The blue dash-dotted and dotted lines in (c) are the UKV model u and v velocity components respectively. (d), (e) and (f) are the sub-grid, resolved and total tracer vertical turbulent fluxes respectively.

double-prime) from the horizontal average (denoted by $\langle \rangle$), are treated as equivalent to time fluctuations from the time average. It can be seen that the UKV model resolved flux is negligible and that the total flux is solely due to the parametrised flux. According to Fig. 3.6, the UKV model W_{1D} is approximately 0.15 at 13:00 UTC, so it was expected that 15% of the vertical mixing would be resolved. The parametrised flux behaves as expected, since it decreases approximately linearly with height from Q at the surface. The reason it falls to zero at $z/z_h \approx 1.1$ rather than $z/z_h \approx 1.0$ is that the profiles are scaled by the analysis region average z_h, and there is some smooth variation of z_h within the analysis region.

The 500 m and 300 m model total vertical turbulent flux profiles in Figs. 3.7d-f do not become negligible until $z/z_h \approx 1.4$. This is consistent with the 500 m and 300 m models having large c above z_h. They have the least linear total flux profiles out of all models. The sub-grid fluxes become negative below z_h. According to Eq. 3.3, the sub-grid flux is negatively proportional to the vertical c derivative. The concentration gradient is positive near z_h consistent with the sub-grid flux being negative. This is analogous to heat flux profiles where there is larger θ above the capping inversion and therefore negative heat flux at $z/z_h \approx 1$. Given that the sub-grid fluxes behave as expected, but the total does not, this is evidence that there are issues with the resolved CBL turbulence at $\Delta_{xy} =$300–500 m in the UM.

The 500 m and 300 m models should resolve approximately 35% and 60% of the vertical mixing respectively in the ML according to W_{1D} in Fig. 3.6. It can be seen that a much larger proportion of the vertical mixing is being resolved than expected by the 300 m model in Figs. 3.7d-f. The 500 m model on average throughout the ML resolves $\sim 35\%$ as expected. However, the ratio of sub-grid to resolved flux varies greatly with height within the ML for the 500 m and 300 m models. This demonstrates that W_{1D} is not adequately representing the partitioning of tracer vertical mixing between resolved and sub-grid.

Inspection of the 500 m model fluxes at hours between 11:00–15:00 UTC (other than 13:00 UTC) reveals that they in general resemble the 300 m model. Too much resolved vertical flux of tracer is observed in the 500 m and 300 m models. This is likely at least in part due to tracer non-conservation issues (as discussed further in Sect. 3.4). The decrease in wind speed near z_h for the 500 m model at 13:00 UTC is particular to that time, indicating the dynamics of the 500 m model were different then.

As seen in Fig. 3.7f, the total flux for the 100 m and 55 m models decreases to zero at $z/z_h \approx 1.2$ rather than $z/z_h \approx 1.0$, and is due to heterogeneity in z_h associated with thermals. The 55 m model has the closest profile to a linear decrease of all models (apart from the UKV model). It deviates most near the surface, where the flux becomes larger than $Q(= 5 \times 10^{-5} \text{ kgm}^{-2}\text{s}^{-1})$. The total flux remains larger for the 100 m and 55 m models compared to the UKV model within the ML. According to W_{1D}, within the ML the 100 m and 55 m models should resolve approximately 95% and 100% of the vertical mixing respectively. Approximately 100% was resolved in both models. The overestimation of total flux was therefore due to the resolved fluxes.

Near the surface a large proportion of the vertical mixing is sub-grid compared to resolved in all models. This is expected since the turbulence is much smaller scale there, and the concentration and gradients of horizontal velocity are very large, meaning that the local term in Eq. 3.3 is also.

The partitioning of resolved and sub-grid vertical mixing does not always behave as expected for several possible reasons (or any combination thereof): 1) there are issues with the resolved turbulence, 2) the dimensionless scaling variable Δ_{xy}/z_h is not an adequate representation of the amount of turbulence that is resolved throughout the entire depth of the BL so that W_{1D} should also become a function of height, 3) the W_{1D} function is not representative of the partitioning of resolved and sub-grid TKE in the UM since it has a different advection scheme to that used in Honnert et al. (2011) and 4) TKE partitioning is not representative of tracer flux partitioning. A full investigation of each of these possible issues is not in scope here, but further discussion of 1) and 2) is presented in Sect. 3.4.

3.3.3.3 Simulated Vertical Tracer Flux and Meteorology at 08:00 UTC

Figures 3.8a-c show horizontally averaged profiles of continuous release tracer concentration, θ and wind speed respectively within the analysis region at 08:00 UTC. This is a period of slow BL growth just before the period of rapid growth (see Fig. 3.6a). As seen from the θ profiles the BL is convective, although the unstable region is only ~ 100 m deep at this time. The wind speed is much smaller than in the afternoon, but like at 13:00 UTC, the flow is predominantly meridional.
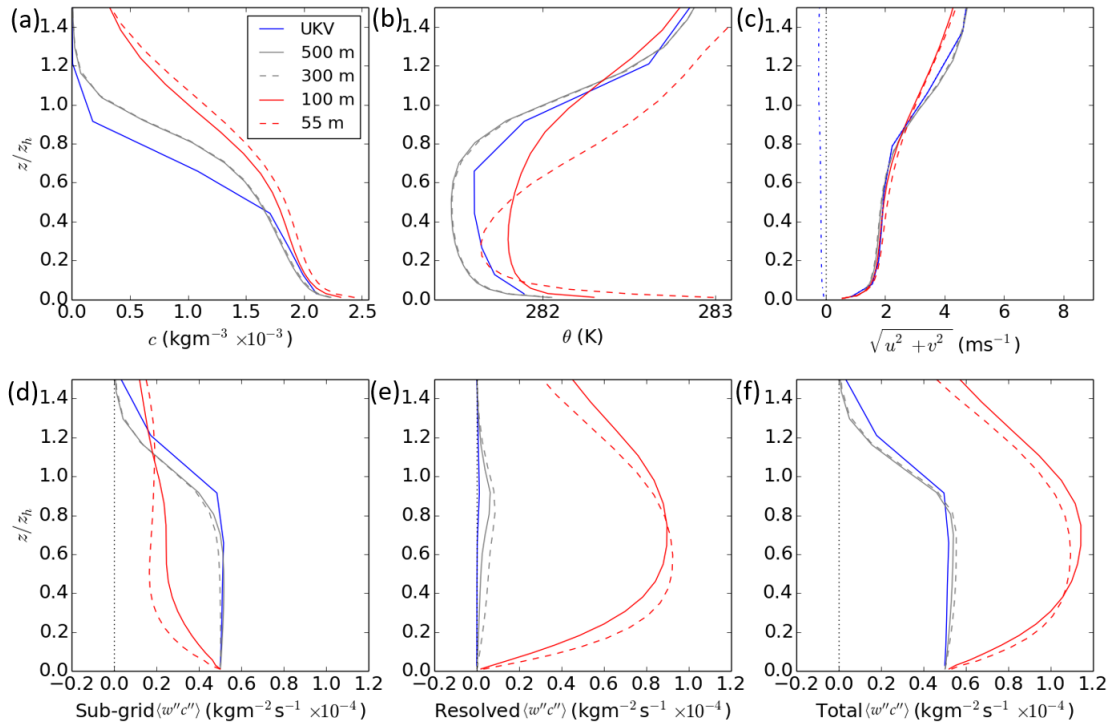
Figure 3.8: As in Fig. 3.7 except at 08:00 UTC.

The 100 m and 55 m models have larger c than the other models, and have large c above z_h. This is likely due to non-conservation issues and grid scale turbulence as discussed in Sect. 3.4.2. The UKV, 500 m and 300 m models have similar shaped c profiles since the majority of the vertical mixing is parametrised as seen in Figs. 3.8d-f. The c decrease starts slightly higher up in the atmosphere for the 500 m and 300 m models than the UKV model because they resolve some vertical tracer transport near z_h. The total fluxes for all models tend to be convex during BL growth (08:00–11:00 UTC), as opposed to linear in the afternoon when the BL is in an approximately steady state.

3.3.3.4 Simulated Vertical Tracer Flux and Meteorology at 21:00 UTC

Figures 3.9a-c show horizontally averaged profiles of continuous release tracer concentration, θ and wind speed respectively within the analysis region at 21:00 UTC. This is

at the very end of BL collapse (see Fig. 3.6a), and as seen from the θ profiles the BL is stable. The wind speed is reduced compared to the afternoon, but as at 08:00 UTC and 13:00 UTC, the flow is predominantly meridional.
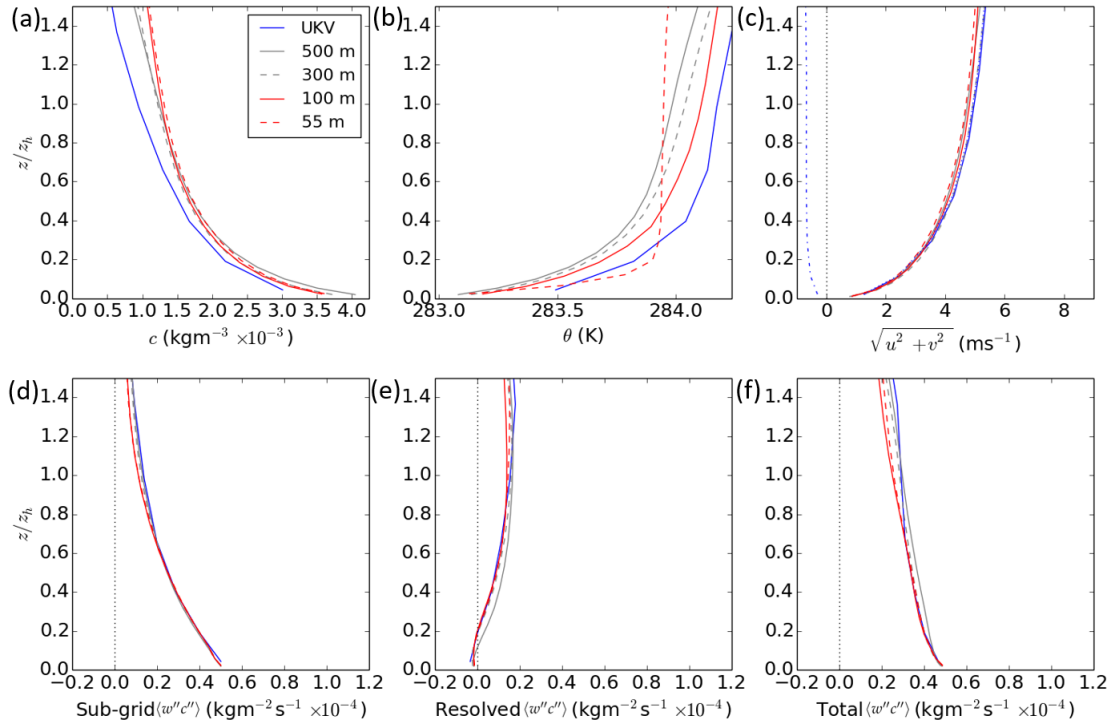
Figure 3.9: As in Fig. 3.7 except at 21:00 UTC.

The profiles generally collapse because vertical turbulent mixing is parametrised in all models. The resolved flux is significant for all models in Fig. 3.9e, which at first seems contrary to the previous statement. However, there was a region of strong horizontal flow convergence within the analysis region at this time, which resulted in large scale non-turbulent resolved vertical transport. The UKV model total flux tended to be concave during BL collapse (16:00-21:00 UTC). The other models however had more variable shaped profiles. This is because of the partially resolved turbulence issue varying across the models when Δ_{xy}/z_h increases during BL collapse and the concentration field being influnced by the non-conservation issues earlier in the day.

3.4   CBL Turbulence and Tracer Conservation in the UM

In the previous section it was found that the total tracer vertical flux profiles were not linear as expected at 13:00 UTC in all models except the UKV model. The 500 m and 300 m models had much more resolved flux than expected, and had negative sub-grid fluxes in a significant proportion of the upper BL. The 100 m and 55 m model total fluxes were closer to linear than the 500 m and 300 m models, particularly above $z/z_h \approx 0.1$.

However, they still tended to have larger resolved and total flux than expected. The 100 m and 55 m models also unexpectedly had large amounts of tracer above z_h at 08:00 UTC, like the 500 m and 300 m models at 13:00 UTC.

In this section the three-dimensional structure of the CBL turbulence is investigated in the 500–55 m models to understand the cause of the unexpected concentration and total flux profiles. The amount of tracer that is produced by non-conservation issues is then quantified by doing a tracer mass budget.

3.4.1 Convective Structures in the 500 m and 300 m Models

Plotted in Fig. 3.10a-c are 300 m model horizontal cross-sections of w, θ and c respectively at $z = 300$ m ($z/z_h \approx 0.2$), 13:00 UTC. Consistent with the results of Lock et al. (2017), spurious structures aligned with the grid in the direction of mean horizontal flow are present in the θ and w fields. In the analysis region the average value of $-z_h/L_{MO}$ is 20 for the 300 m model. The structure of the turbulence should therefore be predominantly open cellular (as discussed in Sect. 1.2.3). The convective structures may be expected to align with the direction of flow to a certain extent but not into the individual linear structures seen in Fig. 3.10. The updrafts should be less sporadic and form polygonal spoke patterns. The w and θ updraft values are generally larger in the 500/300 m models compared to the 100/55 m models where turbulence is better resolved, which is also consistent with Lock et al. (2017).

The tracer concentration in Fig. 3.10c has similar structure to w and θ, with elevated values in updrafts. Downdrafts force air at the surface away from the centre of the down-drafts due to mass continuity. The air converges into lines forming updrafts. Since the air diverging along the surface has large c (as it is in close vicinity to the surface source), it also tends to be large as it ascends in the updrafts.

Figure 3.11 shows a vertical cross-section of c from the 300 m model at 13:00 UTC. The location is given by the solid black line in Fig. 3.10c. c is visibly correlated with w contours. The width of the large tracer regions are one grid point, demonstrating that the updrafts are under resolved structures that have collapsed onto the grid. c is large in grid point updrafts often throughout the entire depth of the BL, with little diffusion into nearby grid cells. This is consistent with the infinite fountain explanation presented by Lock et al. (2017) for grid point updrafts forming linear structures and their associated tracer non-conservation issues (as discussed in Appendix B). Interpolation of horizontal velocity onto the tracer departure grid point from grid points either side results in un-derestimation of convergence, and therefore underestimation of tracer dilution within the plume. The same argument also applies for w and θ.

Structures tend to become well resolved by numerical schemes at $l_f/\Delta_{xy} \approx 5 - 10$ (Beare, 2014). The width of the largest updrafts in CBLs are typically O(0.1-1 km)
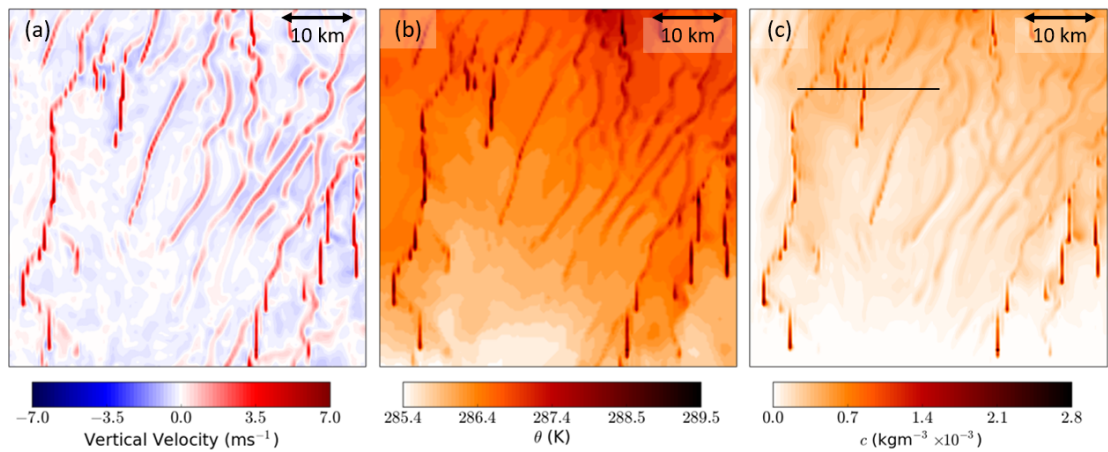
Figure 3.10: 300 m model horizontal cross-sections of (a) w, (b) θ and (c) continuous release tracer at $z = 300$ m, 13:00 UTC. The region plotted corresponds to the 50 km × 50 km continuous release source area. The solid black line in (c) corresponds to the vertical cross-section region plotted in Fig. 3.11.

(Schmidt and Schumann, 1989; Garratt, 1994; Salesky et al., 2017). Therefore at $\Delta_{xy} = 300$ m even the largest updrafts are severely under resolved. The detailed structure of the updrafts and downdrafts at $\Delta_{xy} = 300$ m should not be expected to resemble those observed in LES and laboratory studies. There are two trains of thought in the literature – one that such turbulence should be damped in the model (e.g. in the context of the UM by weighting the blending scheme more towards the 1D BL scheme than 3D Smag) and another that poorly resolved structures are permissible as they are required for initiation of the larger scale turbulence (Honnert et al., 2020). In the latter it is of course assumed that the advection scheme does not have non-conservation issues compounding inaccuracy in the poorly resolved structures.

The 500 m and 300 m model BL scheme diagnosed z_h at 13:00 UTC is plotted in Fig. 3.12a and b respectively. The same spurious linear structures can be seen in the 500 m and 300m model z_h as in the 300 m model prognostically predicted w, θ and c (see Fig. 3.10). Updrafts that remain strong throughout the BL penetrate far above z_h in adjacent grid cells and result in large dispersion of tracer into the troposphere. z_h is large at updraft grid points because θ remains well-mixed to a greater height than at adjacent grid points. Large z_h results in smaller W_{1D}, more explicitly resolved turbulence and reinforcement of the poorly resolved turbulence issues. The strongest updraft in the middle of Fig. 3.11 has $z_h \approx 2$ km. Compared to the average $z_h \approx 1.4$ km this corresponds to a reduction of W_{1D} from 0.4 to 0.24, so that 76% of the vertical mixing is treated as resolved by the model rather than 60%.

In Fig. 3.12a and b, at grid points adjacent to the linear structures z_h tends to be reduced, particularly near the southern boundary of the 100/55 m model domain (marked by a dashed black line). z_h averaged zonally across the southern boundary of the 100/55 m model domain is approximately 700 m and 600 m for the 500 m and 300 m models
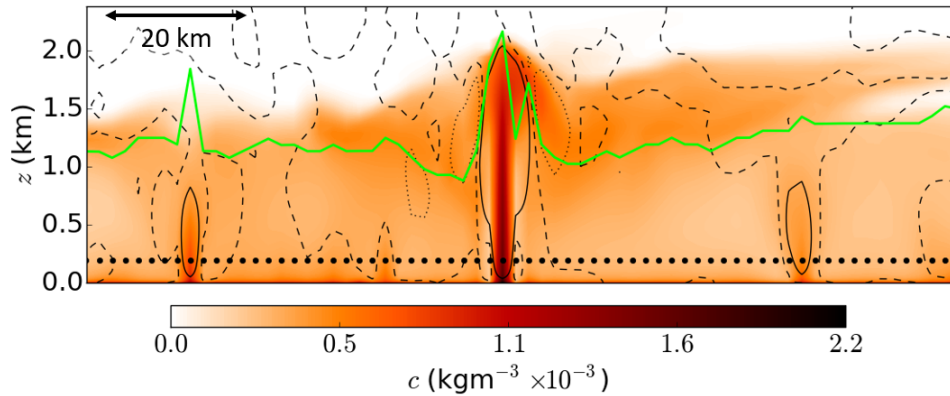
Figure 3.11: 300 m model vertical cross-section of c at 13:00 UTC with location indicated by the solid black line in Fig. 3.10c. Solid black lines, dashed black lines and dotted black lines are -1, 0 and 1 ms^{-1} vertical velocity contours respectively. Large black dots indicate the horizontal locations of grid points and the solid green line is BL scheme diagnosed z_h.

respectively. Compared to the UKV model z_h averaged over the same region, z_h in the 500 m and 300 m models is 42% and 50% smaller respectively. This is why z_h is small at the inflow edge of the 100 m and 55 m model domains, as seen previously in Fig. 3.5. As regional NWP moves to $\Delta_{xy} = 0.1 - 1$ km, so will the use of $\Delta_{xy} = 0.1 - 1$ km meteorological fields to drive offline AQMs. z_h is a crucial parameter in offline AQMs so it is important that it is predicted accurately.

3.4.2 Convective Structures in the 100 m and 55 m Models

3.4.2.1 08:00 UTC

Plotted in Figs. 3.13a and b are horizontal cross-sections of c at 08:00 UTC, $z = 100$ m from the 100 m and 55 m models respectively. The BL is at the start of the morning transition at this time and $z_h \approx 200$ m. $-z_h/L_{MO}$ averaged within the continuous source region is equal to 16 for both the 100 m and 55 m models. The convective structure is therefore expected to be transitioning between horizontal roll and open cell type structure, so that open cells are elongated in the mean flow direction. It is being assumed here that the transition between roll and open cellular structures with $-z_h/L_{MO}$ is similar during BL growth to in a fully developed BL. To the author's knowledge this has not been verified in the literature.

In Figs. 3.13a and b, c is generally fairly smooth on the scale of 1 km. There are some large values which are typically less than 1 km in scale and tend to align with the mean flow. The structures are not like horizontal rolls or open cells. They resemble the spurious structures observed at 13:00 UTC in the 500 m and 300 m models, but an order of magnitude smaller in scale. It is perhaps not surprising that the spurious structures should occur during the morning transition for the 100 m and 55 m models,
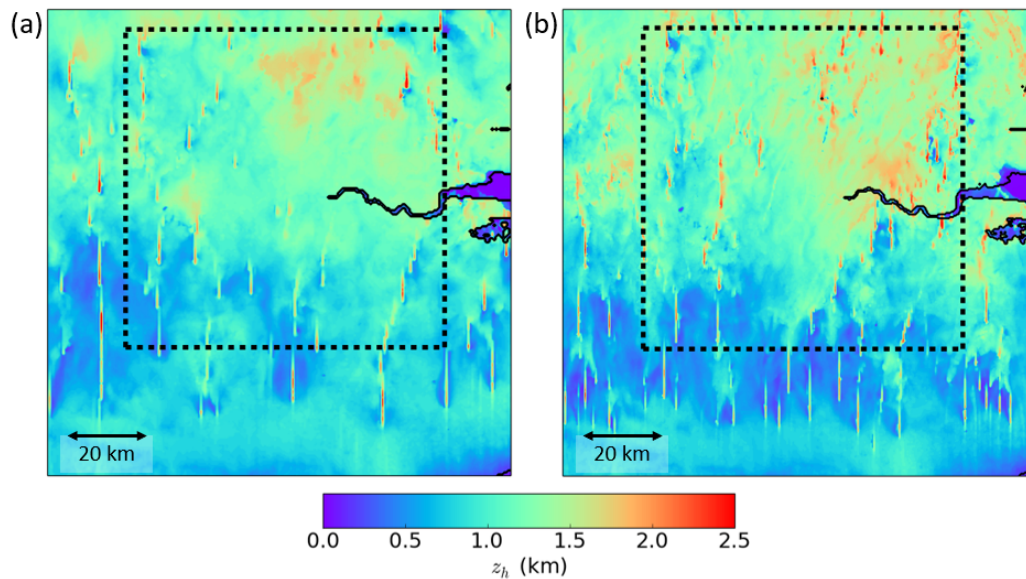
Figure 3.12: Horizontal cross-section of BL scheme diagnosed z_h at 13:00 UTC from (a) the 500 m model and (b) the 300 m model. The region highlighted by a black dashed line is the 100/55 m model domain boundary. The solid black line indicates the UM land/water mask, which here corresponds to the divide between land, and the river Thames and the east coast of England.

when one considers that the scale of the BL eddies and grid length have both decreased proportionally compared to the 500 m and 300 m models at 13:00 UTC. To the author's knowledge this is the first time the SISL advection scheme non-conservation issues have been documented at $\Delta_{xy} = 100/55$ m during the morning transition.

Figures 3.13c and d are vertical cross-sections of c at 08:00 UTC from the 100 m and 55 m models respectively. Vertical velocity contours are also plotted, and it can be seen that updraft vertical velocity and c have grid scale features in the 100 m and 55 m models. Diagnosed z_h at updraft grid points is much larger than the average value, even more so than with the 500 m and 300 m models at 13:00 UTC. This is why in Fig. 3.8a, the 100 m and 55 m models had larger tracer concentration, particularly above horizontal average z_h, compared to the other models.

3.4.2.2   13:00 UTC

The 100 m and 55 m models at 13:00 UTC have $-z_h/L_{MO}$ values of 28 and 30 respectively when averaged within the analysis region. The convective structure should therefore resemble open cells, elongated in the streamwise direction. Plotted in Fig. 3.14c and f are horizontal cross-sections of c at 13:00 UTC, $z = 140$ m ($z/z_h \approx 0.1$) from the 100 m and 55 m models respectively. The convective structure is open cell in both models, with narrow updrafts surrounding broader downdrafts. Visually one can see that there is more fine detail in the 55 m model convective structure than the 100 m model which is expected since it is higher resolution. The same convective structure conclusions can
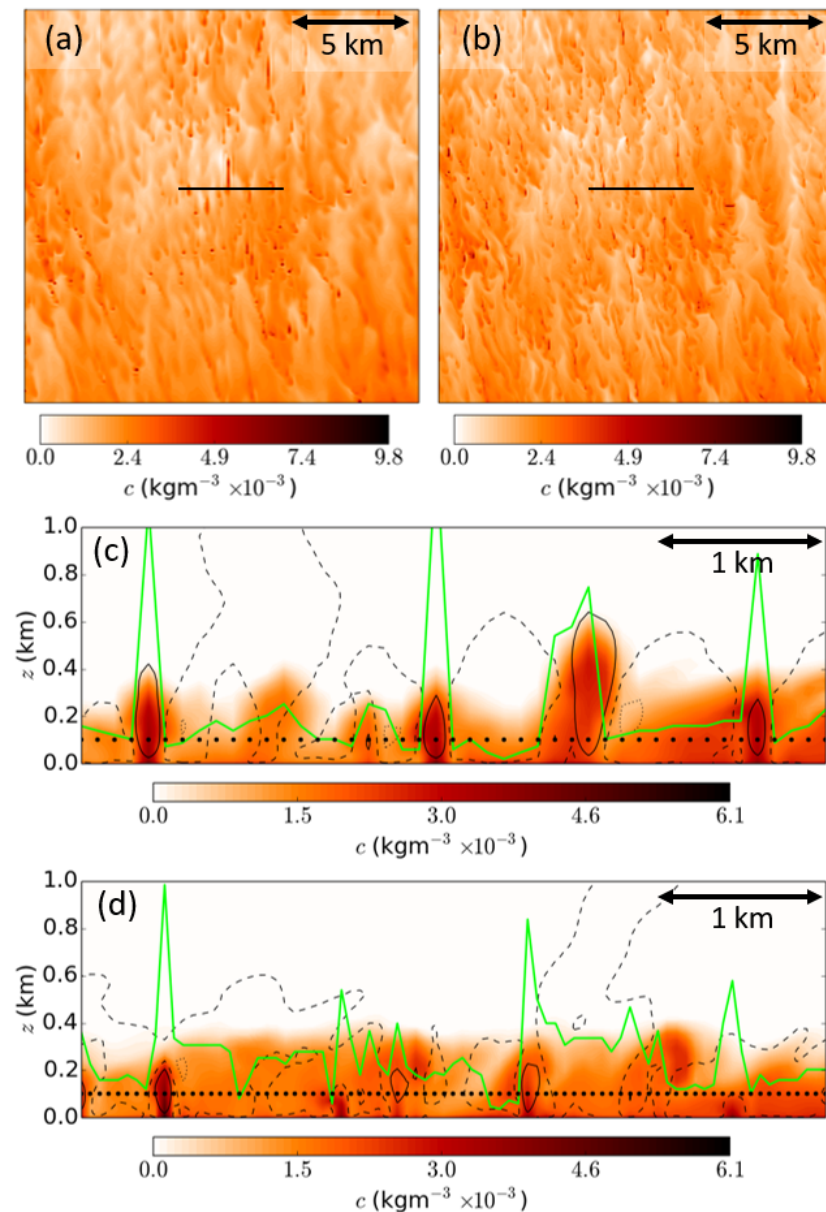
Figure 3.13: (a) 100 m and (b) 55 m model horizontal cross-sections of c at 08:00 UTC, $z = 100$ m. The region is centred on the 50 km $\times$ 50 km continuous source area. (c) and (d) are vertical cross-sections of c at 08:00 UTC from the 100 m and 55 m models respectively, the locations being indicated by the solid black lines in (a) and (b). In (c) and (d) solid black lines, dashed black lines and dotted black lines are -1, 0 and 1 ms^{-1} vertical velocity contours respectively. Large black dots indicate the horizontal locations of tracer grid points and the solid green line is BL scheme diagnosed z_h.

be drawn from the w and θ plots in Figs. 3.14a,b,d,e. Whether the dominant turbulent length scale is the same in the 100 m and 55 m models is explored in Sect. 3.5.

Figure 3.14g shows a 55 m model vertical velocity horizontal cross-section at $z = 700$ m ($z/z_h \approx 0.5$). The vertical velocity structure is broader and updrafts/downdrafts are stronger at $z/z_h \approx 0.5$ than $z/z_h \approx 0.1$. Also, the open cell structure has become less
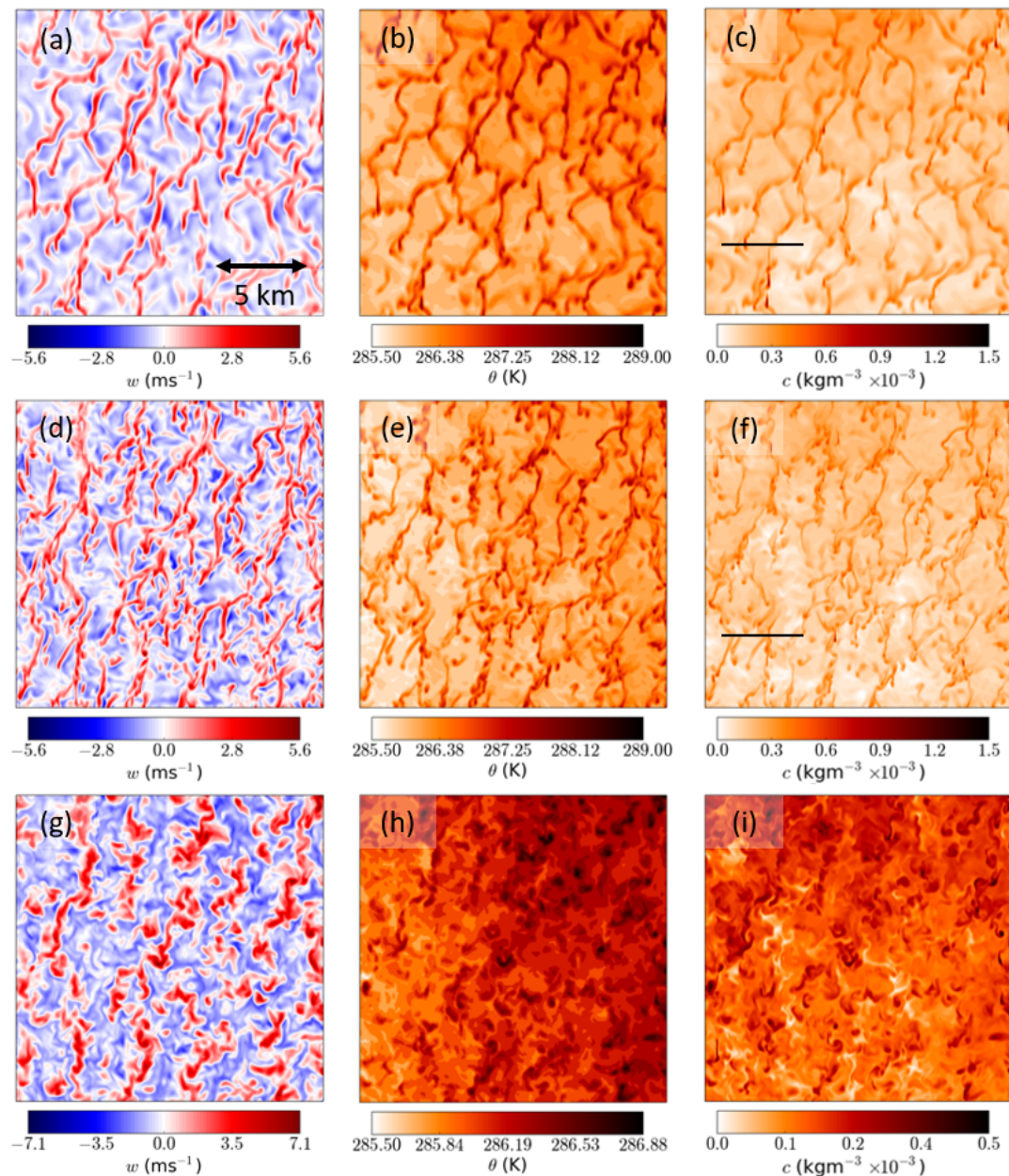
Figure 3.14: Horizontal cross-sections at 13:00 UTC. (a-c) are the 100 m model w, θ and c respectively at $z = 140$ m ($z/z_h \approx 0.1$). (d-f) are the 55 m model w, θ and c respectively at $z = 140$ m ($z/z_h \approx 0.1$). (g-i) are the 55 m model w, θ and c respectively at $z = 700$ m ($z/z_h \approx 0.5$). The cross-sections are centred on the analysis region. The horizontal black lines in (c) and (f) correspond to the locations of the vertical cross-sections in Figs. 3.15a and b respectively.

clear, with updrafts becoming disconnected from their neighbours. This is consistent with LES studies (Deardorff, 1972b; Mason, 1989; Schmidt and Schumann, 1989; Salesky et al., 2017) and the laboratory work of (Willis and Deardorff, 1979), who found that open cells with spoke like patterns are only found in the lower half of the BL. The weaker updrafts tend to merge with stronger ones with increasing height, forming individual large plumes that often span the entire depth of the BL.

It can be seen that w and θ fields in Figs. 3.14d and e respectively have very similar patterns to c in Fig. 3.14f. Plotted in Fig. 3.14h and i are 55 m model θ and c horizontal cross-sections respectively at $z/z_h \approx 0.5$. They are visually very similar, but smoother than w at the same height, consistent with Schmidt and Schumann (1989).

Figures 3.15a and b show vertical cross-sections of c at 13:00 UTC from the 100 m and 55 m models respectively. Large plumes can be seen in the middle of both cross-sections with classical Y-shaped branching, which occurs due to the capping inversion forcing air to spread horizontally, and subsequent overturning of the BL scale eddy. Near the surface however, there is evidence of grid scale updrafts. They penetrate up to $\approx$ 400 m in the 100 m model and $\approx$ 200 m in the 55 m model. They can be identified as small linear streaks, most obviously in the 100 m model horizontal cross-section (Fig. 3.14c) and less obviously in the 55 m model horizontal cross-section (Fig. 3.14f). This occurred throughout the 100 m and 55 m domains between 11:00–15:00 UTC.

Updrafts are smaller scale near the surface than the large plumes that extend the depth of the BL. For example it is well known that there can be updrafts beneath large downdrafts which decay quickly above the surface, that small scale updrafts merge near the surface into larger plumes, and that the base of large plumes are narrow before they broaden with distance from the surface (Schmidt and Schumann, 1989; Garratt, 1994). The formation of convective structures near the surface is poorly resolved in the 100 m and 55 m models (as seen in Fig. 3.15). Despite this a large proportion of the vertical tracer flux in Fig. 3.7e is resolved for the 100 m and 55 m models at $z/z_h \approx 0.05$. The grid scale structures at the base of large updrafts are reminiscent of those observed at 08:00 UTC and 13:00 UTC for the 100/55 m models and 500/300 m models respectively. They are therefore likely associated with non-conservation issues and the cause of the increase in total tracer flux near the surface in the 100 m and 55 m models at 13:00 UTC (see Fig. 3.7f). Non-conservation issues just above the surface act as a tracer source, giving rise to fluxes larger than Q.

Honnert et al. (2011) suggested that the partitioning of TKE between resolved and sub-grid should scale with Δ_{xy}/z_h in the BL. She showed that the scaling was much poorer for $0.05 < z/z_h < 0.2$. There is another grey zone of CBL turbulence near the surface. By using the dimensionless scaling parameter Δ_{xy}/z_h throughout the BL, it is effectively assuming that z_h is the relevant turbulent length scale throughout the BL. However, for $z/z_h < 0.1$, z is the relevant turbulent length scale (Garratt, 1994). It is suggested therefore that a new dimensionless parameter be defined Δ_{xy}/z_l, where z_l is given for example by

$$z_l = z \quad \text{for} \quad z/z_h \leq 0.1,$$
$$z_l = 9z - 0.8z_h \quad \text{for} \quad z/z_h \leq 0.2, \tag{3.9}$$
$$z_l = z_h \quad \text{for} \quad 0.2 < z/z_h < 1.$$

The equation is plotted in Fig. 3.16 and seems a reasonable first guess without doing
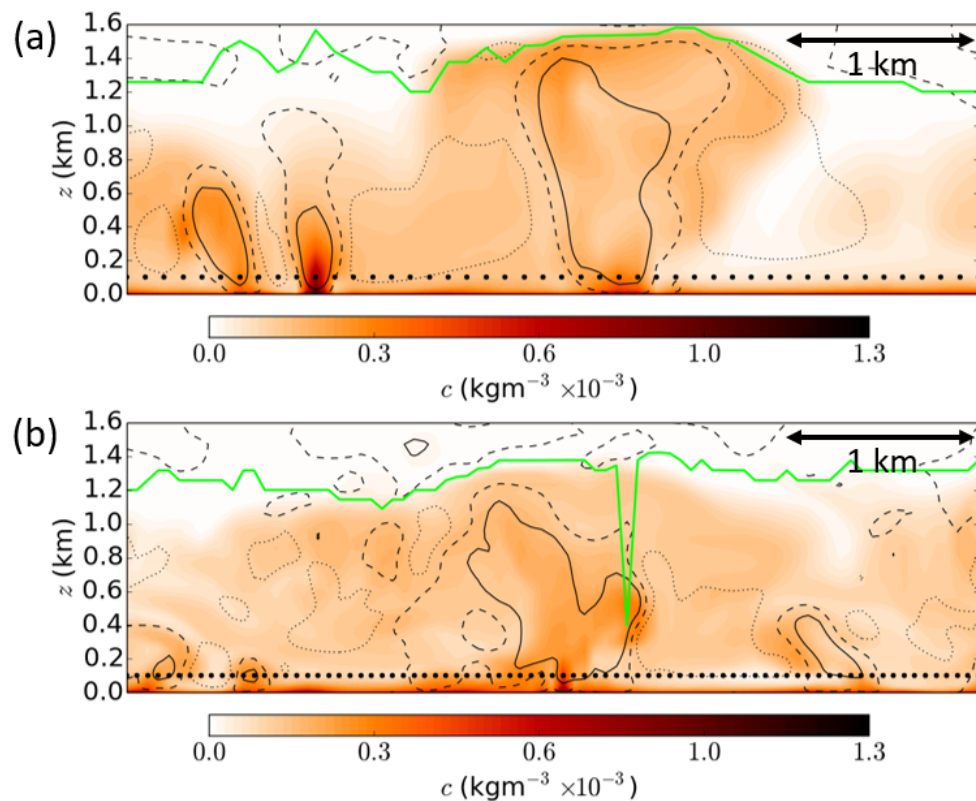
Figure 3.15: (a) 100 m and (b) 55 m model vertical cross-sections of c at 13:00 UTC, the locations being indicated by the solid black lines in Fig. 3.14c and f. Solid black lines, dashed black lines and dotted black lines are -1, 0 and 1 ms^{-1} vertical velocity contours respectively. Large black dots indicate the horizontal locations of grid points and the solid green line is BL scheme diagnosed z_h.

more detailed investigation. It results in Δ_{xy}/z_h scaling in the ML, Δ_{xy}/z scaling in the surface layer, and fast transition between the two. This alternative scaling parameter could easily be tested within the UM. It is likely to ameliorate the SISL advection non-conservation issues associated with poorly resolved updrafts near the surface. Vertical mixing in the surface layer would predominantly use the 1D BL scheme mixing length, which is larger than the 3D Smagorinsky mixing length. This would result in increased sub-grid mixing and dampen grid scale resolved motions. One possible drawback of such an approach is that it could influence convection initiation in the ML, if smaller updrafts and heterogeneity of the flow near the surface are reduced.

3.4.3 Tracer Conservation Tests

It was demonstrated in the previous sections that grid scale, unphysical linear structures were observed in the 500–55 m models. They resemble those observed by Lock et al. (2017), suggesting that they are associated with SISL advection non-conservation issues. It was particularly unexpected that the 100 m and 55 m models had grid scale structures.
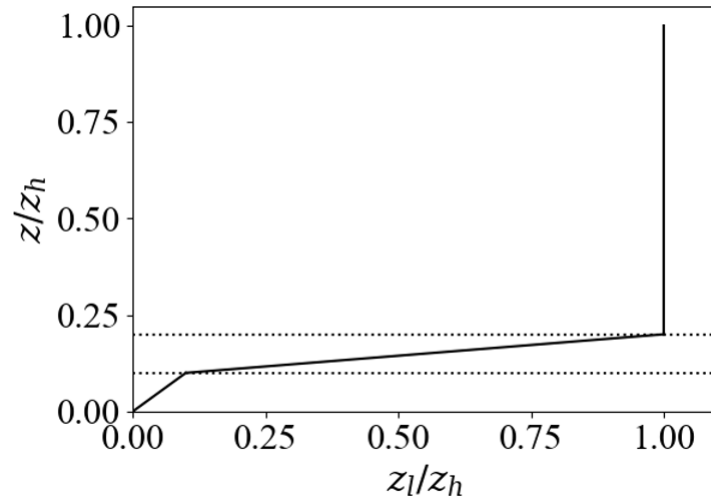
Figure 3.16: Proposed turbulent length scale z_l for use in Eq. 3.2.

The UK Met Office are considering carrying out AQ modelling at O(100 m) horizontal grid lengths, so it is important to quantify the extent to which tracer mass is produced due to non-conservation issues. A tracer mass budget is therefore carried out here.

For the continuous release tracer, if one integrates the continuity equation (Eq. 3.4) over a horizontal area A within the source region, integrates vertically from the surface to infinity, and assumes the divergence of velocity is zero, the result is

$$\int_A \int_0^\infty \frac{\partial c}{\partial t} dz dA = -\int_S c\mathbf{u}.\mathbf{n}dS + QA,$$ (3.10)

where S is the area of the x-z and y-z plane faces of the integrating volume and $\mathbf{n}$ is their outward-facing normal unit vector. Equation 3.10 can be interpreted as the statement that the rate of change of total tracer mass, $\partial m_c/\partial t$, within the integrating volume (the left-hand side term), is equal to the advection of tracer in and out of the volume (the first term on the right-hand side), and the surface emissions into the volume (the second term on the right-hand side). All three terms of Eq. 3.10 can be calculated using output from the UM models. If tracer is conserved within the models, the sum of the advection and source budgets on the right-hand side should equal $\partial m_c/\partial t$ on the left-hand side.

The analysis region is the same one used in the majority of this chapter – 40 km by 15 km in the streamwise and spanwise respectively, in the northern part of the continuous release source region (see Fig. 3.4). The 3D continuous release tracer field was output every 15 min from the UM. The total mass of tracer was calculated by discretising Eq. 3.10, so that

$$m_{c,i+1} = \left(\left(-\int_S c\mathbf{u}.\mathbf{n}dS \right)_i + QA \right) \Delta t + m_{c,i},$$ (3.11)

where i is the ith timestep and $\Delta t = 15$ min. The integration was performed from 06:00 UTC, the start of the continuous source tracer emissions, so that $m_{c,0} = 0$ kg.

Before showing the results from the finite difference calculation, first plotted in Fig. 3.17a is the total mass of tracer within the analysis region for the different models. This was calculated simply by integrating c within the analysis region from the surface to $z \gg z_h$. Since the tracer emissions were the same for all models, differences in total mass should only be due to differences in advection velocity. It can be seen that the mass in the 500–55 m models is greater than in the UKV model, particularly at approximately 09:00 UTC for the 100 m and 55 m models, and between 11:00–19:00 UTC for the 500 m and 300 m models. The UKV model resolves very little BL turbulence, so it is least likely to suffer from non-conservation issues. That the other models have greater tracer mass is therefore indicative of them having non-conservation issues, particularly when one considers that times when the 500–55 m models have their largest m_c discrepancies with the UKV model, correspond to times at which grid scale structures were observed in Sects. 3.4.1 and 3.4.2. Also, after 20:00 UTC when the BL is stable, and the BL turbulence is parametrised in all models, m_c is very similar.

Figure 3.17b shows the UKV, 300 m and 55 m model m_c calculated by simply integrating c within the analysis volume (as in Fig. 3.17a) compared to m_c calculated by solving Eq. 3.11. For all models the finite difference predicted m_c is smaller than the volume integrated m_c. This is particularly the case for the 300 m and 55 m models, where the finite difference calculated m_c becomes negative. Both terms on the right-hand side of Eq. 3.11 are calculated exactly, and on the time scale of Δt the flow does not change significantly, so the finite difference calculation is a reasonable approximation. For $m_c < 0$ the outward flow integral (sink term) must be greater than QA (the source term). This implies there is a missing source term in Eq. 3.11 causing large c, so that that the sink term exceeds the source term. This missing source is the tracer being produced in grid scale updrafts.

An identical model run was performed but with the OCF mass-fixer conservation method switched on (see Appendix B for the details of OCF). OCF is currently only intended for tracers in global models since there is no treatment of tracer advected at the LAM domain boundaries. However, no tracer reaches the domain boundaries in the UKV model during the simulation because it is not advected as far as the domain boundaries by 22:00 UTC. OCF is expected to ensure tracer conservation for the UKV model, but not the other models where tracer does reach the domain boundaries. Figure 3.17c shows the UKV, 300 m and 55 m model m_c as in Fig. 3.17b, except with OCF switched on. For the UKV model there is good agreement between the finite difference calculated and volume integrated m_c. For the 300 m and 55 m models there is reasonable agreement until approximately 09:00 UTC and 11:00 UTC, when tracer starts to exit their domains. After this agreement becomes worse than with OCF switched off, since outflow is seen as a loss term by the OCF scheme. It compensates at the end of each time step by adding mass, which is why the volume integrated m_c is larger with OCF.

It is possible to estimate the size of the non-conservation issues if one takes the UKV
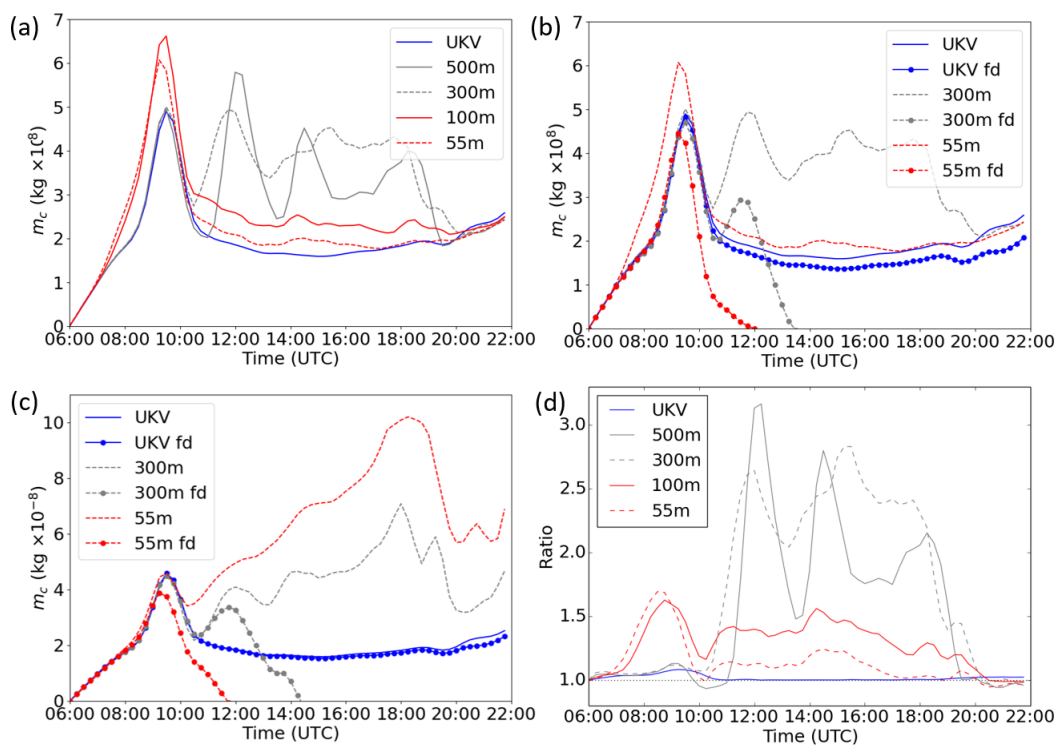
Figure 3.17: (a) Total tracer mass obtained by integrating c within the analysis volume. (b) Comparison for selected models of the total tracer mass obtained by integrating c within the analysis volume and using the finite difference (fd) approach. (c) As in (b) but for a model run with OCF. (d) Ratio of the curves in (a) to the curve of the UKV with OCF model in (c).

model with OCF volume integrated m_c as a robust estimate of the correct m_c. Without non-conservation issues the tracer mass in the analysis region is determined by a balance between tracer emissions and horizontal advection of tracer. The differences in velocities between models in Figs. 3.7-3.9 are negligible at 08:00 UTC and 21:00 UTC, and are typically 10% at 13:00 UTC. Without non-conservation issues, m_c differences between models of no more than 10% would be expected due to variation in velocity between models. Therefore, differences in m_c compared to the UKV model with OCF volume integrated m_c greater than 10% can be attributed to non-conservation issues.

Figure 3.17d shows the ratio of volume integrated m_c from all models without OCF to the UKV model with OCF. It can be seen the UKV model had at most 5% more tracer mass than it should, and in the afternoon non-conservation issues were negligible. Since this comparison only involves the UKV model, differences less than 10% can be attributed to non-conservation issues. In the morning the 500 m and 300 m models had approximately 5% more tracer mass than the UKV OCF model, which could have been due to differences in model dynamics rather than non-conservation issues. However, during the afternoon the 500 m and 300 m models had approximately 2.5 times more tracer mass than they should. The 100 m and 55 m models had largest tracer conservation issues during the morning transition, where they overestimated tracer mass by

approximately 50%. During the afternoon, the 100 m and 55 m models had 40% and 10% more tracer mass than the UKV OCF model, respectively. Therefore the 100 m model had considerable non-conservation issues in the afternoon. It is uncertain to what extent the 55 m model did, since at 13:00 UTC it had approximately 10% lower advection velocity than the UKV model. Given grid point updrafts were observed near the surface in the 55 m model, it is likely some of the 10% more tracer mass can be attributed to non-conservation issues.

By inspecting the times when the models have largest non-conservation issues in Fig. 3.17d and the corresponding z_h values in 3.6, it can be estimated that tracer non-conservation issues are greatest when $z_h/\Delta_{xy} \sim 4$.

Based on the evidence presented here, it is not suitable to run AQMs such as the AQUM at 55 m $< \Delta_{xy} <$ 1.5 km under convective conditions, without modifications that ameliorate SISL advection scheme tracer non-conservation issues. For example, if a pollutant in an AQM has its total mass overestimated by $10 - 20\%$, this approximately corresponds to c overestimation of $10 - 20\%$ in the BL. A mass-fixer type conservation scheme (for example OCF) with treatment of the LAM boundaries (using for example ZLF) would not be a workable solution, since in the afternoon and morning the 500/300 m and 100/55 m models respectively would still have grid scale updrafts and unrealistic spatial pollution distribution. Solutions should involve changing to an inherently conserving advection scheme or be based on OCF and ZLF with some modification to the SISL advection scheme that reduces the grid scale structures.

3.5 Horizontal Tracer Heterogeneity and Turbulence Convergence With Horizontal Grid Length

It is of interest to know how much tracer concentration varies horizontally within the BL due to convective structures. Updrafts originate near the surface in the superadiabatic layer (Garratt, 1994) and as found in previous sections they have the highest concentration of tracer. Variability of pollution concentration within the urban canopy is influenced by the turbulence structure and concentration above the canopy. It is well known that city scale buoyant flows occur and increase ventilation over urban areas (Fan et al., 2017), however the role of individual kilometre scale updrafts and downdrafts on canopy concentrations has not been investigated. Tracer concentration variability within the urban canopy cannot be studied here because buildings and turbulence near the surface cannot be resolved at O(100 m), but investigating tracer heterogeneity at the top of the surface layer is an important first step.

Investigation is limited to the afternoon and the 100 m and 55 m models. The continuous release passive tracer is used throughout. First, the 100 m and 55 m turbulence

statistics are compared, to establish how reliable results from the 55 m model are. The tracer, θ and w turbulence statistics are also compared. There are very few LES and laboratory turbulence studies that include a passive tracer, and to the author's best knowledge this is the first passive tracer study conducted using NWP at O(100 m) grid length. It is not known whether the same turbulence statistics observed in idealised LES and laboratory studies (e.g. Willis and Deardorff, 1974; Deardorff and Willis, 1985; Schmidt and Schumann, 1989; Salesky et al., 2017) are found in NWP at O(100 m) grid length.

3.5.1 Two-point Correlation Functions

The two-point correlation function of two variables χ_1 and χ_2 at height z is given by

$$R_{\chi_1\chi_2}(z,X) = \langle \chi_1''(z,x)\chi_2''(z,x') \rangle / \langle \chi_1''(z,x)\chi_2''(z,x) \rangle, \tag{3.12}$$

where $X \equiv x - x'$ is the separation between x and another point x' displaced along the x axis (east-west axis). Plotted in Fig. 3.18a is R_{ww} for the 100 m and 55 m models at 13:00 UTC, $z/z_h = 0.2$. $R_{\chi_1\chi_2}$ was calculated at each grid point along the y axis (north-south axis) within the analysis region and then averaged, and x was chosen to be at the centre of the analysis region. Also plotted is R_{ww} calculated with x replaced by y in Eq. 3.12. y was chosen at the centre of the analysis region and R_{ww} averaged over all grid points along the x axis within the analysis region. Herein, $R_{\chi_1\chi_2}$ calculated along the x and y axes will be referred to as $R_{\chi_1\chi_2}^x$ and $R_{\chi_1\chi_2}^y$ respectively.

In a CBL the largest eddies are typically O(z_h), contain the majority of the TKE and can therefore be expected to dominate R_{ww} for $X = $ O(z_h). The integral length scale (or Eulerian length scale) defined by $\int_0^\infty R_{ww} dX$ is often used as a measure of the dominant turbulent length scale in turbulent flows. However, the CBL scale eddies consist of alternating updrafts and downdrafts and introduce periodicity into R_{ww}. The integral length scale is therefore not always a good estimate of the dominant turbulent length scale, since positive and negative contributions to the integral partially cancel (Dosio et al., 2005).

From Fig. 3.18a it can be seen that R_{ww}^x for the 100 m and 55 m models equals one at $X/z_h = 0$, and with increasing X/z_h decays quickly, becomes negative at $X/z_h \approx 0.3$ and is approximately zero by $X/z_h = 1.5$. The fast initial decay with X/z_h occurs due to the updrafts becoming unaligned with themselves. The first zero-crossing can be used as an estimate of the typical updraft width and is equal to 0.337 ($\equiv$ 497 m) and 0.304 ($\equiv$ 437 m) for the 100 m and 55 m models, respectively. This seems consistent with visual inspection of Figs. 3.14a, d and g. R_{ww}^x decays slightly slower for the 100 m model than the 55 m model, since updrafts that should be narrower than $\approx$ 500 m are under resolved. Therefore, their width is slightly over predicted.

Between $X/z_h \approx 0.3 - 1.5$, R_{ww}^x is negative due to the updrafts aligning with the
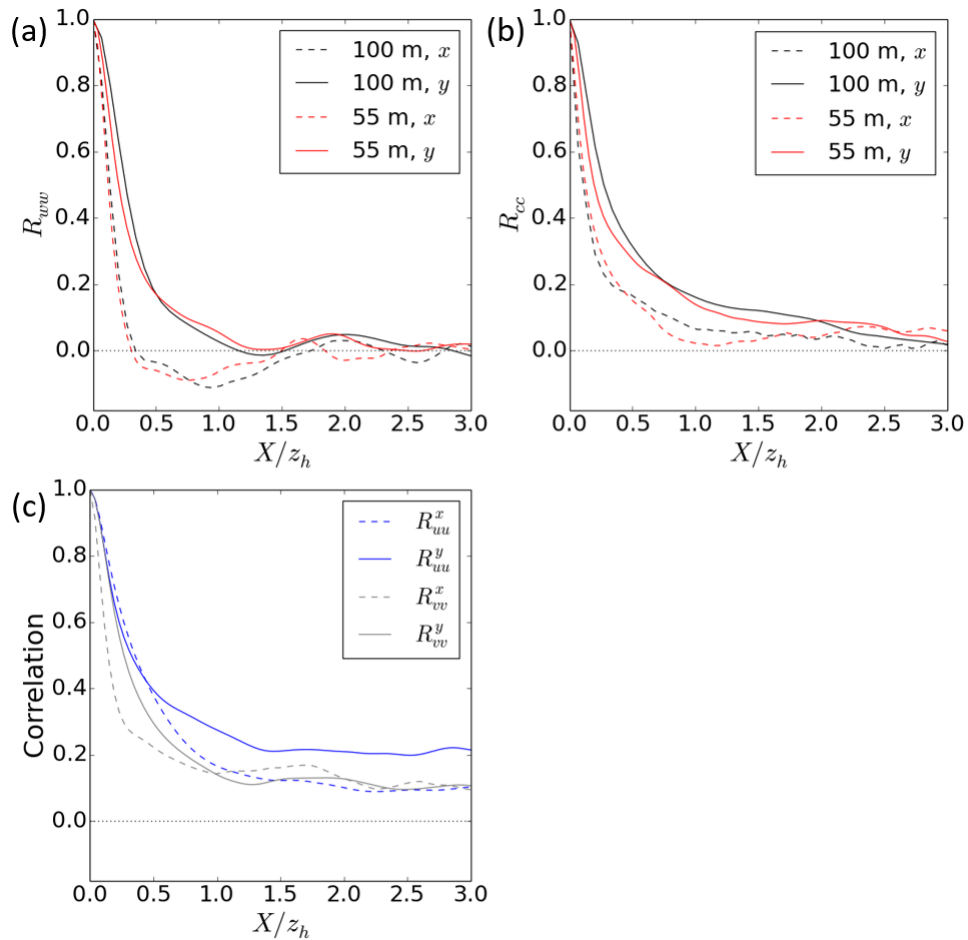
Figure 3.18: Two-point correlations plotted against X/z_h at 13:00 UTC, $z/z_h = 0.2$. (a) and (b) correspond to R_{ww} and R_{cc} respectively. The 100 m and 55 m models are plotted in black and red, respectively. (c) Two-point correlations are from the 55 m model, and blue and grey represent correlations involving u and v, respectively. In (a-c) dashed and solid lines represent two-point correlation functions along the x and y axes, respectively.

broader downdrafts. At $X/z_h = 1.6$ the 55 m model exhibits a small maximum that corresponds to the dominant updraft separation scale (or equivalently the dominant cross-stream width of the elongated open cells). The exact value should be treated with some caution because by $X/z_h = 1.6$, R_{ww}^x has decayed significantly and small statistical fluctuations owing to limited analysis region become more prevalent. However, the estimate seems visually consistent with Figs. 3.14a, d and g. At $X/z_h = 2.0$ the 100 m model exhibits a small maximum, which suggests that it predicts slightly larger open cell structures in the cross-stream direction than the 55 m model.

The 100 m and 55 m model R_{ww}^y decays much more slowly than R_{ww}^x in Fig. 3.18a. This is because the cross-stream structures are less frequent and coherent, as seen in Figs. 3.14a, d and g. When turbulent structure is an intermediate between open cell and horizontal rolls, turbulence is elongated and orientated preferentially in the streamwise. Meandering of the streamwise structures which occurs across a range of X/z_h has a large

contribution to R_{ww}^y.

Given the range of turbulent scales contributing significantly to R_{ww}^y it is difficult to estimate the size of the turbulent structures in the streamwise direction in a way that is consistent with R_{ww}^x. Since there is little oscillatory component to R_{ww}^y, its integral length scale becomes more meaningful and is 564 m and 498 m for the 100 m and 55 m models, respectively. The turbulence in the streamwise as well as the cross-stream has therefore not converged with decreasing Δ_{xy}.

The R_{ww}^x behaviour is similar to R_{ww} behaviour observed in the literature for free convection (Deardorff and Willis, 1985; Mason, 1989) and with $-z_h/L_{MO} = 40$ (Dosio et al., 2005), where turbulence is dominated by open cell turbulence that is very symmetric. The differences in R_{ww}^y and R_{ww}^x behaviour for turbulence that is intermediate between open cell and horizontal rolls, to the author's knowledge has not been described previously.

Literature suggests R_{uu} behaviour is similar to R_{ww}, but has zero crossing at distances $\approx 2-3$ times larger (Deardorff and Willis, 1985; Mason, 1989; Dosio et al., 2005). Deardorff and Willis (1985) found that $R_{\theta\theta}$ tends to behave more like R_{ww} for small X/z_h, but by $X/z_h \approx 0.2$ behaves more like R_{uu}.

In this study, $R_{\theta\theta}^x$ and $R_{\theta\theta}^y$ decayed very slowly from 1 and never reached 0, since there are θ variations on the scale of the analysis region, due to mesoscale dynamics and surface property variations. This occurs in NWP unlike idealised LES and laboratory studies.

Plotted in Fig. 3.18b are R_{cc}^x and R_{cc}^y from the 100 m and 55 m models. Consistent with $R_{\theta\theta}$ in Deardorff and Willis (1985), R_{cc} behaves similarly to R_{ww} for X/z_h less than approximately 0.2. At larger X/z_h, the 100 m and 55 m model R_{cc} does not decay as quickly compared to $R_{\theta\theta}$ in Deardorff and Willis (1985), is not negative near $X/z_h \approx 1$ and does not have a zero-crossing until $X/z_h \approx 5$ (off the axis). The reason that R_{cc}^x does not become negative until $X/z_h \approx 5$ is due to variations in the flow on the scale of the analysis region. In Fig. 3.4b it can be seen that flow was slightly faster in the west than the east of the analysis region, due to a mesoscale flow pattern throughout the domain. The 55 m model R_{cc}^x does exhibit a minimum at $X/z_h \approx 1$, but it is less pronounced compared to R_{ww}^x. R_{wc}^x (not shown) exhibited similar behaviour to R_{ww}^x, demonstrating a large influence from w on c. Since R_{cc}^x and R_{ww}^x do not behave the same, there must have been large influence from more variables than w on R_{cc}^x. Also, tracer has memory of the flow so some of its spatial distribution might be related to past w, resulting in R_{cc}^x having different shape compared to R_{ww}^x and R_{wc}^x which both involve correlation with current w.

Plotted in Fig. 3.18c are R_{uu}^x, R_{uu}^y, R_{vv}^x and R_{vv}^y for the 55 m model. They do not exhibit distinct minima, and like R_{cc}^x and R_{cc}^y they do not become negative. This suggests for R_{cc}^x and R_{cc}^y that when X/z_h is less than approximately 0.2, the relationship with w

is most important, and when X/z_h is greater than approximately 0.2, the relationships with u, v and w are important. The reason R_{uu}^x, R_{vv}^x and R_{cc}^x do not exhibit distinct minima as in Deardorff and Willis (1985) is not clear. It is possibly because of greater flow heterogeneity in NWP compared to their water tank experiment on horizontal scales of $O(1\text{-}10z_h)$, due to the changing roughness and sensible heat flux at the surface in NWP.

3.5.2 Variance Profiles

Figures 3.19a and b show variance profiles of w, and c and θ respectively, at 13:00 UTC from the 100 m and 55 m models. T_* is the convective temperature scale equal to $\langle \theta''w'' \rangle / w_*$. The maximum $\langle w''^2 \rangle$ is at $z/z_h = 0.45$ and $z/z_h = 0.39$ for the 100 m and 55 m models, respectively, in Fig. 3.19b. This is consistent with the vertical velocity cross-sections at $z/z_h \approx 0.5$ in Fig. 3.14 having large heterogeneity associated with very coherent structures.

Salesky et al. (2017) conducted a sensitivity study on horizontal and vertical grid length using LES in free convective conditions. They found that $\langle w''^2 \rangle$ maximum occurs at decreasing height with decreasing Δ_{xy}. The maximum occurred at $z/z_h \approx 0.3$ at $\Delta_{xy} \approx 50$ m. The reason their maximum occurred slightly lower than the 55 m model, is possibly because they had smaller vertical grid length of ≈ 7 m, whereas here at $z/z_h = 0.3$ the vertical grid length was ≈ 34 m. Maximum values of $\langle w''^2 \rangle / w_*^2 \approx 0.45$ observed are consistent with CBL simulations and experiments in the literature (Willis and Deardorff, 1974; Deardorff and Willis, 1985; Schmidt and Schumann, 1989; Salesky et al., 2017).

The c variance is scaled so that it is equal to $\langle T''^2 \rangle / T_*^2$ at the surface in Fig. 3.19b, to aid comparison between c and θ. $\langle c''^2 \rangle$ and $\langle \theta''^2 \rangle$ are minimum in the middle of the BL unlike $\langle w''^2 \rangle$. Scalars become more homogeneous with height because they diffuse whilst they are transported away from the surface in updrafts. $\langle c''^2 \rangle$ and $\langle \theta''^2 \rangle$ share similar shaped profiles in the surface layer and ML. $\langle \theta''^2 \rangle$ tends to be slightly larger nearer the surface. This is likely because the tracer ground source is homogeneous but Q_H is heterogeneous due to variations in urban surface land usage (for example Q_H tends to be smaller over parks).

$\langle c''^2 \rangle$ and $\langle \theta''^2 \rangle$ exhibit peaks at $z/z_h \approx 1.05$ and $z/z_h \approx 1.2$ respectively. The $\langle \theta''^2 \rangle / T_*^2$ maximum is approximately 80 for the 100 m and 55 m models (off the axis). The peak is because of thermals overshooting the horizontal average z_h. At $z/z_h \approx 1$ there are dome structures within the BL, with small c and θ. Adjacent air is tropospheric with very small c and large θ, so that there are large horizontal variations in c and particularly θ. Schmidt and Schumann (1989) saw similar $\langle \theta''^2 \rangle$ behaviour in their LES. The production term in their $\langle \theta''^2 \rangle$ budget equation was equal to the negative product of heat flux and temperature gradient, and they therefore argued that in the entrainment layer large $\langle \theta''^2 \rangle$ is caused by large heat flux and large temperature gradient. This argument
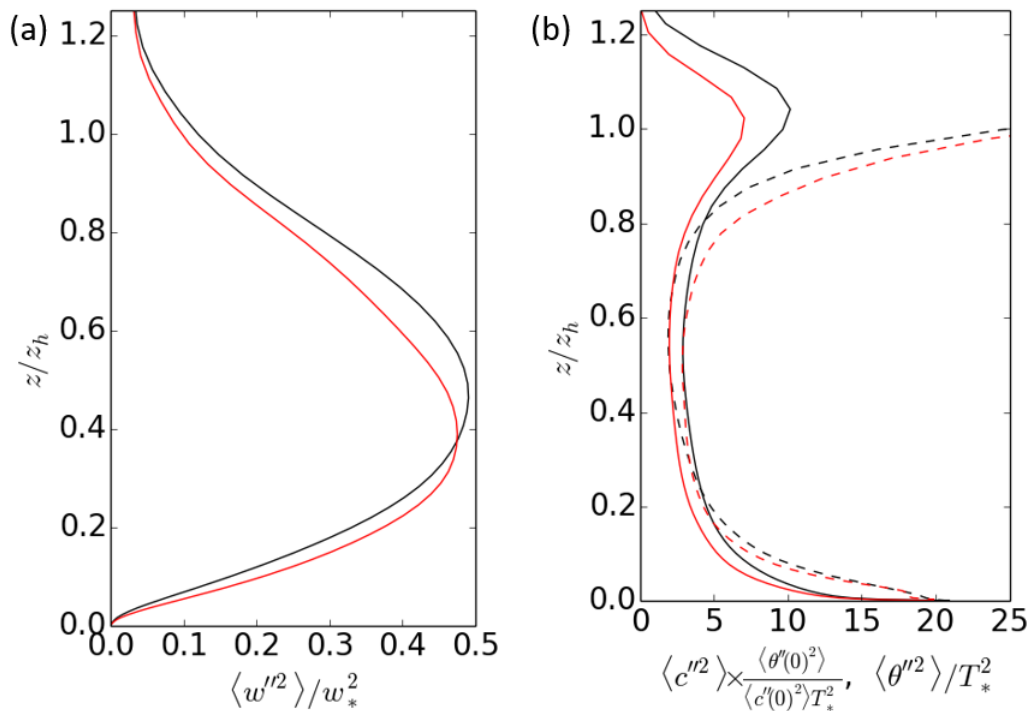
Figure 3.19: (a) Variance of vertical velocity and (b) variance of c and θ (solid and dashed respectively) at 13:00 UTC. Black and red are the 100 m and 55 m models respectively. The analysis region is the 15 km $\times$ 40 km region used in Sect. 3.3.

is consistent with the $\langle c''^2 \rangle$ peak being smaller than the $\langle \theta''^2 \rangle$ peak in the entrainment layer. An equivalent budget for $\langle c''^2 \rangle$ would have a production term that is equal to the negative product of tracer flux and concentration gradient. Tracer flux tends to zero at $z/z_h \sim 1$ unlike heat flux which is negative there, and consequently $\langle c''^2 \rangle$ is smaller. To the author's knowledge this is the first study to demonstrate this difference in θ and c variance behaviour.

The 100 m and 55 m model variances in Fig. 3.19b are within 50% of one another for both θ and c within the BL. When one takes the ratio of the 100 m and 55 m model $\langle c''^2 \rangle / \langle c \rangle^2$, the differences are less than 10% between $0.05 \geq z/z_h \leq 0.75$. This can be seen from the 100 m and 55 m model $\langle c''^2 \rangle^{1/2} / \langle c \rangle$ values at various heights presented in Table 3.2. Scaling by $\langle c \rangle^2$ removes the differences in the 100 m and 55 m model variance caused by the 100 m model having larger c due to tracer non-conservation issues. In Sect. 3.5.1, integral length scales and two-point correlation function first zero-crossing points were different between the 100 m and 55 m models by approximately 10%. A reasonable estimate of the uncertainty in the 55 m model second-order turbulence statistics is 10%. Lean et al. (2019) also found that turbulence statistics in the UM do not converge between 100 m and 55 m horizontal grid length.

3.5.3 Tracer Concentration Probability Distribution Functions

Figure 3.20 shows the tracer concentration probability distribution function, P_c, with normalisation

$$\int_0^\infty P_c dc = 1, \tag{3.13}$$

at several heights in the BL for the 100 m and 55 m models at 13:00 UTC. The mean, turbulent intensity ($\langle c''^2 \rangle^{1/2} / \langle c \rangle$) and skewness ($\langle c''^3 \rangle / \langle c''^2 \rangle^{3/2}$) corresponding to the distributions are given in Table 3.2.

It can be seen that the mode of c tends to remain approximately constant with height in the BL for both the 100 m and 55 m models. The mode is shifted higher for the 100 m model by 17%. This approximately corresponds to the percentage difference between the 100 m and 55 m m_c in Fig. 3.17a at 13:00 UTC. In the lower half of the BL the c distribution is positively skewed, particularly near the surface. This is consistent with Deardorff and Willis (1985), who found θ to be positively skewed in the lower half of the BL in a CBL water tank experiment. It is the open cell structure in the lower half of the BL that leads to the positive skewness. A lower proportion of the flow is in updrafts than downdrafts, and updrafts are associated with large c. Skewness decreases with height since the tracer diffuses from the updrafts and the area occupied by updrafts and downdrafts becomes more equal, so tracer is more evenly distributed in the horizontal.

The skewness of the 100 m model is larger than the 55 m model across all heights. This is possibly due to non-conservation issues near the surface resulting in large c in grid scale updrafts. In the middle of the BL the 55 m model distribution is approximately Gaussian. At $z/z_h = 0.75$ the 55 m model distribution becomes negatively skewed which is likely due to explicitly resolved entrainment of very low c air from above the BL.

The tracer turbulent intensities ($\langle c''^2 \rangle^{1/2} / \langle c \rangle$) in Table 3.2 are maximum near the surface, smallest near the middle of the BL and increase again near the top of the BL, consistent with the variance profiles in Sect. 3.5.2. The tracer turbulent intensity is important for AQ, since large values imply there is a large spread in c. It is not just mean pollu-

Model	z/z_h	$\langle c \rangle$ (kgm^{-3} $\times 10^{-4}$)	$\langle c''^2 \rangle^{1/2} / \langle c \rangle$	$\langle c''^3 \rangle / \langle c''^2 \rangle^{3/2}$
100 m	0.1	2.85	0.32	2.53
100 m	0.25	2.65	0.27	2.35
100 m	0.5	2.57	0.23	1.43
100 m	0.75	2.45	0.26	0.074
55 m	0.1	2.45	0.32	1.67
55 m	0.25	2.29	0.26	1.05
55 m	0.5	2.18	0.22	0.19
55 m	0.75	2.01	0.26	-0.60

Table 3.2:: Tracer statistics corresponding to the distributions plotted in Fig. 3.20.
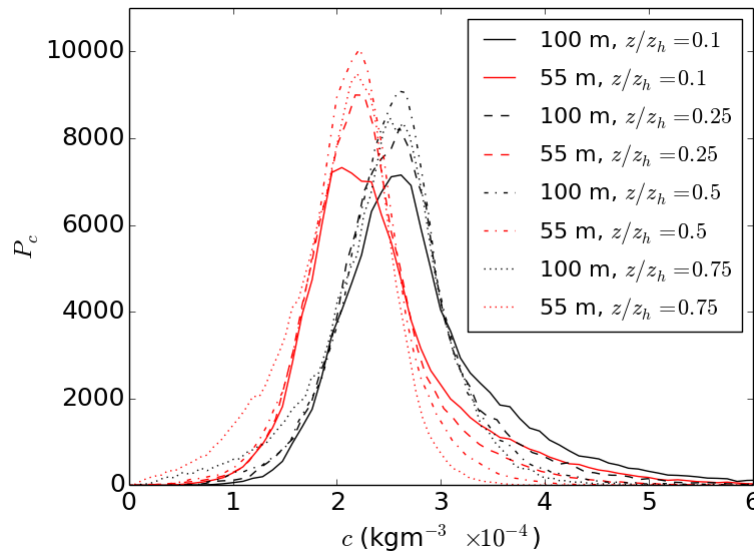
Figure 3.20: 100 m and 55 m model P_c calculated within the analysis region at 13:00 UTC for $z/z_h = 0.1, 0.25, 0.5, 0.75$.

tant concentrations but extreme pollutant concentration levels which are important for human health. At $z/z_h = 0.1$, $\langle c''^2 \rangle^{1/2}/\langle c \rangle$ is equal to 0.32 for both models. Assuming a Gaussian distribution this implies approximately 2.3% of values are greater than $\langle c \rangle + 2\langle c''^2 \rangle^{1/2}(= 1.64\langle c \rangle)$. However, due to the positive skewness near the surface, approximately 5% of values are greater than $1.64\langle c \rangle$, making extreme values of c more likely.

This work has shown there is large spread in c at the top of the surface layer due to convective structures. It is of interest for future studies to investigate the influence of convective structures on c when flow is resolved explicitly within the urban canopy. It is now possible to resolve the most important turbulent eddies within the urban canopy and ML simultaneously using LES. Park and Baik (2014) simulated a CBL over a cube array with highly sheared conditions where horizontal rolls were prevalent. They however were concerned with the influence of the urban roughness on the BL flow, and did not investigate the turbulent structure within the canopy. To the author's knowledge no study like that of Park and Baik (2014) has been conducted with a tracer, under a range of $-z_h/L_{MO}$, and focus paid to the influence of convective structure on c within the canopy.

3.6 Vertical Mixing Timescales

In this section the CBL vertical mixing characteristics are investigated in the UKV, 100 m and 55 m models. First a qualitative investigation is made using vertical profiles of the continuous and puff release tracer concentrations. A reduced analytical model for vertical mixing is then developed which is able to describe the distinct behaviour

of the UKV model and 100/55 m model vertical mixing behaviour. The model is a damped simple harmonic oscillator (DSHO) and is a reduction of the general form of Lagrangian Stochastic Models (LSMs). By fitting DSHO solutions to the UM simulation data, timescales for vertical mixing across UM simulations are obtained.

The 500 m and 300 m models are not investigated due to the non-conservation and grid scale vertical mixing issues detailed in the previous sections. Times are limited to 11:00–15:00 UTC when the 100 m and 55 m model conservation issues are much less pronounced. The 100 m model is included in the analysis to give an estimation of uncertainty in the 55 m model results. If the 100 m and 55 m model vertical mixing behaviour is similar, it gives confidence in the results.

The 15 km × 40 km analysis region presented in Sect. 3.3.1 (see Fig. 3.4 for a schematic) is used throughout this section. It is far enough in from the edges of the 80 km × 80 km puff release source area that no clean (zero tracer) air is advected in during an hour. Flow is reasonably steady between 11:00–15:00 UTC within the analysis region and varies little on the scale of the analysis region as discussed in Sects. 3.3.3.1 and 3.3.1 respectively. This means horizontal advection of tracer in and out of the analysis region is small. This makes the puff release tracer suitable for analysing vertical mixing.

3.6.1 A Qualitative Investigation of Vertical Mixing in the UKV, 100 m and 55 m Models

3.6.1.1 Time Evolution of the Puff Release Concentration Profiles

Figure 3.21 shows the 13:00 UTC puff release concentration profile time evolution for the UKV, 100 m and 55 m models. The UKV model profiles tend towards a steady state with monotonic decrease and increase of concentration near the surface and in the upper BL, respectively. The UKV model concentration decreases monotonically with height at all times.

The 100 m and 55 m model profiles look qualitatively like the UKV model profile at 5 min, which is likely due to vertical mixing near the surface being largely parametrised in all models. However, after 10 min the 100 m and 55 m models have significantly larger proportion of tracer in the upper BL than the UKV model. Between approximately 15–30 min the 100 m and 55 m models have more tracer in the upper BL than the lower BL. This is due to resolved BL scale eddies transporting tracer initially at the surface to high in the BL in updrafts. The surface level concentrations 20 min after release are approximately three times lower for the 55 m model than the UKV model. The lofting of tracer emitted at the surface is an important process controlling surface level pollution concentration.

The 100 m and 55 m profiles in Figs. 3.21b and c, respectively, are qualitatively similar. However, the maximum concentration values between 13:15–13:30 UTC tend to be
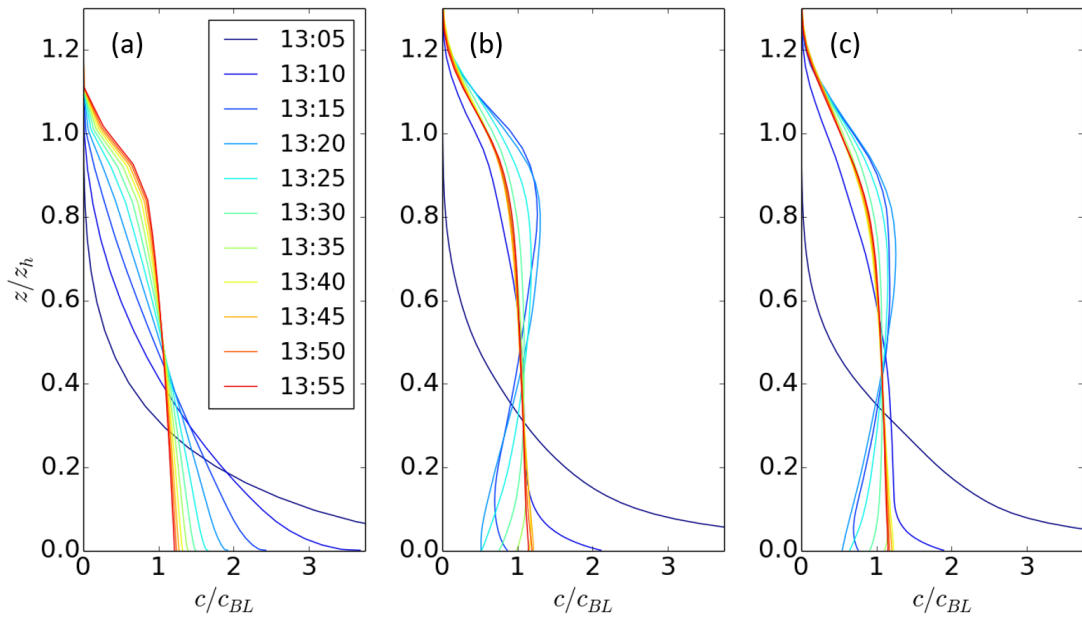
Figure 3.21: Time evolution of the 13:00 UTC puff release concentration profiles for the (a) UKV, (b) 100 m and (c) 55 m models.

slightly lower in the BL for the 55 m model compared to the 100 m model. This is likely due to the better resolved 55 m model having maximum vertical velocity variance lower in the BL (see Fig. 3.19a). Consequently, tracer mixing is less vigorous higher in the BL. The 100 m model at 13:10 UTC and 13:15 UTC has larger concentration near the surface compared to the 55 m model, which is likely due to more of the 100 m model turbulence being parametrised near the surface.

The UKV model continuous release concentration profile at 13:00 UTC in Fig. 3.7a, is much less well-mixed than the UKV model puff release concentration profile at 13:55 UTC in Fig. 3.21a. A large proportion of the UKV model continuous release tracer is not well-mixed within the analysis region. This is consistent with the argument presented in Sect. 3.3.3.2, that the vertical mixing in the UKV model is less efficient than in the 100 m and 55 m models. In Sect. 3.3.3.1, it was estimated that if $2\tau_*$ is the time it takes tracer to become well-mixed, approximately 76% of the continuous release tracer should be well-mixed within the analysis region. A more appropriate timescale than $2\tau_*$ for the time it takes the UKV model (and 100/55 m models) to become well-mixed is explored in Sect. 3.6.5.

3.6.1.2 Evolution of the Continuous Release Concentration Profiles with Down-stream Distance

It is investigated how the continuous release vertical tracer distribution evolves with downstream distance over London. Figure 3.22a shows the UKV and 55 m model pro-

files at 13:00 UTC. They are normalised by the mean concentration within the BL (c_{BL}) in five regions, namely 0–10 km, 10–20 km, 20–30 km, 30–40 km and 40–50 km downstream of the southern edge of the continuous source region. The longitudinal extent (40 km) of the analysis region is the same as the standard analysis region used throughout this section.

The 100 m and 55 m models tend to have more tracer than the UKV model above z_h in Figs. 3.21 and 3.22, due to large z_h heterogeneity. The profiles are scaled by the horizontal average z_h in each of the five regions, rather than scaling the concentration profiles by the grid cell local z_h then calculating the horizontal average concentration profiles. Since the 55 m model has large z_h heterogeneity it means that there are some regions of the BL above horizontal average z_h with large c. If the concentration profiles had been scaled by z_h before horizontal averaging, greater concentration at heights above z_h would have occurred than in the chosen approach where z_h scaling is done after horizontal averaging. This is because the 100 m and 55 m models have small z_h values at individual grid points (see Fig. 3.15), above which there are large tracer values that would have caused large concentrations above z_h.

It is also likely that there was larger detrainment and entrainment of high and low concentration air, respectively, in the 100 m and 55 m models than the UKV model, leading to there being more tracer above horizontal average z_h in the 100 m and 55 m models. Tracer near the top of the BL in regions of large z_h often becomes cut-off from the BL in the 100 m and 55 m models due to resolved motions. This can be seen in Fig. 3.15b at $z \approx 1.4$ km, where there is a small region of $w > 1$ ms^{-1} associated with larger tracer concentration than the surrounding air.

As expected, from Fig. 3.22a it is clear that the 55 m model becomes well-mixed much more quickly than the UKV model. After 10 km downstream of the source edge the 55 m model profiles vary little, but the UKV model profiles are still adjusting 40–50 km downstream. BL vertical mixing parametrisations in NWP do not represent the lofting of tracer and decreases in concentration near the surface at times O($\tau_* \sim 10$ min) after release. Tracers released at times O(τ_*) previously have a propensity to be in the upper BL, so their contribution to the horizontal average of all tracers tends to make the 100 m and 55 m vertical c distribution appear more well-mixed. This unrepresented dynamics is partly why the continuous release UKV model profiles are less well-mixed.

As discussed in Sect. 3.3.3.2, the UKV model continuous release concentration profiles would have become well-mixed more quickly, if a non-local term were included in the tracer vertical mixing parametrisation. However, the non-local term in the UM blending scheme is a function of the surface flux, z and a vertical velocity scaling parameter (Lock et al., 2016). Since it is not a function of the variable being transported (i.e. $c(z)$ here), tracer released at the surface would instantaneously be mixed throughout the BL. When one is interested in the evolution of the concentration distribution before it becomes well-mixed, for example with downstream distance in a city, the non-local
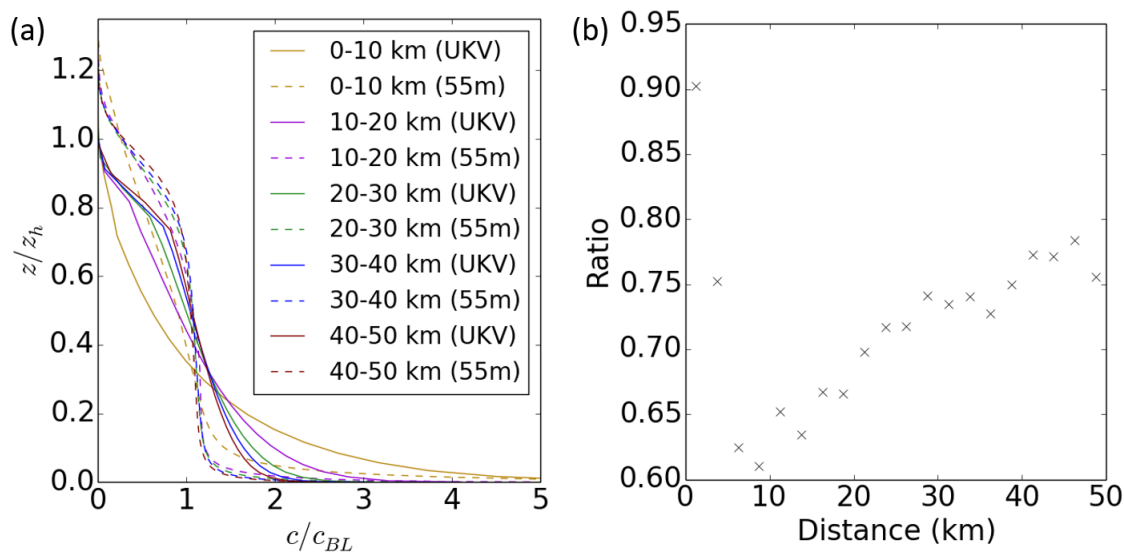
Figure 3.22: (a) UKV and 55 m model continuous release concentration profiles at 13:00 UTC calculated in five regions, 0-10 km, 10-20 km, 20-30 km, 30-40 km and 40-50 km downstream of the southern edge of the continuous source region. (b) Ratio of the 55 m model to the UKV model continuous release concentrations at $z/z_h = 0.02$ normalised by the average concentration in the BL ($c(z/z_h = 0.02)/c_{BL}$) at 13:00 UTC. The ratio was calculated in 2.5 km intervals with increasing distance downstream of the southern edge of the continuous source region. The longitudinal extent of the analysis regions in (a) and (b) was chosen to be the same as the standard analysis region.

parametrisation is not appropriate.

Figure 3.22b shows the ratio of the UKV and 55 m model continuous release concentrations at $z/z_h = 0.02$, normalised by the average concentration in the BL. The analysis is conducted at 13:00 UTC, and ratios are calculated using averages within 2.5 km intervals downstream of the southern edge of the continuous source region. The longitudinal extent is the same as the standard analysis region. $z/z_h = 0.02$ was chosen so that the UKV and 55 m model concentrations could be compared near the surface, but above the two lowermost UKV model grid points. The UKV model vertical grid lengths are approximately two times larger than the 55 m model, and concentration is very sensitive to vertical resolution at the grid points nearest the ground, since concentration gradients are strong there. The choice therefore helps distinguish differences in surface concentration due to vertical mixing representation in the models, from the influence of vertical resolution.

From 3.22b it can be seen that in the first 2.5 km downstream of the continuous source region upstream edge, the ratio is 0.90. The UKV model concentration is not much larger the 55 m model concentration. This is because tracers in the model have only just been released so are near the surface, where differences between the vertical mixing representation in the two models is smallest within the BL. However, the ratio quickly decreases to a minimum value of 0.61 approximately 9 km downstream. This is due to the lofting of tracer in the 55 m model and decrease in concentration near the surface. 9 km down-

stream distance corresponds to a horizontal advection time of approximately 9 km / 7 ms^{-1} = 21 min. This agrees well with the time at which there are largest amounts of tracer lofted in the BL in Fig. 3.21c. This suggests that by explicitly resolving mixing within the UBL, rather than parametrisation using K-theory, up to 40% differences in concentration near the surface can be expected on the city scale. With increasing downstream distance, the ratio begins to increase back towards 1, as a larger proportion of the tracer becomes well-mixed in the two models.

3.6.1.3 Centre of Mass Trajectories

The mean height of tracer is given by the centre of mass

$$\text{CoM} = \frac{\int_A \int_0^\infty c(z)z\,dz\,dA}{\int_A \int_0^\infty c(z)\,dz\,dA},\tag{3.14}$$

where A is the area of the analysis region. By tracking the CoM trajectory with time one can obtain an estimate of how well-mixed the tracer is, since in the limit of being well-mixed $\text{CoM}/z_h \to 0.5$. Plotted in Fig. 3.23 are the UKV, 100 m and 55 m model puff release CoM trajectories at 13:00 UTC. Height is normalised by horizontally averaged z_h. The UKV model CoM increases monotonically with height but the 100 m and 55 m model CoMs overshoot $z/z_h = 0.5$. This is consistent with the concentration profiles observed in Fig. 3.21.

Several methods of determining a timescale for the time it takes tracer to become well-mixed after release were investigated, for example using the first time CoM/z_h intersects 0.5. This is not suitable since the UKV model CoM/z_h never intersects 0.5. As an approximation one could instead arbitrarily choose the time CoM/z_h intersects 0.45. The mixing is very efficient initially for the 55 m and 100 m models so that CoM/z_h intersects 0.45 quickly. The 55 m and 100 m models overshoot $\text{CoM}/z_h = 0.5$ and are still tending towards $\text{CoM}/z_h = 0.5$ after twice the time it takes the CoM to reach $\text{CoM}/z_h = 0.45$. The tracer is therefore not well-mixed at the time CoM/z_h intersects 0.45. Also, with increasing time the UKV model tends towards steady state much more slowly, so that any single mixing timescale would be very sensitive to the chosen CoM/z_h intersection value.

The vertical mixing has different characteristics at short and long times after release in both the UKV and 100/55 m models. This suggests that more than one timescale is required to characterise the vertical mixing in the models. To capture this temporal evolution a reduced analytical model is developed for the CoM.
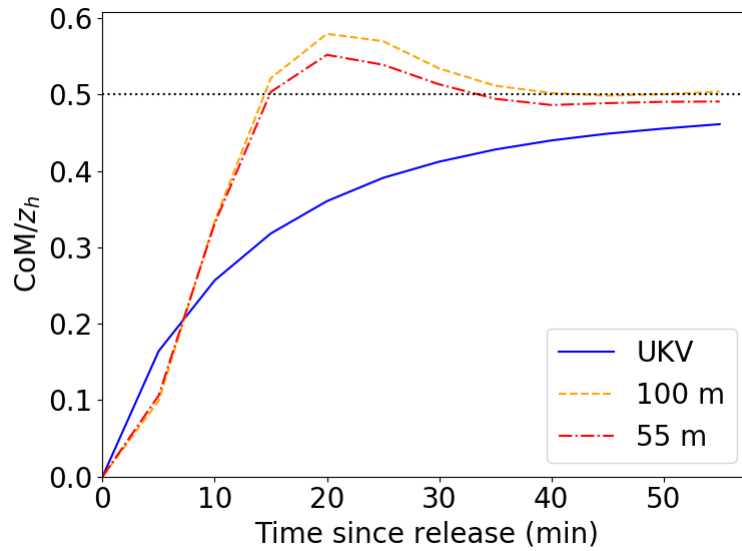
Figure 3.23: UKV, 100 m and 55 m model CoM trajectories for the 13:00 UTC puff release.

3.6.2 Lagrangian Stochastic Models (LSMs)

Taylor (1922) considered the dispersion of particles in unbounded, stationary, homogeneous turbulence. For particles initially at $z = 0$, the time rate of change in the ensemble mean spread is given by

$$\frac{d\sigma_z^2}{dt} = 2\int_0^t \langle w(t)w(t')\rangle dt' = 2\sigma_w^2 \int_0^t R_{ww}^L(\tau_\Delta)d\tau_\Delta, \tag{3.15}$$

where $\tau_\Delta \equiv t - t'$, $R_{ww}^L(\tau_\Delta) = \langle w(t)w(t')\rangle/\sigma_w^2$ is the Lagrangian velocity correlation coefficient, $\sigma_z = \langle z^2\rangle^{1/2}$ and $\sigma_w = \langle w^2\rangle^{1/2}$. In Sect. 3.6 only, $\langle\rangle$ represents the ensemble average over particles (and tracers) rather than the horizontal average.

Let us consider the behaviour of Eq. 3.15 in two limits. First, at small times when turbulence has large memory of the preceding flow (i.e. $w(t') \approx w(t)$ and $R_{ww}^L(\tau_\Delta) \approx 1$), and $\int_0^t R_{ww}^L(\tau_\Delta)d\tau_\Delta \approx t$. The integral of Eq. 3.15 is then equal to $\sigma_z^2 = \sigma_w^2 t^2$. This is known as the ballistic limit where particles simply move at their initial velocity.

Second, let us consider behaviour at times large enough that turbulence becomes uncorrelated i.e. $R_{ww}^L(\tau_\Delta) \to 0$. The upper limit in $\int_0^t R_{ww}^L(\tau_\Delta)d\tau_\Delta$ can then be replaced by ∞. This time limit defines the Lagrangian timescale $\tau_L = \int_0^\infty R_{ww}^L(\tau_\Delta)d\tau_\Delta$. The integral of Eq. 3.15 is equal to $\sigma_z^2 = 2\sigma_w^2\tau_L t$. This is just like Fickian diffusion or Brownian motion, where the mean square displacement increases proportional to time. The solution has no memory of the preceding flow.

τ_L in a CBL is expected to be O(τ_*) which is typically ~ 10 min. The vertical mixing is therefore a mixture of the ballistic and diffusive type in the hour long puff releases. When turbulence is not resolved in the UM, the vertical mixing of tracers is governed by

the tracer continuity equation (Eq. 3.4) with K-theory parametrisation of cw (within the second term on the left-hand side of Eq. 3.4) i.e. the vertical flux of tracer. The UM solves the advection-diffusion equation. This explains why the UKV model only ever exhibits diffusive type behaviour in Fig. 3.23. Tracer can only move down a concentration gradient, and therefore CoM/z_h cannot exceed 0.5 (assuming a negligible amount of tracer leaves the BL during the puff release). The UKV model has no explicit representation of the BL scale motions that lead to BL scale ballistic type transport, so CoM/z_h increases too slowly between 5–15 min in Fig. 3.23. To compute vertical mixing timescales in a way that is comparable between the UKV and 55 m models, an approach is required that can capture the diffusive ($t >$O(τ_L)) and ballistic ($t <$O(τ_L)) behaviours.

The Lagrangian stochastic modelling approach is based on calculating an ensemble of marked fluid element (particle) trajectories through a turbulent flow, given knowledge of Eulerian velocity statistics. The ensemble average of their trajectories defines the concentration distribution. The mathematical form of most Lagrangian stochastic models (LSMs) is that of the generalised Langevin equation (Thomson and Wilson, 2012). It is a stochastic differential equation and stems from application of Newton's second law. Most importantly it has the correct behaviour in the diffusive and ballistic limits, reproducing Taylor's results.

For vertical dispersion in stationary, horizontally homogeneous flows, the form of the Langevin equation is (Thomson and Wilson, 2012)

$$dw = a(z,w)dt + b(z,w)d\xi, \tag{3.16}$$

where $d\xi$ are random velocity increments, and a and b are functions that need to be parametrised. Once w (the vertical velocity of the particle) has been determined one can integrate $dz = wdt$ to find the position of the particle z. Thomson (1987) showed that the random velocity increments must be Gaussian if w is to evolve continuously in time without jumps. More specifically, $d\xi$ becomes a Gaussian random forcing with zero mean and variance dt, and a and b are commonly taken to be (Thomson and Wilson, 2012)

$$a = -\frac{C_0\epsilon w}{2\sigma_w^2} + \frac{1}{2}\left(1 + \frac{w^2}{\sigma_w^2}\right)\frac{\partial\sigma_w^2}{\partial z}, \tag{3.17}$$

and

$$b = (C_0\epsilon)^{1/2}, \tag{3.18}$$

respectively. C_0 is typically treated as a dispersion parameter but more strictly is a universal constant (Monin and Yaglom (1975), p.358) and ϵ is the local rate of dissipation of TKE per unit mass. Equation 3.16 along with Eqs. 3.17 and 3.18 is commonly referred to as a generalised Langevin equation. This LSM fulfils the well-mixed criteria that Thomson (1987) set out, namely that "if the particles of a tracer are initially well-mixed (in

position-velocity space) in a turbulent flow, they should remain so."

The second term on the right-hand side of Eq. 3.16 is the diffusion term and represents the small scale turbulent motions. According to Kolmogorov's similarity theory for locally isotropic turbulence, when dt is in the inertial subrange, the statistics of dw depend only on dt and ϵ. Hence, b is determined by the small scale universal properties of turbulent flows (Wilson and Sawford, 1996). It is common to express b in terms of a decorrelation timescale $\tau_{dc} = (2\sigma_w^2)/(C_0\epsilon)$ so that $b = (2\sigma_w^2/\tau_{dc})^{1/2}$ (Tennekes, 1979; Thomson and Wilson, 2012).

The first term on the right-hand side of Eq. 3.17 is the damping term and represents the fading memory of the turbulence. This can be seen easily by writing it in terms of the decorrelation timescale so that it equals $-w/\tau_{dc}$. The second term on the right-hand side of Eq. 3.17 is the so called drift term and offsets the tendency of simulated particles to accumulate in areas of low σ_w. The form of a is unique if it is imposed that the form of b is that of Eq. 3.18 and Thomson's well-mixed hypothesis is satisfied (Thomson, 1987).

It is well known in CBLs that Eulerian vertical velocity probability distribution functions (PDFs) are not Gaussian but positively skewed (as was also shown for c in Sect. 3.5). The common way of tackling this problem whilst retaining Gaussian random forcing in b and satisfying Thomson's well-mixed condition, is to use a linear combination of two Eulerian vertical velocity PDFs in a (Thomson and Wilson, 2012). Updrafts and downdrafts are assigned different volume fractions of the BL with a set probability of jumping between the two. The updrafts and downdrafts have separate PDFs with different mean vertical velocity and vertical velocity variance and the combination gives the desired horizontal average vertical velocity variance and skewness. Bærentsen and Berkowicz (1984) were the first to employ this method of obtaining the correct Eulerian vertical velocity statistics, but it was not until Luhar and Britter (1989) and Weil (1990) that it was done in a way that satisfied Thomson's well-mixed condition.

3.6.3 Reduction of a LSM to a Damped Simple Harmonic Oscillator (DSHO)

The 55 m model CoM trajectory in Fig. 3.23 resembles that of a DSHO with equilibrium at CoM$/z_h = 0.5$. The equation for a DSHO is

$$m_s\ddot{z}_s = -\gamma_s\dot{z}_s - \omega_s^2 z_s, \qquad (3.19)$$

where m_s is the mass of the DSHO, z_s is the displacement of the DSHO, and γ_s and ω_s are parameters that determine the magnitude of the damping and restoring forces respectively. In this section it is explored whether under some reasonable assumptions, Eqs. 3.16-3.18 might reduce to the form of Eq. 3.19.

By using Eqs. 3.16-3.18 as the starting point for the reduced analytical model it has

been assumed that the flow is stationary, horizontally homogeneous and that the Eulerian vertical velocity distribution is Gaussian. The ensemble average of the second term on the right-hand side of Eq. 3.16 is zero since the Gaussian forcing has equal probability of displacing particles upwards and downwards. The drift term simplifies upon ensemble averaging (since $\langle w^2 \rangle = \sigma_w^2$), so that Eqs. 3.16 and 3.17 can be written as

$$\langle \ddot{z} \rangle = -\frac{\langle \dot{z} \rangle}{\tau_{dc}} + \frac{\partial \sigma_w^2}{\partial z}, \tag{3.20}$$

where $\langle z \rangle$ is the ensemble average particle position (or CoM of the particles). If the turbulence is assumed vertically homogeneous then τ_{dc} is constant, and the damping term in Eqs. 3.19 and 3.20 are in the same form.

Turbulence is not vertically homogeneous in the BL, otherwise the drift term in Eq. 3.20 would be zero and the characteristic lift off behaviour of puff released tracers near the surface would not be reproduced (Luhar and Britter, 1989; Weil, 1990). Therefore, tracers would not spread faster than $\langle z^2 \rangle \propto t$ at times shortly after release and their CoM would not overshoot $z_h/2$. Here a heuristic approximation is made to the drift term, allowing some representation of the vertical heterogeneity in CBL turbulence, even though it is not represented in the damping term. In CBL turbulence σ_w^2 tends to have a maximum at approximately $z_h/2$ (see Fig. 3.19a). The drift term is therefore positive and negative in the bottom and top halves of the BL respectively, and acts to move particles towards $z_h/2$. It is as if the drift term is a restoring force. On this basis the drift term will be represented as being proportional to the negative displacement from the middle of the BL.

Another argument can be made for the drift term being treated as a DSHO restoring force. Given that the Gaussian random forcing term has no influence on the CoM, it must be the dominant energy producing eddies that provide the forcing, and these can only be represented by the drift term. The main energy producing eddies under convective conditions span the entire BL depth, and might roughly be approximated as circular in an $x - z$ plane. A particle released into such an eddy (in the absence of other eddies) would undergo perpetual circular motions analogous to simple harmonic motion.

The LSM has therefore been reduced to a DSHO of the form

$$\langle \ddot{x} \rangle = -2\gamma \langle \dot{x} \rangle - \omega^2 \langle x \rangle, \tag{3.21}$$

where $\langle x \rangle \equiv \langle z \rangle - z_h/2$, $\omega = 2\pi/\tau_\omega$ represents the driving frequency of energy producing eddies, τ_ω is the time period of one driving frequency oscillation and $\gamma = 1/(2\tau_{dc})$ determines the amount of damping.

3.6.4 Analytical Solution to the DSHO

The general solution to Eq. 3.21 is given by

$$\langle x \rangle / z_h = A e^{p_+} + B e^{p_-} = e^{-\gamma t} \left(A e^{\sqrt{\gamma^2 - \omega^2} t} + B e^{-\sqrt{\gamma^2 - \omega^2} t} \right), \tag{3.22}$$

where A and B are dimensionless constants, and $p_\pm = -\gamma \pm \sqrt{\gamma^2 - \omega^2}$.

Let us first consider the overdamped case where $\gamma > \omega$ and $p_\pm < 0$. Given the initial condition $z(0)/z_h = A + B + 0.5$, Eq. 3.22 can be written as

$$\langle z \rangle / z_h = 0.5 + (z(0)/z_h - 0.5 - A)e^{p_- t} + A e^{p_+ t}. \tag{3.23}$$

$\langle z \rangle / z_h$ exponentially decays with two timescales to a steady state (i.e. 0.5) without oscillating.

Next let us consider the underdamped case when $\gamma < \omega$ and $p_\pm = -\gamma \pm i\Omega$ where $\Omega = \sqrt{\omega^2 - \gamma^2}$. Equation 3.22 can be written as

$$\langle z \rangle / z_h = 0.5 + D e^{-\gamma t} \cos(\Omega t + \phi), \tag{3.24}$$

where ϕ is a phase constant. Given the initial CoM height $z(0)$, it follows that $D = (z(0)/z_h - 0.5)/\cos(\phi)$, and

$$\langle z \rangle / z_h = 0.5 + \frac{(z(0)/z_h - 0.5)e^{-\gamma t}\cos(\Omega t + \phi)}{\cos(\phi)}. \tag{3.25}$$

Unlike the overdamped solution (Eq. 3.23), once $\omega > \gamma$, increasing ω does not make the solution tend towards steady state any quicker. $\langle z \rangle / z_h$ oscillates at frequency Ω (slower than ω) with amplitude exponentially decaying to zero with e-folding lifetime $1/\gamma$. Increasing ω does, however, result in the CoM moving quicker from the surface since the oscillations are faster, and $\langle z \rangle / z_h$ overshoots 0.5 more since the solution has had less time to decay at the time of maximum amplitude.

The critically damped solution occurs when $\gamma = \omega$, and is given by

$$\langle z \rangle / z_h = 0.5 + (z(0)/z_h - 0.5 + Jt)e^{-\gamma t}, \tag{3.26}$$

where J is a constant. z/z_h tends to a steady state directly with no overshooting. Larger values of γ (or equivalently ω) tend to make the solution reach steady state quicker with e-folding lifetime $1/\gamma$.

3.6.5 Analysis of Vertical Mixing in the UM Simulations in Terms of DSHO Timescales

In this section the optimal DSHO solutions to the UM simulation puff release CoM trajectories are determined. The UM vertical mixing is understood in terms of the DSHO solution timescales.

Figure 3.24 shows the UKV, 100 m and 55 m model CoM/z_h trajectories and the optimal fit analytical solutions at 13:00 UTC. The optimal solutions were found by varying the parameter values and minimising the root mean square error. The fits are generally good at different times since release for all models. The UKV model optimal solution parameters are $\gamma = 0.076$ min^{-1}, $\omega = 0.062$ min^{-1} and $A = -0.21$ making it overdamped. The 55 m and 100 m model optimal solutions are $\gamma = 0.114$ min^{-1}, $\omega = 0.180$ min^{-1} and $\phi = -45°$, and $\gamma = 0.091$ min^{-1}, $\omega = 0.155$ min^{-1} and $\phi = -38°$ respectively making them both underdamped. This is expected since the UKV and 100/55 m model CoM trajectories do not and do oscillate, respectively.

Presented in Table 3.3 are the UKV, 100 m and 55 m model optimal DSHO solution parameters for the 11:00, 12:00, 13:00 and 14:00 UTC puff releases. One can see that the results presented at 13:00 UTC are similar to those at the other times.

3.6.5.1 UKV model – Overdamped

In both the overdamped and underdamped solutions (Eqs. 3.23 and 3.25 respectively) there are three effective parameters, two of which are associated with timescales. In the overdamped solution the effective parameters are p_+, p_- and A. p_+ and p_- have associated timescales $\tau_{p_+} = -1/p_+$ and $\tau_{p_-} = -1/p_-$, respectively. For the UKV model at 13:00 UTC the optimal value of A was -0.21, so that to a crude approximation $A = B$, and along with the initial condition $z(0)/z_h = 0$, Eq. 3.23 becomes

$$\langle z \rangle / z_h \approx 0.5 - 0.25 e^{-t/\tau_{p_-}} - 0.25 e^{-t/\tau_{p_+}}. \tag{3.27}$$

The optimal values of τ_{p_+} and τ_{p_-} were 31.7 min and 8.3 min respectively. At short timescales ($t < \tau_{p_-}$) in the UKV model the vertical mixing is dominated by the τ_{p_-} exponential decay term. Since the term decays quickly the CoM increases quickly until $t \sim \tau_{p_-}$ (i.e. $\langle z \rangle / z_h \approx 0.25$). At times greater than τ_{p_-} the vertical mixing becomes increasingly dominated by the τ_{p_+} exponential decay term. The time it takes the tracer to become well-mixed (i.e. for $\langle z \rangle / z_h \to 0.5$) in the UKV model is controlled by the longer τ_{p_+} timescale, with e-folding lifetime 31.7 min. This explains why $2\tau_*$ (which is approximately 24 min for the UKV model), is an underestimate of the time it takes the UKV model to become well-mixed.
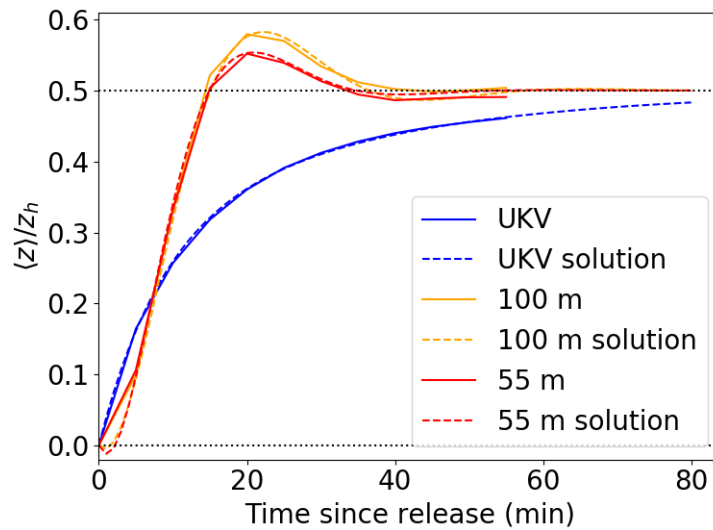
Figure 3.24: UKV, 100 m and 55 m model CoM trajectories at 13:00 UTC with optimal DSHO solutions.

3.6.5.2 100/55 m models – Underdamped

The underdamped solution effective parameters are γ, Ω and ϕ. γ and Ω have associated timescales $\tau_{dc} = 1/(2\gamma)$ and $\tau_\Omega = 2\pi/\Omega$, respectively. In Eq. 3.25, the exponential decay term has e-folding lifetime $2\tau_{dc}$ and oscillates with time period τ_Ω. For the 55 m model at 13:00 UTC the optimal τ_{dc} and τ_Ω were 4.4 min and 39.7 min respectively. The time it takes the tracer to become well-mixed in the 55 m model is controlled by the τ_{dc} timescale in the exponential decay term and has e-folding lifetime 8.8 min. $2\tau_* = 22.6$ min is approximately equal to $5\tau_{dc}$ (i.e. approximately 2.5 e-foldings). $2\tau_*$ is a reasonable estimate for the time it takes tracer to become well-mixed in the 55 m model, despite being only approximately 3 min after the maximum CoM time. The CoM/z_h is never more than 0.04 from $z/z_h = 0.5$ after $t = 2\tau_*$.

The 55 m and 100 m model CoM trajectories increase less quickly during the first 5 min than between 5–15 min. This is because initially tracer is predominantly moving horizontally near the surface and converging towards updraft regions. The 55 m and 100 m model optimal solutions both become negative briefly just after release, which is unphysical since tracer cannot go beneath the ground. The DSHO does not capture the convergence behaviour shortly after release. The optimal DSHO solution has negative ϕ so that the fast CoM increase is delayed, and coincides with the UM simulated increase between 5–15 min. The validity of the analytical solution starts from approximately 5 min.

Simulation	$z(0)/z_h$	A	ϕ	τ_{p_+}	τ_{p_-}	τ_{dc}	τ_Ω	τ_ω	τ_*
UKV (11:00)	0.00	-0.16	-	41.9	9.1	7.5	-	122.5	12.0
UKV (12:00)	0.00	-0.22	-	31.7	8.3	6.6	-	102.1	12.0
UKV (13:00)	0.00	-0.21	-	31.7	8.3	6.6	-	102.1	11.7
UKV (14:00)	0.00	-0.24	-	28.9	7.8	6.1	-	94.2	11.8
55 m (11:00)	0.00	-	-40°	-	-	5.0	42.0	35.0	11.5
55 m (12:00)	0.00	-	-47°	-	-	4.3	40.2	32.2	11.6
55 m (13:00)	0.00	-	-45°	-	-	4.4	39.7	32.2	11.3
55 m (14:00)	0.00	-	-43°	-	-	4.8	41.4	34.0	11.9
100 m (11:00)	0.00	-	-37°	-	-	5.9	42.9	37.1	11.8
100 m (12:00)	0.00	-	-42°	-	-	5.2	41.5	35.0	11.8
100 m (13:00)	0.00	-	-38°	-	-	5.5	40.5	35.0	11.6
100 m (14:00)	0.00	-	-36°	-	-	6.1	42.4	37.1	12.2
T14	0.07	-	-6°	-	-	9.0	60.3	53.3	14.7
T14	0.24	-	-32°	-	-	8.2	62.3	53.3	14.7

Table 3.3:: Optimal fit parameters to the UKV, 100 m and 55 m models at 11:00, 12:00, 13:00 and 14:00 UTC, and LES from Taylor et al. (2014) (T14). $\tau_{p_+} = -1/p_+$, $\tau_{p_-} = -1/p_-$, $\tau_\Omega = 2\pi/\Omega$, $\tau_{dc} = 1/(2\gamma)$, $\tau_\omega = 2\pi/\omega$ and $\tau_* = z_h/w_*$. The unit of all timescales is minutes.

3.6.5.3 UKV Model and 100/55 m Models Comparison

The 55 m model $\langle z \rangle / z_h$ tends to 0.5 much quicker than the UKV model, since it does not have a second slow decay timescale. For $t < \mathrm{O}(2\tau_{dc})$, the 55 m model vertical mixing has large influence from the cosine function, which causes the CoM to increase with time faster than due to the exponential decay alone, and results in maximum $\langle z \rangle / z_h > 0.5$ at $t \approx \tau_\Omega/2$. The UKV model turbulence parametrisation is diffusive, rather than a combination of ballistic and diffusive type dispersion as predicted by Taylor (1922) at $t = \mathrm{O}(\tau_{dc})$. The ballistic type dispersion is what leads to the oscillatory motions and the faster mixing in the 100/55 m models compared to the UKV model.

3.6.5.4 100 m Model and 55 m Model Comparison

The 100 m model 13:00 UTC optimal τ_{dc} and τ_Ω were 5.5 min and 40.5 min respectively. τ_{dc} is approximately 25% larger and τ_Ω approximately the same compared to the corresponding values for the 55 m model. The maximum CoM being higher for the 100 m model than the 55 m model is consistent with τ_{dc} being larger, since it means the 100 m model oscillations were less damped.

The e-folding lifetime $2\tau_{dc}$ of the 100 m model was 11 min compared to 8.8 min in the 55 m model. This gives an uncertainty estimate of around 2 min for the 55 m model e-folding lifetime.

Due to τ_Ω being similar but τ_{dc} being larger when comparing the 100 m model to the 55 m model, it means that τ_ω is smaller for the 55 m model. τ_ω took the values 32.2

min and 35.0 min for the 55 m and 100 m models respectively. Therefore, the driving frequency was higher for the 55 m model than the 100 m model optimal solution, but the 55 m model optimal solution was more heavily damped.

The two-point correlations in Sect. 3.5.3 showed that in general, the BL scale turbulent motions are slightly smaller scale for the 55 m model than the 100 m model. This is consistent with the findings of Bopape et al. (2020) who calculated θ two-point correlation functions ($R_{\theta\theta}$) with data from idealised LES of the CBL at 50 m and 100 m horizontal grid lengths. The 55 m model BL scale overturning motions are therefore likely slightly higher frequency owing to their smaller size, and it explains why τ_ω was smaller for the 55 m model. It is hypothesised that the reason the 100 m model is less damped is that tracers reside in updrafts and downdrafts too long since the eddies are too large, causing the tracers to have larger memory (i.e. larger τ_{dc}).

3.6.6 Analysis of Vertical Mixing in Terms of DSHO Timescales for the LES Runs of Taylor et al. (2014)

Taylor et al. (2014) conducted LES at 50 m horizontal grid length with periodic lateral boundary conditions, $z_0 = 0.01$ m, geostrophic velocity of $5\,\text{ms}^{-1}$, $Q_H = 100\,\text{Wm}^{-2}$, $z_h = 1374$ m, $-z_h/L_{MO} \approx 200$ and spin up time sufficient that turbulence was statistically stationary. Tracer puff releases were carried out at $z/z_h = 0.07$ and $z/z_h = 0.24$. Values of $-z_h/L_{MO} \approx 200$ correspond to highly convective conditions with little wind shear, and thus open cell CBL turbulent structure. The Taylor et al. (2014) simulations will be referred to as T14 herein.

Table 3.3 contains the parameter values for the optimal DSHO solutions to the T14 simulations. Figure 3.25 shows the T14 CoM trajectories, optimal T14 solutions and 55 m model CoM trajectory at 13:00 UTC. It can be seen that when time is scaled by τ_*, maximum CoM height occurs at approximately $t/\tau_* = 1.8$ for T14 with release at $z/z_h = 0.07$ and the 55 m model. The $z/z_h = 0.5$ crossing occurs at $t/\tau_* \sim 1$ for the different models which is smaller than the value of $t/\tau_* = 1.6$ suggested by Deardorff (1972b) (see Sect. 1.2.3 for details of their investigation). Also, the shapes of the T14 $z/z_h = 0.07$ release and the 55 m model CoM trajectories are very similar. It is likely they would have given reasonable collapse if the release heights were the same, suggesting τ_* at least to a first approximation is a good scaling variable for vertical mixing.

The T14 optimal solutions are underdamped because the majority of BL scale eddies were well resolved by the LES. The solutions give a good fit to the CoM trajectories, capturing the initial lift off behaviour and evolution of vertical heterogeneity in tracer concentration. Optimal τ_Ω were 60.3 min and 62.3 min, for the $z/z_h = 0.07$ and $z/z_h = 0.24$ releases respectively. Smaller Q_H largely explains why τ_* and τ_Ω (and τ_ω) are longer by approximately 25% and 50%, respectively, for T14 compared to the 55 m model val-
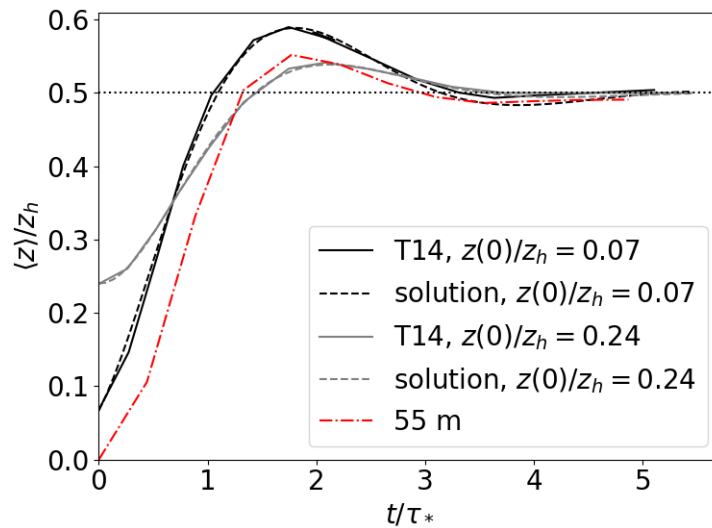
Figure 3.25: T14 $z(0)/z_h = 0.07$ and $z(0)/z_h = 0.24$ CoM trajectories with optimal DSHO solutions. 55 m model CoM trajectory at 13:00 UTC.

ues. T14 had smaller forcing of the BL scale eddies and therefore slower updrafts and downdrafts, but similar z_h limiting the size of the motions.

Optimal τ_{dc} was 9.0 min and 8.2 min for the T14 $z/z_h = 0.07$ and $z/z_h = 0.24$ releases, respectively. This is approximately 100% larger than the 55 m model values, and suggests the T14 tracers were less damped i.e. had longer memory. The T14 tracers having 100% larger τ_{dc} than the 55 m model cannot be explained by the T14 tracers being in slower eddies alone. w_* was only approximately 25% smaller than in the 55 m model. Another possible contributing factor towards the 55 m model having larger damping is that it had larger wind shear, as can be seen by noting $-z_h/L_{MO} \approx 28$ for the 55 m model but $-z_h/L_{MO} \approx 200$ for the T14 simulations. Wind shear also acts to mix the tracer. Given that after the CoM maximum the T14 CoM trajectories oscillate less than their optimal solutions, it is also possible that their damping is underestimated in the long time ($t \gg O(\tau_{dc})$) limit. This could mean that $2\tau_{dc}$ is an overestimate of the e-folding lifetime and that there is more complicated behaviour that the DSHO solution does not represent.

3.7 Summary

Vertical mixing of tracer has been investigated at horizontal grid lengths spanning the regimes where the dominant CBL turbulence is almost fully resolved, partially resolved (the "grey zone") and fully parametrised in the UM. Simulations were conducted with horizontal grid lengths of 1.5 km, 500 m, 300 m, 100 m and 55 m in a one-way nested suite, for a clear-sky CBL case study (04/05/2016) over London. Continuous and puff

release ground sources of tracer were included. The turbulence representation, three-dimensional concentration distribution and tracer vertical mixing within the UBL were investigated across the range of grid lengths.

A comparison of total tracer mass in each model to the amount of tracer mass emitted into each model was made. It was demonstrated that tracer was not conserved in any of the models, which occurs because the UM uses a SISL advection scheme that is not inherently conserving of tracers. The UKV model (1.5 km horizontal grid length) had at most 5% more tracer mass than it should, and in the afternoon non-conservation issues were negligible. If the UM is used at O(1.5 km) grid length for AQ purposes, such overestimates of tracer mass are perhaps tolerable when one is interested in pollutants emitted within a city. However, for pollutants with long lifetimes that are advected over regional scales, pollutant concentration errors could grow much more than 5%. In such situations a correction (such as a mass-fixer scheme) must be included within the SISL advection scheme.

In the afternoon when the 500 m and 300 m models partially resolve the CBL turbulence, they had approximately 2.5 times more tracer mass than they should. The 100 m and 55 m models had largest tracer non-conservation issues during the morning transition when they overestimated tracer mass by approximately 50%. In the morning transition the BL is convective but z_h is only O(300 m), and the 100 m and 55 m models partially resolve the BL scale turbulence. In the afternoon the 100 m and 55 m tracer non-conservation issues were less pronounced, since the majority of the BL scale turbulence was well resolved. During this time tracer mass overestimation was typically 40% for the 100 m model. For the 55 m model in the afternoon there was more uncertainty, and mass overestimation was between $0 - 10\%$. During the course of this study colleagues at the UK Met Office identified similar problems with w and θ (Lock et al., 2017) in the CBL grey zone. However, this is the first time such large errors have been found for tracers. In addition, the 100 m and 55 m models were not known to have such appreciable non-conservation issues in the morning.

The $500 - 55$ m model tracer non-conservation issues occur due to the "infinite fountain" problem (Lock et al., 2017). In poorly resolved updrafts, horizontal flow at adjacent grid points tends to cancel when interpolated onto the SISL advection scheme tracer departure points. Consequently, there is little dilution of tracer and an excess is produced in updrafts. The updrafts were seen to be single grid point in the cross-stream direction and O(10) grid points in the streamwise direction when the models suffered their greatest non-conservation issues. During the afternoon and morning transitions, the 500/300 m and 100/55 m model grid scale updrafts spanned the entire BL respectively. They were associated with large z_h and resulted in large detrainment of tracer from the BL. Where z_h is large due to grid scale updrafts it reinforces the problem, since the UM blending scheme weights the contribution from sub-grid mixing based on z_h. Calculating grid point local z_h based on an average z_h from neighbouring grid points would

likely alleviate the non-conservation issues.

A mass-fixer approach would not be an appropriate solution to the 500–55 m model tracer non-conservation issues. It does not scale the mass correction based on the non-conservation issue severity at each grid point and only ensures the total mass in the domain is correct. The grid point updrafts lead to unphysical transport of tracer, for example very large concentration in updrafts, tracer turbulent flux profiles that are not linearly decreasing with height and excess detrainment of tracer from the BL.

During the afternoon the 100 m and 55 m model grid point updrafts typically only extended from the ground to approximately $0.1z_h$. A modification to the blending scheme weighting function was proposed near the surface so that it scales with z there rather than with z_h. This would result in more of the turbulence being parametrised in the surface layer, where the 100 m and 55 m models poorly resolve the turbulence. This should help ameliorate the 100 m and 55 m model tracer non-conservation issues for O(1 km) deep CBLs.

At 13:00 UTC the CBL was fully developed and $-z_h/L_{MO} \approx 30$ for the 100 m and 55 m models. The turbulence had elongated open cell structure, which was qualitatively consistent with the literature for $-z_h/L_{MO} \approx 30$. Variance profiles of vertical velocity and θ were qualitatively consistent with the literature. However, maximum vertical velocity variance occurred at $z/z_h \approx 0.45$, as opposed to the value $z/z_h \approx 0.3$ often found in the literature. When scaled so that surface values were the same, c and θ variance profiles were similar apart from near $z/z_h \approx 1$, where c variances were smaller. The differences between tropospheric (subsiding) air and BL (thermal) air at $z/z_h \approx 1$ were larger for θ than c (when scaled). To the author's knowledge this is the first time differences in ground released tracer and θ variance at $z/z_h \approx 1$ have been highlighted.

The 100 m and 55 m model two-point correlation functions for vertical velocity in the cross-stream direction (R_{ww}^x) resembled those seen in studies of free CBLs. In the streamwise direction the vertical velocity two-point correlation functions (R_{ww}^y) did not become negative at two-point separations of O(z_h) unlike in the cross-stream direction. This is because when the open cells are elongated there is less cross-stream turbulent structure.

The tracer concentration two-point correlation functions (R_{cc}) were broader than R_{ww}. Also, R_{cc}^x did not become negative at two-point separations of O(z_h). Both are likely due to the influence of horizontal velocity as well as vertical velocity on the horizontal concentration distribution. This is consistent with arguments presented by Deardorff and Willis (1985) for temperature two-point correlation functions. To the author's knowledge this is the first time the R_{ww}^x and R_{ww}^y behaviour has been compared, and the R_{cc} behaviour has been investigated in the literature. Also, all previous studies have been for idealised BLs using LES and water tank experiments.

Probability distribution functions of tracer concentration at various heights within

the BL were consistent with the LES and water tank experiment literature. For the 55 m model at 13:00 UTC and $z/z_h = 0.1$ approximately 5% of values were greater than $1.64\langle c \rangle$. Distributions were positively skewed leading to a greater likelihood of extreme concentration values than would result from a Gaussian distribution with the same mean and variance. Whether such variations in concentration associated with CBL structures would be seen at $z/z_h \approx 0.002$ requires investigation at O(10 m) grid length.

Vertical concentration profiles of puff released tracer demonstrate that the UKV and 100/55 m models have qualitatively different vertical mixing behaviour. The resolved BL scale eddies in the 100 m and 55 m models transported tracer initially at the surface high up in the BL in updrafts. Between approximately 15-30 min the 100/55 m models had more tracer in the upper BL than the lower BL. This ballistic type mixing that occurs on O(τ_{dc}) timescales is not represented by the UKV model, or to the author's knowledge in any other NWP BL vertical mixing parametrisations.

By comparing the UKV and 55 m model continuous release concentrations at $z/z_h = 0.02$, it was shown that the lofting of tracer and associated decrease in tracer concentration near the surface significantly influences the city scale concentration. The 55 m model concentration was 39% less than the UKV model approximately 9 km downstream of the upstream edge of the ground source. This demonstrates that when the CBL vertical mixing is resolved rather than parametrised in online AQ models, substantial prediction improvements can be made at the city scale.

One vertical mixing timescale was insufficient to describe the behaviour across all of the models. To understand the vertical mixing behaviour, starting from the general form of LSMs, a reduced model for the CoM trajectories was formulated. The reduced model was shown to be a DSHO, to which analytical solutions can be obtained for underdamped and overdamped behaviour, each having two effective timescale parameters.

The UKV model optimal solutions were overdamped, so that the vertical mixing behaviour was determined by two exponential decay terms. They had e-folding lifetimes $\tau_{p_-} = 8.3$ min and $\tau_{p_+} = 31.7$ min at 13:00 UTC. At short times (O(τ_{p_-})) the vertical mixing was fastest and at long times it was much slower since vertical mixing is then controlled by the τ_{p_+} term.

The 55 m optimal solutions were underdamped, so that the vertical mixing behaviour was determined by a term involving the product of an exponential and cosine function, with e-folding lifetime $2\tau_{dc} = 8.4$ min and time period $\tau_\Omega = 39.7$ min, respectively, at 13:00 UTC. At times O($2\tau_{dc}$) the 55 m model CoM increased much faster than the UKV model. Although the e-folding lifetime of the 55 m model decay term was similar to the faster decaying of the two UKV model decay terms, the magnitude of the 55 m model decay term was larger. Also, the cosine function tended to make the CoM increase more quickly initially than due to the exponential decay alone. For times greater than O($2\tau_{dc}$) vertical mixing is much more efficient in the 55 m model than in the UKV model, since

it does not have a second slower e-folding lifetime.

The DSHO model can reproduce the salient UKV and 100/55 m model CoM trajectory characteristics. It has been demonstrated quantitatively that the vertical dispersion of tracer in the CBL is faster at short and long times since release for the 100/55 m models compared to the UKV model. To represent the ballistic type dispersion at short times O(100 m) grid length is required in NWP.

Chapter 4

Turbulence Characteristics Across a Range of Idealised Urban Canopy Geometries

This chapter is a near-final draft of a paper being prepared for submission in the journal Bounday-Layer Meteorology. The co-authors are O. Coceal (supervisor: NCAS and UoR), N. Nazarian (external collaborator: UNSW), J. F. Barlow (supervisor: UoR), R. S. Plant (supervisor: UoR), S. I. Bohnenstengel (supervisor: MO) and H. W. Lean (supervisor: MO). Affiliation acronyms: National Centre for Atmospheric Science (NCAS), University of Reading (UoR), University of New South Wales (UNSW) and MetOffice@Reading (MO).

The study was designed by myself and O. Coceal with a 75% : 25% split, respectively. The DNS and LES data was provided by O. Coceal and N. Nazarian, respectively. I performed the research, wrote the first draft of the paper and prepared all the figures. The co-authors gave advice on the structuring of the paper, interpretation of the findings and edited the text of the paper equating to approximately 25% of writing in the final version. Overall approximately 85% of the paper was contributed by me.

4.1 Abstract

Good representation of turbulence in urban canopy models is necessary for accurate prediction of momentum and scalar distribution in and above urban canopies. To develop and improve turbulence closure schemes for one-dimensional multi-layer urban canopy models, turbulence characteristics are investigated here by analysing existing large-eddy simulation (LES) and direct numerical simulation (DNS) data. A range of geometries and flow regimes are analysed that span packing densities of 0.0625 to 0.44, different building array configurations (cubes and cuboids, aligned and staggered arrays, and variable building height), and different incident wind directions ($0°$ and $45°$ with regards to the building face).

Momentum mixing length profiles share similar characteristics across the range of

geometries, making a first-order momentum mixing length turbulence closure a promising approach. In vegetation canopies turbulence is dominated by mixing-layer eddies of a scale determined by the canopy top shear length scale. No relationship was found between the depth-averaged momentum mixing length within the canopy and the canopy top shear length scale in the present study. By careful specification of the intrinsic averaging operator in the canopy, an often-overlooked term that accounts for changes in plan area density with height, is included in a first-order momentum mixing length turbulence closure model. For an array of variable height buildings, its omission leads to velocity overestimation of up to 17%. Additionally, we observe that the von Kármán coefficient varies between 0.20 and 0.51 across simulations, which is the first time such a range of values has been documented. When driving flow is oblique to the building faces, the ratio of dispersive to turbulent momentum flux is larger than unity in the lower half of the canopy. It is thus probable that dispersive momentum fluxes are more significant than previously thought in real urban settings, where the wind direction is almost always oblique.

4.2   Introduction

Urban canopies are highly heterogeneous with unsteady three-dimensional flow. To represent such heterogeneity, particularly in larger-scale simulations that cannot explicitly resolve micro-scale flow characteristics, parametrisations of turbulence, drag, and surface energy exchange are required (e.g. Masson, 2006; Salamanca et al., 2010; Grimmond et al., 2011; Krayenhoff et al., 2014, 2020). These parameterisations of urban canopy processes are critical in Air Quality Models (AQMs) and Numerical Weather Prediction (NWP), both to reliably predict pollution concentration, temperature and wind speed in urban areas, and to provide a lower boundary condition to the larger-scale flow. Modelled urban flow characteristics are also required to inform effective urban planning aimed at mitigating pollution and heat exposure, providing crucial foundations in epidemiological studies.

The simplest approaches to incorporating the influence of the urban canopy on turbulent exchange are based on using bulk morphological surface characteristics or micrometeorological methods to determine momentum roughness length z_0 and displacement height d, which in turn are used in Monin-Obukhov similarity theory (MOST) (Grimmond and Oke, 1999). Most mesoscale NWP models now employ single-layer urban canopy models where the exchange between the air and the urban facets is calculated according to MOST, and the contributions from the facets are combined using aerodynamical resistance networks and coupled at the first atmospheric level above the canopy (Masson, 2000; Kusaka et al., 2001; Porson et al., 2010).

Multi-layer urban canopy models have several layers within the canopy and form

part of the NWP boundary-layer scheme, rather than the surface layer scheme, with coupling between the two at every layer (Martilli et al., 2002; Kondo et al., 2005; Schoetter et al., 2020). This avoids the use of simple relations such as exponential velocity profiles to extrapolate down from the bottom atmospheric level and predict values within the canopy. The time- and horizontally space-averaged (double-averaged) equations of motion are solved with terms explicitly representing turbulence and form drag, enabling a more physically-based parametrisation. Multiple levels within the canopy also in theory enable multiple sources (for example, of anthropogenic emissions) and two-way exchanges with the built environment at multiple heights.

The multi-layer approach becomes increasingly appealing as NWP and climate models move to sub-kilometre horizontal grid lengths (Barlow et al., 2017; Lean et al., 2019), where neighbourhood scale surface characteristics start to become resolved. The flow becomes more statistically similar within each model grid cell, consistent with solving double-averaged equations.

NWP systems that are coupled to multi-layer urban canopy models have been shown to give improved wind speed and temperature prediction in the canopy in comparison with simple MOST surface representations (Gutiérrez et al., 2015), and also compared to single-layer urban canopy models in the case of temperature (Salamanca et al., 2011).

Hamdi and Masson (2008) and Masson and Seity (2009) modified a single-layer urban canopy scheme (Masson, 2000) to include multiple layers within the canopy rather than using an aerodynamical resistance network, but retained coupling at only the first atmospheric model level above the canopy. The approach is less computationally expensive than that of Martilli et al. (2002). However, it does not permit horizontal advection within the canopy, which is particularly important when there are abrupt changes in surface characteristics, e.g. between mid-rise and high-rise buildings in a central business district.

Much of the inspiration for urban canopy turbulence and drag parametrisation development has come from the vegetation canopy literature. The vegetation canopy top shear layer is viewed as a plane mixing-layer (Raupach et al., 1996), where the drag of the canopy elements reduces the flow velocity below the canopy top and causes an inflection in the double-averaged velocity profile, which in turn generates Kelvin-Helmholtz waves. The latter themselves undergo secondary instabilities that lead to the formation of large three-dimensional eddies. Vegetation canopy elements are usually either very close together (for example in wheat crops) or form a porous mesh (for example the foliage in a rainforest crown), so the mixing-layer eddies generated at canopy top are much larger than the separation of canopy elements (Raupach et al., 1996). These eddies are not local to the canopy elements and are the dominant turbulent motions in the canopy, a point that supports the use of a constant turbulent length scale in vegetation canopy models (Finnigan, 2000; Harman and Finnigan, 2007; Finnigan et al., 2015).

There are distinct differences between urban and vegetation canopies. The shear generated at the top of urban canopies is more local to the canopy elements than in vegetation canopies (Coceal et al., 2007a). Also, flow separation occurs at the edges of buildings causing vortex shedding and sometimes also turbulent flapping motions at canopy top (Coceal et al., 2007b; Perret and Savory, 2013). In current urban canopy models that solve the double-averaged equations, a constant turbulent length scale is often used throughout the entire depth of the canopy (Santiago and Martilli, 2010; Schoetter et al., 2020), and the mixing-layer analogy is sometimes used as justification (Hamdi and Masson, 2008). To evaluate this assumption, the extent to which canopy top mixing-layer type turbulence contributes to momentum transport within different urban canopy geometries requires investigation.

Additionally, the solid fraction in urban canopies is typically much larger than in vegetation canopies. The flow has to deviate more around the obstacles, and time-averaged flow patterns exhibit appreciable dispersive transport of momentum which is distinct from turbulent transport. A recent study of a realistic urban canopy geometry conducted by Giometto et al. (2016) found that dispersive momentum flux (DMF) can be as significant as turbulent momentum flux (TMF), which is greater than previously thought. Also, Schmid et al. (2019) argue that due to the non-negligible solid fraction of the urban canopy, more attention needs to be paid to the formal definition of the spatial average operator. When the intrinsic spatial average (an average only within the fluid volume) is applied to vertical derivatives of flow quantities, a generally overlooked term appears that accounts for changing solid fraction with height (see Sect. 4.4.2). The importance of including this term in urban canopy turbulence closures for velocity prediction needs to be investigated.

Despite its well-known limitations, a first-order momentum mixing length turbulence closure approach has been successfully applied in vegetation canopies (Poggi et al., 2004; Harman and Finnigan, 2007), and is simple and flexible requiring no extra prognostic equations. We take inspiration from this pragmatic approach and in Sect. 4.4.4 formulate a momentum mixing length closure suitable for urban canopies, which following Schmid et al. (2019) accounts for the non-negligible urban solid fraction.

There have been various investigations of turbulent and dispersive momentum transport in urban canopies (e.g. Roth, 2000; Belcher, 2005; Coceal et al., 2007a; Takimoto et al., 2011; Nazarian et al., 2020), but this study is unprecedented in the range of LES and DNS datasets available. We take advantage of this rich source of data to: 1) characterise the momentum mixing length behaviour in the urban surface layer and propose a general momentum mixing length profile suitable for a wide range of urban flows (Sects. 4.5.1–4.5.5), 2) determine the impact on predicted velocity when the term accounting for solid fraction height variation is included within the turbulence closure (Sect. 4.5.6), 3) test the mixing-layer analogy for turbulence within urban canopies (Sect. 4.5.7), and 4) explain the differences in DMF characteristics across geometries to motivate future DMF

parametrisations (Sect. 4.5.8).

4.3 CFD Datasets

4.3.1 Large-eddy Simulations

The analysis draws primarily on LES datasets described in Nazarian et al. (2020). A suite of simulations were carried out for idealised urban-like staggered and aligned arrays of cubes of uniform height. The wind was oriented perpendicular to the array, and the stratification was neutral. The cases we study have packing densities (planar area fraction occupied by obstacles) $\lambda_p = 0.0625, 0.11, 0.16, 0.25, 0.35, 0.44$ for staggered cubes, and $\lambda_p = 0.0625, 0.44$ for aligned cubes. A summary of the LES datasets is given in Table 4.1. Schematics in Figs. 4.1a and b are illustrative of the aligned and staggered geometries respectively. The simulations were performed using the Parallelised Large-eddy Simulation Model (PALM) which solves the non-hydrostatic incompressible Boussinesq equations (Raasch and Schröter, 2001; Letzel et al., 2008; Maronga et al., 2015). The sub-grid turbulence parametrisation is based on a 1.5-order closure (Deardorff, 1980) that involves solving the sub-grid scale (SGS) turbulent kinetic energy (TKE) equation.

The flow is driven by a constant pressure gradient force $F_p = \rho u_\tau^2 / H$, where ρ is the density of dry air (taken to be 1 kgm^{-3}), $u_\tau \approx 0.21$ ms^{-1} is the wall friction velocity, $H = 7.4h$ is the domain height, and h is the mean average height of the obstacles. The grid length in the x, y and z directions, Δ_{xyz}, is equal to $h/32$, except above $z = 4h$ where Δ_z slowly increases.

The Reynolds number of the flow is $Re = Uh/\nu \approx 10^6$ which is in the fully rough regime. Here U is the velocity at the top of the domain and ν is the molecular viscosity of air. It has been demonstrated using LES that flow through cube arrays has weak dependency on Re between 5×10^3 and 5×10^6 (Xie and Castro, 2006). For momentum the boundary conditions are no-slip at the ground and building surfaces, free-slip at the domain top, and periodic in the horizontal. Spin up time is $125h/u_\tau$, and data is output every 20 time steps which corresponds to a time interval of 40 s or $0.46h/u_\tau$. The time-averaging interval is $250h/u_\tau$. The time-averaged data is also ensemble averaged over repeating units to effectively increase the averaging time.

4.3.2 Direct Numerical Simulations

Several DNS datasets are included in the analysis as summarised in Table 4.1. Unlike in the LES approach, there is no sub-grid parametrisation in DNS and turbulent scales are resolved through the majority of the dissipation spectrum. As seen in Table 4.1, a compromise is made by reducing Re due to computational demands.

Chapter 4. Turbulence Characteristics Across a Range of Idealised Urban Canopy Geometries

Dataset	Case			Method	N_x	N_y	H	Re
N-0625-S	0.0625	S 0°	cb	LES	6	3	$7.4h$	10^6
N-11-S	0.11	S 0°	cb	LES	6	3	$7.4h$	10^6
N-16-S	0.16	S 0°	cb	LES	6	3	$7.4h$	10^6
N-25-S	0.25	S 0°	cb	LES	6	3	$7.4h$	10^6
N-35-S	0.35	S 0°	cb	LES	6	3	$12h$	10^6
N-44-S	0.44	S 0°	cb	LES	6	3	$7.4h$	10^6
N-0625-A	0.0625	A 0°	cb	LES	5	3	$7.4h$	10^6
N-44-A	0.44	A 0°	cb	LES	5	3	$7.4h$	10^6
B-25-A-0°	0.25	A 0°	cb	DNS	8	8	$8h$	4750
B-25-A-45°	0.25	A 45°	cb	DNS	8	8	$8h$	4750
C-33-A-0°	0.33	A 0°	cd	DNS	6	3	$8h$	6500
C-33-A-45°	0.33	A 45°	cd	DNS	6	4	$12h$	7500

Table 4.1:: LES and DNS datasets: prefixes N, B, and C represent data from Nazarian et al. (2020), Branford et al. (2011) and Castro et al. (2017) respectively. Under "Case" numbers correspond to λ_p, S and A denote staggered and aligned respectively, and cb and cd denote cubes and cuboids respectively. The computational domains have N_x and N_y buildings in the x and y dimensions respectively. H is the domain height.
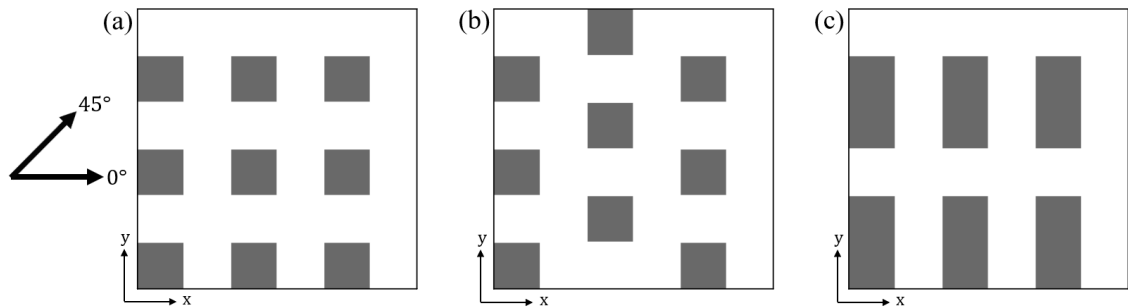
Figure 4.1: Plan view of selected geometries – the $\lambda_p = 0.25$ (a) aligned and (b) staggered cube geometries, and (c) $\lambda_p = 0.33$ aligned cuboid geometry. The large black arrows denote the 0° and 45° driving flow directions. Note that only a subsection of the domains is shown here.

Branford et al. (2011) conducted simulations of flow through an aligned array of $\lambda_p = 0.25$ cubes (see Fig. 4.1a for a schematic). Castro et al. (2017) documented simulations for an aligned array of $\lambda_p = 0.33$ cuboids, with cuboid length to width ratio of $1/2$ and height to length ratio of 1, where the long faces were orientated perpendicular to the flow (see Fig. 4.1c for a schematic). Both studies had neutral stratification, and forcing flow directions of 0° and 45° to the normal of the building faces. $\Delta_{xyz} = h/32$ throughout the entirety of each domain. All time-averaged data are also ensemble-averaged over repeating units.

4.4 Double-averaging Theory

In this section the double-averaged momentum equation and first-order momentum mixing length closure parametrisation of the TMF term are given. The definitions of the spatial average operator and spatial averaging theorem are first presented, since they are necessary in deriving budget equations and parametrisations. The intrinsic first-order momentum mixing length closure is used in later sections to investigate its use as an urban canopy turbulence closure model and to explore the turbulence behaviour across different canopy geometries. Equations are given using the intrinsic average and comprehensive average (where the spatial average is done over the fluid and solid volume). Following Schmid et al. (2019), the importance of representing λ_p height variation in the turbulence closure for predicted values of velocity is investigated in the context of both horizontal averaging approaches (see Sect. 4.5.6).

4.4.1 Intrinsic and Comprehensive Averaging

In NWP models flow through canopies is often modelled at grid lengths much larger than the typical turbulent eddies and obstacle wakes. An increasingly common approach in such circumstances is to apply to the instantaneous equations temporal averaging over a longer interval than the time scale of the slowest eddies and spatial averaging over a length scale greater than the largest spatial deviations in the flow (Raupach and Shaw, 1982; Nikora et al., 2007; Martilli and Santiago, 2007). A one-dimensional representation is taken, assuming quasi-horizontal homogeneity of the flow and canopy geometry within vertically thin horizontal-averaging slabs. Terms arise representing the effects of turbulence, form drag and persistent mean flow structures on vertical transport of momentum and scalars, and can subsequently be parametrised.

In vegetation canopies the obstacles are considered to occupy a negligible fraction of the canopy, and the intrinsic and comprehensive (also known as superficial) averages are equivalent (Finnigan, 2000). In porous media hydrodynamics, as in urban canopies, the volume fraction occupied by obstacles can be more significant. At any given height it is proportional to λ_p and it is well known that vertical changes in λ_p should be treated when applying the spatial average operator (Nikora et al., 2007).

The use of the operators $\langle \phi \rangle$, $\overline{\phi}$, $\tilde{\phi}$ and ϕ', on a variable ϕ defined only within the fluid region, denote its spatial average, time average, dispersive fluctuations ($\tilde{\phi} = \overline{\phi} - \langle \overline{\phi} \rangle$), and turbulent fluctuations ($\phi' = \phi - \overline{\phi}$) respectively. The intrinsic and comprehensive spatial operators are defined by Whitaker (1999) as

$$\langle \phi \rangle_I(t, z) = \frac{1}{V_f} \int_{x,y,z \in V_f} \phi(t, x, y, z) \, dV, \tag{4.1}$$

and

$$\langle\phi\rangle_C(t,z) = \frac{1}{V}\int_{x,y,z\in V_f}\phi(t,x,y,z)\,dV, \tag{4.2}$$

respectively. Here x, y and z are spatial coordinates with z in the vertical, and t is time. $\epsilon(z) = 1 - \lambda_p(z)$ is the fluid fraction: the ratio of fluid volume within a thin horizontal-averaging slab, V_f, to the total volume of the slab including the solid volume, V. The relationship between the comprehensive (subscript C) and intrinsic (subscript I) average of a quantity ϕ is given by $\langle\phi\rangle_C = \epsilon\langle\phi\rangle_I$.

If ϕ is a non-zero constant within the fluid, the dispersive fluctuations are non-zero and zero when the comprehensive and intrinsic spatial average operators are used respectively. Non-zero dispersive fluctuations when ϕ is constant influence the interpretation of quantities involving dispersive fluctuations such as the DMF and the wake production term in the TKE budget. Also, the application of the comprehensive operator twice results in $\langle\langle\phi\rangle_C\rangle_C = \epsilon\langle\phi\rangle_C$, whereas for the intrinsic operator $\langle\langle\phi\rangle_I\rangle_I = \langle\phi\rangle_I$. This means factors of ϵ appear in parametrisations of comprehensive spatially averaged quantities when they are functions of spatially averaged parameters.

There has been some debate in the recent literature on whether the intrinsic or comprehensive spatial average should be used in urban canopy modelling (Xie and Fuka, 2018; Schmid et al., 2019). The double-averaged momentum equation (and budget equations in general) derived using either method are equally valid if done correctly. Equivalently to solving the intrinsic double-averaged momentum equation, one could solve the comprehensive double-averaged momentum equation using parameters that have also been derived using the comprehensive average, and then convert the predicted comprehensive velocity to the intrinsic velocity via division by $\epsilon(z)$. Intrinsic average values are used here since they are more directly representative of the fluid and hence easier to interpret physically. However, neither spatial averaging approach is being advocated in a parametrisation context.

4.4.2 Spatial Averaging Theorem

The relation between averages of spatial derivatives and spatial derivatives of averages is given by the spatial averaging theorem (Whitaker, 1999). For intrinsic averages

$$\left\langle\frac{\partial\phi}{\partial x_i}\right\rangle_I = \frac{\partial\langle\phi\rangle_I}{\partial x_i} + \frac{\langle\phi\rangle_I}{\epsilon}\frac{\partial\epsilon}{\partial x_i} + \frac{1}{V_f}\iint_{S_{\text{int}}}\phi n_i\,dS, \tag{4.3}$$

and for comprehensive averages

$$\left\langle\frac{\partial\phi}{\partial x_i}\right\rangle_C = \frac{\partial\langle\phi\rangle_C}{\partial x_i} + \frac{1}{V}\iint_{S_{\text{int}}}\phi n_i\,dS, \tag{4.4}$$

Chapter 4. Turbulence Characteristics Across a Range of Idealised Urban Canopy Geometries

where x_i ($x_1 = x$, $x_2 = y$, $x_3 = z$) is spatial location, S_{int} is the interface between the fluid and solid regions, and n_i is the unit vector normal to the interface directed from fluid to solid.

The first term on the right-hand side of Eq. 4.3 is the spatial derivative of the intrinsic average ϕ. The second and third terms account for variations in ϵ (i.e. changes in averaging volume) and discontinuities in flow properties over the surface of obstacles respectively. The second term does not appear in Eq. 4.4 since the comprehensive averaging region does not change with height. The first and second terms in the comprehensive spatial averaging theorem have equivalent interpretations to the first and third terms in the intrinsic spatial averaging theorem.

For horizontal derivatives ($i = 1, 2$), the second term on the right-hand side of Eq. 4.3 is zero, since the canopy is assumed horizontally homogeneous within the averaging region, so that ϵ is only a function of z. The third term also vanishes for horizontal derivatives if ϕ is constant at the fluid-solid interface, as is the case for velocity due to the no-slip boundary condition. However, for example pressure is variable at the interface, tending to be larger at the windward than leeward obstacle faces. It is the discontinuity in the pressure field over obstacles that gives rise to form drag.

For vertical derivatives ($i = 3$), the second term on the right-hand side of Eq. 4.3 is non-zero everywhere that $\epsilon(z)$ varies and $\langle \phi \rangle_I \neq 0$. The third term on the right-hand side is only zero for vertical derivatives of quantities like velocity, where $\phi = 0$ at the vertical facing interfaces. Unlike in the horizontal, the tops of the obstacles do not have adjacent fluid-solid interfaces, as the bottoms of the obstacles interface with the ground. Therefore, even if ϕ is constant at the fluid-solid interfaces, so long as $\phi > 0$ there is no cancellation from the adjacent surface integral at the ground.

A special case exists for vertical derivatives when at height z, ϕ in the fluid has the same value as at the fluid-solid interface, and the second and third terms cancel (Schmid et al., 2019). This applies for example to a well-mixed tracer.

4.4.3 Double-averaged Momentum Equation

The approach of solving the double-averaged momentum equations in canopies was first developed by Wilson and Shaw (1977) and Raupach and Shaw (1982). The influence of changing solid fraction was treated as negligible in the context of vegetation canopies, where comprehensive and intrinsic averaged values are approximately equal.

The double-averaged momentum equation can be obtained by applying the time-averaging operator to the instantaneous momentum equation to obtain the time-averaged momentum equation, then applying the spatial averaging operator, taking particular care with use of the spatial averaging theorem. The intrinsic and comprehensive double-averaged momentum equations for a statistically stationary, horizontally homo-

geneous flow at height z in the canopy are given by (Schmid et al., 2019)

$$\frac{\partial \langle \overline{u_i' w'} \rangle_I + \langle \tilde{u}_i \tilde{w} \rangle_I}{\partial z} + \frac{1}{\epsilon} \left(\langle \overline{u_i' w'} \rangle_I + \langle \tilde{u}_i \tilde{w} \rangle_I \right) \frac{\partial \epsilon}{\partial z} = \langle F_p \rangle_I - \frac{1}{\rho} \left\langle \frac{\partial \tilde{p}}{\partial x_i} \right\rangle_I, \quad (4.5)$$

and

$$\frac{\partial \langle \overline{u_i' w'} \rangle_C + \langle \tilde{u}_i \tilde{w} \rangle_C}{\partial z} = \langle F_p \rangle_C - \frac{1}{\rho} \left\langle \frac{\partial \tilde{p}}{\partial x_i} \right\rangle_C, \quad (4.6)$$

respectively. Here ρ is the density of dry air, p is pressure, F_p is a volumetric body force driving the flow and u_i are velocity components ($u_1 = u$, $u_2 = v$, $u_3 = w$). It has been assumed that atmospheric stability is neutral, that the Coriolis force and molecular transport are negligible, and that the viscous drag can be neglected since it is usually only a few percent of the total drag as discussed in Leonardi and Castro (2010).

The first and second terms on the left-hand side of Eqs. 4.5 and 4.6 are the gradients of the TMF and DMF respectively. They are generally negative within the canopy, while above the canopy the TMF gradient is positive and the DMF gradient is negligible.

The third and fourth terms on the left-hand side of Eq. 4.5, which are not usually included in urban canopy literature, appear due to the second term on the right-hand side of Eq. 4.3. When $\epsilon(z)$ increases with height, vertical momentum transport occurs through a larger cross-sectional area, and consequently the intrinsic averaged TMF and DMF decrease. The extra terms offset this effect, such that the contribution of the momentum fluxes to the double-average momentum equation are not underestimated.

The first term on the right-hand side of Eqs. 4.5 and 4.6 is the constant pressure gradient force. It is a body force applied uniformly throughout the fluid and drives the flow in the CFD simulations. It is noted here that a mean streamwise pressure gradient is not actually present within the fluid in the CFD simulations, so $\langle F_p \rangle$ does not arise from spatial averaging of the time-averaged pressure gradient term, $-(1/\rho)\partial \overline{p}/\partial x_i$, and should be included as a separate term in the instantaneous momentum equation when deriving Eq. 4.5. The second term on the right-hand side of Eqs. 4.5 and 4.6 is the form drag exerted by the obstacles and is the sink of momentum in the canopy. It appears after spatial averaging of the time-averaged pressure gradient term.

4.4.4   Parametrisation of Momentum Fluxes

K-theory is often used to parametrise the TMF term in Eqs. 4.5 and 4.6. The momentum eddy-diffusivity $\langle K_{m,i} \rangle$ can be represented using a first-order momentum mixing length closure approach, where $\langle l_{m,i} \rangle$ is the momentum mixing length. $\langle K_{m,i} \rangle$ and $\langle l_{m,i} \rangle$ are parameters representing the global properties of the flow at height z, so are spatially

averaged. The turbulence closure formulation for intrinsic averages is then given by

$$
\begin{aligned}
\langle \overline{u_i'w'} \rangle_I &= - \left\langle \langle K_{m,i} \rangle_I \frac{\partial \overline{u}_i}{\partial z} \right\rangle_I = - \left\langle \left\langle \langle l_{m,i} \rangle_I^2 \left| \frac{\partial \overline{u}_i}{\partial z} \right| \right\rangle_I \frac{\partial \overline{u}_i}{\partial z} \right\rangle_I \\
&= - \langle l_{m,i} \rangle_I^2 \left\langle \left| \frac{\partial \overline{u}_i}{\partial z} \right| \right\rangle_I \left\langle \frac{\partial \overline{u}_i}{\partial z} \right\rangle_I \\
&\approx - \langle l_{m,i} \rangle_I^2 \left| \frac{\partial \langle \overline{u}_i \rangle_I}{\partial z} + \frac{\langle \overline{u}_i \rangle_I}{\epsilon} \frac{\partial \epsilon}{\partial z} \right| \left(\frac{\partial \langle \overline{u}_i \rangle_I}{\partial z} + \frac{\langle \overline{u}_i \rangle_I}{\epsilon} \frac{\partial \epsilon}{\partial z} \right),
\end{aligned}
\tag{4.7}
$$

and for comprehensive averages by

$$
\begin{aligned}
\langle \overline{u_i'w'} \rangle_C &= - \left\langle \langle K_{m,i} \rangle_C \frac{\partial \overline{u}_i}{\partial z} \right\rangle_C = - \left\langle \left\langle \langle l_{m,i} \rangle_C^2 \left| \frac{\partial \overline{u}_i}{\partial z} \right| \right\rangle_C \frac{\partial \overline{u}_i}{\partial z} \right\rangle_C \\
&= - \frac{1}{\epsilon} \langle \langle l_{m,i} \rangle \rangle_C^2 \left\langle \left| \frac{\partial \overline{u}_i}{\partial z} \right| \right\rangle_C \left\langle \frac{\partial \overline{u}_i}{\partial z} \right\rangle_C \\
&\approx - \frac{1}{\epsilon^3} \langle l_{m,i} \rangle_C^2 \left| \frac{\partial \langle \overline{u}_i \rangle_C}{\partial z} \right| \frac{\partial \langle \overline{u}_i \rangle_C}{\partial z}.
\end{aligned}
\tag{4.8}
$$

The modulus operator ensures $\langle K_{m,i} \rangle$ is positive and that turbulent diffusion is only down-gradient. The approximation $\langle |\partial \overline{u}_i / \partial z| \rangle = |\langle \partial \overline{u}_i / \partial z \rangle|$ is made in the last line of Eqs. 4.7 and 4.8, and assumes flow is only down-gradient. The approximation is needed to write the momentum flux in terms of the horizontally-averaged velocity. The ϵ terms in Eq. 4.7 occur due to the second term on the right-hand side of the intrinsic spatial averaging theorem and ϵ^{-3} occurs in Eq. 4.8 due to consecutive applications of the comprehensive spatial averaging operator.

4.4.5 Application to Urban Canopy Geometry

When the urban canopy geometry is either asymmetric about the streamwise axis or has unequal components of the flow in the streamwise and spanwise axes, the turbulent flow exhibits different behaviour in the $i = 1$ and $i = 2$ axes. One could align the x axis with the streamwise axis and derive single turbulent parameters, but in NWP separate equations exist for the momentum equation in the x and y axes. Given urban morphology information such as the frontal area variation with flow angle, it is not inconceivable that parametrisations might be developed that account for flow direction relative to the two axes. We therefore analyse separately the $i = 1$ and $i = 2$ TMF components.

In real-world urban canopies the turbulence is never exactly the same along the two axes, but the 0° driving flow and B-25-A-45° simulations are special cases for which subscript i can be dropped from $\langle l_m \rangle$ and $\langle K_m \rangle$. In the 0° driving flow simulations turbulence is not the same in the two axes but $\langle \overline{v'w'} \rangle \approx 0$ so the $i = 2$ component of the turbulent momentum flux need not be represented. For B-25-A-45° the flow is symmetric in the streamwise axis and there are equal components of the flow in the streamwise

and spanwise directions, so that $\langle l_{m,1} \rangle = \langle l_{m,2} \rangle$ and $\langle K_{m,1} \rangle = \langle K_{m,2} \rangle$. In this study the $i = 1$ and $i = 2$ components only need to be retained for C-33-A-45° where the geometry is asymmetric about the streamwise axis.

A pragmatic approach to parametrising the DMF is to include it with the TMF on the left-hand side of Eq. 4.7 (Simón-Moral et al., 2017; Nazarian et al., 2020). Horizontally-averaged DMF can be negative or positive at different heights within the canopy, but when summed with the horizontally-averaged TMF the total tends to be negative. The DMF can thereby be parametrised using K-theory but avoiding the unphysical scenario where $\langle K_m \rangle$ becomes negative, which would occur if the DMF was parametrised separately.

K-theory assumes that turbulent fluctuations are related to local gradients. Although it seems plausible that downward transport of momentum from higher in the canopy leads to increased velocity lower in the canopy, it has not been demonstrated that there is a strong relation between DMF and local velocity gradients in urban canopies. Time-averaged motions might largely be determined by non-local forcings. For example recirculations within building wakes often span the entire depth of the canopy, and are likely largely driven by strong shear at roof level behind the buildings, rather than local velocity gradients within the wake. An analogy can be drawn from two-dimensional street canyon literature where it is well known that recirculation within the canyon can be modelled as solid body rotation (Caton et al., 2003). Recirculation is driven by the flow above the canyon and occurs due to the requirements that tangential stresses be continuous at cavity top and mass within the cavity be conserved. Flows in urban canopies consisting of cuboidal buildings are more three-dimensional in nature, and streamlines can diverge in the spanwise direction within building wakes, but it seems reasonable to assume canopy recirculations share some properties with two-dimensional street canyons.

Since the aim is for the first-order turbulence parametrisation presented here to be applicable to multi-layer urban canopy models in general and to analyse the turbulent flow properties using $\langle l_m \rangle$, it is chosen not to include the DMF in the turbulence closure. $\langle l_m \rangle$ can be interpreted as a length scale that describes only the turbulence. The horizontal-average and three-dimensional characteristics of the DMF are investigated across geometries in Sect. 4.5.8, as a first step towards developing separate parametrisations of DMF.

4.5 Results and Discussion

4.5.1 Mixing Length Within the Canopy

It is investigated whether $\langle l_m \rangle_I$ (calculated using Eq. 4.7) shares similar characteristics within the canopy across different idealised urban geometries and driving flow direc-

tions. Figures 4.2 and 4.3 correspond to the $0°$ and $45°$ driving flow datasets, respectively. In both figures, plots (a-e) correspond to intrinsic average profiles of velocity, TMF, DMF, the ratio of DMF to TMF and momentum mixing length, respectively. Figure 4.2f also shows $\langle l_m \rangle_I$ normalised by the maximum mixing length $\langle l_{m,\max} \rangle_I$ within the canopy. The DMF profiles are discussed later in Sect. 4.5.8.

4.5.1.1 $0°$ Driving Flow $\langle l_m \rangle_I$ Characteristics

The $0°$ simulation $\langle l_m \rangle_I$ profiles in Fig. 4.2e collapse reasonably well in Fig. 4.2f when normalised by $\langle l_{m,\max} \rangle_I$. The shear is largest near the surface and at canopy top so that $\langle l_m \rangle_I$ is smaller there. $\langle l_{m,\max} \rangle_I$ occurs at $z/h \approx 0.6$, since the minimum gradient of double-averaged velocity tends to occur near the middle of the canopy (Fig. 4.2a), but the magnitude of TMF increases with height within the canopy (Fig. 4.2b). This description of $\langle l_m \rangle_I$ is consistent with Coceal et al. (2006) for a $\lambda_p = 0.25$ staggered cube dataset and is qualitatively similar to the turbulent length scales presented in Fig. 9a of Nazarian et al. (2020).

From Fig. 4.2e it can be seen that $\langle l_{m,\max} \rangle_I$ does not vary monotonically with λ_p for either the aligned or staggered geometries. This has also been observed for staggered geometries when turbulent length scales are calculated with the sum of DMF and TMF, as presented by Nazarian et al. (2020). $\langle l_{m,\max} \rangle_I \approx 0.3$ across the $0°$ simulations apart from the N-11-S and N-16-S simulations which have $\langle l_{m,\max} \rangle_I \approx 0.43$.

The $\langle l_m \rangle_I$ peaks are broader for N-44-A, B-25-A-$0°$ and C-33-A-$0°$ than the other geometries since the double-averaged velocity profiles are approximately linear between $z/h = 0.15 - 0.85$, so that the gradient of double-averaged velocity varies little in the middle of the canopy. The $0°$ aligned simulations tend to have $\langle l_{m,\max} \rangle_I$ higher within the canopy than the $0°$ staggered simulations, since the double-averaged velocity gradient (or shear) near canopy top does not increase significantly until very close to canopy top in the $0°$ aligned simulations. For the same λ_p, the aligned geometries have larger double-averaged velocity and TMF than staggered geometries. The aligned geometries have unobstructed channelling regions (see Fig. 4.1a) where flow is fast and there is large shear, which promotes shear production of TMF.

The magnitude of TMF generally decreases with increasing λ_p throughout the canopy as seen in Fig. 4.2b, particularly for the staggered geometries. A possible explanation is that increasing λ_p results in less mean kinetic energy penetrating into the canopy, particularly for the staggered arrays where there is more flow obstruction, and therefore less conversion into TKE. TMF and TKE have broadly similar dependence on λ_p and aligned versus staggered canopy geometry as seen from Fig. 6 of Nazarian et al. (2020).

Between $z/h = 0.34 - 0.44$ the N-44-S simulation TMF becomes positive so that flow
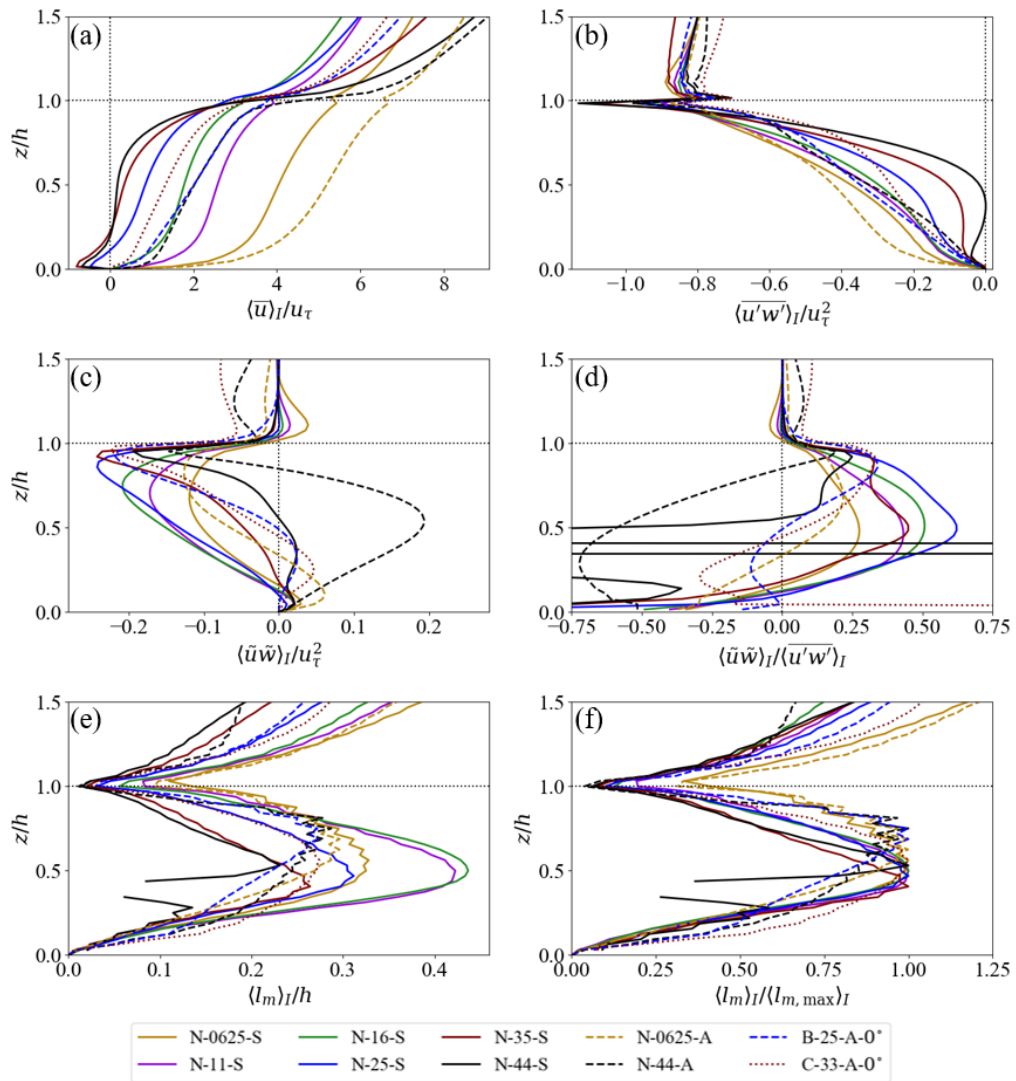
Figure 4.2: Intrinsic double-averaged profiles of the $0°$ driving flows. (a) x-component of velocity, (b) TMF, (c) DMF, (d) ratio of DMF to TMF, (e) $\langle l_m \rangle_I / h$, and (f) $\langle l_m \rangle_I / \langle l_{m,\text{max}} \rangle_I$.

is counter-gradient, and $\langle l_m \rangle_I$ cannot be computed. A first-order momentum mixing length closure approach is less suitable for very high-density idealised staggered arrays. Future investigations are required to explore whether this is the case in more realistic staggered type urban geometries, where there is more horizontal randomness in positioning of buildings.

The N-25-S, N-35-S and N-44-S simulations have negative double-averaged velocity near the surface as seen in Fig. 4.2a. Inspection of individual velocity profiles (not shown) indicates that regions of recirculation, both upstream of the windward and downstream of the leeward faces of the cubes, tend to have negative velocity near the surface. The N-25-S, N-35-S and N-44-S simulations have recirculation regions in a large portion of the flow. In these denser staggered configurations the contribution of negative near-surface flow in the recirculations dominates the spatial average. The aligned sim-

ulations have channelling regions where there is no obstruction of the flow, and there is large positive velocity near the surface. The contribution from such regions to the spatial average results in positive overall double-averaged velocity near the surface. The gradient of double-averaged velocity between the surface and the first grid point above the surface is negative in the N-25-S, N-35-S and N-44-S simulations, and along with TMF being positive above the surface (Fig. 4.2b), means that $\langle l_m \rangle_I$ at the first grid point above the surface cannot be computed, since transport is counter-gradient.

4.5.1.2   Impact of Flow Incidence Angle on $\langle l_m \rangle_I$ Characteristics

The 45° driving flow simulations in Fig. 4.3e have larger $\langle l_m \rangle$ in the canopy than their corresponding 0° driving flow simulations in Fig. 4.2e. This is because the 45° driving flow double-averaged velocity profiles (Fig. 4.3a) have small gradients near the middle of the canopy but significant TMF. There are two possible explanations for the large TMF (i) there is large transport of TMF down into the canopy (see Finnigan (2000), Eq. 2.11 for a definition) and (ii) there is large wake production of TMF. Either way, this indicates that a first-order momentum mixing length closure approach may be less appropriate for oblique flows, since the approach assumes TMF is related to the local flow, while wake production is related to horizontal as well as vertical velocity gradients.

Shear production of TMF is given by

$$P_s = -\overline{\langle u'_j u'_k \rangle} \frac{\partial \langle \overline{u}_i \rangle}{\partial x_j} - \overline{\langle u'_i u'_j \rangle} \frac{\partial \langle \overline{u}_k \rangle}{\partial x_j} - \frac{\langle \overline{u'_j u'_k} \rangle \langle \overline{u}_i \rangle + \langle \overline{u'_i u'_j} \rangle \langle \overline{u}_k \rangle}{\epsilon} \frac{\partial \epsilon}{\partial x_j}, \tag{4.9}$$

and wake production of TMF is given by

$$P_w = -\left\langle \widetilde{u'_j u'_k} \frac{\partial \tilde{u}_i}{\partial x_j} \right\rangle - \left\langle \widetilde{u'_i u'_j} \frac{\partial \tilde{u}_k}{\partial x_j} \right\rangle. \tag{4.10}$$

The third term on the right-hand side of Eq. 4.9 is a new term that does not appear in Eq. 2.11 of Finnigan (2000), and arises due to accounting for changes in λ_p with height when applying the spatial averaging operator to the time-averaged TMF budget equation.

In vegetation canopies it is generally assumed that P_s dominates P_w (Raupach et al., 1986). If the assumption can be made here for urban canopies, it implies there was little TMF production in the 45° simulations, since the gradient of double-averaged velocity gradient was small. Turbulence characteristics within the canopy may be largely non-local, meaning that at a point in space turbulence contributing to TMF is largely transported rather than produced locally. However, the assumption that wake production of TMF is negligible has not been tested for urban canopies, to the authors' knowledge. Wake production involves correlations between spatial fluctuations in the flow, which are known to be larger in urban canopies than in vegetation canopies, owing to their
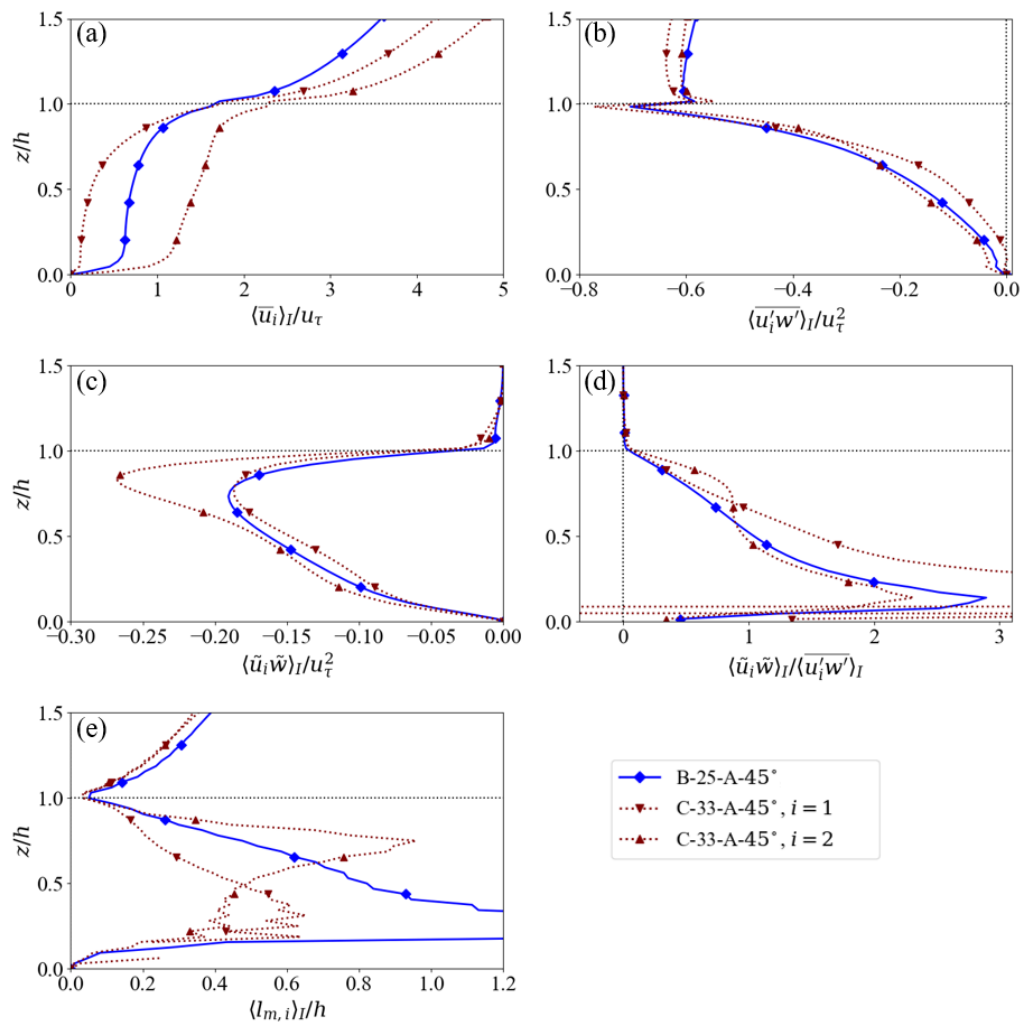
Figure 4.3: Intrinsic double-averaged profiles of the 45° driving flows. (a-e) are the same as in Fig. 4.2 except that both $i = 1$ and $i = 2$ components are given for C-33-A-45°. B-25-A-45° has only one curve because the canopy is symmetric about the flow direction, and the average of the $i = 1$ and $i = 2$ components is plotted.

larger solid fraction. The assumption may therefore be questionable, so that wake production of TMF could be significant.

Figure 4.3e shows that $\langle l_{m,\max} \rangle$ is largest for B-25-A-45°, and is equal to $2.2h$ at $z/h = 0.25$ (off the axis). This is unphysical considering that eddies cannot be so large due to the limiting effect of the ground, and the largest eddies are not expected to exceed h in any case. $\langle l_{m,\max} \rangle_I$ occurs at $z/h = 0.31$ and $z/h = 0.75$ for $\langle l_{m,x} \rangle_I$ and $\langle l_{m,y} \rangle_I$ respectively in the C-33-A-45° simulation. It is evident that turbulence characteristics can be significantly different in the x and y directions when the geometry of the urban canopy is not diagonally symmetric.

4.5.2 Mixing Length at Canopy Top

The behaviour of $\langle l_m \rangle_I$ at $z/h = 1$ can be most easily understood in terms of comprehensively averaged variables. Rearranging Eq. 4.8 for $\langle l_{m,i} \rangle_C^2$, and substituting into $\langle l_{m,i} \rangle_I^2 = \epsilon^2 \langle l_{m,i} \rangle_C^2$ gives

$$\langle l_{m,i} \rangle_I^2 = -\langle \overline{u_i'w'} \rangle_C \epsilon \left/ \left(\left| \frac{\partial \langle \overline{u}_i \rangle_C}{\partial z} \right| \frac{\partial \langle \overline{u}_i \rangle_C}{\partial z} \right) \right. . \tag{4.11}$$
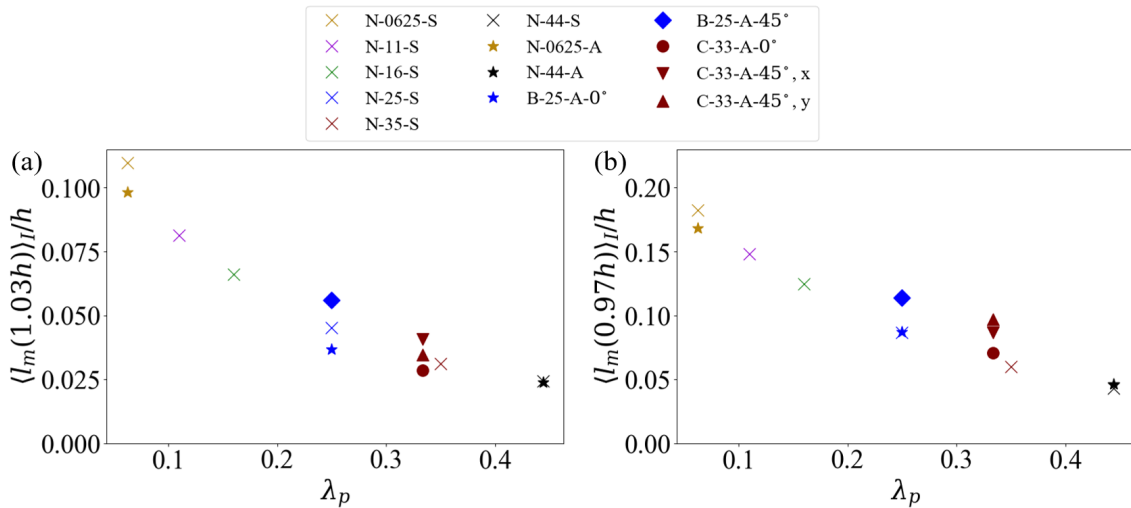
At the height of a perfectly flat roof ϵ, $\langle \overline{u_i'w'} \rangle_C$ and $\partial \langle \overline{u}_i \rangle_C / \partial z$ are finite but discontinuous (Schmid et al., 2019). $\partial \langle \overline{u}_i \rangle_C / \partial z$ increases at $z/h = 1$ due to the sudden contribution of velocity along the roofs, as opposed to beneath the roof where u_i does not contribute since it is not defined within the building. The discontinuities do not necessarily offset one another, so that $\langle l_{m,i} \rangle_I$ is also discontinuous at $z/h = 1$. Parametrising $\langle l_m(h) \rangle_I$ for situations with flat roofed buildings would be challenging. Rather than analyse $\langle l_m \rangle_I$ at h, we instead choose to focus on values just above and below. In practice roofs are not perfectly flat and there is a variety of building heights, so that $\langle l_m(h) \rangle_I$ might reasonably be approximated as a continuous function.

Plotted in Fig. 4.4a and b is $\langle l_m \rangle_I$ on the grid levels just above and below canopy top respectively. $\langle l_m \rangle_I$ is small near canopy top since there are large velocity gradients. $\langle l_m(1.03h) \rangle_I$ and $\langle l_m(0.97h) \rangle_I$ are between 2 and 10 times smaller than $\langle l_{m,\mathrm{max}} \rangle_I$. $\langle l_m(1.03h) \rangle_I$ is approximately a factor of 2 smaller than $\langle l_m(0.97h) \rangle_I$, because $\langle l_m(1.03h) \rangle_I$ has velocity gradient contributions from just above the roofs where there is large shear.

$\langle l_m(1.03h) \rangle_I$ and $\langle l_m(0.97h) \rangle_I$ tend to increase faster than linearly with decreasing λ_p. It is expected that $\langle l_m \rangle$ increases near canopy top with decreasing λ_p since there are fewer buildings generating canopy top shear. In the limit of an infinitely sparse canopy, flow should resemble that over a smooth wall, so that $\langle l_m \rangle \approx \kappa h$, where κ is the von Kármán coefficient. In the limit of a very dense canopy, flow should also resemble that over a smooth wall, except displaced by h so that $\langle l_m \rangle \approx \kappa(z - h)$, and $\langle l_m(h) \rangle \approx 0$. Although neither limit is reached in the geometries examined here, it provides some explanation for the $\langle l_m \rangle$ behaviour near canopy top.

4.5.3 Mixing Length Above Canopy Top

DMF occurs due to spatial deviations in the mean flow, and where it falls to zero can be used as a definition of the roughness sublayer height (Coceal et al., 2007c). As seen in Figs. 4.2d and 4.3d, by $z/h = 1.5$ DMF is generally negligible (apart from N-44-A and C-33-A-0° which is likely due to insufficient averaging time). $\langle l_m \rangle_I$ tends towards an approximately linear increase by $z/h = 1.5$, which is typical of inertial sublayer flow where $\langle l_m \rangle_I \approx \kappa(z - d)$. By inspecting $\langle l_m \rangle_I$, a linear portion was found to exist for $z/h = 1.5$–2.3 across simulations (not shown), and was identified as the inertial sublayer.

Chapter 4. Turbulence Characteristics Across a Range of Idealised Urban Canopy Geometries

Figure 4.4: (a) and (b) correspond to $\langle l_m \rangle_I$ at heights $1.03h$ and $0.97h$ respectively, plotted against λ_p.

Linear regression of $\langle l_m \rangle_I$ against z was performed in the inertial sublayer, where the gradient corresponds to κ. The κ results are plotted in Fig. 4.5. The N-44-A and C-33-A-0° simulations are excluded since they were not linear by $z/h = 1.5$, due to large DMF.

κ varies between 0.20 and 0.51, and has no clear relationship with canopy geometry. Alternative inertial sublayer height range definitions were tested, to investigate the sensitivity of κ. For 1.5–3.0h where top height was extended and 1.1–2.3h where bottom height was extended, the κ ranges were 0.18 to 0.41 and 0.22 to 0.51, respectively. Extending the top height resulted in the $l_{m,x}$ component of C-33-A-45° no longer being linear in the fitting portion, and its linear regression gave reduced κ compared to its original height range value, reducing the upper range of the κ values. Extending the bottom height had little effect on the range of κ values.

For varying magnitude pressure gradients, Nagib and Chauhan (2008) conducted experiments of smooth-wall high-Re pipe, channel and boundary layer flows, and found pressure gradient to influence κ, but by much less than the range of κ presented here. It has also been argued by Frenzen and Vogel (1995) that roughness influences κ through the ratio of TKE production and dissipation in the inertial sublayer. There are other studies which suggest that κ is not a universal constant in rough wall flows, as discussed by Leonardi and Castro (2010). For DNS of flow over packed beds (Breugem et al., 2006) and LES of a staggered array of cubes (Claus et al., 2012), values as low as 0.23 and ≈ 0.3 have been observed, respectively, by logarithmic fitting to simulated velocity in the inertial sublayer. However, to the authors' knowledge this is the first set of results to demonstrate such a range of κ values across a range of geometries in the urban canopy literature.

Jiménez (2004) suggests two conditions must be satisfied so that a region exists where

---

Chapter 4. Turbulence Characteristics Across a Range of Idealised Urban Canopy Geometries
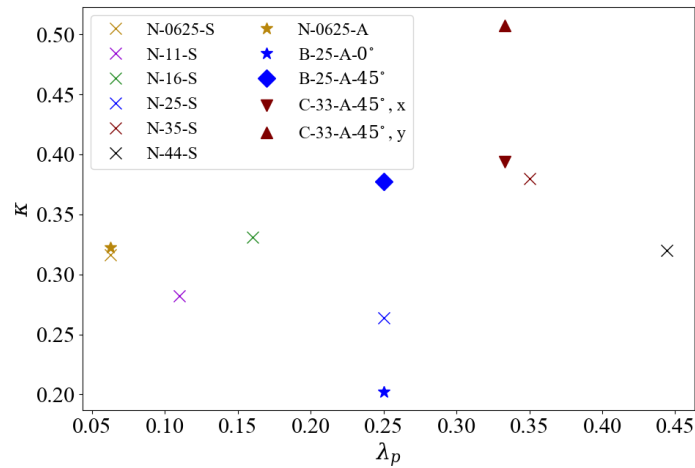
Figure 4.5: κ calculated as the gradient of linear regression between $\langle l_m \rangle_I$ and z for $z/h = 1.5$–2.3, plotted against λ_p.

the only relevant turbulent length scale is the distance from the wall and velocity is truly logarithmic. First $\delta/h > 40$–80, where δ is the boundary layer depth, so that the flow is far enough from the surface that inner-layer turbulence associated with roughness elements does not interact with it. Second $z/\delta < 0.15$, so that the flow is close enough to the wall to not interact with the outer-layer turbulence of scale δ. The first condition may not be met in urban areas under near-neutral atmospheric stability since the atmospheric boundary layer over deeper urban canopies may not grow to $\delta/h > 40$–80. This might explain some of the large variability in relations for z_0 and d which are often found using experimental datasets (e.g. Kent et al., 2017).

In CFD half-channel flow investigations domain height H places a limit on δ. The first condition is not met in the simulations presented here since $H/h = 8$. The second condition becomes $z/H < 0.15$, which is also not met since the region defined earlier as the inertial sublayer corresponds to $z/H = 0.19$–0.29. However, N-35-S and C-33-A-45° have $H/h = 12$, so that the region defined earlier as the inertial sublayer corresponds to $z/H = 0.125$–0.19. Roughly the lower half of the region is then close enough to the wall for the outer-scale turbulence to not interact with the flow according to Jiménez (2004), and might accurately be described as the logarithmic layer (i.e. inertial sublayer). It is therefore interesting that N-35-S, C-33-A-45° x-component and C-33-A-45° y-component have κ values of 0.38, 0.39 and 0.5 respectively, which are generally larger than the other values, and, with the exception of C-33-A-45° y-component, $\kappa \approx 0.4$. This provides tentative evidence that H used in urban canopy modelling can place limitations on δ, and lead to inadequate outer-scale separation.

That H might influence flow in the inertial sublayer does not affect the validity of results presented within the canopy. Turbulence statistics within the canopy have been demonstrated to converge with H by $H/h = 8$ in the DNS study of (Coceal et al., 2006)

and LES simulations with $H/h \approx 8$ have been shown to agree well with experiments (Xie and Castro, 2009; Nazarian and Kleissl, 2016).

4.5.4 General Characteristics of Mixing Length in Urban Canopies

The general features of the $\langle l_m \rangle_I$ profiles for uniform height, flat roofed geometries are summarised in a schematic in Fig. 4.6 and consist of: an increase from zero at the surface to a maximum around the middle of the canopy, a decrease until canopy top, where there is a discontinuity, and a rapid increase above $z/h = 1$, before transitioning to a linear increase by approximately $z/h = 1.5$. The vertical extent of the arrow reflects the fact that the aligned simulations have $\langle l_{m,\max} \rangle_I$ nearer canopy top with increasing λ_p, and that $\langle l_{m,\max} \rangle_I$ can be below the middle of the canopy for 45° driving flow simulations. $\langle l_{m,\max} \rangle_I / h \approx 0.3$ is a reasonable approximation apart from the 45° simulations which have much larger values.

4.5.5 Mixing Length Characteristics of a Variable Height Building Array

The schematic in Fig. 4.6 applies for uniform height, flat roofed buildings. Whether there are variable height, flat roofed buildings or there is a continuous distribution of building heights, $\epsilon(z)$ is still expected to have a significant influence on $\langle l_m \rangle_I$. Using LES Yoshida and Takemi (2018) found that there are multiple $\langle l_m \rangle$ local maxima and minima within the canopy for variable height, flat roofed buildings, and the amount corresponds to the number of building heights. The maxima and minima were larger for the taller buildings.

Xie et al. (2008) conducted a LES of flow through $\lambda_p = 0.25$ staggered cuboids with equal length and width, and varying heights. The horizontal layout was the same as that in Fig. 4.1b. Within each repeating unit there were 16 cuboids ($1 \times 0.27h$, $3 \times 0.63h$, $7 \times 0.98h$, $4 \times 1.33h$ and $1 \times 1.68h$). The dataset offers more realistic variability in $\epsilon(z)$ than uniform height roofs, and is used to investigate the influence of variable building height on the flow.

Plotted in Fig. 4.7a and b are the $\epsilon(z)$ and $\langle l_m \rangle_I$ profiles, respectively. Below h the momentum mixing length profile for the variable height array is similar to the schematic for the uniform building height arrays (Fig. 4.6). $\langle l_{m,\max} \rangle_I$ occurs at $z/h = 0.49$, which is almost identical to $z/h = 0.50$, the height at which $\langle l_{m,\max} \rangle_I$ occurs for N-25-S, a case with identical layout but with uniform height buildings. $\langle l_{m,\max} \rangle_I / h$ equals 0.41 which is 0.1 larger than the N-25-S value. This could be due to contributions from larger scale turbulence associated with buildings taller than the mean height, consistent with Yoshida and Takemi (2018).

Variable height $\langle l_m(h) \rangle_I / h$ was equal to 0.14, and can be compared with the N-25-S simulation at grid points just below and above $z/h = 1$, where $\langle l_m \rangle_I / h = 0.09$ and
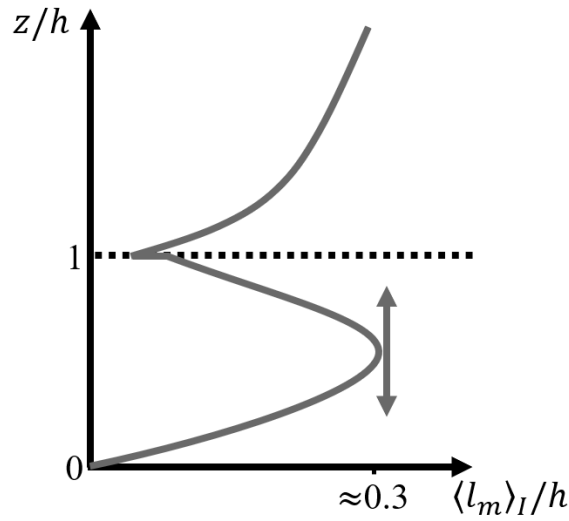
Figure 4.6: Schematic showing the main features of $\langle l_m \rangle_I$ across the various uniform height geometries. The double ended arrow indicates the range of heights over which $\langle l_{m,\max} \rangle_I$ occurs for the different geometries.

0.05, respectively. Smaller values occur for N-25-S because there is a larger proportion of roofs at the mean building height. Flow interacts with the roofs producing large double-averaged velocity gradients (i.e. shear). Using a LES of flow through a portion of Basel's urban canopy with asymmetric building height distribution, Giometto et al. (2016) showed that the double-averaged velocity inflection was strongest at the modal building height rather than h. This indicates that there is generally largest shear and smallest $\langle l_m \rangle_I$ at the modal building height, consistent with arguments presented here.

There are two less pronounced $\langle l_m \rangle_I$ minima above $z/h = 1$ compared to the minima at $z/h = 1$ in Fig. 4.7, and are a result of shear generated at the tops of the $1.33h$ and $1.68h$ buildings. However, within the canopy $\langle l_m \rangle_I$ minima did not occur at the tops of the $0.27h$ and $0.63h$ buildings. This is in contrast to Yoshida and Takemi (2018) who found that minima occurred at each building height. In their geometries there was a large proportion of buildings with the same height below the mean building height, which resulted in large shear at the height of the below mean height buildings. In the Xie et al. (2008) geometry presented here there was a small proportion of $0.27h$ and $0.63h$ buildings. Therefore, there was not much shear associated with the roofs at those heights, and the buildings were deep within the canopy where little time-mean flow penetrates, preventing large shear.

The transition to a linear $\langle l_m \rangle_I$ profile above $z/h = 1$ is much slower compared to the uniform height buildings. $z/h = 3.0 - 4.0$ was taken to represent the inertial sublayer since $\langle l_m \rangle_I$ was linear there, and a straight line was fitted in the region (see Fig. 4.7). Compared to the inertial sublayer fit there was generally a small decrease in $\langle l_m \rangle_I$ between $z/h = 1$–3. This is likely due to shear layers shed from the tops of the taller buildings.
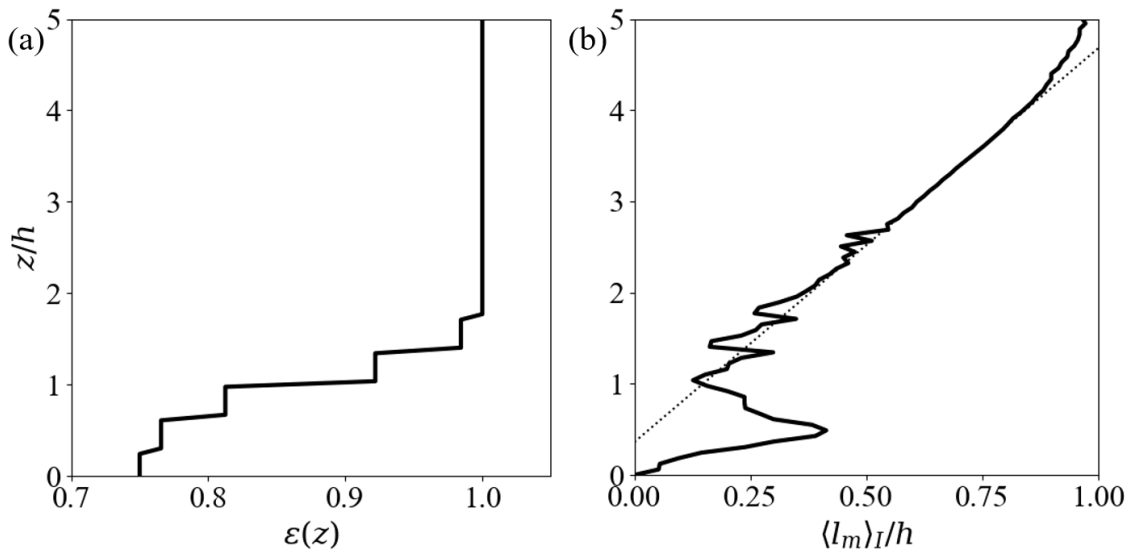
Figure 4.7: Panels (a) and (b) show the $\epsilon(z)$ and $\langle l_m \rangle_I$ profiles respectively, for the Xie et al. (2008) LES of $\lambda_p = 0.25$ staggered cuboids with variable building heights. The black dotted line in (b) is obtained from a linear fit to the solid black line between $z/h = 3.0$–4.0.

4.5.6 Importance of Accounting for Solid Fraction Variation in Mixing Length Turbulence Closures

The importance of accounting for $\epsilon(z)$ in the first-order momentum mixing length closure and the consequent effect on predicted $\langle \overline{u} \rangle$ is now investigated. The variable building height LES of Xie et al. (2008) is used since of the datasets available, its $\epsilon(z)$ is most representative of that in a real urban neighbourhood.

4.5.6.1 Impact of Accounting for Solid Fraction Variation on $\langle l_m \rangle$

Plotted in solid black and dashed blue in Fig. 4.8a are $\langle l_m \rangle_I$ calculated with and without the ϵ terms in Eq. 4.7 respectively. If the ϵ terms are excluded spikes occur at grid levels where there is a discontinuity in $\epsilon(z)$ (see Fig. 4.7a for the $\epsilon(z)$ profile), due to $\partial \langle \overline{u} \rangle_I / \partial z$ discontinuities. This is because at $\epsilon(z)$ discontinuities, in the limit of $\Delta_z \to 0$, $\langle \overline{u} \rangle_I$ has discontinuities of size

$$
\begin{aligned}
\langle \overline{u}(z + \Delta_z) \rangle_I - \langle \overline{u}(z - \Delta_z) \rangle_I &= \frac{\langle \overline{u}(z + \Delta_z) \rangle_C}{\epsilon(z + \Delta_z)} - \frac{\langle \overline{u}(z - \Delta_z) \rangle_C}{\epsilon(z - \Delta_z)} \\
&\approx \langle \overline{u}(z) \rangle_C \left(\frac{\epsilon(z - \Delta_z) - \epsilon(z + \Delta_z)}{\epsilon(z + \Delta_z)\epsilon(z - \Delta_z)} \right),
\end{aligned}
\tag{4.12}
$$

where the fact that $\langle \overline{u} \rangle_C$ is a continuous function has been utilised. When discretised, $\partial \langle \overline{u} \rangle_I / \partial z$ is not discontinuous but tends to be reduced compared to values above and below $\epsilon(z)$ discontinuities, as seen from inspecting the intrinsic average velocity profile (solid black line in Fig. 4.8c), most notably at $z/h = 1$ where $\epsilon(z)$ changes most. $\partial \langle \overline{u} \rangle_I / \partial z$

Chapter 4. Turbulence Characteristics Across a Range of Idealised Urban Canopy Geometries
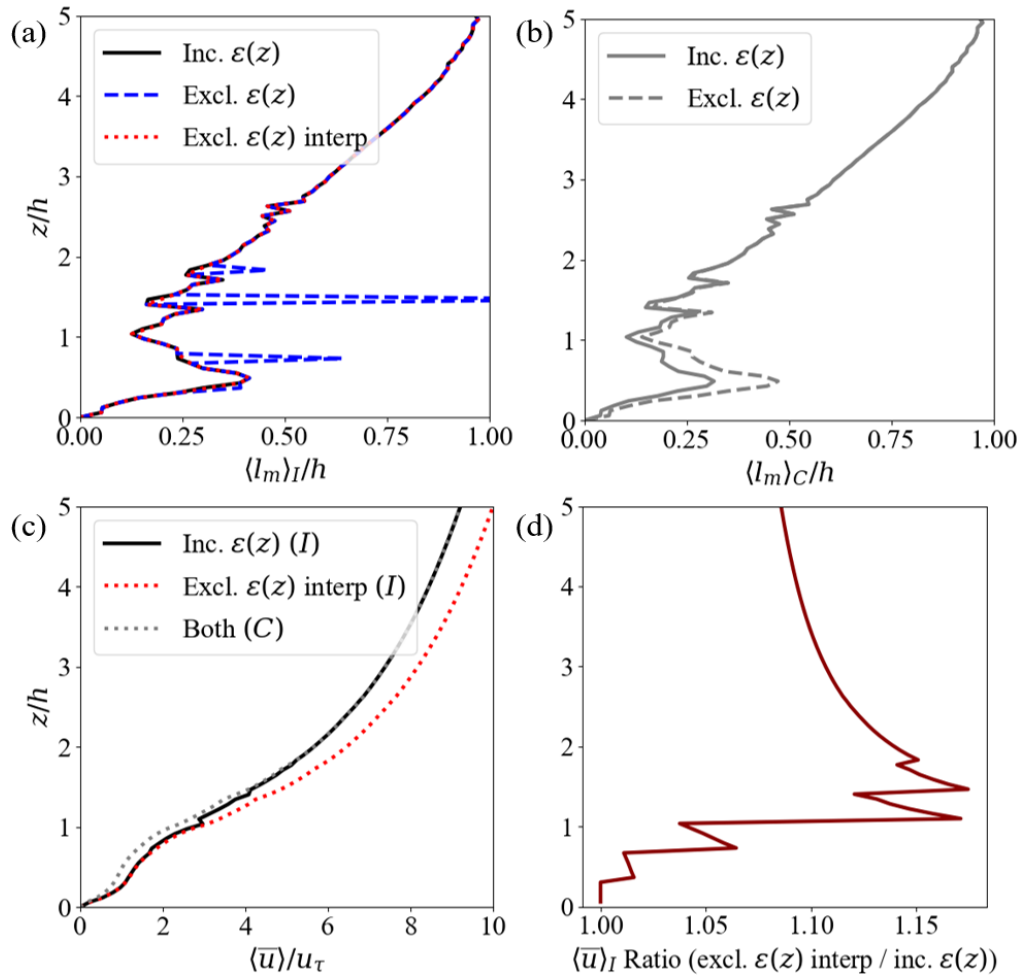
Figure 4.8: (a) Profiles of $\langle l_m \rangle_I$ calculated according to Eq. 4.7: including the ϵ term (black), excluding the ϵ term (dashed blue), and excluding the ϵ term followed by removing the spikes and interpolating (dotted red). (b) $\langle l_m \rangle_C$ calculated according to Eq. 4.8: including (solid) and excluding (dashed) the ϵ^3 factor. (c) Solution to Eq. 4.13 using the full $\langle l_m \rangle_I$ from (a) (solid black), using the interpolated $\langle l_m \rangle_I$ from (a) and excluding the ϵ term (red dotted), alongside the solution to Eq. 4.14 excluding the ϵ^3 factor and using the dashed grey $\langle l_m \rangle_C$ from (b) (dotted grey). (d) The ratio of the dotted red and solid black profiles from (c).

is reduced at $\epsilon(z)$ increases, because $\langle \overline{u} \rangle_I$ is small at the grid level above due to low velocity contributions from flow influenced by the no-slip condition along the roofs. At $z/h = 1$ where there is the largest change in $\epsilon(z)$, the velocity gradient is reduced to the point it turns negative, such that $\langle l_m \rangle_I$ is not well defined if the ϵ term is not included in its calculation (as seen from the absence of the dashed blue curve at $z/h = 1$ in Fig. 4.8a).

If taking the approach of not accounting for $\epsilon(z)$ variation, it would not be possible to incorporate the spikes into a general $\langle l_m \rangle_I$ parametrisation. The best one could do is to ignore the spikes and represent the smooth part of the $\langle l_m \rangle_I$ behaviour. Such an approach might be achieved by linearly interpolating between the points either side of the spikes and this is shown as a dotted red curve in Fig. 4.8a.

Plotted in solid and dashed grey in Fig. 4.8b are $\langle l_m \rangle_C$ calculated with and without accounting for $\epsilon(z)$ variation in Eq. 4.8, respectively. The two profiles are identical up to a factor of $\epsilon(z)^{3/2}$. Neither profile exhibits large spikes since $\langle \overline{u} \rangle_C$ is a continuous function and has small $\langle \partial \overline{u}/\partial z \rangle_C$ discontinuities. It is noted that $\langle l_m \rangle_C = \epsilon(z)\langle l_m \rangle_I$. This is consistent with inspection of the $\langle l_m \rangle_I$ and $\langle l_m \rangle_C$ curves plotted in Fig. 4.8a and 4.8b, when $\epsilon(z)$ variation is accounted for in both their calculations.

4.5.6.2 Impact of Accounting for Solid Fraction Variation on Predicted $\langle \overline{u} \rangle$

Here we investigate the impact on predicted velocity by accounting for solid fraction variation in the momentum mixing length closure formulation. To do so, TMF and $\langle l_m \rangle$ are taken to be known from the LES, and the corresponding double-averaged velocity is solved by discretising the momentum mixing length closure.

A simple discretisation of the intrinsic averaged closure (Eq. 4.7) is given by

$$u_{j+1} = u_j + \Delta_z \left(\frac{\pm (u'w')_{j+1/2}}{l_{m,j+1/2}} \right)^{1/2} - \frac{u_j(\epsilon_{j+1} - \epsilon_j)}{\epsilon_j}, \tag{4.13}$$

where time and spatial averaging symbols, and spatial indices i have been dropped for brevity. j labels the LES grid levels. The $\pm$ is to be taken as negative (positive) when the value within the modulus in Eq. 4.7 is positive (negative). Discretisation of the comprehensive averaged closure (Eq. 4.8) is given by

$$u_{j+1} = u_j + \Delta_z \left(\frac{\pm (u'w')_{j+1/2}\epsilon_{j+1/2}^3}{l_{m,j+1/2}} \right)^{1/2}, \tag{4.14}$$

where $\pm$ is negative (positive) when the value within the modulus in Eq. 4.8 is positive (negative).

The solution to Eq. 4.13 using $\langle l_m \rangle_I$ calculated including the ϵ term is plotted as solid black in Fig. 4.8c. As a simple matter of consistency, this solution reproduces the true $\langle \overline{u} \rangle_I$, since this was used along with $\langle \overline{u'w'} \rangle_I$ to derive $\langle l_m \rangle_I$. Plotted as dotted red in Fig. 4.8c is the solution using $\langle l_m \rangle_I$ calculated when the $\epsilon(z)$ term is excluded and spikes are interpolated. The second term on the right-hand side of Eq. 4.13 was dropped in the calculation for consistency with that approach. Inspecting the ratio of $\langle \overline{u} \rangle_I$ values when the $\epsilon(z)$ term is excluded and included (Fig. 4.8d), reveals that excluding the $\epsilon(z)$ term results in velocity overestimation of up to 17% just above h. Each time there is an $\epsilon(z)$ discontinuity the percentage error increases, and between discontinuities the percentage error decreases, since the magnitude of the error remains constant with increasing height, but the magnitude of the two velocities increases.

So long as the $\epsilon(z)^3$ factor is dropped in Eq. 4.14 as well as in the $\langle l_m \rangle_C$ calcula-

tion, then the factor cancels, and the solution is the same as when the $\epsilon(z)^3$ factor is included. Multi-layer canopy model turbulence closures based on comprehensive averaging therefore do not encounter errors in predicted velocity due to incorrect application of the comprehensive spatial averaging theorem to velocity gradients. The two solutions are plotted as one dotted gray curve in Fig. 4.8c.

4.5.7   Relationship Between Canopy Top Shear Length Scale and Mixing Length

Based on similarity arguments Finnigan et al. (2015) argued that when most of the momentum is absorbed as drag by the canopy elements rather than by the ground, then there is only one relevant length scale in the canopy $(S(z)C_d(z))^{-1}$, which can be interpreted as a drag length scale L_c (Belcher et al., 2003; Coceal and Belcher, 2004). Here $S(z)$ is the sectional obstacle area density (obstacle area facing the wind divided by canopy air volume) and $C_d(z)$ is the sectional drag coefficient. In dense vegetation canopies the approximation that $S(z)$ and $C_d(z)$ are constant with height is also often made. This is consistent with the mixing-layer analogy, which suggests that there is one dominant turbulent length scale in the canopy, determined by the shear length scale $L_s(h)$ associated with the canopy top mixing-layer.

With decreasing vegetation canopy density there is increasing flow penetration into the canopy, and there are length scales other than $L_s(h)$ that become important. For example those associated with eddies originating from shear near the surface (Watanabe and Kondo, 1990), and penetration of inner layer eddies into the canopy and von Kármán street vortexes (Poggi et al., 2004).

It is investigated here to what extent turbulence in urban canopies is dominated by mixing-layer eddies. If mixing-layer eddies are generated with length scale $L_s(h)$ due to the inflection in the double-average velocity profile at canopy top, and are dominant within urban canopies so that only they control turbulent mixing, it would be expected that $L_s(h) = \alpha \langle l_{m,\text{av}} \rangle$ across canopy geometries. α is a constant and $l_{m,\text{av}}$ is the depth averaged value of the momentum mixing length within the canopy.

The shear length scale is defined here as

$$L_{s,i}(z) = \langle \overline{u}_i \rangle_I \left(\frac{\partial \langle \overline{u}_i \rangle_I}{\partial z} + \frac{\langle \overline{u}_i \rangle_I}{\epsilon} \frac{\partial \epsilon}{\partial z} \right)^{-1}. \tag{4.15}$$

This is the same as the definition given by Raupach et al. (1996) but with the addition of the second term in the brackets, which is included to account for the influence of solid fraction on the intrinsic spatial average of the velocity gradient. The component label i has been retained to allow the possibility of the shear being different in the x and y axes, while the shear of vertical velocity is zero since $\langle \overline{w} \rangle_I = 0$.

Figure 4.9 shows $L_s(h)/\langle l_{m,\text{av}} \rangle_I$ plotted against λ_p. The $L_s(h)$ velocity gradient was
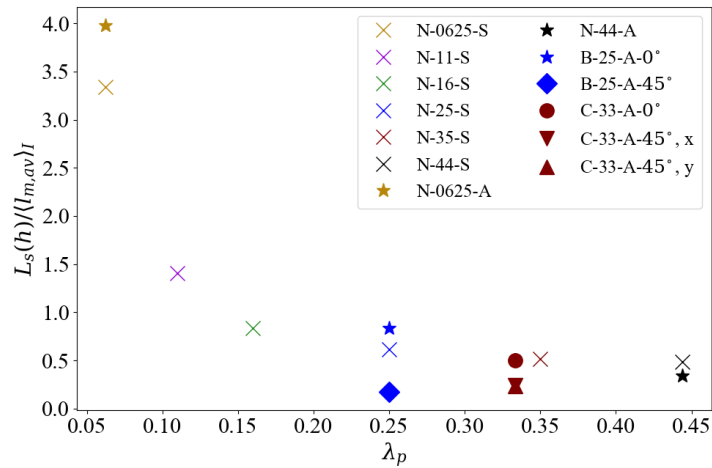
Figure 4.9: $L_s(h)/\langle l_{m,\text{av}}\rangle_I$ plotted against λ_p.

calculated between velocities at $z/h = 0.95$ and $z/h = 1.05$. For the $0°$ aligned and staggered cube geometries it can be seen that with decreasing λ_p the ratio $L_s(h)/\langle l_{m,\text{av}}\rangle_I$ increases faster than linearly. α is not constant suggesting that mixing-layer eddies are not always the dominant turbulence within urban canopies.

Inspection of individual velocity profiles reveals that velocity inflections occur at canopy top behind each roof, consistent with Letzel et al. (2008). The inflections are much weaker $\sim h$ downstream and extend little in the cross-stream. As suggested by Coceal et al. (2007a), the urban canopy top shear layer is highly heterogeneous and velocity profile inflections are local to individual buildings. As the canopy becomes sparser, fewer mixing-layer eddies are produced, and more flow penetrates into the canopy making turbulence increasingly likely to be associated with other turbulence production mechanisms.

Ghisalberti (2009) argues that in 'obstructed shear flows', where part of a flow is obstructed via a permeable medium, that the mixing-layer eddies generated at the interface between the permeable medium and unobstructed flow, cause environmental flows of this type to be dynamically similar. Ghisalberti (2009) observed that across canopy types (e.g. sediment beds, aquatic and terrestrial vegetation canopies, and coral reefs) the depth turbulence penetrates into the canopy is proportional to L_c. However, urban canopies were found to be an outlier with smaller penetration depth. In moderately-dense and dense vegetation canopies $L_s/h \approx 0.1 - 0.5$ (Raupach et al., 1996). For moderately-dense and dense urban canopies ($\lambda_p \geq 0.25$) presented here, L_s/h ranged between 0.06 and 0.16 (not shown). The mixing-layer eddies are generally smaller and more localised to the obstacles than in vegetation canopies, and explains why Ghisalberti (2009) found urban canopy turbulence to penetrate less deep into the canopy than in the other canopy types.

It can be seen from Fig. 4.9 that for the denser ($\lambda_p \geq 0.25$) $0°$ staggered cube geometries that $L_s(h)/\langle l_{m,\text{av}}\rangle_I$ varies less with λ_p. This suggests that mixing-layer eddies likely make a large contribution to turbulent mixing in those geometries. As seen in Figs. 4.2a and b, the velocity and TMF respectively are small within the canopy for the dense staggered geometries, since they have no unobstructed portions of the canopy. It is probable that most of the conversion of time-mean flow into turbulence occurs at canopy top, and is transported into the canopy.

The $45°$ simulations have lower $L_s(h)/\langle l_{m,\text{av}}\rangle_I$ values compared to the $0°$ simulations with the same λ_p (see Fig. 4.9). The $0°$ and $45°$ simulations with the same λ_p have similar $L_s(h)/h$ (not shown). The $45°$ simulations therefore have more TMF within the canopy but similar shear at canopy top. This means that it is unlikely that the larger TMF in the $45°$ simulations was associated with mixing-layer eddies and is more likely that TMF was due to wake production. This is unless the $45°$ simulations have some more efficient mode of transporting mixing-layer eddies into the canopy.

In summary, the relation $L_s(h) = \alpha\langle l_{m,\text{av}}\rangle_I$ does not hold across geometries, and turbulence is not dominated by mixing-layer eddies within the canopy, apart perhaps for the $0°$ dense ($\lambda_p \geq 0.25$) staggered geometries. It has been checked that these conclusions for the average momentum mixing length also apply for the maximum value of momentum mixing length.

4.5.8 Dispersive Momentum Flux Characteristics

As a preliminary step towards developing DMF parametrisations, the behaviour of the three-dimensional DMF fields and horizontally-averaged profiles are investigated across geometries. From Figs. 4.2c and 4.3c, it is seen that generally the horizontal-averaged DMF magnitude increases with height in the canopy until $z/h = 0.7$–0.95. The maximum magnitude of DMF tends to occur lower in the canopy for the sparser geometries. DMF is typically negative in the middle and just below the top of the canopy, and positive near the surface.

Horizontal cross-sections of DMF through canopy geometry repeating units at $z/h = 0.75$ are shown in Fig. 4.10. Dispersive velocities are calculated using intrinsic averages to simplify interpretation as explained in Sect. 4.4.1. Inspecting Figs. 4.10a,c,d,e reveals that DMF is generally negative along the leeward face of the buildings ($\tilde{u} < 0$, $\tilde{w} > 0$) and positive along the windward face ($\tilde{u} < 0$, $\tilde{w} < 0$), in agreement with Coceal et al. (2007c) and Yoshida and Takemi (2018). For the $0°$ driving flows with $\lambda_p < 0.44$, the negative fluxes on the leeward side have significantly larger streamwise extent than the positive fluxes on the windward side (Figs. 4.10a,d), and therefore dominate the spatial average flux. This flow pattern exists in the middle and top portions of the canopy for these cases, and it explains why the horizontal average DMF is generally negative there.

For $\lambda_p = 0.44$ (Figs. 4.10c,e) the streamwise extent of the negative fluxes on the leeward side is much reduced, since recirculations in wakes are very limited by the downstream building separation. In Fig. 4.10c it can be seen that for N-44-A the extent of negative fluxes from the leeward wall is still slightly larger than the positive fluxes at the windward wall. However, the magnitude of the positive fluxes is larger, and positive fluxes dominate the spatial average as seen in Fig. 4.2c. From Fig. 4.10e it can be seen that for N-44-S the positive and negative fluxes occupy similar fractions of the canopy, with comparable magnitude, so that the spatial average DMF is small, as seen in Fig. 4.2c.

The DMF has distinctly different characteristics for B-25-A-45° in Fig. 4.10b, with negative fluxes dominating the cross-section. There are strong negative fluxes in the wakes of the buildings as in the 0° driving flows, but at the windward walls ($x/h = 2$, $y/h = 0 - 1$ and $x/h = 0 - 1$, $y/h = 2$) there are no strong positive fluxes. There are two separate streams either side of each building where flow is diverted around them as also noted by Claus et al. (2012). At the windward walls they have downward motion ($\tilde{w} < 0$), like the flow at the windward walls in the 0° driving flows. The flow streams have large positive horizontal velocity at the windward walls ($\tilde{u}, \tilde{v} > 0$) so correlation with $\tilde{w} < 0$ gives negative fluxes, unlike the 0° driving flows where $\tilde{u} < 0$ at the windward wall so that there are positive fluxes.

Figures 4.2d and 4.3d show the ratio of DMF to TMF. The $\lambda_p = 0.0625$–0.35 simulations with 0° driving flows typically have a ratio of 0.2–0.6 for $z/h = 0.4$–0.9. These values are consistent with other studies (Kanda et al., 2004; Xie et al., 2008; Castro, 2017). DMF for $\lambda_p \leq 0.25$ tends to be convex within the canopy but TMF across all λ_p tends to be concave. The ratio is generally largest at $z/h \approx 0.5$. Near the surface the ratio is negative because DMF is positive there. The regions of negative flux in Figs. 4.10a,d at $z/h = 0.75$ are smaller near the surface, and the large positive fluxes confined close to the windward wall dominate the spatial average.

The ratio has different behaviour when $\lambda_p = 0.44$. The N-44-A ratio is negative below $z/h = 0.85$, with a minimum value of -0.72 at $z/h = 0.3$. The N-44-S ratio is complicated, being generally negative below $z/h = 0.55$ but with both very large positive and negative values in the region due to small values of TMF.

The 45° datasets have particularly large ratios in the lower canopy with values larger than 1 for $0.05 < z/h < 0.5$ (Fig. 4.3d). Unlike in the 0° driving flows where DMF tends to be negative near the surface, in the 45° driving flows it is positive. The ratio is maximum at $z/h \approx 0.15$, and has values 2.9, 129.1 and 2.3 for B-25-A-45°, C-33-A-45° x-component and C-33-A-45° y-component respectively. The ratio of 129.1 is off the axis limit and the particularly large value is due to very small TMF. It has already been shown by Castro et al. (2017) using the C-33-A-45° dataset that DMF is a significant and at times dominant fraction of the total momentum flux. It is demonstrated for the first time here in the B-25-A-45° case, suggesting that this might be a general result for 45°
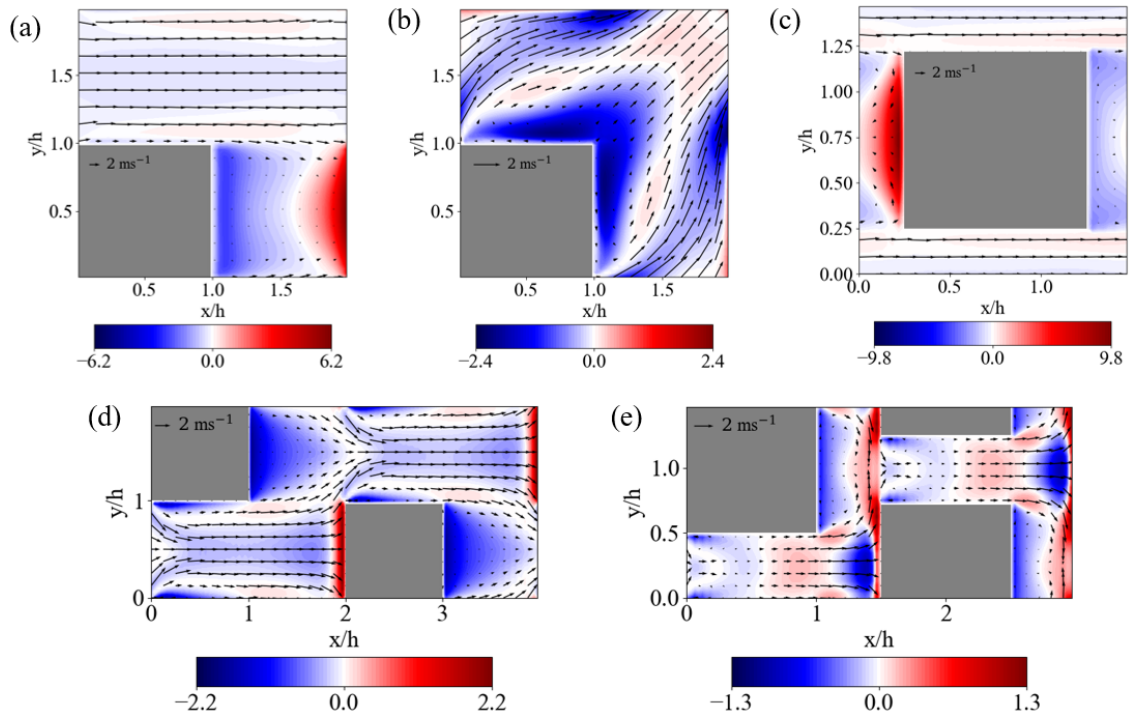
Figure 4.10: Panels (a), (c), (d) and (e) show DMF $\tilde{u}\tilde{w}/u_\tau^2$ cross-sections at $z/h = 0.75$ for B-25-A-0°, N-44-A, N-25-S and N-44-S respectively. Panel (b) shows a $(\tilde{u}\tilde{w} + \tilde{v}\tilde{w})/u_\tau^2$ cross-section at $z/h = 0.75$ for B-25-A-45°.

driving flows.

Using LES, Giometto et al. (2016) found for a portion of Basel's urban canopy ($\lambda_p = 0.5$ near the surface), with two prevailing wind directions, that TMF and DMF are approximately equal up to h. This is consistent with our finding that DMF can be much larger when flow is oblique to building faces. They found the DMF to increase approximately linearly with height up to h, above which it starts to decrease, whereas the TMF peaks above h. The TMF profiles were slightly convex and reasonably similar in shape to the DMF profiles.

That the ratio of DMF to TMF is far from constant across the range of geometries presented here is further evidence that they are not governed by the same processes. DMF is related to the correlation of $\overline{u}$ and $\overline{w}$ (since $\langle \overline{u}\,\overline{w} \rangle = \langle \tilde{u}\tilde{w} \rangle$), and so requires knowledge of the three-dimensional time-averaged flow field. It may be expected that the magnitude of DMF increases with height (if $\lambda_p(z)$ is approximately constant) since $|\overline{u}|$ tends to increase with height. That DMF might increase approximately linearly with height as in Giometto et al. (2016) is less obvious.

It was found here that when $\lambda_p \geq 0.25$, the 0° and 45° driving flows produce concave and convex profiles, respectively. It is possible at high λ_p in realistic geometries where buildings have varying orientations to the flow, that there is a mixture of convex and concave shaped DMF in different regions of the canopy. Upon spatial averaging this

could give rise to approximately linearly increasing spatially averaged DMF with height. More CFD and experimental evidence of realistic urban geometries is required to see if this is the case.

4.6 Conclusions

4.6.1 Summary

The influence of different surface morphologies on urban canopy turbulence characteristics was investigated for numerous urban canopy LES and DNS datasets covering a range of idealised geometries ($\lambda_p = 0.0625$ to 0.44, cubes and cuboids, uniform and variable building heights, driving flows at $0°$ and $45°$ to the building faces, and aligned and staggered arrays). A first-order momentum mixing length turbulence closure was formulated and momentum mixing length profiles examined across geometries, with a view towards developing a new urban canopy turbulence model. The dispersive momentum flux profiles were calculated and interpreted in terms of the three-dimensional flow field.

The intrinsic average of vertical gradients in velocity gives rise to a term that accounts for changes in λ_p with height, and which until recently has been overlooked in urban canopy literature (Schmid et al., 2019). Without it there are large discontinuities in the gradient whenever there are step changes in λ_p, which cause spikes in the momentum mixing length. For a variable-height building geometry it was shown that excluding the extra term in the momentum mixing length closure results in overestimation of predicted velocity by up to 17% near the top of the canopy. For denser urban canopies ($\lambda_p > 0.25$) the error is expected to be larger. The intrinsic averaging approach is used commonly in urban canopy models (Martilli and Santiago, 2007), and when *K*-theory turbulence closures do not account for the extra term large errors can be expected, since they involve horizontal averaging of velocity gradients.

It was found that the shear length scale at the canopy top does not vary with depth-averaged momentum mixing length within the canopy in a systematic way. This suggests that the mixing-layer analogy (Raupach et al., 1996) does not apply to turbulence in urban canopies, unlike in vegetation canopies, since it is not dominated by one length scale associated with mixing-layer eddies generated at canopy top. Shear-generated eddies at the top of urban canopies are local to the buildings (Coceal et al., 2007a), and do not penetrate as far down into the canopy as in vegetation canopies. Flow velocity can be considerable near the surface in unobstructed regions of urban canopies so that significant shear can be generated there. The momentum mixing length might be better interpreted as a combination of two length scales – the distance from the ground and from canopy top, both of which act to block eddies (Coceal et al., 2006).

The momentum mixing length demonstrated common characteristics across urban canopy geometries. For uniform-height, flat-roofed obstacles it increases from zero at the surface to a maximum roughly in the middle of the canopy, decreases until canopy top and increases rapidly above $z/h = 1$, before transitioning to a linear increase by approximately $z/h = 1.5$. The $0°$ driving flows typically have a maximum momentum mixing length in the canopy of $\approx 0.3h$. However, there were some outliers to the trend, specifically the $\lambda = 0.44$ staggered geometry and the $45°$ driving flows as discussed in Sect. 4.5.1.

Using a variable building height dataset, it was demonstrated that the momentum mixing length profile shape and magnitude below mean building height is similar to that with uniform height geometries. Above mean building height, mixing length increases approximately linearly with height, but is slightly reduced from what would be expected in a logarithmic region, due to multiple shear layers associated with the tops of the buildings. A minimum in the mixing length profile occurs at the mean building height but is larger compared to uniform height geometries.

Von Kármán's coefficient κ was calculated from the gradient of linear regressions fitted to momentum mixing length profiles in the inertial sublayer. κ varies between 0.20 and 0.51, and there is no clear relationship between canopy geometry and κ. The simulations with larger domain heights tended to have larger κ. Whether the ratio of roughness height to boundary layer depth is insufficient for adequate scale separation in the logarithmic region, as suggested by Jiménez (2004), requires further investigation.

Dispersive momentum flux profiles for the $0°$ driving flow datasets were in line with those in the literature (Kanda et al., 2004; Xie et al., 2008; Castro, 2017), with dispersive to turbulent momentum flux ratios of 0.2–0.6 for $z/h = 0.4$–0.9 in the $\lambda_p = 0.0625$–0.35 simulations. The $45°$ datasets have larger dispersive momentum flux, and ratios to turbulent momentum flux that exceed 1 for $0.05 < z/h < 0.5$. As dispersive to turbulent momentum flux ratios of approximately unity have also been found for realistic geometries (Giometto et al., 2016), dispersive momentum flux in oblique flows may be more important than previously thought.

4.6.2   Implications for Parametrisation

Many urban canopy models assume turbulent length scales that are constant up to mean canopy height and linearly increasing above (Hamdi and Masson, 2008; Santiago and Martilli, 2010; Nazarian et al., 2020). In NWP the main role of the urban canopy model is to provide a boundary condition for the flow above. The use of a constant turbulent length scale is not necessarily a poor approximation, if its size is determined so that the correct fluxes are provided to the levels above the canopy. However, if vertical profiles of velocity and scalars are of interest within the canopy, then using a turbulent length scale that varies with height in the correct way is important. TMF is proportional to $\langle l_m \rangle^2$ in

first-order momentum mixing length closures and proportional to the turbulent length scale in commonly used $k - l$ TKE closures (Martilli et al., 2002; Schoetter et al., 2020), so the turbulent length scale (of which momentum mixing length is one) is an important parameter.

Models that use a constant turbulent length scale often do not enforce the no-slip condition at the surface, so velocity gradients at the surface are very small. Canopy dispersion parametrisations based on the double-averaging approach involve velocity gradients, so it is necessary to correctly predict velocity for use in determining the vertical scalar distribution. This is especially the case near the surface where there are strong velocity gradients collocated with various scalar sources (e.g. pollution emissions, and anthropogenic and sensible heat).

Based on sensitivity tests (not shown), changing the turbulent length scale alone in urban canopy models does not always improve the predicted velocity profile, if the drag term is not treated properly. It is well known that the $C_d(z)$ tends to be larger near the surface than close to the tops of buildings (Macdonald, 2000; Cheng and Castro, 2002; Coceal et al., 2006; Santiago et al., 2008; Leonardi and Castro, 2010), so it follows that the drag length scale L_c is variable in urban canopies. Future multi-layer canopy models will likely need to account for both turbulent length scales and drag length scales that vary with height in the canopy.

When using a first-order momentum mixing length turbulence closure approach, a complication could occur in realistic scenarios when a significant part of the flow is at angles far from normal to the building faces. In the $45°$ driving flow simulations two possible explanations were proposed (other than localised shear production) to explain why they have large turbulent momentum flux but small double-average velocity gradient – turbulent transport and wake production of turbulent momentum flux. There is limited knowledge on both processes in urban canopies. Investigation of turbulent transport is limited by the number of CFD simulations with triple correlation outputs. Wake production of turbulent momentum flux is likely more significant in urban canopies than in vegetation canopies, where it is treated as negligible (Raupach et al., 1986), since dispersive fluctuations are much larger. It is therefore interesting that the $45°$ driving flow simulations have particularly large dispersive momentum flux.

When turbulent transport of turbulent momentum flux is important then first-order closures are insufficient. A possible pragmatic approach to a higher-order closure is to add an extra term to the first-order momentum mixing length closure, so that $\langle \overline{u'w'} \rangle = -\langle l_m \rangle^2 |\langle \partial \overline{u}/\partial z \rangle| \langle \partial \overline{u}/\partial z \rangle + N_l$, where N_l represents turbulent transport (i.e. the non-local turbulence). Such an extension to the first-order momentum mixing length approach has already been formulated by Wang (2014). This approach could also offer a method of parametrising buoyancy effects which drive non-local momentum transport, in a way analogous to some convective boundary layer schemes (e.g. Lock et al., 2000), whilst maintaining first-order momentum mixing length closure of mechanical turbu-

lence.

It was argued in Sect. 4.5.8 that dispersive and turbulent transport are not governed by the same processes. Rather than representing dispersive momentum flux as part of the turbulence closure it could be treated separately. For example, if it is found more generally that dispersive momentum flux is an approximately linearly increasing function across different realistic geometries, then it could be taken as a function that is scaled with velocity and building morphology parameters such as λ_p. Recirculations in building wakes cause the majority of dispersive momentum flux since they are where large $|\tilde{u}|$ and $|\tilde{w}|$ occur. Recirculations are likely predominantly driven by the flow at canopy top as in street canyons, so that $\langle \overline{u}(h) \rangle$ is the relevant velocity scale.

Acknowledgements

Chapter 5

Conclusions

In the foreseeable future it will be possible to routinely run NWP and AQMs at sub-kilometre horizontal grid length. At such grid lengths CBL turbulence is partially resolved on the model grid and the surface characteristics within each grid cell become much more statistically representative of individual urban neighbourhoods. The parametrisation of time-mean advection and turbulent mixing of scalars in the UBL should reflect this. Towards improved AQ prediction in urban areas, this thesis has investigated the transport processes controlling urban AQ, analysed current NWP CBL turbulence representations and developed parametrisations of urban canopy turbulence. The overarching questions addressed were: 1) how is pollution vertically mixed in the UBL at vertical scales ranging from the urban canopy height to the boundary layer height (z_h)? 2) How should vertical mixing of pollution be represented in NWP and AQMs?

Chapter 2: One- and Two-box Modelling of an Inert Pollutant in London's Boundary Layer

A one-box model was used to predict NO_x concentration in London's BL during a six-day case study with daytime convective conditions. The relative importance and timing of different pollution transport processes was investigated. Small values of z_h were found to play the largest role in determining the timing of concentration peaks. The size of the concentration peaks was largely controlled by how small z_h was and when minimum z_h occurred relative to the morning pollution emissions (q) increase. When z_h growth occurs later in the morning it results in large q coinciding with small z_h, and therefore larger concentration.

Entrainment of lower pollution air through BL growth is an important process in reducing morning concentration peaks. Its impact varies between days and is largest when a small z_h minimum is followed by rapid z_h growth. After initial z_h growth entrainment generally becomes a less effective sink of pollution than horizontal advection. Variation in concentration due to horizontal advection (which depends on the horizontal advection timescale (τ) and background concentration (c_b)) tended to depend on synoptic conditions, so was a lower frequency influence than z_h and q, which vary diurnally.

The sensitivity of the average concentration during convective conditions to the one-

box model parameters was investigated. c_b, τ, z_h and q were roughly equally important. Concentration of entrained air (c_a) was an order of magnitude less important, so improvement of its representation warrants lower priority in AQMs.

It is widely accepted in the AQ modelling community that z_h and q are important parameters. It has also been demonstrated here that velocity in the UBL and c_b are often equally important in controlling UBL concentration, and therefore deserve more attention. Also, even though entrainment through BL growth is an important process controlling morning concentration peaks, its representation gets little attention in the AQ literature. Since morning z_h is the key parameter controlling entrainment through BL growth, development of convective turbulence in the early morning requires good representation in AQMs.

A two-box model was formulated, where the bottom and top boxes represented the UCL and ML respectively. The vertical exchange timescale from the canopy box to the ML box was estimated to be 40 sec on average during the case study. This is approximately three orders of magnitude smaller than the horizontal advection timescale in London's urban canopy. Horizontal advection in the canopy was a negligible sink of concentration, making vertical exchange into the ML the only canopy sink. An analytical steady state solution was found for the canopy box concentration (c_1) that is proportional to only q, $1/(1-\lambda_p)$ where λ_p is the plan area density, $1/v_e$ where v_e is the canopy top exchange velocity and concentration in the ML box (c_2). These three parameters and one variable (c_2) are therefore critical in AQMs for accurate prediction of c_1.

The height of the urban canopy had very little influence on c_1. The two-box model assumed pollution was well-mixed in the canopy, which might be a poorer assumption in deep, dense canopies, and requires future investigation. When the horizontal dimensions of the box were reduced from 50 km to 10 km, c_2 was approximately equal to the background concentration (c_b), and c_2 in the steady state canopy box solution could approximately be replaced by c_b. For small cities representation of UBL processes that affect c_2 are therefore less important than the representation of regional and continental scale pollution transport in AQMs.

The variable c_2 and parameter v_e together control the influence of pollution transport on c_1. c_2 depended crucially on vertical mixing of pollution through changes in z_h due to dilution and entrainment. However, the box models assumed pollution emissions became instantaneously well-mixed so that vertical gradients in concentration could not be investigated. This motivated Chapter 3, where the temporal evolution of the vertical distribution of ground emissions in the CBL was investigated. v_e is determined by turbulent mixing at canopy top. Current parametrisations of the vertical exchange at canopy top often depend on just the external flow conditions, and are largely based on studies of idealised canyon geometries. Turbulent mixing across a range of urban canopy geometries was therefore investigated in Chapter 4.

Chapter 3: NWP in the Urban Boundary Layer Convective Grey Zone

Using a UM nesting suite over London on a clear sky day (04/05/2016), CBL vertical mixing and tracer transport was investigated at horizontal grid lengths of 1.5 km, 500 m, 300 m, 100 m and 55 m. The simulations had a continuous release, homogeneous, 50 km $\times$ 50 km ground source of passive tracer. It was found that at the city scale, the 500 m to 55 m models had significant tracer mass non-conservation issues. They were most severe when $z_h/\Delta_{xy} \sim 4$, in the grey zone of CBL turbulence. The largest issues with the 500 m and 300 m models were seen during the afternoon, when there was often more than 2.5 times the amount of tracer mass that there should have been over London. During morning BL growth the 100 m and 55 m models overestimated tracer mass by approximately 50%. However, in the afternoon the CBL turbulence became much better resolved in the 100 m and 55 m models, and tracer mass was overestimated by between $0 - 10\%$ in the 55 m model.

The tracer was not conserved because SISL advection is non-conservative. This is most problematic when there are strong, grid scale gradients in advected variables. There are sharp gradients in tracer concentration between CBL updrafts and downdrafts. AQMs in the CBL grey zone should use advection schemes that are inherently conserving or SISL advection schemes that are modified to ameliorate the non-conservation issues. Using a mass fixer conservation scheme alone is an inadequate solution to SISL advection non-conservation issues, since grid scale updrafts cause spurious turbulent mixing of tracer.

The vertical mixing of a puff release, homogeneous, ground source of tracer was investigated in the 1.5 km, 100 m and 55 m models. Tracer released at the ground in the 100 m and 55 m models tended to converge horizontally into z_h scale updrafts, which transported tracer rapidly to near the top of the BL. This resulted in puff release tracer CoM trajectories having a brief initial period where they did not rise quickly, followed by a rapid rise, and a period approximately $15 - 30$ min after release where there was more tracer in the top half than the bottom half of the BL. The 1.5 km model did not exhibit this "lift off" behaviour, since the tracer vertical mixing parametrisation is diffusive in the UM. It does not capture the short time ballistic type mixing where tracer moves with the velocity of the dominant turbulent eddies. This is a limitation of NWP vertical mixing parametrisations more generally and highlights one of the benefits of moving to $\Delta_{xy} = O(100\text{m})$. The lift off behaviour also underlines that it takes time for pollution to become well-mixed, and that in Chapter 2 the assumption of instantaneous mixing of pollution in the BL is of limited validity.

An analytical model for the CoM trajectories was developed from a reduced form of the Langevin equation. It captured the salient features of the CoM trajectories when

CBL turbulence was parametrised and resolved by the UM. The reduced model contains parameters that can be directly related to vertical mixing timescales, which were determined by fitting the reduced model to the UM CoM trajectories. The vertical mixing was much slower in the 1.5 km model than the 100/55 m models in both the short and long time limits. The current diffusive type parametrisation used in the UM should be made more efficient at vertical mixing of pollution.

The ratio between the 1.5 km and 55 m model continuous release concentrations was calculated with downstream distance from the upstream edge of the source. The 55 m model generally had smaller concentration near the surface than the 1.5 km model, because it had more efficient vertical mixing. The minimum ratio near the surface was 0.61, approximately 9 km downstream of the upstream edge of the source, and occurred largely as a result of the lift off behaviour in the 55 m model. This provides evidence that improved representation of CBL vertical mixing would have significant impact on the urban canopy pollution concentration predicted by AQMs. The near surface tracer concentration value in the UM is effectively c_2 (i.e. the concentration of air above the canopy top), and as found in Chapter 2, c_2 is a key variable controlling urban canopy concentration. Therefore, both urban canopy scale and UBL scale vertical mixing are crucial for ventilation of pollution from the urban canopy.

Chapter 4: Turbulence Characteristics Across a Range of Idealised Urban Canopy Geometries

Following the finding in Chapter 2 that vertical mixing at urban canopy top is crucial for pollution concentration, LES and DNS of flow through various cuboid arrays was used to investigate urban canopy turbulence. It was demonstrated that the mixing-layer analogy does not govern turbulent mixing in urban canopies, in contrast to vegetation canopies.

The mixing-layer analogy implies that there should be a single, constant turbulent length scale in the urban canopy. However, across a range of urban canopy geometries, it was shown that the momentum mixing length increases from zero at the ground, has a local maximum near the middle of the canopy, decreases to a local minimum at canopy top, before tending towards a linear increase in the ISL. Turbulent length scales employed in most urban canopy models are the momentum mixing length or have similar interpretation. It is therefore likely that urban canopy model turbulence closures would benefit from a height dependent turbulent length scale, with the aforementioned momentum mixing length characteristics. Improved urban canopy turbulence representation would result in more accurate ground level pollution concentration prediction in AQMs and vertical distribution of other scalars such as temperature within the canopy

in NWP.

A first-order mixing length turbulence closure suitable for multi-layer urban canopy models was developed. An often overlooked term was included in the analysis, which accounts for changes in solid fraction with height. It arises from application of the double-averaging operator to the vertical velocity gradient. For an array of variable height buildings, its omission led to velocity overestimation of up to 17% in the canopy. Although the velocity at which pollution is horizontally advected in the canopy is not important for pollution concentration (as shown in Chapter 2), it is important for multi-layer urban canopy model turbulence closures, since they are based on the local velocity gradient.

Another consequence of the non-negligible solid fraction in urban canopies is the generation of time-mean flow patterns in wakes. For cases where flow was oblique to the building faces, vertical transport of momentum due to dispersive stress exceeded turbulent stress in approximately half of the canopy. Dispersive stress is typically neglected in multi-layer canopy models. Accounting for the solid fraction in future urban canopy models and AQMs should be made a priority, as demonstrated here and in Chapter 2 where the analytical steady state solution for c_1 depended on λ_p.

Recommendations for NWP and AQMs

The UK Met Office are currently developing a multi-layer urban canopy model for implementation in NWP, and are looking to develop urban AQMs and continuously running O(100 m) horizontal grid length NWP in the near future. Based on the findings of this thesis the following insights and recommendations are made:

- Non-conservation issues with SISL advection become more apparent in the CBL grey zone. When SISL advection schemes are used in NWP and AQMs at sub-kilometre horizontal grid length, they should either be modified to conserve mass over the entire domain and at least ameliorate local (O(1 km)) non-conservation issues, or be formulated such that they are inherently conserving.

- If a street canyon type urban AQM is developed (e.g. OSPM (Berkowicz, 2000) and SIRANE (Soulhac et al., 2011)), attention should be paid to estimation of v_e since it is a crucial parameter for accurate canopy AQ prediction. Current parametrisations tend to be very simple and only account for stability effects based on scaling relationships that were not developed for urban canopies. Recently improvements have been made in representing stability effects in urban canopy wind-tunnel and CFD experiments, and it is therefore likely parametrisations could be substantially improved.

- Multi-layer urban canopy models represent vertical exchange in the urban canopy

at multiple levels rather than just at canopy top, and are therefore more suitable for predicting pollution concentration in deep, dense canopies where large pollution concentration gradients are likely to exist. To accurately predict vertical distribution of scalars (including pollution) within the RSL, NWP and AQMs should use turbulence and drag length scales that vary with height.

- Improved prediction of the time-mean velocity and turbulence statistics within the urban surface layer in NWP, for example through incorporating a multi-layer urban canopy model, would result in improved vertical mixing of pollution in AQMs. This is regardless of the AQM type since NWP output drives the vertical mixing parametrisations in AQMs.

- NWP at O(100 m) horizontal grid length is able to represent the lift off behaviour of particles released at the ground in CBLs. This means that one of the main advantages of offline Lagrangian AQMs (that are based on the Langevin equation) over online Eulerian AQMs no longer exists at O(100 m) grid length. Online Eulerian AQMs at O(100 m) grid length are attractive since they have the ability to represent the spatial distribution of pollution at the neighbourhood scale, have consistent representation of all processes (unlike offline AQMs where the NWP and CTM often have inconsistent representation of for example urban surface layer turbulence), and enable feedbacks between chemistry and meteorology.

Appendix A

Two-box Model Derivation

The two-box model consists of an urban canopy box coupled via two-way exchange with a box above representing the ML of the BL. A schematic of the two-box model is shown in Fig. A.1. The model predicts the passive tracer concentration time evolution in the two boxes. There is a ground source of tracer in the canopy box. The exchange velocity between the two boxes is the same in the upward and downward directions. The horizontal advection velocity is allowed to differ between the two boxes. The height of the ML box evolves with time, and the entrainment and dilution of tracer by BL growth is represented. The concentration of background air advected into the two boxes is assumed the same. Air flow and tracer are only allowed within the air fraction of the urban canopy.
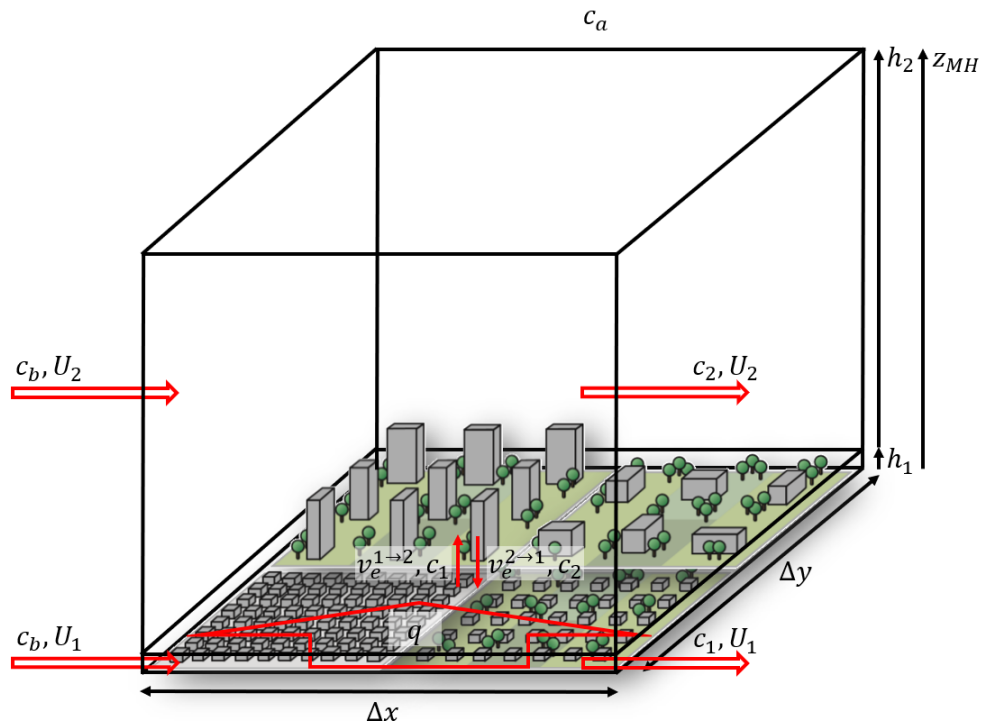
Figure A.1: Schematic of the two-box model. Red horizontal arrows represent horizontal advection of tracer with specified concentration and wind speed (see labels) in and out of the boxes. The two small arrows represent vertical exchange between the canopy and ML boxes with specified concentration and velocity (see labels). The broad, red, vertical arrow represents the canopy emissions. (The urban surface characteristics are adapted from local climate zone (LCZ) schematics presented in Oke et al. (2017))

The box model equations are derived by considering the conservation of tracer mass. The tracer mass sources and sinks through the sides of each box should exactly equal the rate of change of tracer mass in each box. The x axis is aligned with the direction of time-mean flow. Let us define the surfaces of the boxes so that S_1 and S_2 are the bottom of the canopy and ML boxes respectively, S_3 and S_4 are the upstream sides of the canopy and ML boxes respectively (orientated normal to the time-mean flow), S_5 and S_6 are the downstream sides of the canopy and ML boxes respectively, and S_7 and S_8 are the top of the canopy and ML boxes respectively.

The canopy box mass conservation equation can be written as

$$\frac{d(c_1 \Delta x \Delta y h_1 (1 - \lambda_p))}{dt} = \iint_{S_1} (\boldsymbol{q}.\boldsymbol{n}) dS_1 + \iint_{S_3} c_b(\boldsymbol{u_1}.\boldsymbol{n}) dS_3$$
$$+ \iint_{S_5} c_1(\boldsymbol{u_1}.\boldsymbol{n}) dS_5 + \iint_{S_7} c_1(\boldsymbol{v_e^{1 \to 2}}.\boldsymbol{n}) dS_7 + \iint_{S_7} c_2(\boldsymbol{v_e^{2 \to 1}}.\boldsymbol{n}) dS_7,$$

(A.1)

where c_1 and c_2 are the concentrations in the canopy and ML boxes respectively, $\boldsymbol{q}$ is the ground source tracer emissions, Δx and Δy are the streamwise and spanwise horizontal dimensions of the boxes, $\boldsymbol{n}$ is the unit normal vector directed inward of the surface that is being integrated over, h_1 is the depth of the canopy box, $\boldsymbol{u_1}$ is the air velocity in the canopy box, and $\boldsymbol{v_e^{1 \to 2}}$ and $\boldsymbol{v_e^{2 \to 1}}$ are exchange velocities with magnitude v_e, and are directed from the canopy box to the ML box and from the ML box to the canopy box respectively. Performing the integrals on the right-hand side of Eq. A.1 gives

$$\Delta x \Delta y h_1 (1 - \lambda_p) \dot{c}_1 = \Delta x \Delta y (1 - \lambda_p) q + \Delta y h_1 (1 - \lambda_p) c_b U_1$$
$$- \Delta y h_1 (1 - \lambda_p) c_1 U_1 - \Delta x \Delta y (1 - \lambda_p) c_1 v_e + \Delta x \Delta y (1 - \lambda_p) c_2 v_e,$$

(A.2)

where U_1 is the wind speed in the canopy box. h_1 is treated as constant in time since the height of the urban canopy does not vary with time. The $1 - \lambda_p$ factors occur due to flow only being allowed in the air space. Equation A.2 can be rearranged as

$$\dot{c}_1 = \frac{q}{h_1} + \frac{c_b - c_1}{\tau_1} - \frac{c_1 - c_2}{\tau_{ex,1}},$$

(A.3)

where $\tau_1 = \Delta x / U_1$ and $\tau_{ex,1} = h_1 / v_e$ represent the time it takes horizontal advection and vertical mixing at canopy top respectively to flush the air from the urban canopy. Note in Sect. 2.8.1 it is assumed that $\Delta x = \Delta y = L$.

q is the tracer mass emission rate (kgs^{-1}) divided by $\Delta x \Delta y$ (m^2). In the two-box model when λ_p increases the tracer mass emission rate decreases, since the q integral in Eq. A.1 is only defined in the air space, and q consequently decreases. In urban canopies the pollution mass emission rate does not necessarily decrease with increasing λ_p. For example larger emissions are not typically found within wide street canyons compared

to narrow street canyons and there are generally more emissions in dense canopy within Central London than in suburbs with sparser canopy. It is therefore decided to define a new NO_x mass emission rate per unit area of ground, $q_{fix} = q/(1 - \lambda_p)$. The NO_x mass emission rate into London (equal to $q_{fix}\Delta x \Delta y (1 - \lambda_p)$) is then independent of λ_p. The final canopy box equation is given by

$$\dot{c}_1 = \frac{q_{fix}}{h_1} + \frac{c_b - c_1}{\tau_1} - \frac{c_1 - c_2}{\tau_{ex,1}}. \tag{A.4}$$

The ML box mass conservation equation can be written as

$$\begin{aligned}
\frac{d(c_2 \Delta x \Delta y h_2)}{dt} &= \iint_{S_4} c_b(\boldsymbol{u_2}.\boldsymbol{n})dS_4 + \iint_{S_6} c_2(\boldsymbol{u_2}.\boldsymbol{n})dS_6 \\
&+ \iint_{S_2} c_1(\boldsymbol{v_e^{1\to2}}.\boldsymbol{n})dS_2 + \iint_{S_2} c_2(\boldsymbol{v_e^{2\to1}}.\boldsymbol{n})dS_2 \\
&+ \theta_H(-\dot{h}_2)\iint_{S_8} c_2\left(\dot{\boldsymbol{h}_2}.\boldsymbol{n}\right)dS_8 - \theta_H(\dot{h}_2)\iint_{S_8} c_a\left(\dot{\boldsymbol{h}_2}.\boldsymbol{n}\right)dS_8,
\end{aligned} \tag{A.5}$$

where h_2 is the depth of the ML box, $\boldsymbol{u_2}$ is the air velocity in the ML box and θ_H is the Heaviside step function defined to be 1 when its argument is positive and zero otherwise. Performing the integrals on the right-hand side of Eq. A.5 gives

$$\begin{aligned}
\Delta x \Delta y h_2 \dot{c}_2 + \Delta x \Delta y c_2 \dot{h}_2 &= \Delta y h_2 c_b U_2 - \Delta y h_2 c_2 U_2 \\
&+ \Delta x \Delta y (1 - \lambda_p) c_1 v_e - \Delta x \Delta y (1 - \lambda_p) c_2 v_e \\
&+ \theta_H(-\dot{h}_2)\Delta x \Delta y c_2 \dot{h}_2 + \theta_H(\dot{h}_2)\Delta x \Delta y c_a \dot{h}_2,
\end{aligned} \tag{A.6}$$

where U_2 is the wind speed in the canopy box. Noting that $\theta_H(\dot{h}_2) + \theta_H(-\dot{h}_2) = 1$, Eq. A.6 can be rearranged as

$$\dot{c}_2 = \frac{c_b - c_2}{\tau_2} + \frac{c_1 - c_2}{\tau_{ex,2}} + \frac{c_a - c_2}{h_2}\dot{h}_2\theta_H(\dot{h}_2), \tag{A.7}$$

where $\tau_2 = \Delta x/U_2$ and $\tau_{ex,2} = h_2/(v_e(1 - \lambda_p))$ represent the time it takes horizontal advection and vertical mixing at canopy top respectively to flush the air from the ML.

Appendix B

Semi-implicit semi-Lagrangian Advection and Mass Conservation

The UM uses a semi-implicit semi-Lagrangian (SISL) advection scheme (Davies et al., 2005; Wood et al., 2014). SISL enables longer time steps than numerical schemes based on explicit time-stepping without compromising on accuracy (Robert, 1982; Staniforth and Côté, 1991).

Semi-Lagrangian advection is performed in the reference frame of a fluid parcel (i.e. the Lagrangian reference frame) but transported quantities are remapped onto an Eulerian model grid. To better understand the semi-Lagrangian method, let us consider the continuity equation for a tracer χ with specific ratio $\phi_\chi(x, y, z, t) = \rho_\chi/\rho$, where ρ_χ is the tracer density and ρ is the air density. When ϕ_χ is advected by a wind field $\boldsymbol{u}$, and there are no tracer sources or sinks, the equation is given by (Diamantakis, 2013)

$$\frac{D\phi_\chi}{Dt} = \frac{\partial\phi_\chi}{\partial t} + \boldsymbol{u}.\nabla\phi_\chi = 0. \tag{B.1}$$

To find the value of ϕ_χ at a particular grid point at time $t + \Delta t$, one must first calculate the location of the fluid parcel at time t. The former location is known as the arrival point, and the latter location is known as the departure point which is not on the model grid. The departure point is computed using $\boldsymbol{u}$ from the neighbouring grid points. The value of ϕ_χ at the departure point is found by interpolating ϕ_χ from the neighbouring grid points. According to Eq. B.1 the material derivative of ϕ_χ is zero. This means the value of ϕ_χ does not change along the parcel trajectory and $\phi_\chi^d(t) = \phi_\chi^a(t + \Delta t)$, where superscripts d and a denote departure and arrival points respectively.

At no point in the advection calculation is a fixed volume defined, and budgets of ϕ_χ in and out computed. Consequently, there is no step where conservation of ϕ_χ is ensured. $\boldsymbol{u}$ has to be interpolated in calculation of the ϕ_χ departure point. When there are strong gradients in $\boldsymbol{u}$, interpolation errors are largest, and mass non-conservation issues become more prevelant since divergence and convergence computations are less accurate. At horizontal grid lengths greater than 10 km often used in global NWP (where convection is not resolved), the $\boldsymbol{u}$ field is typically quite smooth. In this case mass conservation errors using SISL are less important in short and medium range weather forecasts. How-

ever, in limited area weather forecast models at 1-10 km horizontal grid length or over the longer timescales used in climate models, the errors using SISL are more significant (Diamantakis, 2013).

Methods of ensuring conservation of advected quantities in SISL numerical schemes have been developed and can be broadly split into two classes – inherently conserving and mass-fixer (Diamantakis, 2013). Inherently conserving schemes are based on finding the departure points for all eight corner points of an arrival grid box, calculating the spatial average of ϕ_χ within the departure grid box, and ensuring that the spatial average ϕ_χ in the arrival grid box is the same as in the departure grid box (Lauritzen et al., 2010; Zerroukat and Allen, 2012). SISL schemes based on this approach give local and global conservation of ϕ_χ. However, they are complex and prohibitively expensive, and are rarely used operationally in NWP (Diamantakis, 2013).

The more common way of enforcing global conservation is to use mass-fixer schemes, which do not ensure local conservation. One such scheme implemented in the UM is the Priestley Algorithm (PA) (Priestley, 1993). Values of ϕ_χ are calculated at the departure point in the standard way, but twice, once using higher order interpolation (typically cubic) and again using a lower order interpolation (typically linear) that on its own would give a monotonic solution to the continuity equation. A weighting factor is calculated such that a linear combination of the higher and lower order solutions give the same total ϕ_χ (integrated across all points in the domain) at t and $t + \Delta t$. When for example ϕ_χ is globally overestimated, at grid points where ϕ_χ is greater using cubic interpolation than linear interpolation, the weighting factor applied is more towards the linear interpolation solution. The other grid points, where ϕ_χ is smaller using cubic interpolation than linear interpolation, use only the cubic interpolation solution. The weighting is chosen so that the higher order solution is used as much as possible whilst still ensuring global conservation of ϕ_χ. The recommended conservation method in the UM is the Optimised Conservative Filter (OCF) scheme (Zerroukat and Allen, 2015). OCF is similar to PA but has two weighting factors. Unlike PA it always converges on a solution, even for unsmooth fields such as rain, avoiding the situation where a single weighting factor has to be applied uniformly to all grid points to achieve global conservation (Lock et al., 2019).

In limited area models (LAMs) for global conservation the fluxes through the edges of the domain have to be considered. For example if during a time step moisture is advected out of a LAMs domain, then total moisture at t would be larger than at $t + \Delta t$. If PA or OCF were used alone then they would incorrectly try to scale up the remaining moisture values at $t + \Delta t$, to make them sum to the total moisture at t. The Zero Lateral Flux (ZLF) method (Zerroukat and Shipway, 2017) of accounting for advection at the boundaries is included for moisture in the latest version (11.7) of the UM (Lock et al., 2019). However, no method of accounting for advection at the boundaries is implemented for tracers in version 11.7 (personal communication Dr. Mohamed Zerroukat).

Whenever atmospheric flow structures are partially resolved on the grid (e.g. in the

---

Appendix B. Semi-implicit semi-Lagrangian Advection and Mass Conservation

CBL grey zone), the modelled structures will always lack some of the true physical flow characteristics. This is regardless of the choice of advection scheme. The flow is very heterogenous at the scale of the grid when modelled structures are in the grey zone, so SISL advection tends to have non-conservation issues. They can be accounted for globally using mass-fixer type approaches, but the mass spatial distribution is still inaccurate in regions where mass is not conserved.

A particular example of this has been found recently by the UK Met Office using their operational forecast LAM (the UKV model), which runs at variable horizontal grid length ($\approx$ 1.5 km) over the UK. The work is documented in the so called "blobbiness report" (Lock et al., 2017). Convective rainfall tends to be in "blobs" that have too intense rainfall and there is little rainfall surrounding them. To further investigate this phenomenon, radiative convective equilibrium (RCE) cases were conducted with an LES using an Eulerian advection scheme (at horizontal grid lengths 500 m, 250 m and 100 m) and the UM (at horizontal grid lengths 1.5 km, 1 km, 500 m, 250 m and 100 m). RCE cases are idealised simulations of the tropical atmosphere, where convective heating at the ground is balanced by imposed clear sky cooling. The LES and UM microphysics and sub-grid mixing settings were kept as close as possible. The LES across all grid lengths had large areas of lighter precipitation around the cores of convective cells and tended to align in bands perpendicular to the mean wind. However, the UM rainfall at grid lengths 1.5 km to 250 m tended to be in blobs that were roughly elliptical, with long side aligned with the mean flow direction. The rainfall characteristics were not broadly consistent with the LES until 100 m grid length. This gave first evidence that semi-Lagrangian advection might have issues when convective processes are poorly resolved.

To better understand the issues outlined above, cloud free (i.e. condensation effects turned off) convective boundary layer cases were simulated again using LES and the UM. Domain averaged θ profiles from the 500 m horizontal grid length simulations, as the day progressed, were seen to have increasingly higher values (up to 3.5 K) in the UM compared to LES in the BL. However, simulations at 100 m horizontal grid length were very similar. This indicates that at 500 m grid length there are θ non-conservation issues in the UM. Horizontal cross-sections from the 500 m UM simulation revealed θ and w tend to form linear structures at the scale of the grid, within which they are overestimated.

Combining the occurrence of grid-scale flow structures and lack of conservation, an explanation for systematic generation of excess rain by SISL advection is obtained – the so called infinite fountain. It is illustrated schematically in Fig. B.1. The UM has a Charney-Phillips grid in the vertical and an Arakawa C grid in the horizontal, and the grid points for the different variables in Fig. B.1 are positioned as such. Moist air with specific humidity, q_m, is advected upwards in plumes. At the q_m departure points in a plume little convergence of drier air is seen. The horizontal flow either side of the plume tends to cancel when interpolated onto the q_m departure points, so that there is
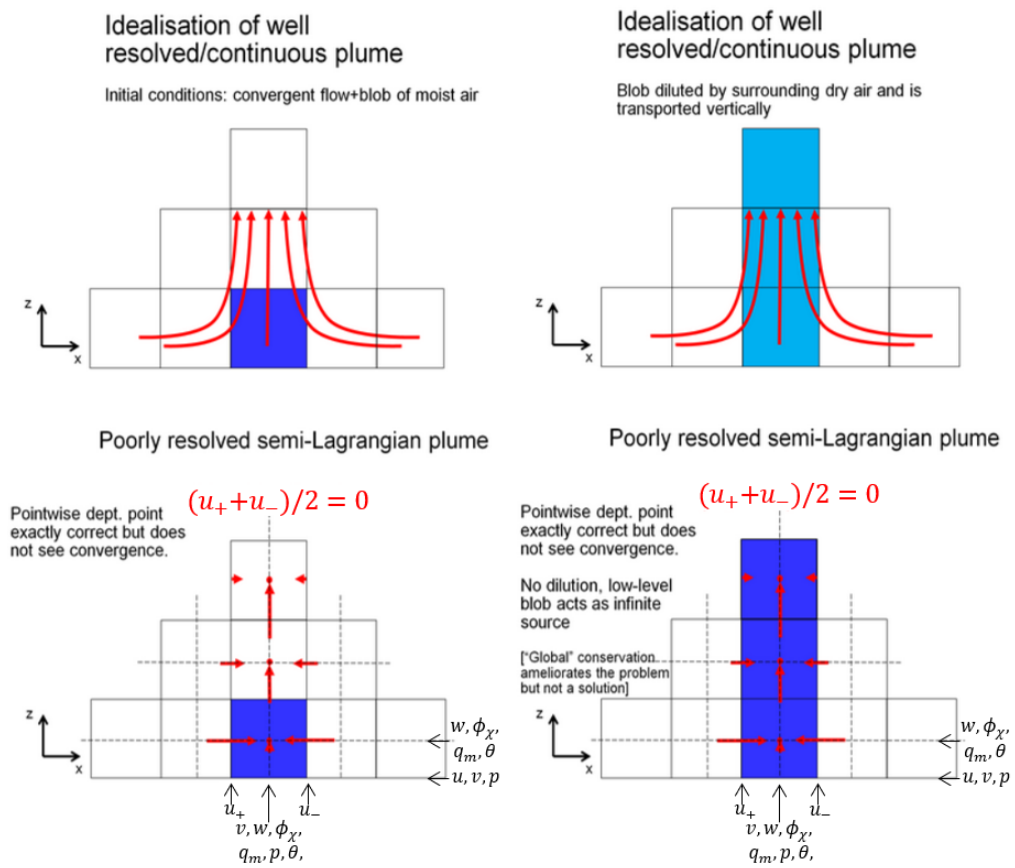
Figure B.1: Schematic of the infinite fountain. (Reproduced from Lock et al. (2017))

no dilution of q_m. Consequently, excess moisture is produced in plumes and q_m is not conserved.

Convection tends to align with the mean wind flow for $-z/L_{MO} > 15$, progressively becoming more horizontal roll like with increasing wind speed (Salesky et al., 2017). When there is lateral divergence in the direction of mean flow within a roll like updraft, this promotes convergence in the cross-stream direction, and shrinks the cross-stream scale of the flow (Lock et al., 2017). In the UM, when the scale of the updraft becomes small enough, semi-Lagrangian moisture non-conservation issues occur, promoting more condensation. This increases w, leading to more convergence and further reduces the cross-stream scale of the flow. The grid scale nature of the modelled flow is thereby reinforced.

Another possible reason for the initial propensity of flow structures to occur at the grid scale in semi-Lagrangian advection is that calculations are point based, rather than grid cell averaged, as in Eulerian (or flux form) advection schemes. Approaches to reduce the problem have been investigated such as adding stochastic noise to the departure point calculation and averaging of adjacent departure point values (Lock et al., 2017). They are analogous to increasing the sub-grid diffusion. Increasing diffusion in

the model does tend to alleviate the problem, however at the expense of resolving less of the structures which were intended to be resolved when running at smaller grid lengths. The dynamical core of the UM is being updated from ENDGame to LFric in the near future, and is designed to be inherently conserving, so that the grid scale structure issues should be less severe and mass non-conservation issues are solved.

Appendix C

Including Passive Tracer Ground Sources in the UM

Including tracer ground area sources involved utilising part of the UM formerly used by the UKCA (United Kingdom Chemistry and Aerosols) framework (Abraham, 2016), since there is no designated or documented way of including passive tracer sources in the UM.

The steps were as follows:

1. In the Rose GUI going to "UM - UM Science Settings - Section 33" and including the desired number of tracers.

2. Creating NetCDF files containing the tracer emissions fields (one could for example modify an existing NetCDF file containing a surface field with the correct dimensions).

3. Converting the NetCDFs to ancillary files using the UM Mule utility xancil.

4. Creating a new UM branch.

5. Within which adding the emissions files in `STASHmaster_A` as single-level ancillary entries and in `bl_trmix_dd.F90` adding code so that at the desired timesteps the `tr_mix` routine picks up the single-level ancillaries.

6. Going to "UM - Reconfiguration and Ancillary Control - Configure ancils and initialise dump fields" and creating a new section that links the tracers specified in step 1 to the single-level ancillaries created in step 5.

The suite used to run the simulations is u-bc220@163228. Links to UKCA training course material and the branch containing code changes can be found at `https://www.ukca.ac.uk/wiki/index.php/UKCA_Chemistry_and_Aerosol_Tutorial_5` and `https://code.metoffice.gov.uk/svn/um/main/branches/dev/lewisblunn/vn10.5_include_tracer_emissions_try1/` respectively. An alternative better supported (and perhaps simpler) approach to including tracers within the UM might be to use the current UKCA framework, but would require the user to learn how to use the UKCA.

Glossary

Acronyms and Abbreviations

AQ	Air Quality
AQM	Air Quality Model
AQUM	Air Quality in the Unified Model
BC	Boundary Condition
BL	Boundary Layer
CBL	Convective Boundary Layer
CFD	Computational Fluid Dynamics
ClearfLo	Clean Air for London
CTM	Chemical Transport Model
DEFRA	UK Department for Food and Rural Environmental Affairs
DMF	Dispersive Momentum Flux
DNS	Direct Numerical Simulation
DSHO	Damped Simple Harmonic Oscillator
EMEP	European Monitoring and Evaluation Program
FA	Free Atmosphere
GIS	Geographic Information System
IBL	Internal Boundary Layer
ISL	Inertial Sublayer Layer
JULES	Joint UK Land Environment Simulator
LAM	Limited Area Model
LBC	Lateral Boundary Condition
LCZ	Local Climate Zone
LES	Large Eddy Simulation
LSM	Lagrangian Stochastic Model
ML	Mixed Layer
MORUSES	Met Office-Reading Urban Surface Exchange Scheme

MOST	Monin-Obukhov Similarity Theory
NAEI	National Atmospheric Emissions Inventory
NAME	Numerical Atmospheric-dispersion Modelling Environment (UK Met Office dispersion model)
NERC	Natural Environment Research Council
NWP	Numerical Weather Prediction
PM	Particulate Matter
RSL	Roughness Sublayer Layer
SEB	Surface Energy Balance
SISL	semi-Implicit semi-Lagrangian
TKE	Turbulent Kinetic Energy
TMF	Turbulent Momentum Flux
UBL	Urban Boundary Layer
UCL	Urban Canopy Layer
UKCA	United Kingdom Chemistry and Aerosols
UM	UK Met Office Unified Model
UN	United Nations
WHO	World Health Organisation

Co-ordinate System Symbols

t	Time
$\boldsymbol{s} = (x, y, z)$	Displacement vector, decomposed into an orthogonal co-ordinate system, with z aligned vertically from the ground and x alignment specified in each chapter (Chapters 1–2: aligned with the time-mean flow, Chapter 3: aligned from west to east and Chapter 4: aligned perpendicular to the widest cuboid face)
$\boldsymbol{u} = (u, v, w)$	Velocity vector, where u, v and w correspond to the wind speed in the x, y and z axes respectively

Averaging and Decomposition Symbols

$\bar{x}$	Time average of a variable x
$\langle x \rangle$	Horizontal space average of a variable x (apart from Sect. 3.6.2 where it represents the ensemble mean)
$x' = x - \bar{x}$	Temporal fluctuations from the time average of a variable x
$x'' = x - \langle x \rangle$	Spatial fluctuations from the horizontal average of a variable x

Other Symbols

a	LSM Deterministic Term Coefficient (ms^{-2})
b	LSM Random Term Coefficient
A_f	Total Frontal Area of Buildings Facing the Wind (m^2)
A_p	Total Plan Area of Buildings (m^2)
A_t	Total Plan Area (m^2)
c	Concentration of Box Model Predicted NO_x or Tracer in the UM (kgm^{-3})
c_a	Box Model Entrainment NO_x Concentration (kgm^{-3})
c_b	Box Model Background NO_x Concentration (kgm^{-3})
c_{BL}	Mean Concentration in the BL Within a Specified Horizontal Region (kgm^{-3})
C_d	Sectional Canopy Drag Coefficient
c_p	Specific Heat Capacity of Air at Constant Pressure ($\mathrm{Jkg}^{-1}\mathrm{K}^{-1}$)
c_1	Pollution Concentration in the Urban Canopy Box (kgm^{-3})
c_2	Pollution Concentration in the ML Box (kgm^{-3})
d	Displacement Height (m)
$d\xi$	Gaussian Random Forcing Term in LSMs (ms^{-1})
E	Wet Deposition Constant (mm^{-1})
f	Coriolis Parameter (rad^{-1})
F_d	Form Drag ($\mathrm{kgm}^{-2}\mathrm{s}^{-2}$)
F_p	Pressure Gradient Force (ms^{-2})
F_{dry}	Dry Deposition Flux ($\mathrm{kgm}^{-2}\mathrm{s}^{-1}$)
F_{wet}	Wet Deposition Flux ($\mathrm{kgm}^{-2}\mathrm{s}^{-1}$)

Glossary

g	Acceleration Due to Gravity (ms^{-2})
G	Wet Deposition Exponent
h	Mean Canopy Height (m)
h_1	Depth of the Urban Canopy Box (m)
h_2	Depth of the ML Box (m)
H	Domain Height of CFD Simulations (m)
k	Wavenumber (m^{-1})
K_m	Local Momentum Diffusivity (m^2s^{-1})
K_χ	Local Diffusivity (m^2s^{-1})
K_χ^{NL}	Non-local Diffusivity (m^2s^{-1})
l_{blend}	Turbulent Mixing Length in the UM Blended BL Scheme (m)
l_f	Filter Length Scale (Effective Resolution of a Model) (m)
l_m	Momentum Mixing Length (m)
$\langle l_{m,\text{max}} \rangle_I$	Maximum Momentum Mixing Length Within the Canopy (m)
$\langle l_{m,\text{av}} \rangle$	Depth Average Momentum Mixing Length Within the Canopy (m)
L	Length of the Base and Width of the Box Models (m)
L_c	Canopy Drag Length Scale (m)
L_{MO}	Obukhov Length (m)
L_s	Shear Length Scale (m)
m_c	Mass of Tracer in UM Tracer Budget Analysis Region (kg)
m_s	Mass of a DSHO (kg)
$\boldsymbol{n}$	Unit Normal Vector (m)
N_l	Non-local Turbulent Transport of TMF (m^2s^{-2})
p	Air Pressure (Pa)
P	Rainfall Rate (mmhr^{-1})
P_c	Tracer Concentration Probability Distribution Function (kg^{-1}m^3)
P_s	Shear Production of Turbulent Momentum Flux (m^2s^{-3})
P_w	Wake Production of Turbulent Momentum Flux (m^2s^{-3})
A, B, D, J, p_+ and p_-	DSHO Model Solution Parameters (dimensionless except J which is s^{-1})
q	Pollution Emissions Per Unit of Horizontal Box Model Area Including Buildings ($\text{kgm}^{-2}\text{s}^{-1}$)

Glossary

q_{fix}	Pollution Emissions Per Unit of Box Model Ground Area ($\text{kgm}^{-2}\text{s}^{-1}$)
q_m	Specific Humidity (gkg^{-1})
Q	UM Continuous Source Tracer Release Rate ($\text{kgm}^{-2}\text{s}^{-1}$)
Q_H	Surface Sensible Heat Flux ($\text{Jm}^{-2}\text{s}^{-1}$)
R_a	Dry Deposition Aerodynamic Resistance Above the Surface (m^{-1}s)
R_b	Dry Deposition Quasi-laminar Resistance in the Air in Contact With the Surface (m^{-1}s)
R_c	Dry Deposition Bulk Surface Resistance (m^{-1}s)
Re	Reynolds Number
Ri	Local Richardson number
R_{mn}	Two-point Correlation Function of Some Variables m and n
R_{ww}^L	Lagrangian Velocity Correlation Coefficient for w
S	Sectional Obstacle Area Density (m^{-1})
T_*	Convective Temperature Scale (K)
$T_{\text{SL},*}$	Friction Temperature (K)
U	One-Box Model Advection Speed (ms^{-1})
U_1	Urban Canopy Box Advection Speed (ms^{-1})
U_2	ML Box Advection Speed (ms^{-1})
u_*	Friction Velocity (ms^{-1})
u_τ	Wall Friction Velocity Set by the CFD Pressure Gradient Force (ms^{-1})
v_d	Dry Deposition Velocity (ms^{-1})
v_e	Two-Box Model Exchange Velocity (ms^{-1})
V	Total Volume (m^3)
V_f	Fluid Volume (m^3)
W	Mean Downstream Building Separation (m)
W_{1D}	UM Blending Scheme Weighting Function
w_*	Convective Velocity Scale (ms^{-1})
z_h	Atmospheric Boundary Layer Height (m)
z_l	Proposed Height Scale for the UM Blending Scheme (m)

Glossary

z_{MH}	Mixing Height (m)
z_s	Displacement of a DSHO (kg)
z_0	Aerodynamic Roughness Length (m)
α	Proportionality Constant Between L_s and $\langle l_{m,\text{av}} \rangle$
γ	DSHO Model Damping Parameter (s^{-1})
γ_χ	Non-local Turbulence Parameter (m^{-1})
γ_s	Parameter Determining the Magnitude of a DSHO Damping Force (kgs^{-1})
δ	Rough Wall Boundary Layer Depth (m)
δ_d	Dirac Delta Function (m^{-1})
Δ_{xy}	Horizontal Grid Length (m)
Δ_z	Vertical Grid Length (m)
ϵ	Fluid Fraction
ζ	ISL Stability Scaling Parameter
θ	Potential Temperature (K)
θ_H	Heaviside Function
θ_s	Wind Angle at Canopy Top Relative to the Long Axis of a Street Canyon
κ	von Kármán Coefficient
λ_f	Building Frontal Area Density
λ_p	Building Packing (or Plan Area) Density
Λ	Washout Coefficient (s^{-1})
ν	Molecular Viscosity of Air (m^{2}s^{-1})
ξ	Random Velocity Increments (ms^{-1})
ρ	Air Density (kgm^{-3})
σ_w	Square Root of the Vertical Velocity Variance for an Ensemble of Tracers (ms^{-1})
σ_z	Square Root of the Mean Square Tracer Displacements (m)
τ	Horizontal Advection Timescale of the One-Box Model (s)
τ_m	Turbulent Momentum Flux (kgm^{-1}s^{-2})
τ_{dc}	LSM Decorrelation Timescale (s)

Glossary

$\tau_{ex,1}$	Vertical Exchange Timescale Between the Urban Canopy Box and ML Box (s)
$\tau_{ex,2}$	Vertical Exchange Timescale Between the ML Box and Urban Canopy Box (s)
τ_{p_+}, τ_{p_-}	DSHO Model Overdamped Solution Timescales (s)
τ_*	Deardorff Convective Timescale (s)
τ_Δ	Time Difference Between Two Specified Times (s)
τ_Ω, τ_ω	DSHO Model Underdamped Solution Timescales (s)
ϕ	Phase Angle of the DSHO Model Underdamped Solution (rad)
Φ_m	ISL Gradient Stability Function for Momentum
χ	Passive Scalar Variable
Ψ_m	ISL Integral Stability Function for Momentum
ω	Driving Frequency of the DSHO Model (s^{-1})
ω_s	Parameter Determining the Magnitude of a DSHO Restoring Force (kg$^{1/2}$s^{-1})
Ω	Oscillation Frequency of the DSHO Model Underdamped Solution (s^{-1})

References

Abraham, L., 2016: United Kingdom Chemistry and Aerosol (UKCA) Technical Description. Unified Model Documentation Paper 84, Met Office.

Angevine, W. M., M. Tjernström, and M. Žagar, 2006: Modeling of the coastal boundary layer and pollutant transport in New England. *Journal of Applied Meteorology and Climatology*, **45**, 137–154.

Aruffo, E., et al., 2014: Aircraft observations of the lower troposphere above a megacity: Alkyl nitrate and ozone chemistry. *Atmospheric Environment*, **94**, 479–488.

Arya, S., 1999: *Air Pollution Meteorology and Dispersion*. Oxford University Press.

Aumont, B., F. Chervier, and S. Laval, 2003: Contribution of HONO sources to the $NO_x/HO_x/O_3$ chemistry in the polluted boundary layer. *Atmospheric Environment*, **37**, 487–498.

Bærentsen, J. H. and R. Berkowicz, 1984: Monte carlo simulation of plume dispersion in the convective boundary layer. *Atmospheric Environment*, **18**, 701–712.

Baklanov, A., et al., 2014: Online coupled regional meteorology chemistry models in europe: current status and prospects. *Atmospheric Chemistry and Physics*, **14**, 317–398.

Barlow, J. and O. Coceal, 2009: A Review of Urban Roughness Sublayer Turbulence. UK Met Office Technical Report no. 527.

Barlow, J., G. Rooney, S. von Hünerbein, and S. Bradley, 2008: Relating urban surface-layer structure to upwind terrain for the Salford Experiment (Salfex). *Boundary-Layer Meteorology*, **127**, 173–191.

Barlow, J., et al., 2017: Developing a research strategy to better understand, observe, and simulate urban atmospheric processes at kilometer to subkilometer scales. *Bulletin of the American Meteorological Society*, **98**, ES261–ES264.

Barlow, J. F., 2014: Progress in observing and modelling the urban boundary layer. *Urban Climate*, **10**, 216–240.

Barlow, J. F., A. Dobre, R. Smalley, S. Arnold, A. Tomlin, and S. E. Belcher, 2009: Referencing of street-level flows measured during the DAPPLE 2004 campaign. *Atmospheric Environment*, **43**, 5536–5544.

Barlow, J. F., T. Dunbar, E. Nemitz, C. R. Wood, M. Gallagher, F. Davies, E. O'Connor, and R. Harrison, 2011a: Boundary layer dynamics over London, UK, as observed using Doppler lidar during REPARTEE-II. *Atmospheric Chemistry and Physics*, **11**, 2111–2125.

Barlow, J. F., C. H. Halios, S. E. Lane, and C. R. Wood, 2015: Observations of urban boundary layer structure during a strong urban heat island event. *Environmental Fluid*

Mechanics, **15**, 373–398.

Barlow, J. F., I. N. Harman, and S. E. Belcher, 2004: Scalar fluxes from urban street canyons. Part I: Laboratory simulation. *Boundary-Layer Meteorology*, **113**, 369–385.

Barlow, J. F., J. Harrison, A. G. Robins, and C. R. Wood, 2011b: A wind-tunnel study of flow distortion at a meteorological sensor on top of the BT Tower, London, UK. *Journal of Wind Engineering and Industrial Aerodynamics*, **99**, 899–907.

Beare, R. J., 2014: A length scale defining partially-resolved boundary-layer turbulence simulations. *Boundary-Layer Meteorology*, **151**, 39–55.

Beevers, S. D., N. Kitwiroon, M. L. Williams, and D. C. Carslaw, 2012: One way coupling of CMAQ and a road source dispersion model for fine scale air pollution predictions. *Atmospheric Environment*, **59**, 47–58.

Belcher, S., N. Jerram, and J. Hunt, 2003: Adjustment of a turbulent boundary layer to a canopy of roughness elements. *Journal of Fluid Mechanics*, **488**, 369–398.

Belcher, S. E., 2005: Mixing and transport in urban areas. *Philosophical Transactions of the Royal Society A: Mathematical, Physical and Engineering Sciences*, **363**, 2947–2968.

Bentham, T. and R. Britter, 2003: Spatially averaged flow within obstacle arrays. *Atmospheric Environment*, **37**, 2037–2043.

Berkowicz, R., 2000: OSPM-A parameterised street pollution model. *Environmental Monitoring and Assessment*, **65**, 323–331.

Best, M., et al., 2011: The Joint UK Land Environment Simulator (JULES), model description–Part 1: energy and water fluxes. *Geoscientific Model Development*, **4**, 677–699.

Blumenthal, D., W. White, and T. Smith, 1978: Anatomy of a Los Angeles smog episode: Pollutant transport in the daytime sea breeze regime. *Atmospheric Environment*, **12**, 893–907.

Bo, M., P. Charvolin-Volta, M. Clerico, C. V. Nguyen, F. Pognant, L. Soulhac, and P. Salizzoni, 2020: Urban air quality and meteorology on opposite sides of the Alps: The Lyon and Torino case studies. *Urban Climate*, **34**, 100 698.

Bohnenstengel, S., S. Evans, P. A. Clark, and S. Belcher, 2011: Simulations of the London urban heat island. *Quarterly Journal of the Royal Meteorological Society*, **137**, 1625–1640.

Bohnenstengel, S., et al., 2015: Meteorology, air quality, and health in London: The ClearfLo project. *Bulletin of the American Meteorological Society*, **96**, 779–804.

Bonin, T., et al., 2017: Evaluation of turbulence measurement techniques from a single Doppler lidar. *Atmospheric Measurement Techniques*, **10**, 3021–3039.

Bonin, T. A., B. J. Carroll, R. M. Hardesty, W. A. Brewer, K. Hajny, O. E. Salmon, and P. B. Shepson, 2018: Doppler lidar observations of the mixing height in Indianapolis using an automated composite fuzzy logic approach. *Journal of Atmospheric and Oceanic Technology*, **35**, 473–490.

Bopape, M.-J. M., R. S. Plant, and O. Coceal, 2020: Resolution dependence of turbulent structures in convective boundary layer simulations. *Atmosphere*, **11**, 986.

Bou-Zeid, E., C. Meneveau, and M. B. Parlange, 2004: Large-eddy simulation of neutral atmospheric boundary layer flow over heterogeneous surfaces: Blending height and effective surface roughness. *Water Resources Research*, **40**, W02 505.

Bougeault, P. and P. Lacarrere, 1989: Parameterization of orography-induced turbulence in a mesobeta–scale model. *Monthly Weather Review*, **117**, 1872–1890.

Boutle, I., J. Eyre, and A. Lock, 2014: Seamless stratocumulus simulation across the turbulent gray zone. *Monthly Weather Review*, **142**, 1655–1668.

Boutle, I., A. Finnenkoetter, A. Lock, and H. Wells, 2016: The London Model: forecasting fog at 333 m resolution. *Quarterly Journal of the Royal Meteorological Society*, **142**, 360–371.

Branford, S., O. Coceal, T. Thomas, and S. Belcher, 2011: Dispersion of a point-source release of a passive scalar through an urban-like array for different wind directions. *Boundary-Layer Meteorology*, **139**, 367–394.

Breugem, W., B. Boersma, and R. Uittenbogaard, 2006: The influence of wall permeability on turbulent channel flow. *Journal of Fluid Mechanics*, **562**, 35–72.

Briggs, D. J., et al., 1997: Mapping urban air pollution using GIS: a regression-based approach. *International Journal of Geographical Information Science*, **11**, 699–718.

Britter, R. and S. Hanna, 2003: Flow and dispersion in urban areas. *Annual Review of Fluid Mechanics*, **35**, 469–496.

Brown, S. S., R. K. Talukdar, and A. Ravishankara, 1999: Rate constants for the reaction OH+ NO2+ M → HNO3+ M under atmospheric conditions. *Chemical Physics Letters*, **299**, 277–284.

Busch, N. E., S. W. Chang, and R. A. Anthes, 1976: A multi-level model of the planetary boundary layer suitable for use with mesoscale dynamic models. *Journal of Applied Meteorology*, **15**, 909–919.

Byun, D., 1999: Science algorithms of the EPA Models-3 community multiscale air quality (CMAQ) modeling system. Environment Protection Agency, accessed: 2021-02-28, `https://cfpub.epa.gov/si/si_public_file_download.cfm?p_download_id=524687&Lab=NERL`.

Castro, I. P., 2017: Are urban-canopy velocity profiles exponential? *Boundary-Layer Meteorology*, **164**, 337–351.

Castro, I. P., Z.-T. Xie, V. Fuka, A. G. Robins, M. Carpentieri, P. Hayden, D. Hertwig, and O. Coceal, 2017: Measurements and computations of flow in an urban street system. *Boundary-Layer Meteorology*, **162**, 207–230.

Caton, F., R. Britter, and S. Dalziel, 2003: Dispersion mechanisms in a street canyon. *Atmospheric Environment*, **37**, 693–702.

CERC, 2017: ADMS-Urban User Guide. Accessed: 2020-08-20, `http://www.cerc.co.uk/environmental-software/assets/data/doc_userguides/CERC_ADMS-Urban4.1.1_User_Guide.pdf`.

Cheng, H. and I. P. Castro, 2002: Near wall flow over urban-like roughness. *Boundary-*

Layer Meteorology, **104**, 229–259.

Cherin, N., Y. Roustan, L. Musson-Genon, and C. Seigneur, 2015: Modelling atmospheric dry deposition in urban areas using an urban canopy approach. *Geoscientific Model Development*, **8**, 893–910.

Cimorelli, A. J., et al., 2005: AERMOD: A dispersion model for industrial source applications. Part I: General model formulation and boundary layer characterization. *Journal of Applied Meteorology*, **44**, 682–693.

Clark, P., N. Roberts, H. Lean, S. P. Ballard, and C. Charlton-Perez, 2016: Convection-permitting models: a step-change in rainfall forecasting. *Meteorological Applications*, **23**, 165–181.

Claus, J., O. Coceal, T. G. Thomas, S. Branford, S. E. Belcher, and I. P. Castro, 2012: Wind-direction effects on urban-type flows. *Boundary-Layer Meteorology*, **142**, 265–287.

Coceal, O. and S. Belcher, 2004: A canopy model of mean winds through urban areas. *Quarterly Journal of the Royal Meteorological Society*, **130**, 1349–1372.

Coceal, O., A. Dobre, T. Thomas, and S. Belcher, 2007a: Structure of turbulent flow over regular arrays of cubical roughness. *Journal of Fluid Mechanics*, **589**, 375–409.

Coceal, O., A. Dobre, and T. G. Thomas, 2007b: Unsteady dynamics and organized structures from DNS over an idealized building canopy. *International Journal of Climatology: A Journal of the Royal Meteorological Society*, **27**, 1943–1953.

Coceal, O., E. V. Goulart, S. Branford, T. G. Thomas, and S. E. Belcher, 2014: Flow structure and near-field dispersion in arrays of building-like obstacles. *Journal of Wind Engineering and Industrial Aerodynamics*, **125**, 52–68.

Coceal, O., T. Thomas, I. Castro, and S. Belcher, 2006: Mean flow and turbulence statistics over groups of urban-like cubical obstacles. *Boundary-Layer Meteorology*, **121**, 491–519.

Coceal, O., T. G. Thomas, and S. E. Belcher, 2007c: Spatial variability of flow statistics within regular building arrays. *Boundary-Layer Meteorology*, **125**, 537–552.

Collins, W., D. S. Stevenson, C. Johnson, and R. Derwent, 1997: Tropospheric ozone in a global-scale three-dimensional Lagrangian model and its response to NO_x emission controls. *Journal of Atmospheric Chemistry*, **26**, 223–274.

Crawford, B., C. S. B. Grimmond, H. C. Ward, W. Morrison, and S. Kotthaus, 2017: Spatial and temporal patterns of surface–atmosphere energy exchange in a dense urban environment using scintillometry. *Quarterly Journal of the Royal Meteorological Society*, **143**, 817–833.

Dacre, H. F., S. L. Gray, and S. E. Belcher, 2007: A case study of boundary layer ventilation by convection and coastal processes. *Journal of Geophysical Research: Atmospheres*, **112**, D17 106.

Dacre, H. F., et al., 2011: Evaluating the structure and magnitude of the ash plume during the initial phase of the 2010 Eyjafjallajökull eruption using lidar observations and NAME simulations. *Journal of Geophysical Research: Atmospheres*, **116**, D00U03.

Davies, T., M. J. Cullen, A. J. Malcolm, M. Mawson, A. Staniforth, A. White, and

N. Wood, 2005: A new dynamical core for the Met Office's global and regional modelling of the atmosphere. *Quarterly Journal of the Royal Meteorological Society*, **131**, 1759–1782.

de Leeuw, F. A., E. D. van Zantvoort, R. J. Sluyter, and W. A. J. van Pul, 2002: Urban air quality assessment model: UAQAM. *Environmental Modeling & Assessment*, **7**, 243–258.

Deardorff, J., 1972a: Theoretical expression for the countergradient vertical heat flux. *Journal of Geophysical Research*, **77**, 5900–5904.

Deardorff, J. and G. Willis, 1985: Further results from a laboratory model of the convective planetary boundary layer. *Boundary-Layer Meteorology*, **32**, 205–236.

Deardorff, J. W., 1972b: Numerical investigation of neutral and unstable planetary boundary layers. *Journal of the Atmospheric Sciences*, **29**, 91–115.

Deardorff, J. W., 1980: Stratocumulus-capped mixed layers derived from a three-dimensional model. *Boundary-Layer Meteorology*, **18**, 495–527.

DEFRA, 2018: Clean Air Strategy 2018. Accessed: 2018-06-11, `https://consult.defra.gov.uk/environmental-quality/clean-air-strategy-consultation/user_uploads/clean-air-strategy-2018-consultation.pdf`.

DEFRA, 2020: Department for environment, food and rural affairs (defra): Pollution forecast. Accessed: 2020-11-18, `https://uk-air.defra.gov.uk/forecasting/`.

Department for Transport, 2020: Provisional Road Traffic Estimates, Great Britain: October 2019 – September 2020. Accessed: 2020-12-11, `https://assets.publishing.service.gov.uk/government/uploads/system/uploads/attachment_data/file/940319/tra2501.ods`.

Diamantakis, M., 2013: The semi-Lagrangian technique in atmospheric modelling: current status and future challenges. European Centre for Medium-Range Weather Forecasts, accessed: 2021-02-28, `https://www.ecmwf.int/sites/default/files/elibrary/2014/9054-semi-lagrangian-technique-atmospheric-modelling-current-status-and-pdf`.

Dickerson, R. R., et al., 1987: Thunderstorms: An important mechanism in the transport of air pollutants. *Science*, **235**, 460–465.

Dosio, A., J. V. Guerau de Arellano, A. A. Holtslag, and P. J. Builtjes, 2005: Relating Eulerian and Lagrangian statistics for the turbulent dispersion in the atmospheric convective boundary layer. *Journal of the Atmospheric Sciences*, **62**, 1175–1191.

Dosio, A., J. Vilà-Guerau de Arellano, A. A. Holtslag, and P. J. Builtjes, 2003: Dispersion of a passive tracer in buoyancy-and shear-driven boundary layers. *Journal of Applied Meteorology*, **42**, 1116–1130.

Durran, D. R., 2010: *Numerical methods for fluid dynamics: With applications to geophysics*. Springer Science & Business Media.

Dyer, A. and B. Hicks, 1970: Flux-gradient relationships in the constant flux layer. *Quarterly Journal of the Royal Meteorological Society*, **96**, 715–721.

Eliasson, I., B. Offerle, C. Grimmond, and S. Lindqvist, 2006: Wind fields and turbulence statistics in an urban street canyon. *Atmospheric Environment*, **40**, 1–16.

Elminir, H. K., 2005: Dependence of urban air pollutants on meteorology. *Science of the Total Environment*, **350**, 225–237.

Esler, J., P. Haynes, K. Law, H. Barjat, K. Dewey, J. Kent, S. Schmitgen, and N. Brough, 2003: Transport and mixing between airmasses in cold frontal regions during Dynamics and Chemistry of Frontal Zones (DCFZ). *Journal of Geophysical Research: Atmospheres*, **108**, 4142.

Essery, R. L. H., M. J. Best, R. A. Betts, P. M. Cox, and C. M. Taylor, 2003: Explicit representation of subgrid heterogeneity in a GCM land surface scheme. *Journal of Hydrometeorology*, **4**, 530–543.

Evans, S., 2009: 3D cities and numerical weather prediction models: An overview of the methods used in the LUCID project. Centre for Advanced Spatial Analysis.

Fan, Y., J. C. R. Hunt, and Y. Li, 2017: Buoyancy and turbulence-driven atmospheric circulation over urban areas. *Journal of Environmental Sciences*, **59**, 63–71.

Finnigan, J., 2000: Turbulence in plant canopies. *Annual Review of Fluid Mechanics*, **32**, 519–571.

Finnigan, J., I. Harman, A. Ross, and S. Belcher, 2015: First-order turbulence closure for modelling complex canopy flows. *Quarterly Journal of the Royal Meteorological Society*, **141**, 2907–2916.

Finnigan, J. J., R. H. Shaw, and E. G. Patton, 2009: Turbulence structure above a vegetation canopy. *Journal of Fluid Mechanics*, **637**, 387–424.

Frenzen, P. and C. A. Vogel, 1995: On the magnitude and apparent range of variation of the von karman constant in the atmospheric surface layer. *Boundary-Layer Meteorology*, **72**, 371–392.

Garratt, J., 1994: *The Atmospheric Boundary Layer*. Cambridge University Press.

Ghannam, K. and M. El-Fadel, 2013: Emissions characterization and regulatory compliance at an industrial complex: an integrated MM5/CALPUFF approach. *Atmospheric Environment*, **69**, 156–169.

Ghisalberti, M., 2009: Obstructed shear flows: similarities across systems and scales. *Journal of Fluid Mechanics*, **641**, 51.

Gimson, N., 1997: Pollution transport by convective clouds in a mesocale model. *Quarterly Journal of the Royal Meteorological Society*, **123**, 1805–1828.

Giometto, M., A. Christen, C. Meneveau, J. Fang, M. Krafczyk, and M. Parlange, 2016: Spatial characteristics of roughness sublayer mean flow and turbulence over a realistic urban surface. *Boundary-Layer Meteorology*, **160**, 425–452.

Giorgi, F. and F. Meleux, 2007: Modelling the regional effects of climate change on air quality. *Comptes Rendus Geoscience*, **339**, 721–733.

Gloster, J., H. Champion, J. Sørensen, T. Mikkelsen, D. Ryall, P. Astrup, S. Alexandersen, and A. Donaldson, 2003: Airborne transmission of foot-and-mouth disease virus from Burnside Farm, Heddonon-the-Wall, Northumberland, during the 2001 epidemic in the United Kingdom. *Veterinary Record*, **152**, 525–533.

Gopalakrishnan, S. and R. Avissar, 2000: An LES study of the impacts of land surface heterogeneity on dispersion in the convective boundary layer. *Journal of the Atmospheric Sciences*, **57**, 352–371.

Greater London Authority, 2016: London atmospheric emissions inventory 2013. Accessed: 2017-05-30, `https://files.datapress.com/london/dataset/london-atmospheric-emissions-inventory-2013/2017-01-26T15:56:49/2%20-%20Grid%20Emissions%20Summary%20-%20Excel%20Files.zip`.

Greater London Authority, 2020: London atmospheric emissions inventory – summary dashboards. Accessed: 2020-11-01, `https://data.london.gov.uk/download/london-atmospheric-emissions-inventory--laei--2016/df1bb6e9-f67c-49e3-976e-cb143e0ded4a/LAEI_2016_Emissions_Summary_Dashboard.zip`.

Grimmond, C. and T. R. Oke, 1999: Aerodynamic properties of urban areas derived from analysis of surface form. *Journal of Applied Meteorology*, **38**, 1262–1292.

Grimmond, C. S. B., et al., 2011: Initial results from phase 2 of the international urban energy balance model comparison. *International Journal of Climatology*, **31**, 244–272.

Grossman, R. L., 1982: An analysis of vertical velocity spectra obtained in the BOMEX fair-weather, trade-wind boundary layer. *Boundary-Layer Meteorology*, **23**, 323–357.

Gutiérrez, E., J. E. González, A. Martilli, R. Bornstein, and M. Arend, 2015: Simulations of a heat-wave event in New York City using a multilayer urban parameterization. *Journal of Applied Meteorology and Climatology*, **54**, 283–301.

Halios, C. H. and J. F. Barlow, 2018: Observations of the morning development of the urban boundary layer over London, UK, taken during the ACTUAL project. *Boundary-Layer Meteorology*, **166**, 395–422.

Hamdi, R. and V. Masson, 2008: Inclusion of a drag approach in the Town Energy Balance (TEB) scheme: Offline 1D evaluation in a street canyon. *Journal of Applied Meteorology and Climatology*, **47**, 2627–2644.

Hamer, P. and D. Shallcross, 2007: Modelling the impact of oxygenated VOC and meteorology upon the boundary layer photochemistry at the South Pole. *Atmospheric Science Letters*, **8**, 14–20.

Hanley, K. E., R. S. Plant, T. H. Stein, R. J. Hogan, J. C. Nicol, H. W. Lean, C. Halliwell, and P. A. Clark, 2015: Mixing-length controls on high-resolution simulations of convective storms. *Quarterly Journal of the Royal Meteorological Society*, **141**, 272–284.

Harman, I. N., J. F. Barlow, and S. E. Belcher, 2004: Scalar fluxes from urban street canyons part II: model. *Boundary-Layer Meteorology*, **113**, 387–410.

Harman, I. N. and J. J. Finnigan, 2007: A simple unified theory for flow in the canopy

and roughness sublayer. *Boundary-Layer Meteorology*, **123**, 339–363.

Harman, I. N. and J. J. Finnigan, 2008: Scalar concentration profiles in the canopy and roughness sublayer. *Boundary-Layer Meteorology*, **129**, 323–351.

Held, I. M., 2005: The gap between simulation and understanding in climate modeling. *Bulletin of the American Meteorological Society*, **86**, 1609–1614.

Hertwig, D., et al., 2018: Evaluation of fast atmospheric dispersion models in a regular street network. *Environmental Fluid Mechanics*, **18**, 1007–1044.

Hoek, G., R. Beelen, K. De Hoogh, D. Vienneau, J. Gulliver, P. Fischer, and D. Briggs, 2008: A review of land-use regression models to assess spatial variation of outdoor air pollution. *Atmospheric Environment*, **42**, 7561–7578.

Honnert, R., 2019: Grey-zone turbulence in the neutral atmospheric boundary layer. *Boundary-Layer Meteorology*, **170**, 191–204.

Honnert, R., V. Masson, and F. Couvreux, 2011: A diagnostic for evaluating the representation of turbulence in atmospheric models at the kilometric scale. *Journal of the Atmospheric Sciences*, **68**, 3112–3131.

Honnert, R., et al., 2020: The Atmospheric Boundary Layer and the "Gray Zone" of Turbulence: A critical review. *Journal of Geophysical Research: Atmospheres*, e2019JD030317.

Hood, C., I. MacKenzie, J. Stocker, K. Johnson, D. Carruthers, M. Vieno, and R. Doherty, 2018: Air quality simulations for London using a coupled regional-to-local modelling system. *Atmospheric Chemistry and Physics*, **18**, 11221–11245.

Hunt, J., R. Holroyd, and D. Carruthers, 1988: Preparatory studies for a complex dispersion model. *CERC Report HB9/88*.

IARC, 2016: International Agency for Research on Cancer (IARC) monographs on the evaluation of carcinogenic risks to humans. Accessed: 2020-10-30, `https://publications.iarc.fr/538`.

Inoue, E., 1963: On the turbulent structure of airflow within crop canopies. *Journal of the Meteorological Society of Japan*, **41**, 317–326.

Jensen, N. O. and E. L. Petersen, 1979: The box model and the acoustic sounder, a case study. *Atmospheric Environment*, **13**, 717–720.

Jiménez, J., 2004: Turbulent flows over rough walls. *Annual Review of Fluid Mechanics*, **36**, 173–196.

Jin, S. and K. Demerjian, 1993: A photochemical box model for urban air quality study. *Atmospheric Environment. Part B. Urban Atmosphere*, **27**, 371–387.

Jones, A., D. Thomson, M. Hort, and B. Devenish, 2007: The UK Met Office's next-generation atmospheric dispersion model, NAME III. *Air Pollution Modeling and its Application XVII*, Springer, 580–589.

Kanda, M., 2006: Large-eddy simulations on the effects of surface geometry of building arrays on turbulent organized structures. *Boundary-Layer Meteorology*, **118**, 151–168.

Kanda, M., R. Moriwaki, and F. Kasamatsu, 2004: Large-eddy simulation of turbulent organized structures within and above explicitly resolved cube arrays. *Boundary-Layer*

Meteorology, **112**, 343–368.

Karroum, K., Y. Lin, Y.-Y. Chiang, Y. B. Maissa, M. El Haziti, A. Sokolov, and H. Delbarre, 2020: A Review of Air Quality Modeling. *Journal of Metrology Society of India*, 1–14.

Kaser, L., et al., 2017: The effect of entrainment through atmospheric boundary layer growth on observed and modeled surface ozone in the Colorado Front Range. *Journal of Geophysical Research: Atmospheres*, **122**, 6075–6093.

Katul, G. G., L. Mahrt, D. Poggi, and C. Sanz, 2004: One-and two-equation models for canopy turbulence. *Boundary-Layer Meteorology*, **113**, 81–109.

Kealy, J. C., G. A. Efstathiou, and R. J. Beare, 2019: The onset of resolved boundary-layer turbulence at grey-zone resolutions. *Boundary-Layer Meteorology*, **171**, 31–52.

Kent, C. W., S. Grimmond, J. Barlow, D. Gatey, S. Kotthaus, F. Lindberg, and C. H. Halios, 2017: Evaluation of urban local-scale aerodynamic parameters: implications for the vertical profile of wind speed and for source areas. *Boundary-Layer Meteorology*, **164**, 183–213.

Kondo, H., Y. Genchi, Y. Kikegawa, Y. Ohashi, H. Yoshikado, and H. Komiyama, 2005: Development of a multi-layer urban canopy model for the analysis of energy consumption in a big city: Structure of the urban canopy model and its basic performance. *Boundary-Layer Meteorology*, **116**, 395–421.

Kormann, R. and F. X. Meixner, 2001: An analytical footprint model for non-neutral stratification. *Boundary-Layer Meteorology*, **99**, 207–224.

Kotthaus, S. and C. S. B. Grimmond, 2014: Energy exchange in a dense urban environment–part 1: Temporal variability of long-term observations in central london. *Urban Climate*, **10**, 261–280.

Kotthaus, S., C. H. Halios, J. F. Barlow, and C. Grimmond, 2018: Volume for pollution dispersion: London's atmospheric boundary layer during ClearfLo observed with two ground-based lidar types. *Atmospheric Environment*, **190**, 401–414.

Krayenhoff, E., A. Christen, A. Martilli, and T. Oke, 2014: A multi-layer radiation model for urban neighbourhoods with trees. *Boundary-Layer Meteorology*, **151**, 139–178.

Krayenhoff, E. S., et al., 2020: A multi-layer urban canopy meteorological model with trees (BEP-Tree): Street tree impacts on pedestrian-level climate. *Urban Climate*, **32**, 100 590.

Kukkonen, J., et al., 2012: A review of operational, regional-scale, chemical weather forecasting models in Europe. *Atmospheric Chemistry and Physics*, **12**, 1–87.

Kusaka, H., H. Kondo, Y. Kikegawa, and F. Kimura, 2001: A simple single-layer urban canopy model for atmospheric models: Comparison with multi-layer and slab models. *Boundary-Layer Meteorology*, **101**, 329–358.

Lamb, R. G., 1984: Diffusion in the convective boundary layer. *Atmospheric Turbulence and Air Pollution Modelling*, Springer, 159–229.

Lane, S., J. Barlow, and C. Wood, 2013: An assessment of a three-beam Doppler lidar wind profiling method for use in urban areas. *Journal of Wind Engineering and Industrial*

Aerodynamics, **119**, 53–59.

Lauritzen, P. H., R. D. Nair, and P. A. Ullrich, 2010: A conservative semi-Lagrangian multi-tracer transport scheme (CSLAM) on the cubed-sphere grid. *Journal of Computational Physics*, **229**, 1401–1424.

Lean, H. W., J. F. Barlow, and C. H. Halios, 2019: The impact of spin-up and resolution on the representation of a clear convective boundary layer over London in order 100 m grid-length versions of the Met Office Unified Model. *Quarterly Journal of the Royal Meteorological Society*, **145**, 1674–1689.

Lean, H. W., P. A. Clark, M. Dixon, N. M. Roberts, A. Fitch, R. Forbes, and C. Halliwell, 2008: Characteristics of high-resolution versions of the Met Office Unified Model for forecasting convection over the United Kingdom. *Monthly Weather Review*, **136**, 3408–3424.

Lee, J., et al., 2019: Ceilometer monitoring of boundary-layer height and its application in evaluating the dilution effect on air pollution. *Boundary-Layer Meteorology*, **172**, 435–455.

Lee, J. D., S. J. Moller, K. A. Read, A. C. Lewis, L. Mendes, and L. J. Carpenter, 2009: Year-round measurements of nitrogen oxides and ozone in the tropical North Atlantic marine boundary layer. *Journal of Geophysical Research: Atmospheres*, **114**.

Lee, J. D., et al., 2015: Measurement of NO_x fluxes from a tall tower in central London, UK and comparison with emissions inventories. *Environmental Science & Technology*, **49**, 1025–1034.

Leelőssy, Á., F. Molnár, F. Izsák, Á. Havasi, I. Lagzi, and R. Mészáros, 2014: Dispersion modeling of air pollutants in the atmosphere: a review. *Central European Journal of Geosciences*, **6**, 257–278.

Leonardi, S. and I. P. Castro, 2010: Channel flow over large cube roughness: a direct numerical simulation study. *Journal of Fluid Mechanics*, **651**, 519–539.

Leroyer, S., S. Bélair, S. Z. Husain, and J. Mailhot, 2014: Subkilometer numerical weather prediction in an urban coastal area: A case study over the Vancouver metropolitan area. *Journal of Applied Meteorology and Climatology*, **53**, 1433–1453.

Lettau, H. H., 1970: Physical and meteorological basis for mathematical models of urban diffusion processes. *Proceedings of Symposium on Multiple Source Urban Diffusion Models, USEPA Publication AP-86*.

Letzel, M. O., M. Krane, and S. Raasch, 2008: High resolution urban large-eddy simulation studies from street canyon to neighbourhood scale. *Atmospheric Environment*, **42**, 8770–8784.

Li, X.-X., C.-H. Liu, D. Y. Leung, and K. M. Lam, 2006: Recent progress in CFD modelling of wind field and pollutant transport in street canyons. *Atmospheric Environment*, **40**, 5640–5658.

Lilly, D., 1967: The representation of small-scale turbulence in numerical simulation experiments. *In Proceedings of IBM Scientific Computing Symposium on Environmental Sci-*

ences, 195–210.

Liu, C. and D. Leung, 2001: Turbulence and dispersion studies using a three-dimensional second-order closure Eulerian model. *Journal of Applied Meteorology*, **40**, 92–113.

Liu, C.-H. and D. Y. Leung, 2008: Numerical study on the ozone formation inside street canyons using a chemistry box model. *Journal of Environmental Sciences*, **20**, 832–837.

Lo, J. C., A. K. Lau, F. Chen, J. C. Fung, and K. K. Leung, 2007: Urban modification in a mesoscale model and the effects on the local circulation in the Pearl River Delta region. *Journal of Applied Meteorology and Climatology*, **46**, 457–476.

Lock, A., I. Boutle, and C. Smith, 2017: Blobbiness Working Group Progress Report. Accessed: 2020-08-12, `https://code.metoffice.gov.uk/trac/rmed/wiki/pegs/blobbiness/KDreport_Sept17`.

Lock, A., I. Boutle, and C. Smith, 2019: Semi-Lagrangian Advection. Unified Model Documentation Paper 18, Met Office.

Lock, A., A. Brown, M. Bush, G. Martin, and R. Smith, 2000: A new boundary layer mixing scheme. Part I: Scheme description and single-column model tests. *Monthly Weather Review*, **128**, 3187–3199.

Lock, A., J. Edwards, and I. Boutle, 2016: The parametrization of boundary layer processes. Unified Model Documentation Paper 24, Met Office.

Lugon, L., K. Sartelet, Y. Kim, J. Vigneron, and O. Chrétien, 2020: Nonstationary modeling of NO_2, NO and NO_x in Paris using the Street-in-Grid model: coupling local and regional scales with a two-way dynamic approach. *Atmospheric Chemistry and Physics*, **20**, 7717–7740.

Luhar, A. K. and R. E. Britter, 1989: A random walk model for dispersion in inhomogeneous turbulence in a convective boundary layer. *Atmospheric Environment*, **23**, 1911–1924.

Macdonald, R., 2000: Modelling the mean velocity profile in the urban canopy layer. *Boundary-Layer Meteorology*, **97**, 25–45.

Macdonald, R., R. Griffiths, and D. Hall, 1998: An improved method for the estimation of surface roughness of obstacle arrays. *Atmospheric Environment*, **32**, 1857–1864.

Marlier, M. E., A. S. Jina, P. L. Kinney, and R. S. DeFries, 2016: Extreme air pollution in global megacities. *Current Climate Change Reports*, **2**, 15–27.

Maronga, B., et al., 2015: The parallelized large-eddy simulation model (PALM) version 4.0 for atmospheric and oceanic flows: model formulation, recent developments, and future perspectives. *Geoscientific Model Development*, **8**, 2515–2551.

Martilli, A., A. Clappier, and M. W. Rotach, 2002: An urban surface exchange parameterisation for mesoscale models. *Boundary-Layer Meteorology*, **104**, 261–304.

Martilli, A. and J. L. Santiago, 2007: CFD simulation of airflow over a regular array of cubes. Part II: analysis of spatial average properties. *Boundary-Layer Meteorology*, **122**, 635–654.

Marucci, D. and M. Carpentieri, 2020: Dispersion in an array of buildings in stable and

convective atmospheric conditions. *Atmospheric Environment*, **222**, 117 100.

Masiol, M. and R. M. Harrison, 2015: Quantification of air quality impacts of London Heathrow Airport (UK) from 2005 to 2012. *Atmospheric Environment*, **116**, 308–319.

Mason, P., 1988: The formation of areally-averaged roughness lengths. *Quarterly Journal of the Royal Meteorological Society*, **114**, 399–420.

Mason, P. J., 1989: Large-eddy simulation of the convective atmospheric boundary layer. *Journal of the Atmospheric Sciences*, **46**, 1492–1516.

Masson, V., 2000: A physically-based scheme for the urban energy budget in atmospheric models. *Boundary-Layer Meteorology*, **94**, 357–397.

Masson, V., 2006: Urban surface modeling and the meso-scale impact of cities. *Theoretical and Applied Climatology*, **84**, 35–45.

Masson, V. and Y. Seity, 2009: Including atmospheric layers in vegetation and urban offline surface schemes. *Journal of Applied Meteorology and Climatology*, **48**, 1377–1397.

McHugh, C., D. Carruthers, and H. Edmunds, 1997: ADMS-urban: an air quality management system for traffic, domestic and industrial pollution. *International Journal of Environment and Pollution*, **8**, 666–674.

Middleton, D., 1998: A new box model to forecast urban air quality: Boxurb. *Environmental Monitoring and Assessment*, **52**, 315–335.

Monin, A. and A. Yaglom, 1975: *Statistical fluid mechanics: mechanics of turbulence*. MIT Press.

Monin, A. S. and A. M. Obukhov, 1954: Basic laws of turbulent mixing in the surface layer of the atmosphere. *Contributions of the Geophysical Institute of the Academy of Sciences USSR*, **151**, e187.

Murena, F., 2012: Monitoring and modelling carbon monoxide concentrations in a deep street canyon: application of a two-box model. *Atmospheric Pollution Research*, **3**, 311–316.

Nagib, H. M. and K. A. Chauhan, 2008: Variations of von kármán coefficient in canonical flows. *Physics of Fluids*, **20**, 101 518.

National Radiological Protection Board, 1984: Models to allow for the effects of coastal sites, plume arise and buildings on dispersion of radionuclides and guidance on the value of deposition velocity and washout coefficients. Accessed: 2017-06-26, `https://admlc.files.wordpress.com/2014/09/r157.pdf`.

Nazarian, N. and J. Kleissl, 2016: Realistic solar heating in urban areas: air exchange and street-canyon ventilation. *Building and Environment*, **95**, 75–93.

Nazarian, N., E. S. Krayenhoff, and A. Martilli, 2020: A one-dimensional model of turbulent flow through "urban" canopies (MLUCM v2. 0): updates based on large-eddy simulation. *Geoscientific Model Development*, **13**, 937–953.

Nepf, H., M. Ghisalberti, B. White, and E. Murphy, 2007: Retention time and dispersion associated with submerged aquatic canopies. *Water Resources Research*, **43**, W04 422.

Nieuwstadt, F. and J. De Valk, 1987: A large eddy simulation of buoyant and non-

buoyant plume dispersion in the atmospheric boundary layer. *Atmospheric Environment*, **21**, 2573–2587.

Nikora, V., I. McEwan, S. McLean, S. Coleman, D. Pokrajac, and R. Walters, 2007: Double-averaging concept for rough-bed open-channel and overland flows: Theoretical background. *Journal of Hydraulic Engineering*, **133**, 873–883.

Oke, T., 1995: The heat island of the urban boundary layer: characteristics, causes and effects. *Wind Climate in Cities*, Springer, 81–107.

Oke, T. R., G. Mills, and J. Voogt, 2017: *Urban climates*. Cambridge University Press.

Padhra, A., 2010: Estimating the Sensitivity of Urban Surface Drag to Building Morphology. Ph.D. thesis, University of Reading.

Park, S.-B. and J.-J. Baik, 2014: Large-eddy simulations of convective boundary layers over flat and urbanlike surfaces. *Journal of the Atmospheric Sciences*, **71**, 1880–1892.

Peake, D., H. Dacre, J. Methven, and O. Coceal, 2014: Meteorological factors controlling low-level continental pollutant outflow across a coast. *Atmospheric Chemistry and Physics*, **14**, 13 295–13 312.

Pearce, J. L., J. Beringer, N. Nicholls, R. J. Hyndman, P. Uotila, and N. J. Tapper, 2011: Investigating the influence of synoptic-scale meteorology on air quality using self-organizing maps and generalized additive modelling. *Atmospheric Environment*, **45**, 128–136.

Perret, L., K. Blackman, R. Fernandes, and E. Savory, 2017: Relating street canyon vertical mass-exchange to upstream flow regime and canyon geometry. *Sustainable Cities and Society*, **30**, 49–57.

Perret, L. and E. Savory, 2013: Large-scale structures over a single street canyon immersed in an urban-type boundary layer. *Boundary-Layer Meteorology*, **148**, 111–131.

Poggi, D., A. Porporato, L. Ridolfi, J. Albertson, and G. Katul, 2004: The effect of vegetation density on canopy sub-layer turbulence. *Boundary-Layer Meteorology*, **111**, 565–587.

Porson, A., P. A. Clark, I. Harman, M. Best, and S. Belcher, 2010: Implementation of a new urban energy budget scheme in the MetUM. Part I: Description and idealized simulations. *Quarterly Journal of the Royal Meteorological Society*, **136**, 1514–1529.

Priestley, A., 1993: A quasi-conservative version of the semi-Lagrangian advection scheme. *Monthly Weather Review*, **121**, 621–629.

Pugh, T., et al., 2010a: Simulating atmospheric composition over a South-East Asian tropical rainforest: performance of a chemistry box model. *Atmospheric Chemistry and Physics*, **10**, 279–298.

Pugh, T. A. M., et al., 2010b: Modelling chemistry in the nocturnal boundary layer above tropical rainforest and a generalised effective nocturnal ozone deposition velocity for sub-ppbv NOx conditions. *Journal of Atmospheric Chemistry*, **65**, 89–110.

Raasch, S. and M. Schröter, 2001: PALM–a large-eddy simulation model performing on massively parallel computers. *Meteorologische Zeitschrift*, **10**, 363–372.

Raupach, M., P. Coppin, and B. Legg, 1986: Experiments on scalar dispersion within a

model plant canopy part I: The turbulence structure. *Boundary-Layer Meteorology*, **35**, 21–52.

Raupach, M., J. Finnigan, and Y. Brunet, 1996: Coherent eddies and turbulence in vegetation canopies: the mixing-layer analogy. *Boundary-Layer Meteorology*, **78**, 351–382.

Raupach, M. R. and R. Shaw, 1982: Averaging procedures for flow within vegetation canopies. *Boundary-Layer Meteorology*, **22**, 79–90.

Raynaud, L. and F. Bouttier, 2017: The impact of horizontal resolution and ensemble size for convective-scale probabilistic forecasts. *Quarterly Journal of the Royal Meteorological Society*, **143**, 3037–3047.

Rigby, M., R. Timmis, and R. Toumi, 2006: Similarities of boundary layer ventilation and particulate matter roses. *Atmospheric Environment*, **40**, 5112–5124.

Rigby, M. and R. Toumi, 2008: London air pollution climatology: Indirect evidence for urban boundary layer height and wind speed enhancement. *Atmospheric Environment*, **42**, 4932–4947.

Robert, A., 1982: A semi-Lagrangian and semi-implicit numerical integration scheme for the primitive meteorological equations. *Journal of the Meteorological Society of Japan. Ser. II*, **60**, 319–325.

Robins, A. and C. McHugh, 2001: Development and evaluation of the ADMS building effects module. *International Journal of Environment and Pollution*, **16**, 161–174.

Ronda, R., G. Steeneveld, B. Heusinkveld, J. Attema, and A. Holtslag, 2017: Urban finescale forecasting reveals weather conditions with unprecedented detail. *Bulletin of the American Meteorological Society*, **98**, 2675–2688.

Rotach, M., 1993: Turbulence close to a rough urban surface. Part I: Reynolds stress. *Boundary-Layer Meteorology*, **65**, 1–28.

Roth, M., 2000: Review of atmospheric turbulence over cities. *Quarterly Journal of the Royal Meteorological Society*, **126**, 941–990.

Sabatino, S. D., R. Buccolieri, B. Pulvirenti, and R. E. Britter, 2008: Flow and pollutant dispersion in street canyons using FLUENT and ADMS-Urban. *Environmental Modeling & Assessment*, **13**, 369–381.

Salamanca, F., A. Krpo, A. Martilli, and A. Clappier, 2010: A new building energy model coupled with an urban canopy parameterization for urban climate simulations – part I. formulation, verification, and sensitivity analysis of the model. *Theoretical and applied climatology*, **99**, 331.

Salamanca, F., A. Martilli, M. Tewari, and F. Chen, 2011: A study of the urban boundary layer using different urban parameterizations and high-resolution urban canopy parameters with WRF. *Journal of Applied Meteorology and Climatology*, **50**, 1107–1128.

Salesky, S. T., M. Chamecki, and E. Bou-Zeid, 2017: On the nature of the transition between roll and cellular organization in the convective boundary layer. *Boundary-Layer Meteorology*, **163**, 41–68.

Salizzoni, P., M. Marro, L. Soulhac, N. Grosjean, and R. J. Perkins, 2011: Turbulent trans-

fer between street canyons and the overlying atmospheric boundary layer. *Boundary-Layer Meteorology*, **141**, 393–414.

Salizzoni, P., L. Soulhac, and P. Mejean, 2009: Street canyon ventilation and atmospheric turbulence. *Atmospheric Environment*, **43**, 5056–5067.

Santiago, J., O. Coceal, A. Martilli, and S. Belcher, 2008: Variation of the sectional drag coefficient of a group of buildings with packing density. *Boundary-Layer Meteorology*, **128**, 445–457.

Santiago, J. and A. Martilli, 2010: A dynamic urban canopy parameterization for mesoscale models based on computational fluid dynamics Reynolds-averaged Navier–Stokes microscale simulations. *Boundary-Layer Meteorology*, **137**, 417–439.

Savage, N. H., P. Agnew, L. S. Davis, C. Ordóñez, R. Thorpe, C. E. Johnson, F. M. O'Connor, and M. Dalvi, 2013: Air quality modelling using the Met Office Unified Model (AQUM OS24-26): model description and initial evaluation. *Geoscientific Model Development*, **6**, 353.

Schaap, M., et al., 2015: Performance of European chemistry transport models as function of horizontal resolution. *Atmospheric Environment*, **112**, 90–105.

Schlünzen, K. and R. Sokhi, 2008: Joint report of COST action 728 and GURME – overview of tools and methods for meteorological and air pollution mesoscale model evaluation and user training. World Meteorological Organization, accessed: 2021-02-28, `https://library.wmo.int/doc_num.php?explnum_id=9397`.

Schmid, M. F., G. A. Lawrence, M. B. Parlange, and M. G. Giometto, 2019: Volume Averaging for Urban Canopies. *Boundary-Layer Meteorology*, **173**, 349–372.

Schmidt, H. and U. Schumann, 1989: Coherent structure of the convective boundary layer derived from large-eddy simulations. *Journal of Fluid Mechanics*, **200**, 511–562.

Schoetter, R., Y. T. Kwok, C. de Munck, K. K. L. Lau, W. K. Wong, and V. Masson, 2020: Multi-layer coupling between SURFEX-TEB-v9. 0 and Meso-NH-v5. 3 for modelling the urban climate of high-rise cities. *Geoscientific Model Development*, **13**, 5609–5643.

Seinfeld, J. H. and S. N. Pandis, 2016: *Atmospheric chemistry and physics: from air pollution to climate change*. John Wiley & Sons.

Seity, Y., P. Brousseau, S. Malardel, G. Hello, P. Bénard, F. Bouttier, C. Lac, and V. Masson, 2011: The AROME-France convective-scale operational model. *Monthly Weather Review*, **139**, 976–991.

Simón-Moral, A., A. Dipankar, M. Roth, C. Sánchez, E. Velasco, and X.-Y. Huang, 2020: Application of MORUSES single-layer urban canopy model in a tropical city: Results from Singapore. *Quarterly Journal of the Royal Meteorological Society*, **146**, 576–597.

Simón-Moral, A., J. L. Santiago, and A. Martilli, 2017: Effects of unstable thermal stratification on vertical fluxes of heat and momentum in urban areas. *Boundary-Layer Meteorology*, **163**, 103–121.

Skamarock, W. C., et al., 2019: A Description of the Advanced Research WRF Version 4. NCAR Tech. Note NCAR/TN-556+STR.

Slowik, J., et al., 2011: Photochemical processing of organic aerosol at nearby continental sites: contrast between urban plumes and regional aerosol. *Atmospheric Chemistry and Physics*, **11**, 2991–3006.

Smagorinsky, J., 1963: General circulation experiments with the primitive equations: 1. The basic experiment. *Monthly Weather Review*, **91**, 99–164.

Sofiev, M., P. Siljamo, I. Valkama, M. Ilvonen, and J. Kukkonen, 2006: A dispersion modelling system SILAM and its evaluation against ETEX data. *Atmospheric Environment*, **40**, 674–685.

Soulhac, L., G. Lamaison, F.-X. Cierco, N. B. Salem, P. Salizzoni, P. Méjean, P. Armand, and L. Patryl, 2016: SIRANERISK: modelling dispersion of steady and unsteady pollutant releases in the urban canopy. *Atmospheric Environment*, **140**, 242–260.

Soulhac, L., P. Salizzoni, F.-X. Cierco, and R. Perkins, 2011: The model SIRANE for atmospheric urban pollutant dispersion; part I, presentation of the model. *Atmospheric Environment*, **45**, 7379–7395.

Soulhac, L., P. Salizzoni, P. Mejean, D. Didier, and I. Rios, 2012: The model SIRANE for atmospheric urban pollutant dispersion; part II, validation of the model on a real case study. *Atmospheric Environment*, **49**, 320–337.

Staniforth, A. and J. Côté, 1991: Semi-Lagrangian integration schemes for atmospheric models—A review. *Monthly Weather Review*, **119**, 2206–2223.

Stockie, J. M., 2011: The mathematics of atmospheric dispersion modeling. *SIAM Review*, **53**, 349–372.

Stockwell, W., P. Middleton, and P. Chang, 1990: The second generation regional acid deposition model chemical mechanism for regional air quality modeling. *Journal of Geophysical Research: Atmospheres*, **95**, 16 343–16 367.

Stull, R. B., 2012: *An introduction to boundary layer meteorology*. Springer Science & Business Media.

Sullivan, P. P., C.-H. Moeng, B. Stevens, D. H. Lenschow, and S. D. Mayor, 1998: Structure of the entrainment zone capping the convective atmospheric boundary layer. *Journal of the Atmospheric Sciences*, **55**, 3042–3064.

Takimoto, H., A. Sato, J. F. Barlow, R. Moriwaki, A. Inagaki, S. Onomura, and M. Kanda, 2011: Particle image velocimetry measurements of turbulent flow within outdoor and indoor urban scale models and flushing motions in urban canopy layers. *Boundary-Layer Meteorology*, **140**, 295–314.

Taylor, A. C., R. J. Beare, and D. J. Thomson, 2014: Simulating dispersion in the evening-transition boundary layer. *Boundary-Layer Meteorology*, **153**, 389–407.

Taylor, G. I., 1922: Diffusion by continuous movements. *Proceedings of the London Mathematical Society*, **2**, 196–212.

Tennekes, H., 1977: Observations on the dynamics and statistics of simple box models with a variable inversion lid (for air quality simulation). *Symposium on Atmospheric Turbulence, Diffusion, and Air Quality, 3 rd, Raleigh, N. C*, 397–402.

Tennekes, H., 1979: The exponential lagrangian correlation function and turbulent diffusion in the inertial subrange. *Atmospheric Environment*, **13**, 1565–1567.

The Environment Agency, 2008: Review of modelling methods of near-field acid deposition. Accessed: 2017-06-26, `https://www.gov.uk/government/uploads/system/uploads/attachment_data/file/290995/scho0508bobz-e-e.pdf`.

Thomson, D., 1987: Criteria for the selection of stochastic models of particle trajectories in turbulent flows. *Journal of Fluid Mechanics*, **180**, 529–556.

Thomson, D. and J. Wilson, 2012: History of Lagrangian stochastic models for turbulent dispersion. *Lagrangian Modeling of the Atmosphere*, 19–36.

Topçu, N., B. Keskinler, M. Bayramoğlu, and M. Akcay, 1993: Air pollution modelling in Erzurum city. *Environmental Pollution*, **79**, 9–13.

Townsend, A., 1980: *The structure of turbulent shear flow*. Cambridge University Press.

UK Met Office, 2012: Surface analysis charts. Accessed: 2020-10-30, `http://www1.wetter3.de/archiv_ukmet_dt.html`.

UN, 2018: The 2018 Revision of the World Urbanization Prospects, Population Division of the United Nations Department of Economic and Social Affairs (UN DESA). Accessed: 2020-10-30, `https://www.un.org/development/desa/publications/2018-revision-of-world-urbanization-prospects.html`.

Vardoulakis, S., B. E. Fisher, K. Pericleous, and N. Gonzalez-Flesca, 2003: Modelling air quality in street canyons: a review. *Atmospheric Environment*, **37**, 155–182.

Venkatram, A. and A. J. Cimorelli, 2007: On the role of nighttime meteorology in modeling dispersion of near surface emissions in urban areas. *Atmospheric Environment*, **41**, 692–704.

Wang, W., 2014: Analytically modelling mean wind and stress profiles in canopies. *Boundary-Layer Meteorology*, **151**, 239–256.

Watanabe, T. and J. Kondo, 1990: The influence of canopy structure and density upon the mixing length within and above vegetation. *Journal of the Meteorological Society of Japan. Ser. II*, **68**, 227–235.

Webster, H. and D. Thomson, 2018: NAME– Model Description. User Guide for NAME, UK Met Office.

Weckwerth, T. M., T. W. Horst, and J. W. Wilson, 1999: An observational study of the evolution of horizontal convective rolls. *Monthly Weather Review*, **127**, 2160–2179.

Weil, J., 1990: A diagnosis of the asymmetry in top-down and bottom-up diffusion using a Lagrangian stochastic model. *Journal of the Atmospheric Sciences*, **47**, 501–515.

Weil, J. C., W. H. Snyder, R. E. Lawson, and M. S. Shipman, 2002: Experiments on buoyant plume dispersion in a laboratory convection tank. *Boundary-Layer Meteorology*, **102**, 367–414.

Wesely, M., 1989: Parameterization of surface resistances to gaseous dry deposition in

regional-scale numerical models. *Atmospheric Environment*, **23**, 1293–1304.

Wesely, M. and B. Hicks, 2000: A review of the current status of knowledge on dry deposition. *Atmospheric Environment*, **34**, 2261–2282.

Whitaker, S., 1999: *The Method of Volume Averaging. Theory and applications of transport in porous media*. Springer, Dordrecht.

WHO, 2005: Air Quality Guidelines – Global Update 2005. Accessed: 2020-10-30, `https://www.euro.who.int/__data/assets/pdf_file/0005/78638/E90038.pdf?ua=1`.

Williams, M., R. Barrowcliffe, D. Laxen, and P. Monks, 2011: Review of air quality modelling in DEFRA. DEFRA Air Quality Modeling Steering Group, accessed: 2021-02-28, `https://uk-air.defra.gov.uk/assets/documents/reports/cat20/1106290858_DefraModellingReviewFinalReport.pdf`.

Williams, M. D., M. J. Brown, B. Singh, and D. Boswell, 2004: QUIC-PLUME theory guide. Los Alamos National Laboratory, accessed: 2021-02-28, `https://www.lanl.gov/projects/quic/quicplume.shtml`.

Willis, G. and J. Deardorff, 1974: A laboratory model of the unstable planetary boundary layer. *Journal of the Atmospheric Sciences*, **31**, 1297–1307.

Willis, G. and J. Deardorff, 1976: A laboratory model of diffusion into the convective planetary boundary layer. *Quarterly Journal of the Royal Meteorological Society*, **102**, 427–445.

Willis, G. and J. Deardorff, 1979: Laboratory observations of turbulent penetrative-convection planforms. *Journal of Geophysical Research: Oceans*, **84**, 295–302.

Willis, G. E. and J. W. Deardorff, 1981: A laboratory study of dispersion from a source in the middle of the convectively mixed layer. *Atmospheric Environment*, **15**, 109–117.

Wilson, J. D. and B. L. Sawford, 1996: Review of lagrangian stochastic models for trajectories in the turbulent atmosphere. *Boundary-Layer Meteorology*, **78**, 191–210.

Wilson, N. R. and R. H. Shaw, 1977: A higher order closure model for canopy flow. *Journal of Applied Meteorology*, **16**, 1197–1205.

Wise, E. K. and A. C. Comrie, 2005: Meteorologically adjusted urban air quality trends in the Southwestern United States. *Atmospheric Environment*, **39**, 2969–2980.

Wood, C., et al., 2010: Turbulent flow at 190 m height above London during 2006–2008: a climatology and the applicability of similarity theory. *Boundary-Layer Meteorology*, **137**, 77–96.

Wood, N., et al., 2014: An inherently mass-conserving semi-implicit semi-Lagrangian discretization of the deep-atmosphere global non-hydrostatic equations. *Quarterly Journal of the Royal Meteorological Society*, **140**, 1505–1520.

Wyngaard, J. C., 2004: Toward numerical modeling in the "Terra Incognita". *Journal of the Atmospheric Sciences*, **61**, 1816–1826.

Wyngaard, J. C. and R. A. Brost, 1984: Top-down and bottom-up diffusion of a scalar in the convective boundary layer. *Journal of the Atmospheric Sciences*, **41**, 102–112.

Xie, S., Y. Zhang, L. Qi, and X. Tang, 2003: Spatial distribution of traffic-related pollutant concentrations in street canyons. *Atmospheric Environment*, **37**, 3213–3224.

Xie, Z. and I. P. Castro, 2006: LES and RANS for turbulent flow over arrays of wall-mounted obstacles. *Flow, Turbulence and Combustion*, **76**, 291.

Xie, Z.-T. and I. P. Castro, 2009: Large-eddy simulation for flow and dispersion in urban streets. *Atmospheric Environment*, **43**, 2174–2185.

Xie, Z.-T., O. Coceal, and I. P. Castro, 2008: Large-eddy simulation of flows over random urban-like obstacles. *Boundary-Layer Meteorology*, **129**, 1.

Xie, Z.-T. and V. Fuka, 2018: A note on spatial averaging and shear stresses within urban canopies. *Boundary-Layer Meteorology*, **167**, 171–179.

Yoshida, T. and T. Takemi, 2018: Properties of mixing length and dispersive stress in airflows over urban-like roughness obstacles with variable height. *Scientific Online Letters on the Atmosphere*, **14**, 174–174.

Zerroukat, M. and T. Allen, 2012: A three-dimensional monotone and conservative semi-Lagrangian scheme (SLICE-3D) for transport problems. *Quarterly Journal of the Royal Meteorological Society*, **138**, 1640–1651.

Zerroukat, M. and T. Allen, 2015: On the monotonic and conservative transport on overset/Yin–Yang grids. *Journal of Computational Physics*, **302**, 285–299.

Zerroukat, M. and B. Shipway, 2017: ZLF (Zero Lateral Flux): a simple mass conservation method for semi-Lagrangian-based limited-area models. *Quarterly Journal of the Royal Meteorological Society*, **143**, 2578–2584.

Zhang, J. P., et al., 2012a: The impact of circulation patterns on regional transport pathways and air quality over Beijing and its surroundings. *Atmospheric Chemistry and Physics*, **12**, 5031–5053.

Zhang, Y., 2008: Online-coupled meteorology and chemistry models: history, current status, and outlook. *Atmospheric Chemistry and Physics*, **8**, 2895–2932.

Zhang, Y., M. Bocquet, V. Mallet, C. Seigneur, and A. Baklanov, 2012b: Real-time air quality forecasting, part I: History, techniques, and current status. *Atmospheric Environment*, **60**, 632–655.

Zhong, J., X.-M. Cai, and W. J. Bloss, 2015: Modelling the dispersion and transport of reactive pollutants in a deep urban street canyon: Using large-eddy simulation. *Environmental Pollution*, **200**, 42–52.

Zhong, J., X.-M. Cai, and W. J. Bloss, 2016: Coupling dynamics and chemistry in the air pollution modelling of street canyons: A review. *Environmental Pollution*, **214**, 690–704.